Low Density Plasma Waveguides for Multi-GeV Laser Wakefield Accelerators

Alexander Picksley

St John's College, University of Oxford

Abstract

Particle accelerators are vital tools for discovery in the fields of medicine, engineering, life sciences and physics. These machines, however, are becoming increasingly large, technically challenging to construct, and uneconomical. Laser wakefield accelerators (LWFAs) provide immense accelerating fields, and offer the potential to reduce the size of particle accelerators by a factor of 1000, though several challenges are yet to be overcome. One such challenge is the development of a low density plasma waveguide capable of guiding high-intensity laser pulses of distances up to a metre to form the basis of a multi-GeV LWFA stage. It has been shown that Hydrodynamic Optical-Field-Ionsied (HOFI) plasma channels can support low-density LWFA stages operating at a high repetition rate ($f_{\mathrm{rep}} \gtrsim 1\,\mathrm{kHz}$).

This thesis focuses on the development of low density, HOFI plasma channels through experiments and simulation. Optical guiding is demonstrated of laser pulses with a peak input intensity of $6 \times 10^{17}\,\mathrm{W\,cm^{-2}}$ through 100 mm long plasma channels with on-axis densities measured to be as low as $n_{\mathrm{e0}} = (1.0 \pm 0.3) \times 10^{17}\,\mathrm{cm^{-3}}$. It is found that the attenuation lengths of HOFI plasma channels were limited by the channel depth and radial extent to $L_{\mathrm{att}} \lesssim 100\,\mathrm{mm}$.

To account for this, a new method for extending such plasma channels to the metre-scale is proposed. Through transverse interferometry measurements taken as the guided pulse arrives, it is shown that a neutral collar of gas which surrounds the initial HOFI channel is ionised by the guided pulse. The attenuation length increased instantaneously from $L_{\mathrm{att}} = (15 \pm 8)\,\mathrm{mm}$ to $L_{\mathrm{att}} = (0.42 \pm 0.01)\,\mathrm{m}$. Particle-in-cell simulations demonstrate that the leading edge of a conditioning pulse injected into this structure ionises the neutral gas in its transverse wings, forming a deep plasma channel which guides the bulk of the pulse with low propagation losses.

Design of an experiment employing a metre-scale CHOFI plasma channel and of electron acceleration to the multi-GeV level is presented, including a novel gas cell design. Simulations

demonstrating propagation and electron acceleration in CHOFI plasma channels for the first time are discussed. Two different injection mechanisms capable of injecting electrons without significantly increasing experimental complexity are considered — ionisation injection, and density transition injection. It is shown that electron bunches with peak energies $\Delta W = 3.57\,\mathrm{GeV}$ with a relative energy spread of just $2.5\,\%$ can be generated.

It is clear that CHOFI plasma channels are likely to be very well suited to high repetition rate, multi-GeV LWFA stages.

Acknowledgments

It is without doubt that the past four years have been the most interesting and challenging of my life. First and foremost, I thank Simon for being such a brilliant supervisor and mentor, and for giving me so many great opportunities. The countless discussions via zoom, in-person and email, and late-night phone calls whilst on experiment have taught me so much about laser-plasma physics, and how to become a better scientist. Even through some strange circumstances, you have consistently gone above and beyond. I must also thank Roman in the same way, for providing such great insights and discussions, especially when I tried my hand at simulations.

A highlight of my time in the Oxford LPA group has been the great people I have had to work with along the way. Back when I first joined, I am indebted to Rob and to Chris for mentoring me and helping me get off the ground running in my first months. There have been so many late night shifts and 4pm tea breaks made better by everyone who I have worked with in the Oxford LPA group — Laura, Jimmy, Aaron, James Cowley, James Chappell, Rob, Chris, Jakob, Alex VB, Aimee, Oscar, Warren, Emily and Linus. It's been an absolute pleasure to work alongside every one of you.

I also acknowledge useful discussions and experimental help from all the people I've collaborated with over the last four years — Howard, Bo and Linus from the University of Maryland, Laura, Harry and Lewis from the Liverpool group, Stefan, Andreas and Katinka from the Munich group, and Nicolas and Chris Thornton at RAL. My thanks go out to everyone in the field who I've had such fruitful discussions in places ranging from the Lamb and Flag to the beach in Elba. Matt Streeter, Charlotte Palmer, Stuart Mangles, and Stefan Karsch have all been so helpful in teaching me experimental skills, and improving my understanding.

To my mum, my dad, my Grandad, and everyone else in my family, I thank you for always being supportive and helping me get through the last four years. To my friends Gav, Niki

and Andrew, I thank you for being there always and almost as long as I can remember. I hope that I can repay you over the years to come. To all the friends I've made in Oxford, Ben, Laure, Silas, Guy, Rob H, Samvida, Anna, you've made my time in this lovely city so brilliant and full of excitement. To Oscar and Ben, my running buddies, thanks for getting me out of bed in the morning and for the many kms.

Above all, thanks to Ria for being the most amazing and wonderful person, and for being so caring and thoughtful every step of the way.

List of Publications

Shalloo, R. J., Arran, C., **Picksley, A.,** Boetticher, A. Von, Corner, L., Holloway, J., Hine, G., Jonnerby, J., Milchberg, H. M., Thornton, C., Walczak, R., Hooker, S. M. *Physical Review Accelerators and Beams*, **22**(4), 41302. (2019)

"Low-density hydrodynamic optical-field-ionized plasma channels generated with an axicon lens"

https://doi.org/10.1103/PhysRevAccelBeams.22.041302

Ross, A. J., Alejo, A., von Boetticher, A., Cowley, J., Holloway, J., Jonnerby, J., **Picksley, A.,** Walczak, R., and Hooker, S. M. *Journal of Physics: Conference Series*, **1596**, 012049. (2020)

"Numerical modelling of chromatic effects on axicon-focused beams used to generate HOFI plasma channels"

https://doi.org/10.1088/1742-6596/1596/1/012049

Picksley, A., Alejo, A., Cowley, J., Bourgeois, N., Corner, L., Feder, L., Holloway, J. Jones, H., Jonnerby, J., Milchberg, H. M., Reid, L. R., Ross, A. J., Walczak, R., and Hooker, S. M. *Physical Review Accelerators and Beams*, **23**(8), 81303. (2020)

"Guiding of high-intensity laser pulses in 100mm-long hydrodynamic optical-field-ionized plasma channels"

https://doi.org/10.1103/PhysRevAccelBeams.23.081303

Picksley, A., Alejo, A., Shalloo, R. J., Arran, C., von Boetticher, A., Corner, L., Holloway, J. A., Jonnerby, J., Jakobsson, O., Thornton, C., Walczak, R., and Hooker, S. M. *Physical Review E*, **102**(5), 53201. (2020)

"Meter-Scale, Conditioned Hydrodynamic Optical-Field-Ionized Plasma Channels"

https://doi.org/10.1103/PhysRevE.102.053201

Jonnerby, J., Bourgeois, N., Corner, L., Holloway, J., **Picksley, A.,** Ross, A. J., Walczak, R., and Hooker, S. M., *Manuscript in preparation*
"Measurements of Ion Motion in Laser Wakefield Accelerators."

Alejo, A., Cowley, J., **Picksley, A.,** Walczak, R., and Hooker, S. M., *Submitted*
"Demonstration of kilo-Hertz operation of Hydrodynamic Optical-Field-Ionized Plasma Channels."

Contents

List of Figures

List of Tables

Chapter 1

Introduction

1.1 Advanced Accelerator Concepts

Particle accelerators, machines that use electric fields to increase the energy of charged particles, have become vital tools for discovery in the fields of medicine, engineering, life sciences and physics. Since the first particle accelerator was constructed by Cockroft and Walton in 1932 [1], accelerators have underpinned scientific development; a recent study claimed that around $28\,\%$ of all Nobel Prizes awarded in Physics had a direct contribution from accelerator physics [2].

Medical particle accelerators constitute around a third of the 40,000 particle accelerators worldwide, providing cancer treatments and advanced medical imaging techniques [3]. A further $64\,\%$ are used in industry, providing beams for imaging jet-engine parts, producing consumer electronics, and several other applications. At the energy frontier of particle accelerators, machines are used for research in a wide number of scientific disciplines including high-energy physics, materials science, engineering, and life sciences. Light sources, such as the Diamond Light Source in the United Kingdom, harness the power of electrons with energies around 3 to 10 GeV to produce bright X-ray light that can be used to study a wealth of different samples. The highest energy accelerators drive particle colliders, such as the Large Hadron collider at CERN, which smash together particles with energies up to 10's

of TeV, and allow physicists to probe the fundamental building blocks of Nature.

Conventional particle accelerators rely on chains of radiofrequency (RF) cavities to generate the large electric fields required to accelerate charged particles. These cavities are fundamentally limited by the maximum field that can exist inside the cavity; when the electric field exceeds around $100\,\mathrm{MV\,m^{-1}}$, electrical breakdown occurs in the cavity, and acceleration is disrupted. This means that light sources and energy frontier particle colliders are becoming increasingly large, technically challenging to construct, and expensive.

For almost a century, developing and adopting novel accelerator physics technologies has advanced the field of particle accelerators and paved the way for subsequent discovery in other fields of physics. In a seminal paper by Tajima and Dawson in 1979 [4] it was noted that the interaction of a high-intensity laser pulse with a plasma, a fluid comprised of free electrons and ions, could generate accelerating fields 1000 times larger than those produced by RF cavities, allowing facilities to be significantly reduced in both size and cost. This was the birth of the laser plasma accelerator (LPA).

The principle idea is that the laser's intense electric field $\vec{E}$ imparts a force on the free electrons in the plasma called the ponderomotive force $\vec{F}_{\mathrm{pond}}$, pushing them away from regions of high laser intensity. For a laser of wavelength λ

$$\vec{F}_{\mathrm{pond}} = -\frac{e^2\lambda^2}{16\pi^2 m_{\mathrm{e}} c^2}\nabla\vec{E}^2, \tag{1.1}$$

where $e = 1.602 \times 10^{-19}\,\mathrm{C}$ and $m_{\mathrm{e}} = 9.109 \times 10^{-31}\,\mathrm{kg}$ are the electron charge and mass respectively. The heavier ions remain stationary on these timescales, and thus a charge separation is generated. Once the laser has passed, the charge separation acts to pull the electrons back towards the laser axis, and they begin to oscillate, generating a longitudinal electron plasma wave.

The characteristic frequency at which the electrons oscillate depends solely on the plasma

density n_e and is known as the plasma frequency

$$\omega_p = \sqrt{\frac{n_e e^2}{m_e \epsilon_0}}, \tag{1.2}$$

where ϵ_0 is the permittivity of free space.

When the free electrons oscillate and charge separation occurs, drastically higher electric fields than conventional cavities can be sustained because the media is already ionised and "broken down". The maximum field that can be sustained can be estimated by the cold wavebreaking field

$$\begin{aligned} E_{wb} &\approx \frac{m_e c \omega_p}{e} \\ &\approx 100\sqrt{n_e\ [\mathrm{cm}^{-3}]}\ [\mathrm{V\,m}^{-1}]. \end{aligned} \tag{1.3}$$

For example the maximum field for $n_e = 10^{18}$ cm^{-3} is ~ 100 GV m^{-1}, around 1000 times larger than the maximum field that can be sustained in RF cavities.

1.1.1 Early Progress in Laser Plasma Acceleration

When Tajima and Dawson first proposed their "Laser electron accelerator", they realised that intense lasers with pulse durations τ_L of 100 fs or less would be required, since the ideal pulse duration occurs when τ_L is half the plasma period, $\omega_p \tau_L \approx \pi$ [4]. With these systems unavailable, the first laser-driven plasma accelerators were formed by plasma beat-wave acceleration (PBWA) using Nd:Glass and CO_2 laser systems [4, 5]. In this scheme, two co-propagating laser pulses with frequencies ω_1 and ω_2 beat to give a modulated laser pulse $\Delta\omega = \omega_2 - \omega_1$. The modulation frequency can be matched to the plasma frequency $\Delta\omega \approx \omega_p$ to excite the wakefield. The first observation of plasma wave generation via this scheme was achieved by Clayton *et al.* in 1985 [6] using a CO_2 laser, and acceleration of electrons was observed in a PBWA in 1992 [7]. PBWA suffers the problem that the beat-wave shifts out of resonance as the plasma wakefield amplitude increases and electron motion becomes

relativistic [5, 6].

In the self-modulated laser wakefield accelerator (SM-LWFA), a single long laser pulse is modulated at the "local" plasma frequency. This scheme utilises the fact that long laser pulses focus and defocus in regions of low and high electron density respectively [8]. Unlike PBWA, modulation is driven by the local oscillation of the plasma, hence is automatically resonant with ω_p and remains resonant as motion becomes relativistic. Electron acceleration in this scheme has been demonstrated, but the energy spectra are typically very broad [9–11].

In 2002, simulations showed that there existed a robust regime of acceleration (the "bubble regime") in which in which the longitudinal and transverse dimensions of the focused laser pulse were smaller than λ_p. Provided a_0 is sufficiently large, the $\vec{F}_{pond}$ is large enough to completely expel electrons, forming an ion cavity behind the laser pulse, ideal for acceleration. Some of the expelled electrons are self-injected back into the back of the cavity, trapped, and accelerated to produce a quasi-monoenergetic electron beam. In 2004, three separate groups demonstrated quasi-monoenergetic $\sim$ 100 MeV electron beams by operating in this regime [12–14].

The progress in the electron beam energy following this, has been rapid, and is shown in figure 1.1. In 2006, the use of a plasma waveguide to guide the laser pulse over 33 mm and increase the acceleration length resulted in the first GeV electron beams being demonstrated [15]. Aided by increasing laser power available, and improved knowledge of the laser-plasma interaction, electrons reaching the multi-GeV level have been generated [16–19]. Today, the highest reported electron beam energy from a LWFA is $7.8\,\mathrm{GeV}$ [19].

1.2 Physics of Laser Wakefield Acceleration

To understand the physics of laser wakefield generation, it is necessary to consider the propagation of electromagnetic waves in a plasma. This section provides a short outline of the physics of laser wakefield accelerators (LWFAs), illustrates the limitations to acceleration, and introduces concepts that will be used throughout the thesis. More detailed theoretical

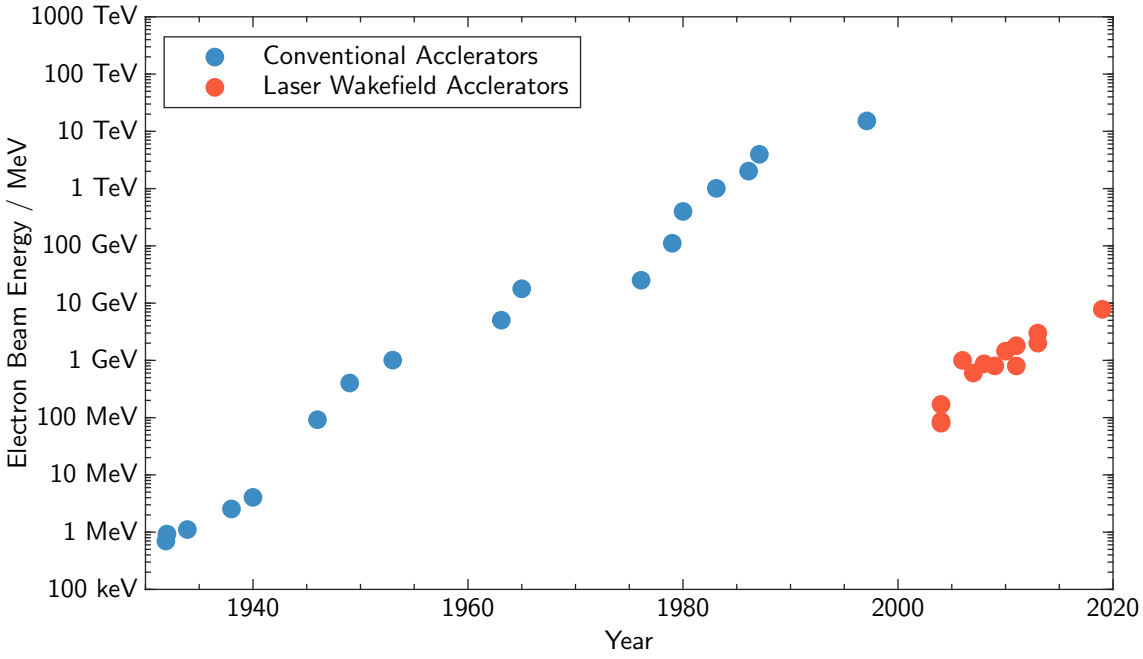

Figure 1.1: Livingston plot showing the growth in the energy gain of conventional lepton accelerators (blue) and laser wakefield accelerators (red) [12–25]

reviews are available [26–28]. An important parameter in the discussion of intense laser-plasma interactions is the normalised vector potential of the laser $\vec{a} = e\vec{A}/(m_e c^2)$ where $\vec{A}$ is the vector potential of the laser. The peak amplitude of $\vec{a}$ is called the laser strength parameter a_0 and is related to the peak intensity I_{peak} and wavelength of the drive laser; for a linearly polarised laser pulse, it can be approximated by

$$a_0 \approx 8.85 \times 10^{-10} \lambda\ [\mu m] \sqrt{I_{peak}\ [W\,cm^{-2}]}. \tag{1.4}$$

1.2.1 Operating Regimes

Linear Regime

In the linear regime, where $a_0 < 1$ and the the amplitude of the electron density perturbation $\delta n_e / n_e \ll 1$, the generation of a cold electron wave can be derived using the fluid equations

[26, 29]

$$m_e\left(\frac{\partial \vec{v}}{\partial t} + (\vec{v}\cdot\nabla)\vec{v}\right) = -e(\vec{E} + \vec{v}\times\vec{B}), \tag{1.5}$$

$$\frac{\partial n_e}{\partial t} + \nabla\cdot(n_e\vec{v}) = 0, \tag{1.6}$$

and Gauss' law

$$\nabla\cdot\vec{E} = \frac{e}{\epsilon_0}(n_e - n_i), \tag{1.7}$$

where $\vec{v}$ is the electron velocity, $\vec{E}$ and $\vec{B}$ are the electric and magnetic fields respectively, and n_i is the number density of the stationary ions. It can be shown that [29] in the non-relativistic limit, the transverse component of the electron velocity is given by $\vec{v_\perp} = e\vec{A}/m_e$. And hence the momentum equation can be re-written as

$$-m_e(\vec{v}\cdot\nabla)\vec{v} - e(\vec{v}\times\vec{B}) = -\frac{e^2}{2m_e}\nabla\left|\vec{A}\right|^2, \tag{1.8}$$

which is the linear ponderomotive force stated in section 1.1. To derive the linear wake equation, the fluid equations and Gauss' law are expanded in small quantities about their equilibrium values by setting $n_e = n_0 + \delta n_e$. Linearity is enforced by setting terms containing higher orders of small quantities to zero. This gives

$$\left(\frac{\partial^2}{\partial t^2} + \omega_p^2\right)\frac{\delta n}{n_e} = -\frac{c^2}{2}\frac{\partial^2 a_0}{\partial z^2}, \tag{1.9}$$

indicating that the plasma wave is a driven oscillator with natural frequency ω_p and the driver being the gradient of the ponderomotive force. It is normal to transform to a co-moving

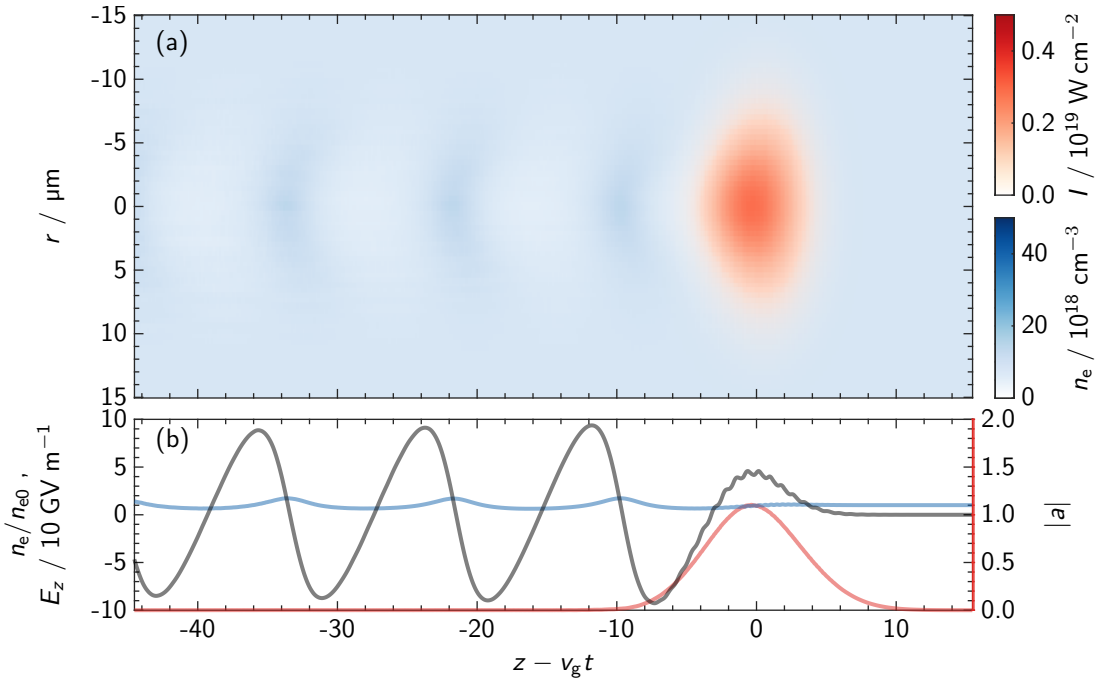

Figure 1.2: Simulation of a LWFA operating in the linear regime carried out in FBPIC. (a) Transverse laser and plasma profiles. The laser driver (red) has a spot-size $w_0 = 10\,\mu$m, and normalised peak vector potential $a_0 = 1.0$. It can be seen that a plasma wave is driven by the laser pulse as $\vec{F}_{\text{pond}}$ expels electrons from the cavity behind the laser pulse. (b) Lineouts along the optical axis of the laser normalised vector potential (red), the density perturbation (blue) and the longitudinal electric field (grey). The density perturbation and electric field are periodic, and close to sinusoidal.

co-ordinate system $\xi = z - ct$, $\tau = t$ in which case the density perturbation becomes

$$\left(\frac{\partial^2}{\partial\xi^2} + k_p^2\right)\delta n_e = -\frac{n_e}{2}\frac{\partial^2 a_0}{\partial\xi^2}. \tag{1.10}$$

In the co-moving frame, Gauss' law implies $\vec{E}$ is also sinusoidal with a wavelength λ_p. Figure 1.2 shows the generation of a linear wake by a laser with $a_0 = 1.0$ and $\tau_L = 40\,$fs. In this regime, where the wakefield is approximately sinusoidal, independent control of the longitudinal and transverse focusing forces is in principle possible by controlling the shape of the laser profile.

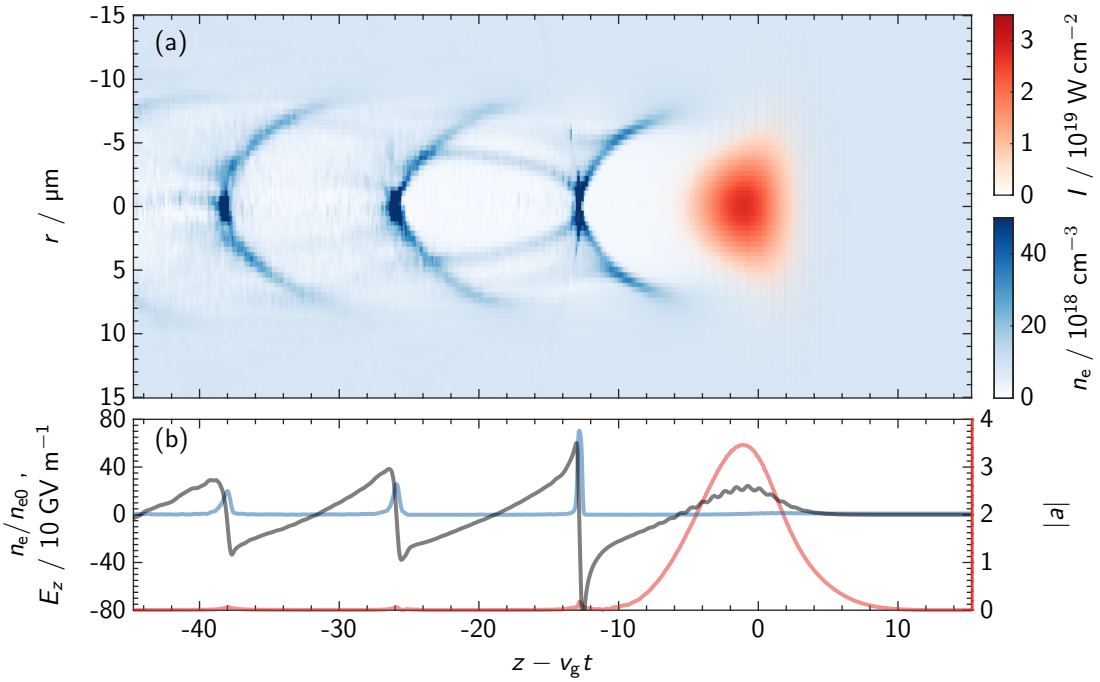

Figure 1.3: Simulation of a LWFA operating in the non-linear regime carried out in FBPIC. (a) Transverse laser and plasma profiles. The laser driver (red) has a spot-size $w_0 = 10\,\mu$m, and normalised peak vector potential $a_0 = 2.0$. It can be seen that a significant plasma wave is driven by the laser pulse as $\vec{F}_{\text{pond}}$ expels almost all of the electrons from the cavity behind the laser pulse. (b) Lineouts along the optical axis of the laser normalised vector potential (red), the density perturbation (blue) and the longitundinal electric field (grey). Rather than sinusoidal, the electric field now has a sawtooth-like profile.

Non-linear Regime

A number of methods have been derived to extend the model of wakefield generation to incorporate a fully relativistic 1D wake, either from first principles as above [26, 29, 30], or using a Hamiltonian method [31]. However, the general case of arbitrary drive laser strength has no 3D-solution, and hence phenomenological scalings based on particle-in-cell calculations (see section 3.4.1) are employed [30, 32].

Rather than a sinusoidal plasma wave, the intense laser expels a significant number of electrons from the cavity behind it, resulting in a sawtooth profile of the wakefield (see figure 1.3). At high enough intensities, the electrons are completely expelled, generating an ion cavity. In turn, $\vec{E}$ is no longer sinusoidal, for $a_0 \gtrsim 2$, it can be approximated as a linear

function of z.

1.2.2 Limitations on Energy Gain

Diffraction

In any focused laser pulse, diffraction reduces the intensity after a certain distance. To achieve the high intensities required for LWFAs using lasers currently available, spot sizes of around $10\,\mu m$ to $100\,\mu m$ are required. For a focused Gaussian laser pulse, where the intensity profile $1/e^2$ radius in vacuum is w_0, the spot size evolution with propagation along the optical axis z is given by

$$w(z) = w_0 \sqrt{1 + \left(\frac{z}{z_R}\right)^2}, \tag{1.11}$$

where

$$z_R = \frac{\pi w_0^2}{\lambda}, \tag{1.12}$$

is the Rayleigh range — the distance over which the spot size increases from w_0 to $\sqrt{2}w_0$. It is thus simple to show that the intensity varies along the laser axis as

$$I(0, z) = \frac{I_{peak}}{1 + (z/z_R)^2}. \tag{1.13}$$

In vacuum, over one z_R, the peak intensity drops by a factor of 2 and therefore unless diffraction is mitigated with a mechanism to guide the focused pulse over many Rayleigh lengths, the laser pulse can only drive a significant wakefield over $L_{acc} \sim z_R$.

Electron Dephasing

Electrons trapped in a plasma wakefield reach velocities closer to c than the laser group velocity. This means that electron bunches will catch up with the laser pulse and eventually outrun the wakefield, entering a decelerating phase of the wakefield. The distance over which an electron can travel before it enters the decelerating and defocusing field is called the dephasing length L_d. In the linear regime, this corresponds to the distance over which a relativistic electron phase slips by $\lambda_\mathrm{p}/4$, hence

$$L_\mathrm{d} \approx \frac{\lambda_\mathrm{p}}{2}\frac{\omega^2}{\omega_\mathrm{p}^2}. \tag{1.14}$$

To date, electron dephasing is the main limitation of energy gain in LWFAs. For a drive laser with $\lambda = 800\,\mathrm{nm}$, the electron dephasing length is limited to $L_\mathrm{d} \approx 0.93\,\mathrm{mm}$ for a density of $n_\mathrm{e} = 10^{19}$ cm^{-3}, but extends to $L_\mathrm{d} \approx 0.93\,\mathrm{m}$ for $n_\mathrm{e} = 10^{17}$ cm^{-3}.

Pump Depletion

During propagation, the laser energy is transferred to the wake, depleting its energy. Eventually, the laser energy will be completely depleted and the acceleration ends. The length over which this occurs is the pump depletion energy L_pd. By considering the energy density in the wake $(1/2)\epsilon_0 E_z^2$ which contained in the volume $\pi w_0^2 L_\mathrm{pd}$, and the laser energy density $(1/2)\epsilon_0 E_0^2$ which is contained in the volume $\pi w_0^2 c\tau_\mathrm{L}$, the pump depletion length in the linear regime can be approximated as

$$L_\mathrm{pd} \approx \frac{\lambda_\mathrm{p}}{a_0^2}\frac{\omega^2}{\omega_\mathrm{p}^2}, \tag{1.15}$$

which, like electron dephasing scales as $L_\mathrm{pd} \propto 1/n_\mathrm{e}^{3/2}$.

1.2.3 Modulation of Intense Pulses in Plasma

When a high intensity laser pulse ($a_0 \gtrsim 1$) propagates through a plasma, it modifies the plasma density via the ponderomotive force. The leading order motion of the electrons is the quiver motion $\vec{p}_\perp = m_e c\vec{a}$, hence $\gamma_\perp = \sqrt{1+a^2}$. It should be emphasised that since γ and ω can be affected by the dynamical response of the plasma to laser propagation, the refractive index of the plasma η is a non-linear function of $\vec{E}(x,y,z)$, and the laser propagation is intensity dependent. The theoretical framework for high-intensity pulse propagation in ionising gases and plasmas has been studied in detail since the late 1980's, and there exist excellent reviews by Esarey *et al.* [26, 33], and Mori [34] that discuss mathematical treatments.

In the weakly-relativistic limit, the refractive index can be expanded to first order [33], and is given by

$$\eta \approx 1 - \frac{\omega_p^2}{2\omega^2}\left(1 + \frac{\Delta n_e}{n_0} + \frac{\delta n_e}{n_0} + \frac{a_0^2}{4}\right), \tag{1.16}$$

where the local density perturbation has been split into two terms, one describing the effect of a preformed plasma channel $\Delta n_e/n_0$ (see section 1.2.3), and one the local density perturbation due to the ponderomotive expulsion of electrons $\delta n_e/n_0$.

Relativistic Self-Focusing and Ponderomotive Self-Channelling

The final term $a_0^2/4$ describes the influence of the relativistic electron gamma factor $\gamma_\perp$ on the local refractive index. For a focused laser pulse, the intensity is significantly higher at the centre than in the wings of the pulse, thus $\gamma_\perp$ decreases away from the axis of the laser pulse. Parts of the laser pulse further from axis experience a larger phase velocity, resulting in a wavefront curvature (and thus curvature of the Poynting vector). This effect, known as relativistic self-focusing counteracts the natural diffraction of the laser pulse and can allow the pulse to be guided and sustain high I_{peak} over several z_R.

The threshold for relativistic self-focusing is found by equating self-focusing with diffraction

in equation 1.16 leading to the condition [34, 35]

$$a_0^2 w_0^2 \geq \frac{32c^2}{\omega_p^2}. \tag{1.17}$$

This can be associated to a critical power P_{crit} above which self-focusing can occur

$$\begin{aligned} P_{crit} &= \frac{8\pi\epsilon_0 m_e^2 c^5 \omega^2}{e^2 \omega_p^2} \\ &= 17.4 \frac{\omega^2}{\omega_p^2} \text{ [GW]}. \end{aligned} \tag{1.18}$$

A laser pulse with power P focused to a spot-size w_0 in plasma diffracts if $P < P_{crit}$, remains guided for $P = P_{crit}$, and is focused for $P > P_{crit}$. Higher-order non-linearities prevent catastrophic self-focusing, and the spot-size oscillates. Experimental studies of this are discussed in section 2.2.

In addition, when $P > P_{crit}$, the ponderomotive force of the laser expels electrons from the the axis of propagation, changing the refractive index profile. This process is referred to as ponderomotive self-channelling [26, 36], and increases the self-focusing effect since the electron density on the axis becomes reduced. Relativistic self-focusing and ponderomotive self-channellling frequently occur together, and have been observed in several early LPA experiments [37–39] primarily in the SM-LWFA regime. It has also been shown that self-guiding of laser pulses generates a plasma channel in which a subsequent pulse can be guided [39].

Plasma Waveguides

Diffraction is one of the most fundamental problems with accelerating electrons in LWFAs. Without a guiding mechanism, acceleration is limited to a distance of approximately z_R. Extension of the acceleration length of LWFAs can be achieved by a plasma waveguide. These are plasma structures that can act like optical fibres for high-intensity laser pulses, applying a focusing effect to the laser pulse to mitigate diffraction. In an ideal waveguide,

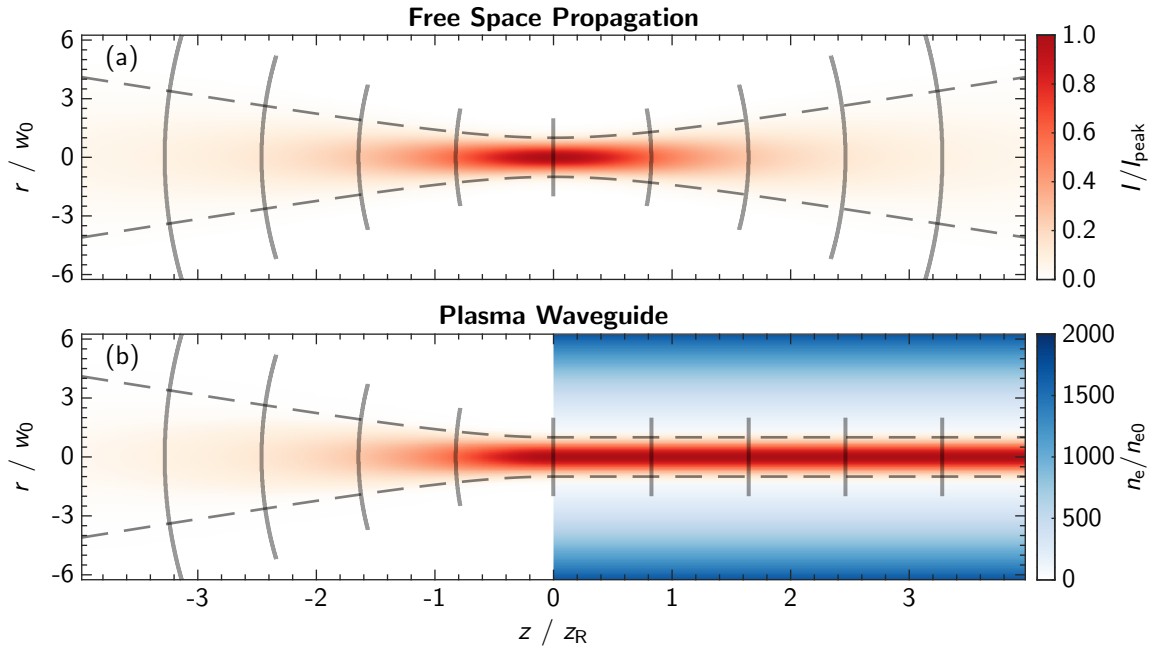

Figure 1.4: (a) Example of a Gaussian beam diffracting in free space (red). The wavefronts are shown in grey, and are curved towards the axis when the beam is focusing, and away from the axis as the beam diffracts. The dashed lines are contours at $\pm 2w_0$. The beam remains intense for a distance of $\approx 2z_R$. (b) Example of a Gaussian beam focusing into an infinite parabolic plasma waveguide (blue). The electron density is minimised on axis, increasing radially outwards to counteract the diffracting wavefronts.

an example of which is shown in figure 1.4, the effects of diffraction are perfectly cancelled out and the laser properties remain unchanged during propagation. By use of a plasma waveguide, acceleration up to the dephasing length is made possible, drastically increasing the potential electron energy gain. A detailed discussion of plasma waveguides is given in Chapter 2.

Temporal Pulse Modification

Following the treatment by Mori [34], changes of the refractive index along the propagation direction can be written in a similar form to the the transverse modification

$$\eta(\xi) \approx 1 - \frac{1}{2}\left(\frac{\omega_p}{\omega}\right)^2 \left(1 + \frac{\delta n_e(\xi)}{n_0} - \frac{a^2(\xi)}{2} - 2\frac{\delta\omega(\xi)}{\omega}\right), \tag{1.19}$$

where the second term accounts for the longitudinal variation in the laser intensity, and the last term describes the evolution of the pulse chirp. It can be shown that the modulation in frequency follows the local change in refractive index via

$$\frac{1}{\omega}\frac{\partial\omega}{\partial\tau} = -\frac{1}{\eta^2}\frac{\partial\eta}{\partial\xi}. \tag{1.20}$$

In a LWFA, where the laser pulse length $c\tau_\mathrm{L}$ is close to the plasma wavelength $c\tau_\mathrm{L} \lesssim \lambda_\mathrm{p}$, the leading edge of the laser pulse will be red shifted, whilst the falling edge of the laser pulse will be blue shifted, causing the laser spectrum to broaden, known as self-phase modulation. The $\delta n_\mathrm{e}(\xi)/n_0$ term corresponds to the local change in refractive index in the propagation direction caused by the leading edge of the laser pulse driving a plasma wave. This density slope results in the front of the pulse decelerating, and the back of the pulse accelerating, compressing the pulse. These have been observed in experiment [40–42] and can be approximated as

$$\tau_\mathrm{comp} = \tau_\mathrm{L} - \frac{n_0 L_\mathrm{acc} e^2}{2cm_\mathrm{e}\epsilon_0\omega^2}. \tag{1.21}$$

Spectral Modulations

If the pulse is shorter than $\lambda_\mathrm{p}/2$, then the pulse sits in the red-shifting phase of the wakefield [33]. If a pulse is propagating though a gas, and is intense enough to ionise the gas species (see section 2.7.1 for details on laser ionisation), but not intense enough to drive a significant wakefield ($a_0 \ll 1$), then the density gradient is opposite to that of LWFA, and the front edge of laser pulse experiences blue shift.

For pulse lengths $c\tau_\mathrm{L} \gg \lambda_\mathrm{p}$, such as those used in PBWA and SM-LWFA experiments, parts of the pulse are red-shifted, and parts are blue-shifted. Since these shifts are periodic, this leads to peaks that are evenly spaced in frequency space by ω_p. As well as contributing to the physics of LWFA, these spectral shifts are a useful tool for diagnosing wakefields (see Chapter 6).

1.2.4 Electron Injection

The injection of electrons into the wakefield significantly impacts the overall beam quality of the accelerated electrons. To accelerate an electron bunch whilst maintaining a small energy spread and emittance, it is necessary that a high-quality bunch is injected into the correct phase region of the wakefield with a bunch length that is small compared to the plasma wavelength. This corresponds to bunch lengths as low as as a few fs, an order of magnitude shorter than those typically produced by conventional accelerators.

LWFAs operating in the bubble regime have the advantage that electrons are self-injected into the ion cavity. For an experimentalist, this technique is the most straightforward approach since it simply relies on wavebreaking, and electrons at the back of the bubble finding themselves trapped [12, 30, 43]. The trouble with self-injection is that trapping can occur throughout the length of the accelerator, leading to electron beams with a large momentum spread. Furthermore, since the process relies on highly non-linear processes, many self-injection experiments lack shot-to-shot stability.

Instead, to produce low energy spread, low emittance electron bunches from a LWFAs, a method of controlled and localised injection is required. In contrast to self-injection, controlled injection schemes are suitable when the LWFA stage is operated below the wavebreaking limit. Many schemes have been presented to tackle this, and it is still an active area of research. The schemes can be arranged into three broad categories: (i) density transition injection; (ii) ionisation injection, and (iii) optical injection.

Density Transition Injection

Here, injection is triggered in the accelerator stage by tailoring the longitudinal density profile such that $\partial n_e/\partial z < 0$ at a defined position. The plasma wavelength elongates $\lambda_p \propto 1/n_e^{1/2}$ and the back of the plasma wave momentarily slows down, thus lowering the injection threshold and causing self trapping.

When the length of the density transition is longer than the plasma wavelength, $L_{tr} > \lambda_p$,

the wave is gradually slowed down and the scheme is known as down-ramp injection [44]. When $L_{tr} < \lambda_p$, the increase in λ_p is effectively instantaneous; a significant portion of the electrons that constituted the wakefield peak (the back of the bubble) suddenly find themselves in an accelerating phase of the wakefield and become trapped. Since the trapped electrons all find themselves in a similar phase of the wake, they are exposed to the same accelerating field, making this technique ideal for very low energy spread electron bunch generation. This technique has been investigated numerically [45–47] and experimentally [48–50]. Typically a razor blade is placed above a supersonic gas jet to generate a sharp, narrow shock front which gives the desired rapid change in density profile.

Ionisation Injection

Ionisation injection is triggered when a high-Z gas (such as nitrogen or argon) or a mixture of a low-Z and high-Z gas is used as the species for the accelerator stage [23, 51, 52]. Electrons on the innermost shell (K-shell) have a much larger ionisation potential than outer shells, or the valence electrons of low-Z gases, and hence the laser intensity required to ionise the electron I_{th} will be significantly higher (see section 2.7.1). Whilst almost all of the electrons are ionised by the far leading edge of a high intensity laser pulse, K-shell electrons that are ionised when $I_{th} \approx I_{peak}$ will find themselves close to an accelerating phase of the wakefield and can be injected [53].

Optical Injection

Optical injection encompasses schemes that employ a dedicated laser pulse to trigger electron injection into the accelerating structure. The first scheme proposed and demonstrated was colliding pulse injection [54] where a second laser pulse of lower intensity than the wakefield driver counter-propagates and beats with the main wakefield driver pulse. This beating causes localised and instantaneous heating of background electrons, some of which get injected into the wakefield of the driver pulse.

Other injection schemes have been proposed that use a co-propagating laser pulse that can ionise a dopant species at a localised position without affecting the wakefield of the driver pulse to produce electron bunches with ultra low emittance and low energy spread [55, 56].

Achieving High Energy Gain

The total energy gain of an electron is determined by the longitudinal electric field of the wake $E_z(z)$ and the acceleration distance L_{acc}

$$\Delta W = -e \int_0^{L_{\text{acc}}} E_z(z)\, \mathrm{d}z. \tag{1.22}$$

In the absence of diffraction, L_{acc} is limited by the smallest of the dephasing and pump depletion lengths. In the linear regime, dephasing limits L_{acc}, whilst in the non-linear regime, pump depletion often limits L_{acc}. However, if there is no guiding mechanism to overcome diffraction, then acceleration simply stops when the laser diffracts.

In the linear regime, with a plasma waveguide employed to guide the laser pulse,

$$\Delta W_{\text{max}} = 2\frac{m_{\text{e}}^2 c^2 \epsilon_0}{e^2}\frac{\omega^2}{n_{\text{e}}}, \tag{1.23}$$

which for a fixed laser wavelength and intensity, is only dependant on the plasma density. In the non-linear regime, ΔW_{max} is also inversely proportional to density. Combining equations 1.14 and 1.23 indicates that a $1\,$GeV stage can be achieved if the laser pulse is guided over $\sim 29\,$mm at a plasma density of $n_{\text{e}} = 10^{18}$ cm^{-3}. However, compared to a 1 GeV stage, a 10 GeV accelerator requires a decrease in the plasma density by an order of magnitude, and an increase in the accelerator length by a factor of 30. This places extremely challenging requirements on a plasma waveguide for a 10 GeV stage.

1.3 State of the Field

Compact laser driven particle accelerators, have become the subject of a vast global research effort covering many intricate parts of the interaction. These include understanding the complex laser-plasma interaction [57], increasing the electron beam energy [15, 16, 18, 19], measuring and improving the stability of LPAs [58, 59], increasing the repetition rate of LPAs [60, 61], electron injection [25, 49, 55, 56, 62], diagnosing the physics of plasma wakefields [57, 63], and applications of wakefield accelerators [64–67].

Figure 1.5 shows experimental scalings of LWFA experiments through reported results [12–25, 51, 52, 54, 67–83]. As one might expect, progress towards to higher electron energy gain ΔW has been driven by lower plasma densities, and increasing laser power available. A comparison between LWFA stages utilising plasma waveguides and those relying on relativistic self-focusing is shown in figure 1.5(a)-(c). The data suggests that LWFA stages employing plasma waveguides are more efficient in terms of laser power. Electron energy gain is compared for different injection mechanisms in figure 1.5(d). Most studies employ self-injection; of the controlled techniques, ionisation injection has produced the highest energy beams to date. The reason for this could be its simplicity to implement.

The common goal of these areas of research is an accelerator facility that can support users with electron (and positron) beams, and photon beams whilst offering significantly reduced size and cost than conventional accelerator facilities. A facility like this could have applications in hospitals, universities and also provide the next generation of particle acclerators for scientific discovery such as free electron lasers, or high-energy colliders.

For example, the EuPRAXIA project [84, 85] envisages a dedicated LWFA facility (along with beam driven plasma accelerator facilities) that is capable of driving a free electron laser in a total facility length of just 180 m. For this, a laser system containing $5 - 100$ J on target in pulse durations of $20 - 60$ fs and $f_{\text{rep}} = 20 - 100$ Hz is required. The LWFA stage will be $0.25 - 1$ m in length, at a density of $n_e = 1 \times 10^{17}$ cm^{-3}, to generate electron beams of up to 6 GeV with ~ 30 pC of charge, and $0.1 - 0.9\,\%$ energy spread. To achieve this, several

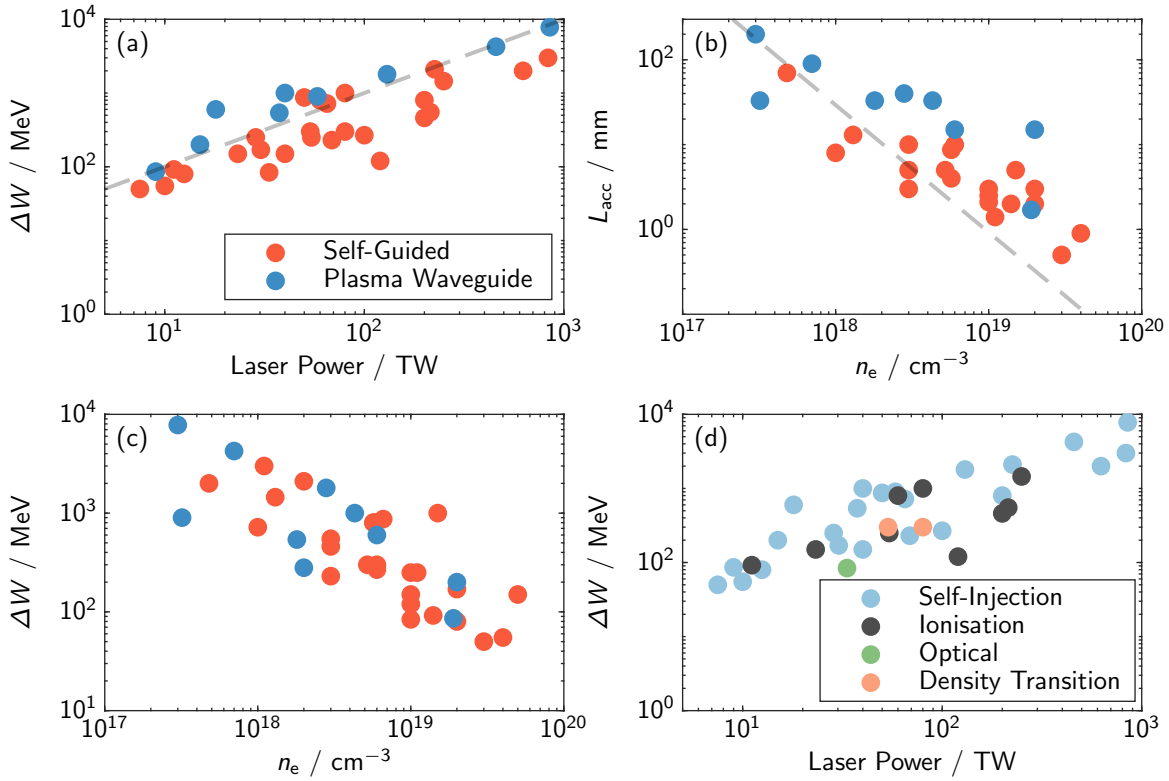

Figure 1.5: Experimental scalings from previous LWFA experiments [12–25, 51, 52, 54, 67–83]. (a)-(c) compares the use of plasma waveguides with experiments where self-guiding is relied upon, whilst (d) compares different injection techniques. (a) Reported electron energy gain ΔW as a function of drive laser power. The grey dashed line indicates an energy gain of $10\,\mathrm{MeV\,TW^{-1}}$. (b) Accelerator length as a function of plasma density. It is clear that longer accelerators require lower density. The grey dashed line indicates the linear regime dephasing length (equation 1.14). (c) The energy gain as a function of plasma density. As one expects, progress towards higher energy gain requires lower plasma density. (d) Same plot as (a) but comparing different injection schemes.

challenges still remain on each of these frontiers of the field.

1.3.1 Current Challenges

The latest conventional accelerators offer excellent beam quality with low energy spread and low emittance, highly stable and reproducible accelerated beams, and repetition rates f_{rep} up to MHz. LPAs aim to attain a similar bunch quality and stability.

Improving Stability and Control

Even when LPAs are operated in the quasilinear regime, there are non-linear aspects to the laser-plasma interaction, and to the injection schemes, resulting in large shot-to-shot fluctuations (jitter) in the accelerated electron bunch. Unlike conventional accelerators, LPAs generate a new accelerating cavity with every shot. Thus, small fluctuations in the experimental conditions can cause significant shot-to-shot variation in the electron-beam performance. Most electron acceleration experiments to date have exhibited energy jitter in the range of $1-5\,\%$, accelerated charge jitter of up to $50\,\%$, and beam pointing jitter between 0.5 and 3 mrad. These values are significantly larger than those produced by conventional accelerators.

A vital component to stabilising the accelerated electron bunches is controlling the injection into the accelerating structure. Excellent progress has been made in this area, with experimental results demonstrating low-energy spread beams at with peak energies of around 100 MeV using all three of the controlled injection schemes described in the previous section.

A second, vital requirement of generating stable and reproducible electron beams is a stable and reproducible drive laser. Shot-to-shot stability of TW and PW laser systems is increasing rapidly, with aided by the development and inclusion of active pointing stabilisation in the laser chain [86], however still remains an area for improvement. Recently, Maier *et al.* [58] demonstrated 24 hours of continuous operation of a $f_{\text{rep}} = 1$ Hz LPA with stable accelerated electron beams, and were able to correlate input laser and electron parameters by using a wealth of laser chain diagnostics. Importantly, they were able to predict electron energy drifts with accuracy better than $1\,\%$ based on the measured laser parameters. Following this, the use of Bayesian optimisation to improve the beam quality and stability of LWFAs has been demonstrated [59, 87].

Increasing Single Stage Electron Energy Gain

Since the dephasing length is shorter for higher plasma densities, increasing the energy gain in a single stage requires lower plasma densities. However, it is only possible to take advantage of lower n_e if the laser can drive a wakefield and maintain acceleration over the dephasing length, $L_{acc} \sim L_d$. Although self-focusing can extend the interaction length beyond z_R significantly, equation 1.18 indicates that the effect of self-focusing is suppressed at lower densities. If the laser pulse is guided by a plasma waveguide, n_e can be chosen for conditions where $L_d \gg z_R$ and $P \ll P_{crit}$. This provides the possibility for very high single stage energy gain.

Increasing the Repetition Rate and Efficiency of Driving Laser Systems

The lasers used to drive LPAs are typically joule-level Ti:sapphire chirped pulse amplification (CPA) systems (see section 3.1 for a detailed description) which operate at $f_{rep} \lesssim 1\,\text{Hz}$ with powers ranging from 10 TW to 1 PW and wall-plug efficiencies of less than $0.1\,\%$. The repetition rate and low efficiencies are limited by poor thermo-optical properties of the pump lasers. Increasing f_{rep} from $\sim 1\,\text{Hz}$ to a few kHz will require the development of new laser technology able to operate at substantially higher average powers and with significantly increased wall-plug efficiencies.

Advancing compact, high average power, high peak power laser technologies whilst also maintaining and improving shot-to-shot stability and laser pulse quality is a difficult challenge. Technologies under consideration are thin-disk and fibre-based lasers, and optical parametric chirped pulse amplification (OPCPA). It is also worth noting that driving the wakefield with a train of laser pulses spaced λ_p could reduce the energy required per driving laser pulse by an order of magnitude or more [88–90]. It may also be possible to drive stable LWFAs by incoherent combination of several laser pulses [91].

1.3.2 Future Applications

Synchrotron light sources are reliable sources of short radiation pulses that are tunable up to kilo-electron-volt photon energies, which make them useful for structural analysis of matter, and have applications across science. Demonstrations of soft undulator radiation from LWFAs has been achieved [64, 92], showing that these plasma accelerators are capable of significantly reducing the size and cost of synchrotron light source facilites. Importantly, due to the strong radial focusing forces in laser driven wakefields, trapped electrons undergo oscillations as they accelerate (betatron oscillations), and these radiation properties are similar to synchrotron light sources, decreasing the required accelerator length further.

The development of free-electron lasers (FELs) has led to a vast increase in the coherence and brilliance of the generated photons. Potentially the most promising application of LWFAs are compact FELs. Since electron beams generated in LWFAs are a few fs in length, compared to the ps lengths of conventional accelerators, LWFAs offer a significant further advantage to future FELs beside accelerating gradient [93]. A major obstacle for LWFA driven FELs is the comparably high initial values of divergence and energy spread. Very recently, FEL amplification using electrons from a laser wakefield accelerator was demonstrated for the first time [94].

In the longer term, it is possible that staging multiple LWFAs could provide beams for high-energy particle colliders. RF-based future collider designs are reaching even larger and drastically more expensive scales, though LWFAs could mitigate these practical size and cost limitations. Design studies for TeV-scale laser-driven particle colliders have been produced [95].

There also exists a wide range of other applications. In medical physics, plasma accelerators have been investigated for cancer treatment. While research in this field is still in the very early stages, very-high energy electron therapy (VHEET) [96, 97] and phase-contrast imaging (PCI) [65, 66] are of interest.

1.3.3 Advanced Accelerators Driven by Particle Beams

It is also possible to use a beam of high energy charged particles to generate a plasma wave suitable for acceleration. A particle bunch with high energy, travelling close to the speed of light generates a plasma wake capable of accelerating a witness bunch. The force here is not the ponderomotive force of the laser, but the space-charge force of the drive electron beam. Unlike laser pulses which travel at $v_g < c$, relativistic particle beam drivers travel close to c, hence the onset of dephasing is significantly delayed. Instead, pump depletion of the driver to the witness bunch limits the acceleration. Like LPAs, the field of beam-driven plasma wakefield acceleration is also growing, and a potential candidate for future advanced accelerators.

Unlike multi-TW and PW ultrashort pulse lasers which are commercially available, currently there exists only a few facilities worldwide capable of generating a high-quality electron bunch for beam-driven plasma wakefield studies. Therefore beam-driven plasma wakefield studies are less common. In 2007, the 42 GeV electron beam at SLAC (USA) was used to drive a strong plasma wake and accelerate the electrons at the back of this beam from 42 GeV up to 85 GeV in an 85 cm long plasma [98]. This is a remarkable energy gain when one considers that it took 3 km for the electrons to reach 42 GeV in the SLAC accelerator. Litos *et al.* improved on this, demonstrating significantly increased energy transfer efficiency (up to $30\,\%$) and reduced energy spread. The same facility has also been used to demonstrate the generation of a positron beam driven wakefield [99]. In 2018, the AWAKE experiment at CERN demonstrated acceleration of electrons in the plasma wakefield of a 400 GeV, self-modulated proton bunch [100].

1.4 Thesis Objectives

The development of plasma waveguides with properties suitable for LPAs has been an active area of research for several decades. This thesis focuses on the development of Hydrodynamic

Optical-Field-Ionised (HOFI) plasma channels, a type of waveguide first proposed by the group at the University of Oxford [101] as an extension to hydrodynamically formed, inverse bremsstrahlung heated plasma channels. Importantly, HOFI plasma channels can support low-density LWFA stages operating at a high repetition rate ($f_{\text{rep}} \gtrsim 1\,\text{kHz}$).

Prior to this work, the formation of, and guiding in, 16 mm long HOFI channels produced by an axicon lens, with an on-axis densities as low as $n_{\text{e0}} \approx 1.5 \times 10^{17}\,\text{cm}^{-3}$ has been demonstrated [102]. Guiding of a high intensity laser pulse was achieved at $f_{\text{rep}} = 5\,\text{Hz}$, limited by the available channel-forming laser and vacuum pumping system.

The objectives of this thesis are to:

1. examine the required properties of a plasma waveguide suitable for a multi-GeV LWFA stage;
2. form and guide high intensity laser pulses in $\gtrsim 100\,\text{mm}$ long HOFI plasma channels with axial densities $\sim 1 \times 10^{17}\,\text{cm}^{-3}$;
3. characterise and increase the guided laser transmission in HOFI plasma channels;
4. simulate multi-GeV stages formed using HOFI plasma channels;
5. develop experimental design for HOFI plasma channel experiments using PW-class laser facilities.

1.4.1 Outline of the Thesis

Progress towards these objectives is outlined in the following chapters.

Chapter 2 outlines the requirements of a plasma waveguide suitable for a multi-GeV LWFA accelerator stage operating at a high repetition rate. Techniques for generating these waveguides are compared and contrasted.

Chapter 3 describes the experimental and computational methods that are used throughout the thesis. This includes high-power laser pulses, experimental diagnostics, pulse propagation in plasma waveguides, and particle-in-cell simulations.

Chapter 4 reports results from the first experiment to employ HOFI plasma at PW scale laser facilities, undertaken at the TA3 Gemini laser at the Rutherford Appleton Laboratory (RAL). Generation of, and guiding in 100 mm long plasma channels is demonstrated.

Chapter 5 demonstrates through experiments and numerical simulations that low-density, low-loss, metre-scale plasma channels can be generated by employing a conditioning laser pulse to ionise the neutral gas collar surrounding a HOFI plasma channel.

Chapter 6 describes experimental design and particle-on-cell simulations of experiments intended to demonstrate guiding of PW scale laser pulses in conditioned HOFI (CHOFI) plasma channels, and accelerate electrons to multi-GeV levels.

1.4.2 Role of the Author

All of the experiments detailed in this thesis were performed by teams of scientists working together. The role of the author in those teams is outlined here.

For the experiment detailed in Chapter 4, the experimental design and planning was led by the author with specific contributions to the gas cell design from Dr. Aarón Alejo, and the probe beam design by Jakob Jonnerby and Barnaby Matthews. The experimental campaign was also led by the author, who was assigned the "Target Area Operator" role for the duration of the campaign. The team was comprised of: A. Picksley, A. Alejo, J. Cowley, N. Bourgeois, L. Corner, L. Feder, J. Holloway, H. Jones, J. Jonnerby, H. M. Milchberg, L. R. Reid, A. J. Ross, R. Walczak, and S. M. Hooker. The analysis of all experimental results presented here were written and performed by the author, with input from Dr. Aarón Alejo.

For the experiments detailed in Chapter 5, the design and setup was led by Dr. Robert Shalloo and Dr. Christopher Arran who acted as "Target Area Operators" for the experiment.

The experiment setup and data taking was carried out by R. J. Shalloo, C. Arran, A. Picksley, A. von Boetticher, L. Corner, J. Holloway, G. Hine, J. Jonnerby, H. M. Milchberg, C. Thornton, R. Walczak, and S. M. Hooker. The experimental analysis presented here was undertaken by the author, and further analyses has been presented in the thesis of Dr. Robert Shalloo [103]. The hydrodynamic simulations presented in this work were all undertaken by Dr. Aarón Alejo and are shown here for completion. The particle-in-cell simulations undertaken were all carried out by the author, with input from Dr. Aarón Alejo and Oscar Jakobsson.

For the experimental design detailed in Chapter 6, the design was carried out by the author with specific contributions from Aimee Ross and Oscar Jakobsson on the laser diagnostics, and James Cowley and Warren Wang on the electron diagnostics. The concept design of the novel large volume gas target is the work of the author, with significant input from Barnaby Matthews on the CAD drawing including making it variable length, and mounting the axicon lens. The particle-in-cell simulations were carried out by the author with input from Oscar Jakobsson and Emily Archer. The work on the truncated plasma channel injection scheme is that of the author.

A parallel experiment is being undertaken by the group at the University of Maryland to investigate multi-GeV acceleration in low density plasma channels. The author made a significant contribution to this through leading the simulation campaign, and input on options for electron injection.

The author made a significant contribution to the commissioning of the new OxfordX 25 TW laser system. Specifically on installation of laser chain diagnostics for alignment, probe beamline installation, alignment of the new vacuum compressor, and commissioning of the experimental chamber. The first experiments using the OxfordX laser are still ongoing.

Finally, the author made contributions to an experiment led by Jakob Jonnerby and Dr. James Holloway to investigate ion motion and the decay of linear wakefields through frequency domain holography. Specifically, the author was part of the experimental team for the eight-week campaign, and worked on pulse duration measurement diagnostics.

Chapter 2

Waveguides for Future Multi-GeV LWFA Stages

2.1 Requirements of a Waveguide for a Multi-GeV Stage

In conventional optics, continuous wave or low-power laser pulses can be guided over many Rayleigh lengths by use of an optical fibre, a technology that has become ubiquitous in everyday life. Most fibres are step-index, containing an inner core of a higher refractive index than the surrounding cladding. Light is confined to the core by total internal reflection at the boundary between the two layers. Optical fibres an also be gradient index, where refractive index $\eta(\lambda, r)$ is peaked on axis such that $\partial\eta/\partial r < 0$, and the phase fronts curve inwards, generating a focusing effect that can balance diffraction.

In an ionising gas or plasma, this picture becomes much more complex. High-intensity laser pulses experience diffraction, refraction, and nonlinear self-focusing as described in section 1.2.3. In turn, they also affect the local refractive index through ionisation; ponderomotive forces that lead to plasma wave generation; and heating, which leads to hydrodynamic motion of plasma. Since high-intensity, sub-picosecond laser pulses were first demonstrated, several different methods of mitigating diffraction of these focused pulses have been presented. Early proposed applications of guiding included nuclear fusion [104], pumping of X-ray lasers [105,

Intensity to be guided, I_{peak}	$\gtrsim 10^{18}$ W cm^{-2}
Matched spot-size, w_m	$10 - 100$ µm
Axial density, n_{e0}	$\lesssim 10^{17}$ cm^{-3}
Length, L_{acc}	$0.25 - 1$ m
Channel shape, $n_e(r)$	Tunable to match accelerator
Transmission $T(z = L_{acc})$	$\sim 100\,\%$
Gas species	Low-Z (H_2, He)
Repetition rate, f_{rep}	$\gtrsim 1$ kHz
Lifetime	$> 10^8$ shots
Stability	High
Energy cost	$\lesssim 10\,\%$ of total stage energy
Diagnostic access	Transverse and longitudinal

Table 2.1: Required performance characteristics of a plasma waveguide suitable for a multi-GeV LWFA accelerator stage.

106], and high-harmonic generation [107]. Today, the most prominent application is LWFA.

LWFAs require laser pulses with peak intensities close to or exceeding 1×10^{18} W cm^{-2}, which using today's TW- and PW-class laser systems requires laser pulses focused down to spot radii w_0 in the range 10 µm to 100 µm. This corresponds to a vacuum Rayleigh length z_R on the order of 0.3 mm to 30 mm. For accelerating gradients in the range of 10 GV m^{-1} to 40 GV m^{-1}, the acceleration distance required to attain 10 GeV electron bunches is $L_{acc} = 0.25 - 1$ m. Thus, in order to extend the interaction length to lengths comparable to L_{acc}, diffraction of the laser pulse must be mitigated and the pulse propagated over many Rayleigh lengths.

Additionally, to support a high repetition rate, multi-GeV laser wakefield accelerator stage, several other performance characteristics must be considered. A detailed list of these is displayed in table 2.1, each having immense impact on both the design of the accelerator stage and the long-term operation of the accelerator. First and foremost, it must be possible to access the low axial densities required to achieve multi-GeV acceleration in a single stage for laser spot radii in the range 10 µm to 100 µm. It must also be possible to generate a uniform waveguide of the required axial density and matched spot-size over lengths of up to ~ 1 m.

In order to prevent ionisation induced defocusing, the plasma must not be further ionised

by the guided laser pulse, and thus low-Z gases (e.g. hydrogen and helium) are required. Importantly, much like optical fibres, high-intensity laser pulses can suffer transmission and coupling losses due to the waveguide. These must be minimised as much as possible so that most of the energy loss goes towards driving the wakefield. To function as an accelerator, the limiting repetition rate must be $\geq 1\,\mathrm{kHz}$ and have a lifetime $\geq 10^8 - 10^9$ shots (8.6×10^7 shots corresponds to 24hr operation at 1 kHz) or be easily replaced under vacuum. Since fluctuations in the waveguide parameters described here could affect accelerated electron bunch parameters significantly, shot-to-shot stability and reliability of the plasma waveguide formation is of high importance. Finally, as with all accelerator components, the energy cost of operating the waveguide must be as low as possible, and certainly $\lesssim 10\,\%$ of the drive laser energy for each stage.

2.2 Self-Guiding of Ultrashort Pulses

Initially, one can ask the question — can we avoid an external guiding mechanism? With the difficult challenge of generating a preformed waveguide meeting the desired parameters, perhaps it can be avoided all together. As described in the last chapter, the last two terms of equation 1.16 indicate that the refractive index profile is altered by the laser intensity and the ponderomotive expulsion of electrons.

Relativistic guiding and ponderomotive self-channelling of laser pulses in gas jets and gas-filled chambers has been widely studied [37–39, 108], however the theory [109] was derived under the assumption that the laser pulse length $c\tau_\mathrm{L} > \lambda_\mathrm{p}$. It was asserted that relativistic self-focusing was ineffective at mitigating diffraction for pulses of lengths suitable for LWFA, because the index of refraction is modified on the laser frequnecy timescale (ω_p^{-1}) not the laser frequency timescale. Particle-in-cell simulations seemed to agree that ultrashort pulses could not be self-guided due to diffraction of the leading edge of the pulse.

However, in the early 1990's Decker *et al.* [110] suggested that self-guiding may be possible for ultrashort pulses. In 2007, Thomas *et al.* [111] demonstrated, for the first

time, self-guided propagation of ultrashort pulses ($c\tau_L < \lambda_p$) in 3 mm long helium gas jets at densities of $n_e \sim 1 \times 10^{19}\,\mathrm{cm}^{-3}$, and estimated that the size of the guided spot was approximately λ_p.

Theoretical work by Lu *et al.* [30, 32] provided further insight by outlining the required conditions for the blowout regime ($a_0 > 2$). When an ultrashort pulse of this intensity propagates through a uniform plasma, the electron density structure resembles a spherical cavity of radius r_b (the blowout radius). The leading edge of the pulse locally pump depletes, driving a wakefield, before it diffracts and the main body of the pulse is still self-guided. It can be shown that efficient self-guiding is achieved when the laser waist w_0 is matched to the blowout radius of the electrons

$$w_{sf} = \frac{2\sqrt{a_0}}{k_p}. \tag{2.1}$$

For $P/P_{crit} > 1$ and $w_0 > w_{sf}$, the laser pulse will self-focus to and remain at w_{sf}. Experiments by Ralph *et al.* [112] demonstrated guiding of ultrashort pulses, $\tau_L = (50 \pm 3)$ fs, in helium gas jets up to 8.5 mm long in plasma densities ranging from $n_e = 4 \times 10^{18}\,\mathrm{cm}^{-3}$ to $n_e = 1 \times 10^{19}\,\mathrm{cm}^{-3}$. Notably, the length over which guiding occurred matched closely to the non-linear pump depletion length, showing that the limit of self-guided propagation of ultrashort pulses was pump depletion of the laser pulse, and not diffraction of the leading edge.

Wang *et al.* [16] demonstrated self-guiding of 100 J, $\tau_{FWHM} = 160$ fs over 70 mm, generating electron beams with energies $\gtrsim 2$ GeV. The authors noted that exceptional spatial mode quality is required for efficient self-guiding and increase in electron beam energy. In 2018, Poder *et al.* [113] presented a detailed comparison of self-guiding over extended distances between $f/20$ and $f/40$ focusing geometries, in which they demonstrated self-guiding over 90 mm at $n_e = 9.5 \times 10^{17}\,\mathrm{cm}^{-3}$. The measured size of the guided spot as a function of plasma density was compared to scalings presented by Lu *et al.* (equation 2.1) [32], Sprangle *et al.* [109], and Thomas *et al.* ($w_0 \sim \lambda_p$) [111]. The $f/20$ data closely

matched the Lu scaling, however the $f/40$ data did not match any of the scalings. The authors suggested that due to near field imperfections, poor coupling of light into the guided filament occurred. This was exacerbated in the $f/40$ geometry for which the Rayleigh length was longer.

Self-guiding is a frequently employed technique in LWFA experiments owing to the ease with which it can be implemented. Auxiliary laser pulses or external waveguide structures are not required. Further, fulfilling the condition $P > P_{\text{crit}}$ often leads to self-injection of electrons into the wakefield, meaning more complex injection mechanisms are not required. However, as outlined in section 1.2.4, this leads to a lack of control over injection, and hence a large energy spread.

2.3 Hydrodynamic Plasma Waveguides formed by Inverse Bremsstrahlung

2.3.1 Channel Formation

The first successful technique for generating preformed plasma waveguides was pioneered by the group at the University of Maryland, College Park (UMD). In their first paper in 1993 [114], an auxiliary "channel-forming" laser pulse with $\tau_{\text{FWHM}} \approx 100\,\text{ps}$ and peak intensities around $10^{13} - 10^{14}\ \text{W}\,\text{cm}^{-2}$ was focused by an axicon lens to form a J_0 Bessel beam and ionise a high-Z gas (Ar, Xe or N_2) [115]. The axicon lens generated a plasma column around 1 cm in length, and heated electrons via inverse bremsstrahlung (IB). After the laser had passed, some electrons were subsequently further ionised by collisional ionisation. A well-defined boundary emerged between the hot plasma on-axis, and the surrounding neutral gas, which in turn caused a large pressure gradient. The plasma electrons expanded radially outwards at the speed of sound, dragging the colder ions with them, and a shock front was formed due to collisions between the ions in the expanding plasma and atoms in the weakly ionised surrounding gas. The decreased axial electron density and the radially increasing

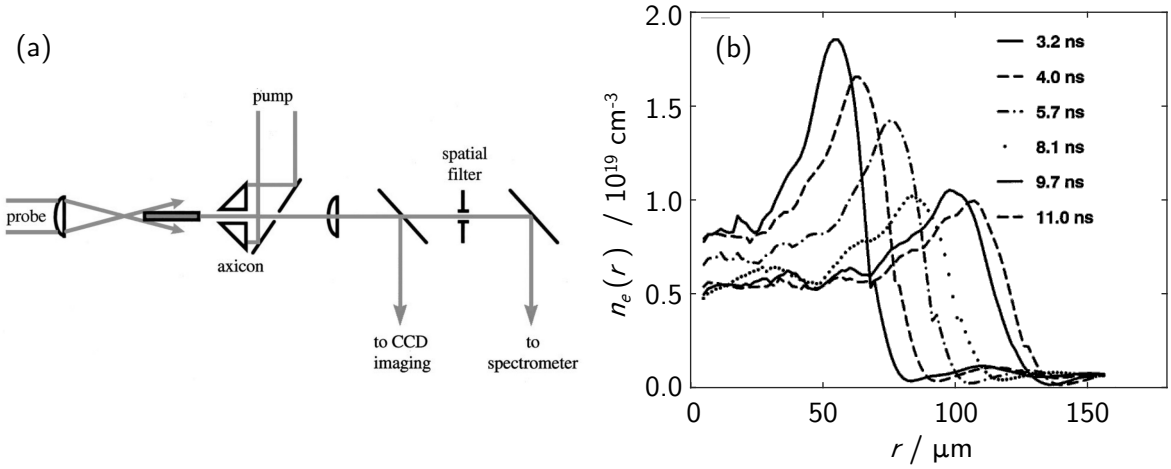

Figure 2.1: (a) Example setup of a guiding experiment in a hydrodynamic plasma channel formed by inverse bremsstrahlung heating. The channel-forming (pump) pulse is focused by an axicon from the right, and forms the cm-scale plasma channel. The counter-propagating guided (probe) pulse is focused by a lens from the left. The guided laser at the exit of the plasma channel is reimaged onto a CCD. Reprinted with permission from [116]. Copyright 2000 by the American Physical Society. (b) First reported measurements of the electron density profile evolution of a hydrodynamic plasma channel, obtained via transverse interferometry. Reprinted with permission from [117]. Copyright 1997 by the American Physical Society.

density to the shock front formed a gradient refractive index waveguide.

Pulses with energies up to 40 mJ were split from the channel forming laser using a beamsplitter and focused to a spot radius of 10 µm at the opposite end of the axicon line focus (see figure 2.1). With the "channel-forming" laser present, the measured spot radius at the end of the waveguide was 25 µm, compared to 240 µm without the laser present, thus demonstrating guiding over approximately 24 Rayleigh lengths.

At low pressures (< 65 mbar) ionisation during the laser pulse was attributed to field ionisation, leading to ionisation out to 10 µm [114, 115, 118]. For higher pressures, it was found that avalanche ionisation contributed more significantly to the ionisation; the average level of ionisation of each atom increased, and occurred out to around 30 µm.

The first direct measurements of plasma waveguides were undertaken by the same group in 1997 [117]. Via interferometry, axial densities of $n_{e0} = 5 \times 10^{18}$ cm^{-3} to $n_{e0} = 1 \times 10^{19}$ cm^{-3}

were measured. The shock front radius as a function of time showed good agreement with the Sedov-Taylor theory for expansion of a cylindrical blast wave (see section 3.2.2) and was strongly dependent on the initial plasma electron temperature T_e^{init}. The blast wave travelled outwards at the local ion sound speed

$$c_s = \sqrt{\frac{\langle Z \rangle k_B T_e}{m_i}}, \tag{2.2}$$

where $\langle Z \rangle$ is the average ionisation level. The thickness of the shock front scaled approximately inversely with the plasma density. It was found, consistent with hydrodynamic simulations, that initially $T_e = 80\,\text{eV}$, and this quickly decreases as the shock rapidly expands. After 350 ps, it was already 20 eV and after 2 ns, $T_e < 5\,\text{eV}$.

2.3.2 High-Intensity Guiding

Guiding high-intensity laser pulses ($I_{\text{peak}} > 1 \times 10^{17}\,\text{W cm}^{-2}$) of femtosecond duration was demonstrated by focusing 10 mJ, 90 fs pulses from a Ti:Sapphire laser system into hydrodynamic plasma channels [119]. Only around 30 % energy transmission was achieved due to poor coupling of the guided pulse at the entrance of the waveguide. The intensity and density-dependent heating mechanism caused the plasma channels to narrow significantly at the entrance and exit where the laser intensity dropped significantly. This reduced the matched spot size and preventing light from being coupled in. Additionally, since the target was a backfill chamber, the high-intensity guided pulse ionised gas as it was being brought to the focus, resulting in ionisation induced refraction and further reducing the amount of light coupled into the waveguide.

Some of these problems were reduced by using a gas jet [120, 121], and coupling efficiencies up to 50 % were achieved. However, the undesired taper at the entrance was still present due to the pressure transition between the vacuum and gas jet.

2.3.3 Issues and Proposed Fixes

Tapered Plasma Channels

Kim *et al.* [122] accounted for channels narrowing at the entrance by employing a funnel-ended waveguide. The entrance of the plasma channel was ionised by a second channel-forming pulse that arrived up to $10\,\mathrm{ns}$ before the main channel-forming pulse. Improved coupling of a guided pulse, $\tau_{\mathrm{FWHM}} \approx 70\,\mathrm{fs}$ and $I_{\mathrm{peak}} \approx 1 \times 10^{17}\,\mathrm{W\,cm^{-2}}$, was inferred by measuring the guided mode at the end of the plasma channel, however this solution increases the complexity of these experiments.

Low-Z Gases

The channels demonstrated by UMD were only partially ionised. Further ionisation could result in wakefield drive pulses incurring ionisation-induced defocusing, or unwanted ionisation injection. To overcome this, the group at Lawrence Berkeley National Laboratory (LBNL) proposed the ignitor-heater technique [123] in which hydrogen gas was first field-ionised (ignited) by an ultrashort laser pulse with $\tau_{\mathrm{FWHM}} \lesssim 100\,\mathrm{fs}$ and $I_{\mathrm{peak}} \approx 5 \times 10^{14}\,\mathrm{W\,cm^{-2}}$, and then heated through inverse bremsstrahlung by a longer, lower intensity pulse. In the first experimental demonstration, the ignitor and heater pulses were focused by cylindrical optics to generate line foci, forming a one-dimensional plasma channel. Guiding of lasers pulses with $I_{\mathrm{peak}} = 5 \times 10^{17}\,\mathrm{W\,cm^{-2}}$ was demonstrated in one dimension only, over $10 z_{\mathrm{R}}$.

In 2000, Gaul *et al.* [124] proposed an alternative technique to generate fully ionised plasma channels. In that paper, helium gas was ionised by an electrical discharge rather than via field-ionisation by an auxiliary laser pulse, and subsequently heated by a $0.3\,\mathrm{J}$, $\tau_{\mathrm{FWHM}} = 100\,\mathrm{ps}$ laser pulse. A laser pulse with peak intensity $I_{\mathrm{peak}} \approx 1 \times 10^{17}\,\mathrm{W\,cm^{-2}}$ was guided over $15\,\mathrm{mm}$ with a transmission efficiency of $50\,\%$.

Clustered Gases

Since rapid collisional ionisation of the plasma is a strong function of the initial gas density, it is difficult to generate plasma channels with axial densities $\lesssim 5 \times 10^{18}\,\mathrm{cm}^{-3}$. At this density, the dephasing length is a few mm, and maximal energy gain is severely limited.

A solution to this is to use clustered gases, which due to their local density being 1000 times higher than monoatomic gases of the same density, exhibit much higher absorption of laser pulse energy and more efficient heating of the plasma electrons. Waveguide formation in clustered gases was first demonstrated by Ditmire *et al.* [125] in 1998 by focusing $2\,\mathrm{ps}$ laser pulses into argon clusters of average diameter $8\,\mathrm{nm}$ (corresponding to ~ 5000 atoms per cluster). A prepulse with peak intensity $I_{\mathrm{peak}} \sim 10^{13}\ \mathrm{W\,cm}^{-2}$ ionised the Ar^{2+} $15\,\mathrm{ps}$ before the main pulse, generating a plasma channel in which the main pulse was guided.

In 2005, Kumarappan *et al.* [126] demonstrated that clustered gases could be used in order to reduce the axial density of collisionally heated plasma channels, and eliminate tapering at the entrance and exit of the plasma channel. A $70\,\mathrm{fs}$ pump pulse was focused by an $f/5$ lens into an 8 mm long cluster jet, which formed a plasma throughout the jet due to self-focusing in the cluster gas medium [127, 128], and a following probe pulse, $I_{\mathrm{peak}} = 3 \times 10^{17}\,\mathrm{W\,cm}^{-2}$, also focused by an $f/5$ lens was guided through the plasma channel with a coupling efficiency of up to $50\,\%$. The same experiment was also able to demonstrate a $3\,\mathrm{mm}$ long, fully ionised, hydrogen cluster target, however the coupling efficiency of the guided pulse was limited to just $5\,\%$. The minimum axial density measured in these plasma channels was $n_{\mathrm{e0}} \approx 1 \times 10^{18}\,\mathrm{cm}^{-3}$ [126, 129].

2.4 Ponderomotive Plasma Channels

Another method for generating a plasma waveguide with an auxiliary laser pulse is via ponderomotive plasma channels [39, 130]. In 1997, Krushelnick *et al.* [39] observed the formation of a plasma waveguide by a self-guided laser using a $2\,\mathrm{TW}$ laser pulse of duration

$\tau_{\mathrm{FWHM}} \approx 0.4\,\mathrm{ps}$. The channel-forming pulse was focused to an intensity of approximately $6 \times 10^{18}\,\mathrm{W\,cm^{-2}}$ at the front a 2 mm long hydrogen gas jet of density $n_{\mathrm{e}} = 10^{19}\,\mathrm{cm^{-3}}$, and self-guided over the length of the jet due to relativistic self-focusing and ponderomotive self-channelling (see section 1.2.3). A trailing probe laser pulse was observed was observed to guide over $20z_{\mathrm{R}}$ for delays up to $50\,\mathrm{ps}$ after the channel-forming pulse. It's spot-size at the exit was found to closely match that of the input spot. The formation of a plasma waveguide was attributed to the ponderomotive force of the channel-forming pulse it propagated through the plasma, driving ions outwards to leave a plasma channel.

Further studies directly measured the emission of energetic ions transverse to the direction of propagation of the channel-forming pulse [131–133]. For example, in 1999, Krushelnick *et al.* [131] directly measured the emission of energetic helium ions from a similar experiment in which a 50 J laser pulse, duration $0.9\,\mathrm{ps}$ was self-guided through a 4 mm long helium gas jet of density $5 \times 10^{19}\,\mathrm{cm^{-3}}$. Ions with energies exceeding 300 keV were observed primarily at $90\,\mathrm{deg}$ to the propagation of the self-guided pulse. In that paper, they noted that the self-focusing mechanism was not stable shot-to-shot due fluctuations density gradients in the gas jet, in the input spatial profile of the laser pulse. Further measurements by Wei *et al.* [133] using laser pulses exceeding $I_{\mathrm{peak}} = 3 \times 10^{20}\,\mathrm{W\,cm^{-2}}$ demonstrated the production of helium ions with energies of $13.2\,\mathrm{MeV}$. Particle-in-cell simulations indicated that channels with a axial density depression of around $70\,\%$ could be formed as the electrons and ions shocked outwards (simulations employed an initial density of $n_{\mathrm{e}} = 1.4 \times 10^{20}\,\mathrm{cm^{-3}}$).

2.5 Capillary Tubes

Dielectric capillary tubes with optically smooth inner surfaces act as step-index waveguides; laser beams are guided by internal reflections from the capillary wall, making it possible to achieve guiding in vacuum or low-density plasma [134–136]. Since the guiding mechanism is independent of the laser power and the initial plasma density, capillary tubes offer a large degree of flexibility. Initial experimental parameters can be determined solely by the needs of

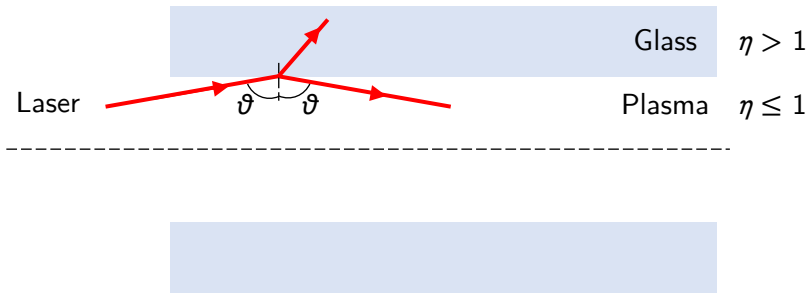

Figure 2.2: Capillary tube with a glass wall and containing plasma; the laser reflects from the inner walls.

the accelerator.

Solving Maxwell's equations for a refractive index profile of this type results in a set of eigenmodes described by Bessel functions (EH_{1m} modes), each with their own group velocity. An incident Gaussian pulse can be coupled in and excite these modes [137]. Each reflection from the dielectric wall results in a loss associated with refraction of the pulse inside the dielectric wall, leading to a power attenuation length for each mode that scales with R_{cap}^3. Higher order modes attenuate faster; the length of the stage is limited by this power attenuation length and the subsequent laser transmission.

It can be shown that 98 % of an incident incident Gaussian beam can be coupled into the lowest order mode of the capillary tube when $R_{\text{cap}} \approx 1.55 w_0$. In this case, 1 % of the energy is coupled into higher order modes, whilst 1 % of the energy is lost into the front surface of the capillary. For an Airy beam (the transverse profile achieved from focusing a flat-top laser pulse), the maximum amount of energy that can be coupled into the lowest order mode is only 83 %.

This technique was first demonstrated in 1995 by the group at the Naval Research Laboratory [134], who guided 900 fs, 1 TW laser pulses in hollow, glass capillaries. Cylindrical capillaries of 50 µm radius by 3 cm in length, and 133 µm radius by 12.6 cm in length were used, with peak measured output intensities of approximately 10^{16} W cm^{-2}. For the shorter capillaries, only two capillary modes were excited, whilst up to 8 were excited in the longer

capillary tubes. In 1999, Dorchies *et al.* [135] demonstrated single mode, high-intensity guiding over 100 Rayleigh lengths using hollow, glass capillary tubes. 1 J, 900 fs laser pulses focused to peak intensities $2 \times 10^{17}\,\mathrm{W\,cm^{-2}}$ were guided through a 126 mm-long capillary with 26 % energy transmission, though the mode quality a the exit was poor. Transmissions measured for different values of R_{cap} matched well with theoretical predictions.

Laser Induced Damage

One of the clear limitations of grazing-incidence capillaries is damage. This occurs at the front surface due to light that does not couple in, and to the inner surface upon reflections. To examine the latter, Cros *et al.* [137] considered the ratio of the radial component of the Poynting vector at the capillary wall (which determines energy dissipated in the dielectric) to the longitudinal Poynting vector on-axis. If all laser energy is coupled into the fundamental mode, the limiting intensity that can be guided without ionisation of the glass wall is around $1 \times 10^{19}\,\mathrm{W\,cm^{-2}}$ ($a_0 \approx 2.1$). Higher order modes dissipate energy into the capillary faster, reducing the limiting intensity. The measured lifetime of capillaries in experiments reported to date is short. In an early study of electron acceleration the lifetime without active stabilisation of the input laser was just 100 shots [138, 139], but increased significantly with active stabilisation.

2.6 Capillary Discharge Waveguides

2.6.1 Early Developments

Plasma waveguides have been formed in capillaries via a "Z-pinch" mechanism. Here, a fast discharge (lasting approximately 15 ns) is struck in a capillary of a few millimetres in diameter. Rapid ionisation occurs close to the capillary wall, and the plasma is subsequently compressed by a magnetic pinch, driving a radial shock wave towards to axis of the capillary.

Just before the shock front reaches the axis, a plasma channel is formed. Hosoakai *et al.* [140, 141] demonstrated guiding of laser pulses with $I_{\text{peak}} > 1 \times 10^{17}\,\text{W cm}^{-2}$ by striking a 4.8 kA discharge with half period 15 ns in a 20 mm long, helium filled capillary. The measured energy transmission was $64\,\%$, however the guided spot quality was very poor.

Partially ionised plasma channels have been generated by passing a slow electrical discharge through an initially evacuated capillary made of polypropylene [142, 143]. In these discharge ablated waveguides, the capillary wall itself is heated and ionised by the discharge. Due to the heat transfer from capillary wall to the plasma, an approximately parabolic transverse electron density profile is formed. Optical guiding of $400\,\text{fs}$ laser pulses with peak intensity $I_{\text{peak}} = 4 \times 10^{17}\,\text{W cm}^{-2}$ has been demonstrated [144, 145]. The measured energy transmission was $75\,\%$ in a $20\,\text{mm}$ long capillary. However, in this mechanism, not only is the plasma channel partially ionised, but also since material from the capillary wall must be ablated every shot, the capillary lifetime is limited to around 1000 shots, making it unsuitable for high-repetition rate applications.

2.6.2 Hydrogen-Filled Capillary Discharges

To overcome these problems, the hydrogen-filled capillary discharge waveguide (CDW) was developed at the University of Oxford [146–148]. The capillary is first filled with hydrogen gas via inlets placed at several points along the capillary. This generates a controllable, and longitudinally uniform gas density inside the capillary, and a slow discharge fully ionises the gas (see figure 2.3). In 2002, optical guiding of laser pulses with $I_{\text{peak}} = 1.2 \times 10^{17}\,\text{W cm}^{-2}$ was demonstrated over 50 mm (approximately 40 z_{R}) [149]. Ablation of the plasma channel was greatly reduced compared to that of the discharge ablated technique; the capillary lifetime was estimated to be $> 10^6$ shots.

Simulations by Bobrova *et al.* [151] identified three stages of evolution in the CDW. In the first $50\,\text{ns}$, the plasma is ionised and heated by the discharge pulse. In the following $30\,\text{ns}$, the plasma becomes fully ionised and hence the rising current begins to increase T_{e} more

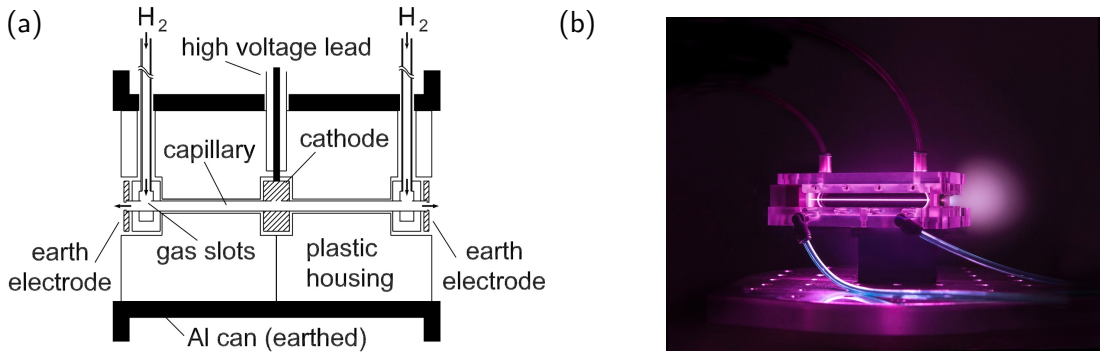

Figure 2.3: (a) Schematic of a gas-filled capillary discharge waveguide used in early experiments undertaken by the group at the University of Oxford. The laser to be guided is focused to the capillary entrance on the left, and guided in the generated plasma channel to the exit on the right. Reprinted with permission from [149]. Copyright 2002 by the American Physical Society. (b) 90 mm long CDW used by group at LBNL to accelerate electrons to 4.2 GeV [18]. Image source [150].

rapidly. The plasma is cooled at the walls of the capillary, generating a radial temperature profile that is peaked on axis. Since the plasma responds on a timescale faster than the discharge timescale, the plasma pressure is homogeneous and an axial minimum in n_e is therefore formed. For times later than 80 ns, the plasma is in a quasi-stady-state equilibrium, and the plasma channel is relatively constant for 10s of ns.

One of the disadvantages of this type of plasma source is that optical access to the plasma channel is limited due to surface roughening of the inner wall by the electrical discharge. Gonsalves *et al.* [152] performed transverse interferometry measurements of square cross-section capillaries to derive scaling laws for the matched spot size and axial electron density based on the initial hydrogen density and diameter of the capillary; these were in close agreement to a non-local thermodynamic equilibrium (LTE) model of the discharge reported by Broks *et al.* [153].

Recent work by the LBNL group has extended the length of CDWs to 40 cm [154] ($n_{e0} < 10^{18}$ cm^{-3}) in capillaries with D_{cap} up to 2000 µm, however the matched spot size was limited to $w_m > 100$ µm. High stability of the generated plasma waveguide over 2000 shots was reported; w_m varied by just $0.05\,\%$.

High Repetition-Rate Operation

In 2016 Gonsalves, now at LBNL, investigated whether capillary discharges were capable of operating at repetition rates one kilohertz or above [155]. This work consisted of two stages. Initially, a low-repetition rate experiment in which a 33 mm long, 250 µm diameter capillary operated at $f_{\text{rep}} = 1$ Hz was used to determine the minimum peak discharge current required to form a plasma channel. By measuring the transmission of a 1 µJ, 40 fs laser pulse focused to the capillary entrance, it was shown that currents as low as 50 A were suitable for waveguide formation with axial densities $n_{\text{e0}} \sim 1 \times 10^{18}\,\text{cm}^{-3}$. In the second stage, it was shown that operation (without a guided laser pulse) at $f_{\text{rep}} = 1$ Hz could be extended to $f_{\text{rep}} = 1$ Hz by water cooling the capillary to mitigate the power dissipated into the capillary walls by the current pulse, and by adjusting the flow rate to account for the increase in gas temperature. Less than 0.6 µm erosion of capillary wall was observed over 10^7 shots, or 2.45 hours of operation.

Optical guiding of high intensity laser pulses at kHz repetition rates in CDWs is yet to be demonstrated and could significantly increase the erosion rate of the capillary wall, however work by Maier *et al.* [58] in 2020 used a 4 mm long square-sided capillary as a gas cell to demonstrate stable LWFA operation at $f_{\text{rep}} = 1$ Hz over 24 hours. Aided by high transverse beam quality and stable laser parameters, each CDW structure supported approximately 2×10^6 shots before it had to be replaced.

2.6.3 Laser-Assisted Capillary Discharge Waveguides

To reduce damage to the capillary from petawatt laser pulses, larger capillary diameters are necessary. However for large D_{cap} and low n_{e0} it is not possible to achieve matched spot sizes $w_{\text{m}} \lesssim 140$ µm [19, 152]. In 2013, it was proposed [156] that by propagating a "heater" pulse through the plasma channel, increase in T_{e} close to the axis would occur through inverse bremsstrahlung, and hydrodynamic motion would deepen the channel. This would both reduce the matched spot size, and the axial plasma density.

This scheme was demonstrated by in 2019 by Gonsalves *et al.* [157]. Initially, a weak channel was formed with a large matched spot size in an 800 µm diameter capillary. A heater pulse that contained 300 mJ at centre wavelength $\lambda = 532$ nm and with $\tau_{\mathrm{FWHM}} = 8$ ns was focused to the front of the channel. The front edge of the pulse was poorly confined by the weak waveguide generated by the discharge, however the portions of the pulse arriving later experienced a deeper channel, through the self-focusing mechanism. A few nanoseconds after the peak of the heater pulse, the axial density was reduced, and the channel was significantly deepened. Through this setup, efficient guiding of laser pulses with peak power exceeding 850 TW and spot radius 61 µm was achieved in 200 mm-long plasma channels, and 7.8 GeV electron bunches were generated.

One limitation of this method is that the spot size of the heater pulse is not well matched, it undergoes spot-size oscillations as it propagates through the channel, altering the heating locally and hence generating an undesirable longitudinal density modulation. Very recently, simulations these axial non-uniformities could be mitigated by carefully tuning the delay between the discharge and the heater pulse, and the heater pulse and the femtosecond guided pulse [158].

2.7 Hydrodynamic Optical-Field-Ionised Waveguides

Recently, a new type of plasma waveguide specifically designed for low density, high repetition rate operation was proposed by the group at the University of Oxford, and developed in collaboration with the University of Maryland. The mechanism is an extension of the hydrodynamically formed waveguides discussed in section 2.3. Waveguides are formed by hydrodynamic expansion of a plasma column that is formed and heated by optical field ionisation (OFI). Since OFI acts on the atomic level, the electron heating is independent of the initial density. Hydrodynamic Optical-Field-Ionised (HOFI) waveguides are suited to low-Z gases allowing fully ionised plasmas to be generated. Like all waveguides formed via hydrodynamic expansion, they require no physical structure, which gives them the potential

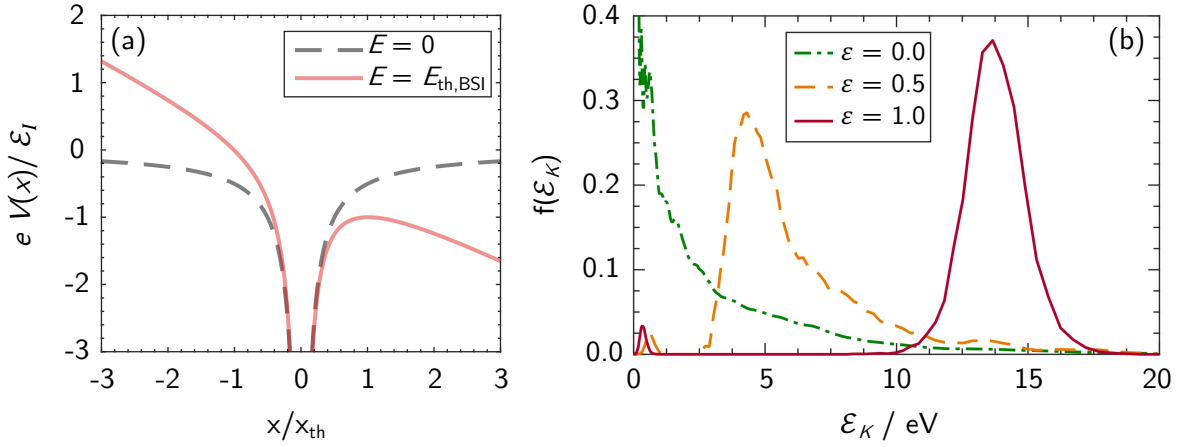

Figure 2.4: (a) Perturbed atomic potential $V(x)$ for no applied electric field (grey dashed) and applied electric field $E = E_{\text{th,BSI}}$ (red). (b) Simulated electron energy distributions resulting from OFI for hydrogen using a laser pulse with intensity $2.5 \times 10^{14}\,\text{W}\,\text{cm}^{-2}$ and varying laser ellipticities. Reprinted with permission from [101]. Copyright 2018 by the American Physical Society.

to be immune to damage — even for extended periods of high repetition rate operation.

2.7.1 Ionisation with Intense Laser Pulses

The rate at which electrons are liberated from atoms in an intense, ultrashort pulse laser field depends many factors including relating to both the ionising laser and the gas species [159–161]. Optical field ionisation (OFI) occurs when the strength of the laser electric field becomes comparable to the field binding valence electrons to the atoms. The simplest models to understand this are barrier-suppression ionisation (BSI) where the laser electric field is sufficiently strong to overcome the Coulomb potential of the atom, at which all electrons would be liberated at once, and tunnelling ionisation (TI) where electrons begin to tunnel through the barrier before it is completely suppressed by the laser field (see figure 2.4).

Barrier Suppression Ionisation

The potential an electron at a distance x from the atom feels is given by

$$V(x) = -\frac{Ze}{4\pi\epsilon_0 |x|} - Ex, \tag{2.3}$$

where the first time describes the Coulomb field binding the electron to the atom, and the second term describe the intense laser field. This implies that the potential has a maximum value

$$V_{\text{max}} = -2\sqrt{\frac{Ze}{4\pi\epsilon_0}E}. \tag{2.4}$$

If V_{max} is less than the bound potential of the electron, then the barrier preventing the electron escaping is completely suppressed [161, 162]. Hence the threshold laser field strength for barrier-suppression ionisation is

$$E_{\text{th,BSI}} = \frac{2\pi\epsilon_0}{Ze^2}\mathcal{E}_{\text{I}}^2. \tag{2.5}$$

It can be shown that the threshold laser intensity is

$$I_{\text{th,BSI}} = (1+\varepsilon)\frac{\pi^2\epsilon_0^3 c}{2e^6 Z^2}\mathcal{E}_{\text{I}}^4, \tag{2.6}$$

where ε is the ellipticity of the laser pulse, $\varepsilon = 0$ corresponds to linear polarisation and $\varepsilon = 1$ corresponds to circular polarisation. For a hydrogen atom and circular polarisation, $I_{\text{th,BSI}} = 2.8 \times 10^{14}\,\text{W cm}^{-2}$. Note also that this simple model implies that the ionisation rate is infinite, since all atoms are ionised instantaneously at the first moment $I > I_{\text{th,BSI}}$ is satisfied.

Tunnel Ionisation

Electrons are able to tunnel through a partially suppressed Coulomb barrier, and hence ionisation occurs at intensities below $I_{\mathrm{th,BSI}}$, implying a finite ionisation rate [163]. To calculate the tunnelling ionisation rate, the Ammosov, Delone and Krainov (ADK) model is employed [164]. This predicts an ionisation rate with an exponential dependence on the laser electric field. The ionisation rate thus increases rapidly around a threshold electric field given by

$$E_{\mathrm{th,ADK}} = \frac{4}{3}\sqrt{\frac{2m_e e}{\hbar^2}}\mathcal{E}_{\mathrm{I}}^{3/2}. \tag{2.7}$$

Electron Energy Distribution from Optical Field Ionisation

When an electron is ionised from its target atom by the intense laser, its subsequent motion has two components — a driven oscillation at the laser frequency, and a constant drift [161]. Once the laser pulse has passed, only the drift component remains, with a momentum

$$\vec{p}(t) = -e\int_{t_0}^{t}\vec{E}(t')\,\mathrm{d}t'. \tag{2.8}$$

The laser pulse can be written as $\vec{E}(t) = \Re\left[\vec{E}_0 f(t)\exp(-i\omega t)\right]$ where $\vec{E}_0$ is a time-independent vector describing the laser polarisation, and $f(t)$ is a slowly varying envelope function. Integrating by parts, ignoring the time derivative of the envelope function leads to

$$\vec{p}(t) = \frac{e}{\omega^2}\left[\frac{\partial\vec{E}(t)}{\partial t} - \frac{\partial\vec{E}(t_0)}{\partial t}\right]. \tag{2.9}$$

After the laser has passed $E(t) \to 0$, and hence so does the derivative. This leads to an expression for the kinetic energy of the ionised electron

$$\mathcal{E}_K = \frac{e^2}{2m_e\omega^4}\left|\frac{\partial\vec{E}(t_0)}{\partial t}\right|^2. \tag{2.10}$$

Since $\partial\vec{E}(t_0)/\partial t = \omega E(t_0)$, the kinetic energy of the electron depends on the amplitude of the laser field *at the moment of ionisation*.

In the case of BSI, the electron is ionised when the laser field first reaches $E_{\text{th,BSI}}$. For an elliptically polarised laser pulse, this leads to

$$\begin{aligned}\mathcal{E}_K &\approx \frac{e^2}{2m_e\omega^2}\varepsilon^2 E_{\text{th,BSI}}^2 \\ &\approx \varepsilon^2 U_p(t_0),\end{aligned} \tag{2.11}$$

where $U_p(t_0) = e^2E_{\text{th,BSI}}^2/(2m_e\omega)$ is the ponderomotive potential of the laser at the moment of ionisation. Hence, it is expected that the electron energy distribution will exhibit well defined peaks, the position of which depend on the laser ellipticity, and charge and ionisation state of the gas species. Figure 2.4 shows the calculated kinetic energy distributions $f(\mathcal{E}_K)$ of the electrons produced by OFI of hydrogen atoms with various laser ellipticities. These calculations were undertaken by Dr. Chris Arran using the particle-in-cell code EPOCH [101].

Thermalisation of the Plasma

Magnetohydrodynamic (MHD) codes such as FLASH [165] and HELIOS [166], which are used for studying shock expansion in plasmas, study the movement of fluid elements which are assumed to have Maxwellian energy distributions defined by the temperature of the fluid (known as the fluid approximation). However the energy distributions that result from OFI are not well described by these approximations, since they are contain a number of distinct peaks defined by the ponderomotive energies required to ionise electrons. The timescales for thermalisation, where the electron energy distribution becomes closer to a Maxwellian, can be estimated to assess the validity of modelling the shock expansion with fluid codes.

Electron-electron collisions in the plasma cause thermalisation of the electrons. The time over which this occurs is approximately the Spitzer electron-electron collision time [167]

$$\tau_{\text{col}}^{ee} \approx 2.7 \times 10^5 \frac{T_e^{3/2}}{n_e \ln\Lambda}, \tag{2.12}$$

where $\Lambda = (4/3)\pi n_e(\epsilon_0 k_B T_e/n_e e^2)^{3/2}$ is the Coulomb logarithm. For the majority of the plasma channels generated in this thesis, $T_e \approx 10\,\text{eV}$ and $n_{e,\text{init}} = 1 - 3 \times 10^{18}\,\text{cm}^{-3}$, and thus $\tau_{\text{col}}^{ee} \approx 1\,\text{ps}$. In this situation, after a few picoseconds, electrons will comprise a single thermal and isotropic population.

The ions are not heated by the ionising laser pulse, and initially remain at room temperature. However, they begin to exchange energy with electrons through collisions. The time over which the electron and ion species thermalise can be estimated by the equipartition time [167]

$$\tau_{\text{eq}}^{ei} \approx 5.87 \times 10^6 \frac{m_e m_{\text{ion}}}{m_p^2 n_e Z_{\text{ion}}^2 \ln\Lambda} \left(\frac{m_p T_e}{m_e} + \frac{m_p T_{\text{ion}}}{m_{\text{ion}}} \right)^{3/2}, \tag{2.13}$$

where m_p is the proton mass, and m_{ion}, T_{ion}, Z_{ion} are the ionic mass, temperature and charge respectively. For parameters investigated here, $\tau_{\text{eq}}^{ei} \approx 1.5\,\text{ns}$.

2.7.2 Progress

In 2013, Lemos *et al.* [168–170] investigated the use of $\tau_{\text{FWHM}} \approx 400\,\text{fs}$ laser pulses to form relatively high density ($n_{e0} \gtrsim 1 \times 10^{18}\,\text{cm}^{-3}$) plasma channels by OFI. Hydrogen and singly-ionised helium channels were generated up to $8\,\text{mm}$ long using both linear and circular polarisation. In those papers, the authors noted that collisional heating contributed in part to T_e, due to the pulse length and initial plasma density.

In 2018, the group at the University of Oxford [101] demonstrated the formation of low density HOFI plasma channels with a spherical lens. The shock expansion, measured interferometrically, matched well to the Sedov-Taylor solution for expansion of ideal gases (a full description of which is provided in section 3.2.2). Plasma channels with densities as low as $n_{e0} = 1.5 \times 10^{17}\,\text{cm}^{-3}$, and matched spot sizes in the range $33\,\mu\text{m} \lesssim w_m \lesssim 61\,\mu\text{m}$ were measured.

This thesis discusses the subsequent development of HOFI plasma channels. A detailed discussion of the formation, evolution, and properties of these plasma channels is presented in Chapter 3. Experimental results of subsequent experiments generating long plasma channels with axicon lenses are discussed in Chapters 4, 5 and 6.

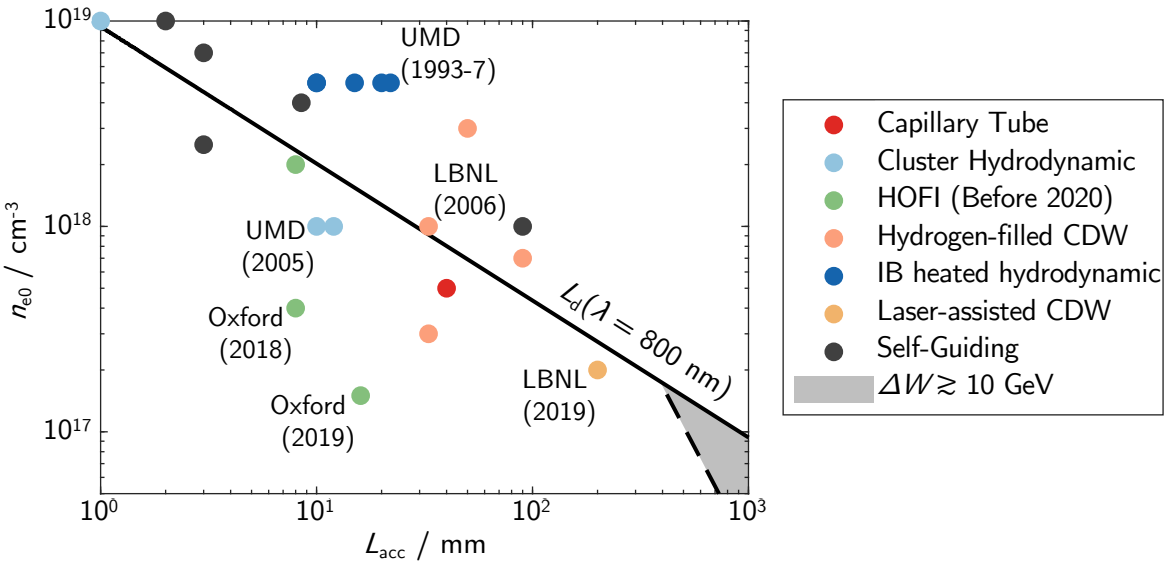

Figure 2.5: Previously reported experimental results of plasma waveguides suitable for LWFA [38, 67, 101, 102, 111, 112, 114, 117–120, 125, 126, 129, 135, 148, 149, 152, 168, 169, 171–173]. Only studies prior to the start of this work have been included. The solid black line shows the dephasing length in the linear regime (equation 1.14) for a laser wavelength $\lambda = 800\,\text{nm}$. The dashed grey line denotes the approximated required stage length to achieve $10\,\text{GeV}$ acceleration for $a_0 = 1$. The shaded grey area indicates suitable choices of L_{acc} and n_{e0} to achieve a single-stage energy gain $\Delta W \gtrsim 10\,\text{GeV}$.

2.8 Comparison of Plasma Waveguides

Figure 2.5 shows how progress towards a long, low-density pre-formed plasma waveguide has developed. Only studies published prior to the start of this work have been included. Conditions for which $w_m \gtrsim 100\,\mu\text{m}$ have been omitted. The solid black line indicates the linear dephasing limit L_d for a laser wavelength of $\lambda = 800\,\text{nm}$ given by equation 1.14. The dashed black line denotes the minimum required length for a $10\,\text{GeV}$ LWFA stage for $a_0 = 1$ at an axial plasma density of n_{e0}, derived by combining equations 1.14 and 1.23.

Outlined in table 2.2 are the demonstrated characteristics of each of the waveguides discussed here. To date, CDWs have demonstrated the highest energy transmission values. Laser-based waveguides have lower measured transmissions, due to both coupling and attenuation of the leaky modes in the waveguide. Capillary tubes have the potential to be useful here due to their relative simplicity, but first issues due to laser induced damage (especially at high f_{rep}) must be addressed.

	Lowest n_{e0} / cm^{-3}	w_m / µm	L_{acc} / m	$T(z = L_{acc})$	Fully Ionised	Lifetime
IB heated Hydrodynamic	1×10^{18}	~ 15	~ 0.02	$\sim 50\,\%$	No	Indestructible
Capillary Tubes	1×10^{17}	$\sim 25 - 50$	$\sim 0.5 - 1$	$\sim 13\,\%$	Yes	$\sim 10^3$ shots
Hydrogen-filled CDW	3×10^{17}	$30 - 100$	0.4	$\approx 100\,\%$	Yes	$\sim 10^7$ shots
Laser-assisted CDW	2×10^{17}	$65 - 100$	0.2	$\approx 100\,\%$	Yes	Unknown
HOFI (Prior to this work)	1×10^{17}	$25 - 40$	0.016	$\sim 50\,\%$	Yes	Indestructible

Table 2.2: Reported characteristics of selected plasma waveguide techniques that are candidates for a multi-GeV LWFA accelerator stage. Cells coloured red indicate that the current reported characteristic is not suitable for a multi-GeV stage. Orange boxes are characteristics that might be suitable, and green coloured cells indicate that reported waveguide characteristics are suitable for a high repetition-rate, multi-GeV stage.

HOFI waveguides are able to generate fully ionised plasma channels at low densities. Since they are immune to damage and energy efficient, they are extremely attractive to future accelerator stages. However, further work is needed to improve the overall energy transmission.

2.9 Conclusion

Until the 2010's, the issues of repetition-rate, lifetime and stability of a plasma waveguide had received very little attention. The first, and most important challenge was to find a waveguide that was capable of operating at a given density and with a matched spot-size suitable for LWFA. Since, progress on the electron beam energy frontier of LWFA has been driven forwards by the development of longer, lower density waveguides, as well as developments in laser technology [13, 15, 19]. As the next generation of laser technology heads towards high peak power, high average power lasers, and towards multi-PW facilities capable of driving $\gtrsim 10$ GeV stages, it is vital that

repetition-rate and lifetime receive significant consideration, as well as meeting the demands on n_{e0} and L_{acc}.

Chapter 3

Methods

3.1 High Intensity Laser Pulses

The development of ultrashort, high-intensity laser pulses has paved the way for research across a vast number of scientific disciplines [174, 175], and for this reason, the development of chirped pulse amplification (CPA) was worthy of the 2018 Nobel Physics Prize [176–178]. This section outlines some key properties of high-intensity laser pulses, and some important techniques for experimental characterisation of these pulses.

3.1.1 Short Pulse Lasers

Due to the time-bandwidth theorem, a laser pulse of duration τ_{FWHM} must have a finite spectral bandwidth $\Delta\nu$ satisfying the equality $\tau_{\mathrm{FWHM}}\Delta\nu \geq a$, where $a \sim 1$ is a constant that depends on the pulse shape, $a = 0.441$ for a pulse that is Gaussian in time*. The methods to achieve this are Q-switching and mode-locking, descriptions of which are beyond the scope of this thesis, however a review of these techniques can be found in Hooker and Webb [179].

*In this thesis, the $1/e^2$ temporal duration of the pulse, consistent with the definition used in FBPIC (see section 3.4.1), is labelled τ_{L}, and the full-width at half maximum, which is the more commonly quoted temporal duration, is labelled τ_{FWHM}. Most ultrashort laser pulses of interest here are approximately Gaussian, and hence it is simple to relate the two, $\tau_{\mathrm{FWHM}} = 2\sqrt{2\ln 2}\tau_{\mathrm{L}}$.

3.1.2 Fourier Optics

Full calculation of the distribution of radiation as it propagates through optical systems requires solving the Helmholtz equation, which for a harmonic electric field is given by

$$\left(\nabla^2 + k^2\right) u(x, y, z) = 0, \tag{3.1}$$

where $u(x, y, z)$ is the scalar field, and k is the wavenumber of the medium. The theoretical foundation of scalar diffraction of light is Fourier Optics, a full treatment of which can be found in the text by Goodman [180]. The amplitude of radiation at the focal plane of a spherical or parabolic lens is calculated using the Fraunhofer approximation. For a scalar field $U(x', y')$ incident on the optic, focal length f, located in the x', y' plane, the distribution at focus is

$$E(x, y) \propto \int_{-\infty}^{\infty} \int_{-\infty}^{\infty} U(x', y') \exp\left[-\frac{ik}{f}(x'x + y'y)\right] \mathrm{d}x'\mathrm{d}y', \tag{3.2}$$

proportional to a Fourier transform of the incident field.

It is normal to assume that the collimated transverse intensity profile, or near-field, of a laser beam is Gaussian since this is usually the lowest order mode emanating from an optical cavity. For the lowest-order Gaussian, the intensity at the focal plane is thus given by

$$I_{\mathrm{gauss}}(r) = I_{\mathrm{peak}} \exp\left(-\frac{2r^2}{w_0^2}\right), \tag{3.3}$$

where I_{peak} is the peak intensity and w_0 is the spot-size.

In reality, few laser beams propagate as perfect, lowest-order Gaussian beams. In fact, for high-power laser systems, it is more desirable that the near-field be closer to a top-hat or super-Gaussian profile in order to maximally extract laser energy from the crystal. For a top-hat collimated intensity profile of diameter D, the intensity at the focal plane is the Airy disc

$$I_{\mathrm{top\,hat}}(r) \propto \left[\frac{1}{r} J_1\left(\frac{kDr}{2f}\right)\right]^2, \tag{3.4}$$

where $J_1(x)$ is a Bessel-function of the first kind. In this case, the $1/e^2$ radius is given by $w_0 \approx 0.82\lambda f/D$.

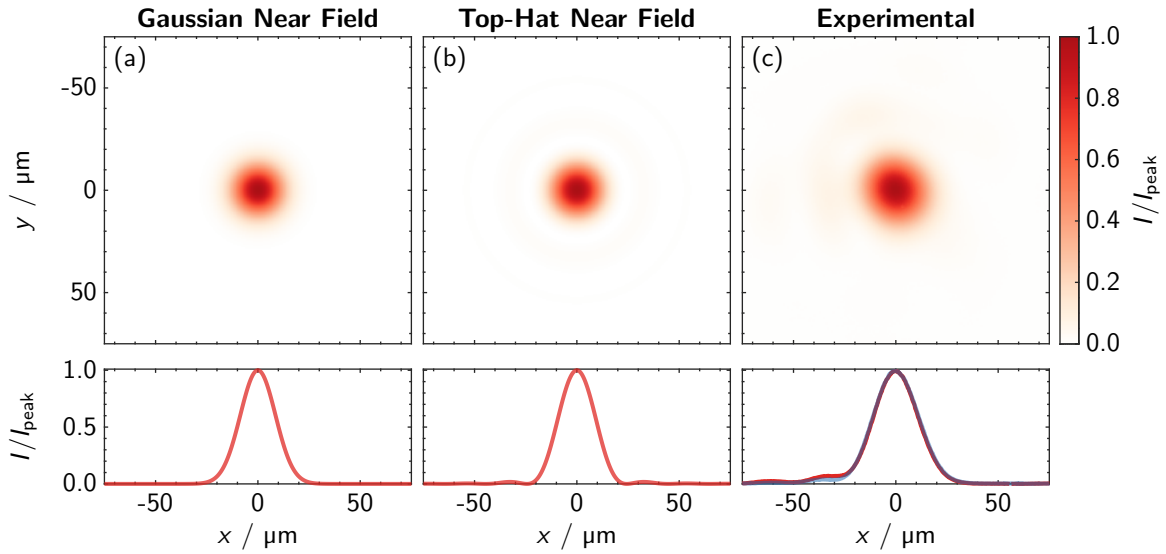

Figure 3.1: Far-field profiles (top) and lineouts along the centroid (bottom) for: (a) simulation with Gaussian near-field, $w_{\text{col}} = 15\,\text{mm}$, (b) simulation with top-hat near-field $D = 30\,\text{mm}$, and (c) measured spot focused by off-axis parabola, where wavefront fluctuations were minimised by a deformable mirror. Unlike the simulated profiles, the beam is not perfectly azimuthally symmetric, and there is a low intensity background on which the central maxima sits.

In reality, irregularities in the amplitude and wavefront arise from surface imperfections of the beam optics, small misalignments of focusing optics, and nonlinearities in the pulse amplification process. These manifest as aberrations in the far-field, which redistribute laser energy away from the central spot, increase the spot-size, and reduce the peak intensity. Such aberrations can significantly affect the beam propagation, and hence the performance of a LWFA [181, 182], thus are usually mitigated as much as possible using a deformable mirror. Figure 3.1 illustrates the simulated far-field for a Gaussian and top-hat near-field profiles, and compares them to an experimentally measured profile with the same parameters.

For a pulsed laser, the laser pulse energy $\mathcal{E}$ is the integral of the laser intensity over space and time

$$\mathcal{E} = \int_{-\infty}^{\infty} \int_{S} I(\vec{r}_{\perp}, t)\, \mathrm{d}S \mathrm{d}t. \tag{3.5}$$

It is usually desired to calculate the peak intensity given the known energy and duration of the pulse and focusing optic. For example, a laser pulse that is Gaussian in space and time defined by

$I(r,t) = I_{\text{peak}} e^{-2r^2/w_0^2} e^{-2t^2/\tau_L^2}$, equation 3.5 can be calculated giving

$$I_{\text{peak}} = \left(\frac{2}{\pi}\right)^{3/2} \frac{\mathcal{E}}{w_0^2 \tau_L}. \tag{3.6}$$

The peak intensity of more complex spots (or temporal profiles) can be calculated by solving equation 3.5 numerically.

3.1.3 Experimental Far-Field Characterisation

Spot-Size Characterisation

In experiment, a consistent method of measuring the spot-size is necessary to measure the laser properties at both the input and exit of the plasma channel. Throughout this thesis, the ISO standard D4σ method [183] is employed to measure the spot size. The D4σ beam diameter along the x-axis is given by

$$\text{D4}\sigma = 4\sqrt{\frac{\int_{-\infty}^{\infty} I(x,y)(x-\bar{x})^2 \,\mathrm{d}x\mathrm{d}y}{\int_{-\infty}^{\infty} I(x,y)\,\mathrm{d}x\mathrm{d}y}}, \tag{3.7}$$

where $\bar{x}$ is the beam centroid, given by

$$\bar{x} = \frac{\int_{-\infty}^{\infty} I(x,y)x \,\mathrm{d}x\mathrm{d}y}{\int_{-\infty}^{\infty} I(x,y)\,\mathrm{d}x\mathrm{d}y}. \tag{3.8}$$

The spot-size is defined as $w_0 = \text{D4}\sigma/2$. Since the D4σ method relies on calculating the second moment of the beam distribution, it is sensitive to any background noise. Thus, careful subtraction of the background signal is required to achieve high accuracy.

Pulse Length Measurements

Temporal characterisation of ultrashort pulses has been of interest since pulses shorter than the typical response time of a fast photodiode (a few tens of ps) were first generated. Several techniques have been developed that can fully retrieve temporal profile of ultrashort pulses [184–187]. The most common are frequency-resolved optical gating (FROG) [184, 188], and spectral phase interferometry

for electric-field reconstruction (SPIDER) [185], both of which are commercially available.

More recently, methods have become available to fully characterise the spatiotemporal electric field, including spatiotemporal couplings (STCs) [189, 190]. These are still subject to some development and are not yet as widely used as pulse length diagnostics.

Measuring the Peak Intensity and Enclosed Energy

For a given wavelength of light, scientific charge-coupled device (CCD) and complimentary-metal-oxide-semiconductor (CMOS) detectors provide a signal which varies linearly with incident optical flux, provided that they are not saturated. Hence, to estimate I_{peak} a given laser shot from a given measured optical flux in pixels $i_{\text{det}}(x, y)$, one can normalise the summed pixel count, provided any background signal has been accounted for, to the input laser energy (which is usually measured in the amplification chain) and pulse duration. From equation 3.5, it is evident that intensity for a measured optical flux is

$$I(x, y) = \frac{1}{\sqrt{\pi}\tau_{\text{L}}} \frac{\mathcal{E}}{\Delta x \Delta y} \frac{i_{\text{det}}(x, y)}{\sum_{m,n} i_{\text{det}}(x_m, y_n)}, \tag{3.9}$$

where τ_{L} is the pulse duration (which is assumed to be Gaussian) measured by the FROG or SPIDER diagnostics, and $\Delta x \Delta y$ is the area of one pixel of the detector, accounting for any magnification in the imaging system. From this, it is simple to estimate I_{peak}. It should be noted that for temporal envelopes which are not Gaussian, the pre-factor $1/\sqrt{\pi}$ must be adjusted. An underlying assumption made here is that there are no STCs present in the focused, compressed laser pulse.

As with peak intensity, the energy enclosed within the contour of the central spot is a crucial parameter determining the performance of a LWFA stage, and for guiding experiments. The final electron beam energy scales with the laser energy enclosed in the central maxima [191, 192], *not* the total energy of the laser pulse. The energy enclosed within a radius r_0 of the laser beam centroid is defined as

$$\eta_{\text{enc}}(r_0) = \frac{1}{\mathcal{E}} \int_{\theta=0}^{2\pi} \int_{r=0}^{r_0} I(\vec{r}_{\perp}) r \, \mathrm{d}r\mathrm{d}\theta. \tag{3.10}$$

Figure 3.2 shows the enclosed energy as a function of radius for the example laser spots in figure

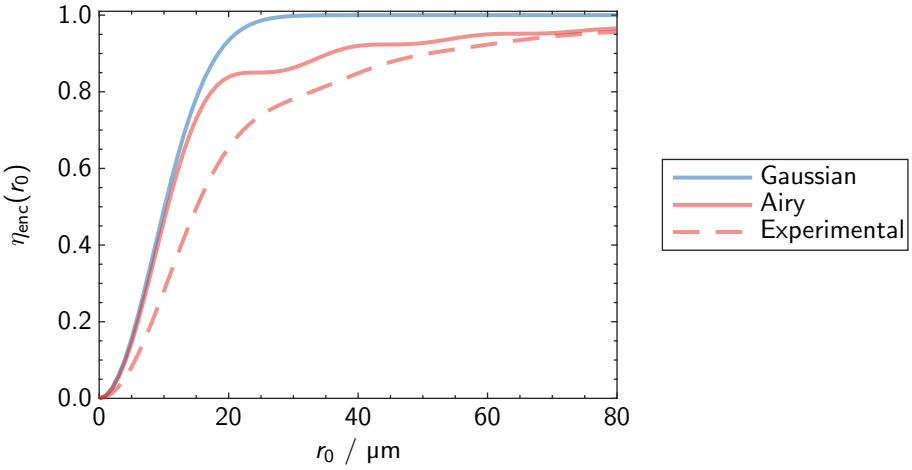

Figure 3.2: The fraction energy enclosed $\eta_{enc}(r_0)$ by a circle of radius r_0, centred on the beam centroid, for the three far-field profiles in figure 3.1.

3.1. For a perfect Airy pattern, $85\,\%$ of the energy is enclosed in the central spot ($r_0 = 1.22\lambda f/D$), however for the real spot, only $70\,\%$ is enclosed. In order to account for imperfections in real laser beams, when simulating LWFA it is common to scale the laser energy by the ratio energy enclosed within central maxima to that expected by a perfect Airy pattern [57], which for this example would be $82\,\%$ of the total laser energy.

An inherent requirement of peak intensity and enclosed energy measurements is the use of a detector with suitable dynamic range; images taken with low bit depth detectors cannot capture the underlying background which contains significant portions of the laser energy, and hence will over-estimate both the peak intensity and the quality of the focus.

3.2 Formation of Hydrodynamic Optical-Field-Ionised Plasma Channels

3.2.1 Plasma Channels Formed by Axicon Lenses

Since parabolic focusing optics (see section 3.1.2) direct incident radiation to a single point on the optical axis and subsequently diffract over z_R, they are not suited to generating long, uniform cylindrical columns of plasma. Axicons are conical optics that direct the incident radiation towards

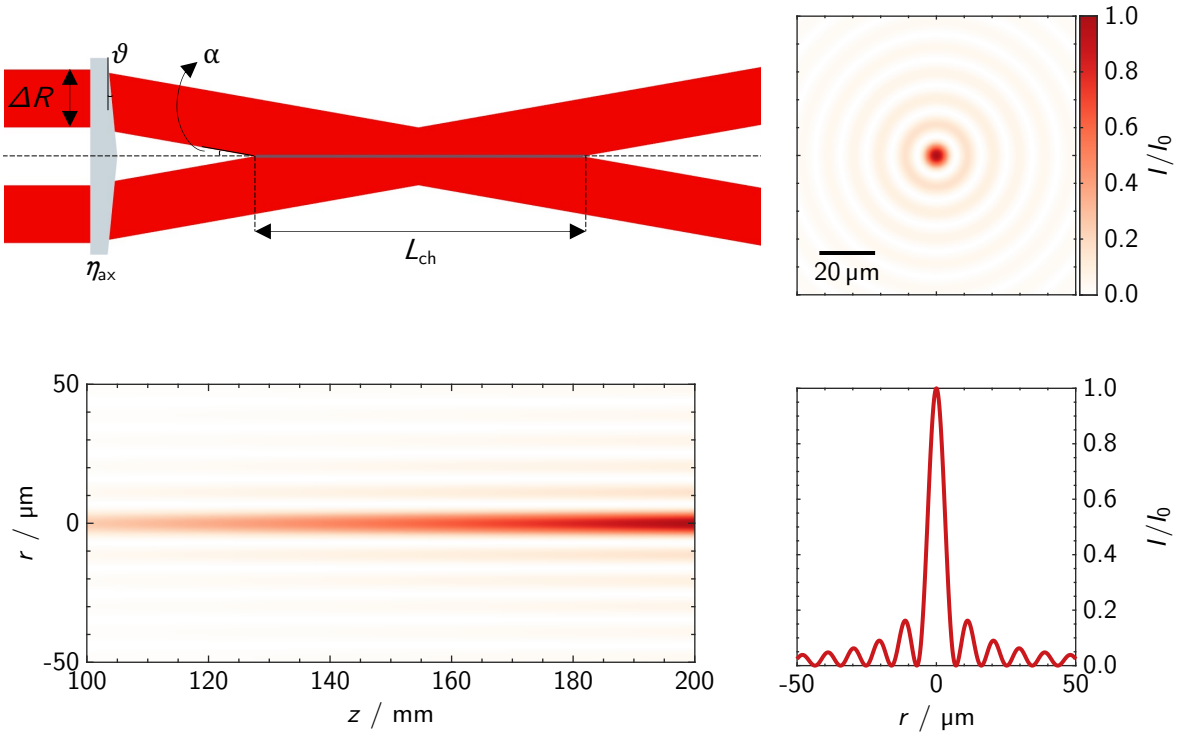

Figure 3.3: (a) Cartoon of a transmissive axicon with refractive index η_{ax} and base angle ϑ focusing an annulus of light to form a line focus of length L_{ch}. (b) Transverse intensity profile of the focused light. (c) Longitudinal intensity profile of the axicon focus. (d) Lineout of the transverse intensity profile.

the optical axis at the same angle α (see figure 3.3), creating a line focus. For a transmissive axicon with refractive index $\eta_{ax}(\lambda)$ and cone base angle ϑ, the approach angle of rays is given by $\alpha(\lambda) = \arcsin\left[\eta_{ax}(\lambda)\sin\vartheta\right] - \vartheta$.

At any position along the focal region, rays converge on the axis and interfere to generate the same interference pattern. For an incident laser beam with radial intensity profile $I(R)$ possessing zero angular momentum, the interference pattern is a zeroth order Bessel function of the first kind $J_0(\beta)$. It can be shown that intensity profile in the focal region is described by

$$I(r,z) = \frac{4\pi^2}{\lambda} I(z\alpha)\alpha^2 z J_0^2\left(\frac{2\pi r\alpha}{\lambda}\right). \tag{3.11}$$

where a small angle approximation has been made for α and $R = z\alpha$ has been used.

For a perfect top-hat near field, $I(R) = I_{col} = F_{col}/(\sqrt{\pi}\tau_L)$, where F_{col} is the energy per unit

area in the collimated beam, hence the peak intensity at a given position along the optical axis is given by

$$I_{\text{peak}}^{\text{ax}}(z) = \frac{4\pi^2}{\lambda}\frac{F_{\text{col}}}{\sqrt{\pi}\tau_{\text{L}}}\alpha^2 z, \tag{3.12}$$

which occurs at the position $r = 0$. The first transverse minimum occurs at

$$r_0 = \frac{2.4048\lambda}{2\pi\alpha}, \tag{3.13}$$

showing that to increase the spot-size of the axicon pulse, one must reduce α, or increase the laser wavelength.

For ultrashort laser pulses, the wavelength dependence of equation 3.11 results in chromatic aberrations at the focus. For example, a pulse with 30 nm spectral bandwidth centred at $\lambda_0 = 800\,\text{nm}$ and a reflective axicon with $\alpha = 2.5\,\text{deg}$, the position of the first minima of the focus ranges between $r_0 = 6.886\,\mu\text{m}$ and $7.149\,\mu\text{m}$, which is amounts to a variation of $4\,\%$. Axicon lenses have additional chromatic effects arising from the wavelength dependence on $\alpha(\lambda)$, however it can be shown that this effect does not reduce the laser intensity in the focal region by more than a few percent. The propagation of ultrashort pulses thorough transmissive axicons can reduce the focal intensity through self-phase modulation (B-integral) and group velocity dispersion. Calculations of the latter by Aimee Ross [193] have shown that for the axicon lenses used in this thesis, an incident pulse with $\tau_{\text{FWHM}} = 30\,\text{fs}$ is stretched by a factor of approximately 2, reducing the intensity by the same factor [193]. It is possible to mitigate the chromatic effects arising from the wavelength dependence on $\alpha(\lambda)$ and the self-phase modulation using reflective axicons.

Generation of Plasma Columns with Axicon Foci

Since there is a linear mapping between the incident radial position of a ray and the its axial focus position, the length of the focal region and thus length of the plasma channel L_{ch} is set by the size of the collimated beam and the axicon approach angle (see figure 3.3). For an annular beam of thickness ΔR, the length of the plasma column is $L_{\text{ch}} = \Delta R/\tan\alpha$. The initial radius of the plasma column is set by the approach angle α (see equation 3.13), the peak intensity $I_{\text{peak}}^{\text{ax}}$, and

the threshold ionisation intensity for the constituent gas. Given that the second maxima of the Bessel focus has an intensity $0.18I^{ax}_{peak}$, the maximum radius out to which ionisation can occur in the central maxima without ionising occurring in the outer rings is given by $r_{ion} = 1.69\lambda/(2\pi\alpha)$. If one assumes that all ionisation occurs at the point where the laser pulse $I(r, z, \tau) = I_{th}$, a plasma column or radius r_{ion} will be formed. At higher intensities, ionisation in the outer Bessel rings will occur increasing the initial number of electrons ionised but leaving areas of unionised gas close to the intensity minima. It should be noted that since $I(r, z)$ increases linearly with z, the condition $I(r_{ion}, z) = I_{th}$ can only be truly satisfied at one position along the plasma column. However, for the lengths of channel and values of z considered in this thesis, the longitudinal variation in intensity of the focal region has little observable effect on the plasma channel. In future experiments, it would be simple to remove, or even control, the z dependence by employing an appropriate apodising filter on the collimated laser pulse.

Critical Density and Turning Point Density

The critical density of a plasma, that is the maximum density at which waves of a given frequency can propagate through a plasma, is given by

$$n_{crit} = \frac{m_e \epsilon_0 \omega^2}{e^2}, \tag{3.14}$$

where ω is the laser frequency. At densities higher than this, the plasma is referred to as overdense, and light of frequency ω is reflected. For a laser with $\lambda = 800\,\text{nm}$, the critical plasma density is $n_{crit} = 1.75 \times 10^{21}\,\text{cm}^{-3}$, much greater than the desired axial densities $n_{e0} \sim 10^{17}\text{cm}^{-3}$ in this thesis. However, for light incident on a plasma at an angle $\pi/2 - \alpha$ (measured from the normal), the "turning point density" of the plasma is $n_{tp} = n_{crit} \sin^2 \alpha$ [129]. For example, focusing light with an axicon with $\alpha = 2.5\,\text{deg}$ gives $n_{tp} = 3.23 \times 10^{18}\,\text{cm}^{-3}$, almost three orders of magnitude lower than the case of normal incidence.

Pulse Energy Required for Plasma Column Formation

For $I(r_{\mathrm{ion}}, z) = I_{\mathrm{th}}$, and an initial plasma density corresponding to n_{tp}, the total number of electrons N_{e} per unit length ionised by the laser pulse is approximately

$$\begin{aligned} N_{\mathrm{e}} &\approx \pi r_{\mathrm{ion}}^2 n_{\mathrm{tp}} \\ &= \pi \left(\frac{1.69\lambda}{2\pi\alpha}\right)^2 \frac{m_{\mathrm{e}}\epsilon_0}{e^2} \left(\frac{2\pi c}{\lambda}\right)^2 \sin^2\alpha \\ &= \frac{1.69^2 \pi m_{\mathrm{e}}\epsilon_0 c^2}{e^2} \\ &\approx 5 \times 10^{12}\,\mathrm{cm}^{-1}, \end{aligned} \tag{3.15}$$

where a small angle approximation has been used for α. Importantly, N_{e} is independent of both the choice of axicon and laser system. Decreasing the axicon approach angle increases the initial spot radius but decreases n_{tp} by the same factor. However, that is not to say that all plasma channels formed will expand in the same way regardless of the chosen α. In fact, the expansion could be significantly different for different α, since blast wave theory predicts a dependence on the initial plasma column radius (see section 3.2.2).

The energy per unit length $\mathcal{E}_{\mathrm{l,ax}}$ that can be coupled into the initial plasma column is the product of the average kinetic energy of the ionised electrons U_{k} and the number of electrons per unit length, $\mathcal{E}_{\mathrm{l,ax}} = U_{\mathrm{k}} N_{\mathrm{e}}$. Thus for a given laser system, $\mathcal{E}_{\mathrm{l,ax}}$ can only be varied by changing the gas species used, and the ellipticity of the laser pulse. For hydrogen, $\langle U_{\mathrm{k}} \rangle \approx 13.7\,\mathrm{eV}$, which is more than an order of magnitude lower than that achieved for higher density plasma columns heated by inverse bremsstrahlung [117].

Of interest to efficient waveguide formation is the energy per unit length required to form the plasma column. A perfect top-hat near field of radius R incident on an axicon contains energy $\mathcal{E} = F_{\mathrm{col}} \pi R^2$. The infinitesimal energy $\delta\mathcal{E}$ contained within an annulus of thickness δr located at radial position r is

$$\delta\mathcal{E} = 2\pi r \delta r F_{\mathrm{col}}. \tag{3.16}$$

By using the relation $r = z/\alpha$ in the small angle approximation, 3.16 can be rewritten as

$$\frac{\delta\mathcal{E}}{\delta z} = 2\pi F_{\text{col}} z\alpha^2. \tag{3.17}$$

Since $I^{\text{ax}}_{\text{peak}}$ increases linearly with z, the energy per unit length does as well. Combining equations 3.12 and 3.17 provides the minimum energy per unit length $\mathcal{E}_z$ required to form a plasma column of radius r_{ion}

$$\mathcal{E}_z = \frac{2\pi}{\lambda} A I_{\text{th}} \tau, \tag{3.18}$$

where $A \gtrsim 1$ is a constant which accounts for the fact that $I^{\text{ax}}_{\text{peak}}$ has to be larger than I_{th} in order that $I(r = r_{\text{ion}}) \geq I_{\text{th}}$. For hydrogen, and a $\lambda = 800\,\text{nm}$ laser pulse of duration $\tau = 45\,\text{fs}$, $\mathcal{E}_z \approx 1\,\text{mJ}\,\text{cm}^{-1}$.

It is interesting to compare $\mathcal{E}_z$ to the energy per unit length that is actually used to ionise a gas species with ionisation potential U_{ion}. This can be simply approximated as $\mathcal{E}_{\text{ion}} \approx N_{\text{e}} U_{\text{ion}}$. For the hydrogen example above, $\mathcal{E}_{\text{ion}} \approx 0.01\,\text{mJ}\,\text{cm}^{-1}$, making the plasma formation process just $\sim 1\,\%$ efficient; around 99 % of the focusing pulse is transmitted through the plasma without depletion.

From equation 3.18, it is clear that the efficiency can thus be significantly improved by reducing the pulse length. This argument is valid provided that the assumptions underlying ADK are still valid, and thus are not valid for few-cycle pulses. Nevertheless, a laser such as the L1 Allegra laser at ELI-Beamlines provides $20\,\text{mJ}$ pulses in $15\,\text{fs}$ at $f_{\text{rep}} = 1\,\text{kHz}$ [194], and would be capable of generating hydrogen plasma columns with lengths up to 1 m.

3.2.2 Waveguide Expansion

After the initial ionisation and heating by the laser pulse, hot plasma will expand outwards rapidly into the surrounding cold, neutral gas, driving a radial blast wave. Blast wave theory, originally developed by Sedov [195] and Taylor [196], is highly non-linear and involves several complex physical processes. Shortly after the initial explosion, the hot material from the axis resides in a thin expanding shell, forming the shock front. According to the self-similar Sedov-Taylor solution

for a cylindrical shock [197], the shock front position evolves in time as

$$r_{\mathrm{shock}}^4(t) = \frac{(\gamma_\mathrm{A}+1)^2 \mathcal{E}_\mathrm{l}}{\pi\rho} t^2, \tag{3.19}$$

where γ_A is the adiabatic index of the medium, $\mathcal{E}_\mathrm{l}$ is the energy per unit length contained within the initial plasma at $\tau = 0$, and ρ is the mass density of the surrounding, unperturbed region.

The solution in equation 3.19 postulates that all the energy in the plasma comes from an infinitesimally small radius at $t = 0$, which is clearly unrealistic. Instead, one can consider a time difference $t_0 = t - t'$ where t', and require that the plasma column radius at t_0 is the initial plasma column radius, $r_{\mathrm{shock}}(t_0) = r_0$. Accounting for this, it can be shown that for a cylindrical plasma column of radius r_{ion} ionised by an axicon, self-similar blast wave theory predicts the shock radius to expand as

$$r_{\mathrm{shock}}(t) = \sqrt{(\gamma_\mathrm{A}+1)\left(\frac{\mathcal{E}_{\mathrm{l,ax}}}{m_\mathrm{p}}\right)^{\frac{1}{2}} r_{\mathrm{ion}}\, t + r_{\mathrm{ion}}^2}, \tag{3.20}$$

showing the dependence on r_{ion}; increasing r_{ion} permits the shock to expand to a larger radius.

Experiments to this point [101, 102, 198] have indicated that the at a given time after the formation of the plasma column, τ, $n_{\mathrm{e0}}(\tau) \propto n_{\mathrm{init}}$. Thus, decreased α results in both a smaller initial plasma radius, and a higher axial density at a given delay.

A secondary effect of the plasma expansion is that the shock front depletes energy as it expands into the unionised gas. By considering the work done by the expanding plasma on the surrounding gas at room temperature T_{gas}, one can estimate the radius at which the blast wave depletes its energy

$$\frac{r_\mathrm{f}}{r_{\mathrm{ion}}} \approx 1 + \sqrt{\frac{Z\mathcal{E}_{\mathrm{l,ax}}}{k_\mathbf{B}\, T_{\mathrm{gas}}}}, \tag{3.21}$$

where T_{gas} is the temperature of the surrounding gas. Assuming $T_{\mathrm{gas}} \approx 293\,\mathrm{K}$, $r_\mathrm{f}/r_{\mathrm{ion}} \sim 21$.

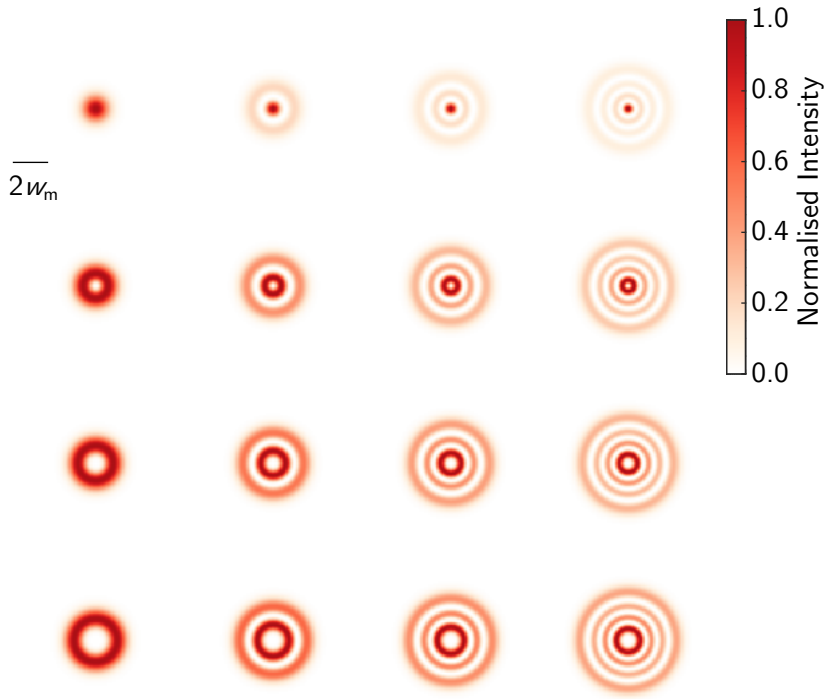

Figure 3.4: The first 16 Laguerre-Gauss intensity modes $I_{p,m}(r,\theta,z) \propto |E_{p,m}(r,\theta,z)|^2$. Radial index p increases left to right, whereas azimuthal index m increases top to bottom.

3.3 Pulse Propagation in Plasma Channels

3.3.1 Transverse Mode Structure of Plasma Channels

An infinite parabolic transverse electron density profile described by

$$n_e(r) = n_{e0} + \frac{1}{\pi r_e w_m^4} r^2, \tag{3.22}$$

[see figure 3.5(a)] will guide a laser pulse with a Gaussian transverse profile matched to the plasma channel, $w_0 = w_m$, with zero propagation losses. In fact, a general solution to the Helmholtz equation for the infinite parabolic plasma channel given by equation 3.22 is a Laguerre-Gauss (LG) mode

$$E_{p,m}(r,\theta,z) = E_0 \left(\frac{2r^2}{w_m^2}\right)^{\frac{m}{2}} \exp\left(\frac{-r^2}{w_m^2}\right) L_p^m\left(\frac{2r^2}{w_m^2}\right) \exp(im\theta) \exp(i\beta z), \tag{3.23}$$

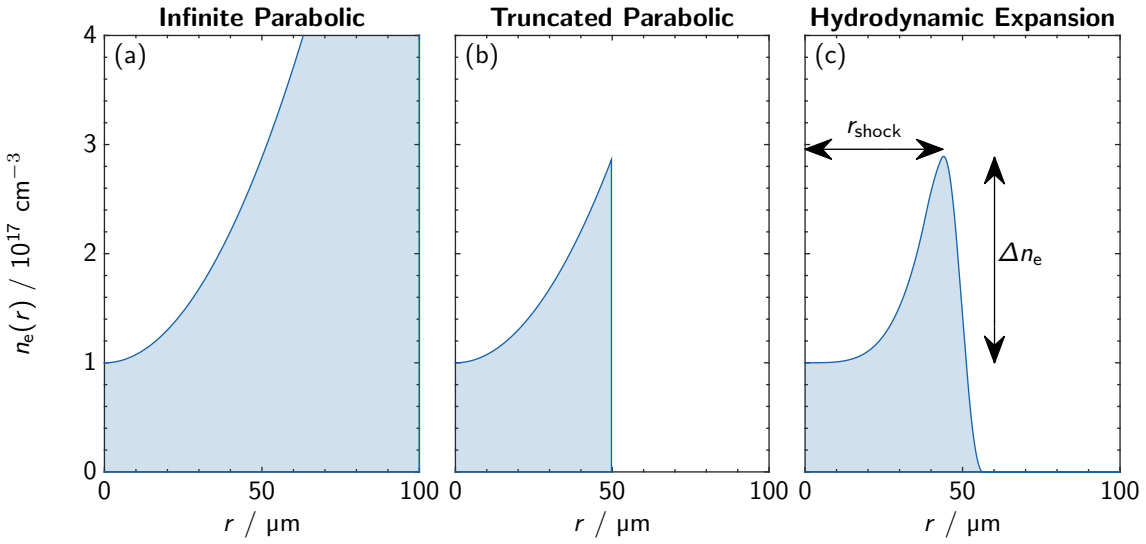

Figure 3.5: Example electron density profiles for (a) an infinite parabolic plasma channel with $w_m = 35\,\mu m$ and $n_{e0} = 1 \times 10^{17}\,cm^{-3}$, (b) a truncated parabolic plasma channel with $w_m = 35\,\mu m$ and $r_f = 50\,\mu m$, (c) a hydrodynamic expansion of a cylindrical plasma column. Electrons and ions close to the axis have moved from the axis to the shock front r_{shock}, generating a channel depth $\Delta n_e = n_e(r_{shock}) - n_{e0}$. Note that $n_e(r)$ is not parabolic close to the axis, but a refractive index profile suitable for guiding is still present.

where E_0 is the mode amplitude, $L_p^m(x)$ is the generalised Laguerre polynomial, and p and m are the radial and azimuthal modes respectively. Figure 3.4 shows the first 16 LG intensity modes, where by $I_{p,m}(r,\theta,z) \propto |E_{p,m}(r,\theta,z)|^2$.

In reality it is not possible to generate plasma channels with infinite parabolic profiles. Clark *et al.* [116] proposed the following treatment to calculate the transverse mode structure of light propagating in a plasma channel with arbitrary electron density profile. Waves travelling along the axis of the plasma channel (z-axis) can be written as $E(\vec{r}_\perp, z) = u(\vec{r}_\perp)\exp(i\beta z)$ where β is the complex propagation wavenumber.

Solving the Helmholtz equation for these waves leads to

$$\left[\nabla_\perp^2 + \kappa^2(\vec{r}_\perp, \omega)\right]\vec{E}(\vec{r}_\perp) = 0, \tag{3.24}$$

where $\kappa(\vec{r}_\perp, \omega)$ is the transverse wavenumber and $\nabla^2 = \nabla_\perp^2 + \partial^2/(\partial z^2)$. $\kappa(\vec{r}_\perp, \omega)$ can be broken down into contributions from the plasma refractive index $n_e(\vec{r}_\perp)/n_{crit}$, and the electric susceptibility

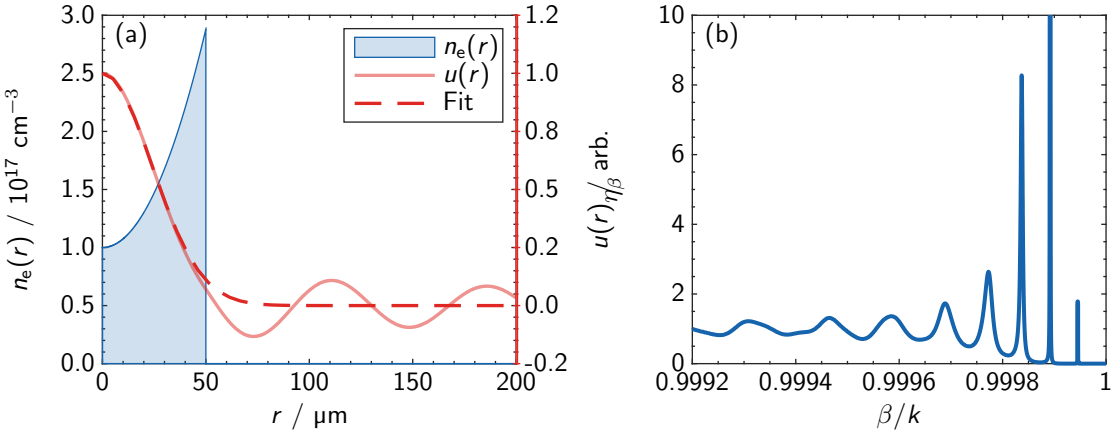

Figure 3.6: (a) Truncated parabolic profile (blue) with $w_m = 35\,\mu m$ and $r_f = 50\,\mu m$. Calculated lowest order quasi-bound mode (red, solid) for the plasma channel, matched spot size was $w_m = 35\,\mu m$, and attenuation length $L_{att} = 21.2\,mm$. For $r < r_f$, the quasi-bound mode very closely approximates a Gaussian mode (red, dashed) with the same w_m. (b) Ratio η_β as a function of β/k where k is the free space propagation wavenumber. The lowest order mode is clearly observed as a sharp peak at $\beta = 0.99994k$, and higher order modes can be observed as broader peaks, indicating faster leakage.

of the ions and neutrals which can be calculated from the Drude model to be $4\pi\chi(\vec{r}_\perp, \omega)$,

$$\kappa^2(\vec{r}_\perp, \omega) = k^2 \left[1 - \frac{\beta^2}{k^2} - \frac{n_e(\vec{r}_\perp)}{n_{crit}} + 4\pi\chi(\vec{r}_\perp, \omega)\right], \tag{3.25}$$

To proceed, it is assumed that the ions and the neutrals make insignificant contribution compared to the plasma electrons, and thus the final term can be dropped. The solutions to equation 3.24 can be split into three categories according to the behaviour of κ^2. If $\kappa^2 > 0$ for all $\vec{r}_\perp$, κ is real everywhere, the solutions are freely propagating modes and no laser confinement is achieved. A bound mode is described by $\kappa^2 > 0$ out to some radius $r < r_w$ (where $r = |\vec{r}_\perp|$), but $\kappa^2 < 0$ for all radial positions beyond this. These modes, are completely confined to $r < r_w$. In reality, n_e drops to zero beyond some radius r_f, as is the case for the truncated parabolic plasma channel and electron density profiles driven by hydrodynamic expansion. When this occurs, $\kappa^2 < 0$ over some finite range $r_w < r < r_f$, after which $\kappa^2 > 0$ again and propagating waves are allowed. Some confinement is achieved, however waves can tunnel to $r > r_f$ and freely propagate away from the axis at a shallow angle [116]. These modes are called leaky, or quasi-bound modes since a portion of the bound mode leaks away during propagation.

To find the quasi-bound modes that propagate in plasma channel, equation 3.24 is solved numerically, and resonances around discrete frequencies of $k_\perp$ are observed. Figure 3.6 shows an example of this for a truncated parabolic channel. This build up of quasi-resonant field is analogous to resonant loading of a Fabry-Perot cavity. Writing β as $\beta = \beta_r + i\alpha_{1/e}$, it can be shown that β_r sets the propagation wavenumber, and that the FWHM quasi-resonant peak $\Delta\beta$ gives the propagation losses of a given mode to leakage $\Delta\beta = 2\alpha_{1/e}$. It is then expected the transmission of each mode decays exponentially with a $1/e$ attenuation length $L_{\text{att}} = 1/\Delta\beta$ as $T(z) \propto \exp(-z/L_{\text{att}})$.

3.3.2 Beam Propagation Method

Although numerically solving equation 3.24 provides the transverse mode structure of the channel, and the attenuation length of each mode, it does not provide information about the propagation of imperfectly matched modes. As discussed in section 3.1.2, it is not possible to achieve arbitrary focal profiles experimentally in order to match to the plasma channels. Azimuthal asymmetries, aberrations, and spot-size mismatching all affect the propagation of the injected beam. Hence, it is useful to calculate the propagation of a beam (or pulse) with an arbitrary transverse profile through an arbitrary electron density profile. There are many methods of solving this problem, which as in section 3.3.1, amounts to solving the Helmholtz equation. In this thesis, the Fast-Fourier Transform Beam Propagation Method (FFT-BPM) is used.

Solutions of the form $E(x, y, z) = u(x, y, z)e^{-ikz}$ are sought. The paraxial approximation

$$\left|\frac{\partial^2 u}{\partial z^2}\right| \ll \left|2k\frac{\partial u}{\partial z}\right|, \tag{3.26}$$

can be employed to derive the paraxial Helmholtz equation

$$\frac{\partial u}{\partial z} = -\frac{i}{2k}\nabla_\perp^2 u - \frac{ik}{2}[\eta(x, y, z) - 1]. \tag{3.27}$$

The first term on the right hand side of equation 3.27 represents scalar diffraction, whilst the second term represents refraction by the medium. The FFT-BPM method solves this equation using a split-step operation. First, the field is propagated forwards half a step $\delta z/2$ using a diffraction

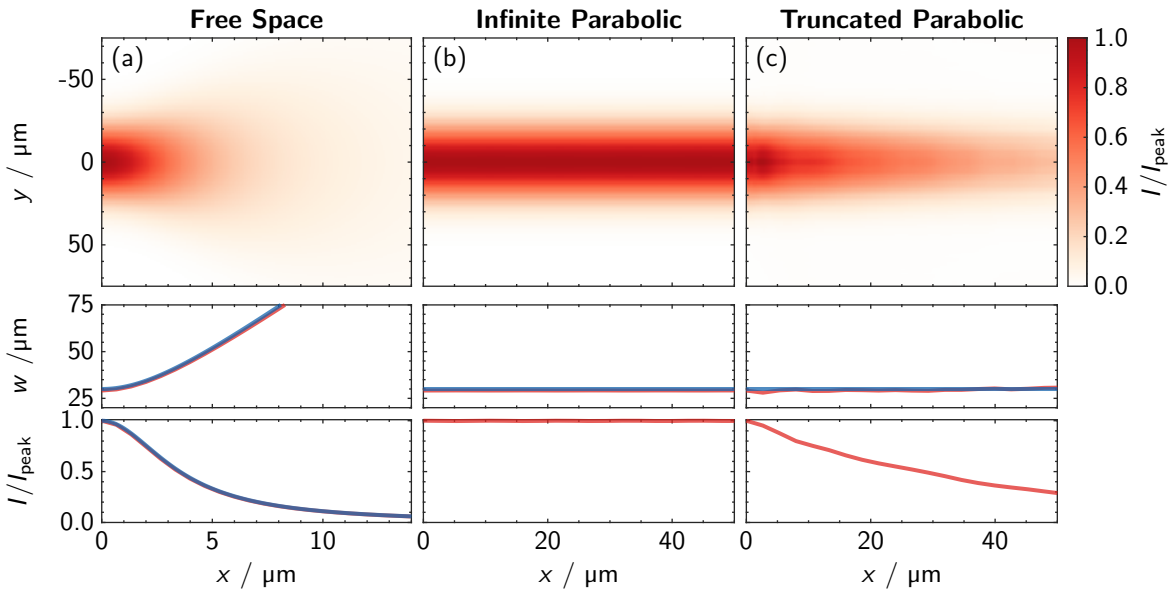

Figure 3.7: Example FFT-BPM calculations of a laser $\lambda = 800\,\text{nm}$ propagating through (a) free space, (b) an infinite parabolic plasma channel, and (c) a truncated parabolic plasma channel. Top: transverse lineout of the laser intensity. Middle: calculated spot-size variation with z. Bottom: calculated peak intensity variation with z. In (a), the blue curves compare the simulation to Gaussian beam theory, showing the propagation behaves as expected. In (b) and (c), the blue curve represents the calculated w_m from the method in section 3.3.1.

operator $\hat{D} = -(i/2k)\nabla_\perp^2$ corresponding to the first term on the right hand side. Then, the field is propagated a full step using a refraction operator corresponding to the second term on the right hand side $\hat{R} = -(ik/2)(\eta - 1)$. Finally, it is propagated another half step using the diffraction operator $\hat{D}$. Hence, the updated scalar field after one full step is given by

$$u(x, y, z + \delta z) = \exp\left(\frac{\delta z}{2}\hat{D}\right) \exp(\delta z \hat{R}) \exp\left(\frac{\delta z}{2}\hat{D}\right) u(x, y, z). \tag{3.28}$$

The FFT-BPM code used in this thesis was written in *Python* by the author, and verified by a similar code written by Dr. Aarón Alejo. The code provides a good estimate of the transverse mode $u(\vec{r}_\perp)$ as a function of z, but does not include any effects related to ultrashort pulse propagation such as ionisation, dispersion, ponderomotive effects, or wakefield generation.

Figure 3.7 shows three examples of the use of the FFT-BPM code to calculate free space propagation and matched guiding in an infinite parabolic channel and a truncated parabolic channel. In all cases excellent agreement with the expected propagation is observed.

3.4 High-Intensity Laser Pulse Propagation

3.4.1 Particle-In-Cell Simulations

For laser pulses with $a_0 \gtrsim 1$, corresponding to $I_{\text{peak}} \gtrsim 2 \times 10^{18}\,\text{W}\,\text{cm}^{-2}$, then ponderomotive effects and the response of the plasma electrons to the leading edge of the laser pulse will become significant and must be included. The transverse mode structure calculations and beam propagation methods discussed previously are not then sufficient to encapsulate the physics of pulse propagation.

In order to calculate the laser pulse evolution and plasma response most accurately, it is necessary to solve the full electromagnetic fields of the laser and the plasma using Maxwell's equations. However, maintaining maximum fidelity in the modelling of the plasma would require simulating the trajectory of every particle, which is impossible even for the latest supercomputers available. The most common alternative approach is to use particle-in-cell (PIC) simulations; the electromagnetic fields are defined on the vertices of a Eulerian grid, and the trajectories of macroparticles (each of which represents a cloud of physical plasma particles) in response to these fields are calculated.

The general PIC algorithm consists of four cyclical steps [199, 200]: (i) the position of each particle is updated according to the Lorentz force equation; (ii) the charge and currents are deposited on the grid by summing over the particle positions and accounting for their weights; (iii) the electromagnetic fields are advanced using Maxwell's equations; (iv) the new fields are interpolated back onto the positions of each particle, either conserving momentum or energy (depending on the code used) but not both simultaneously. Each step in the loop only involves quantities local to each macroparticle, making it simple to parallelise the the calculation. PIC codes also feature modules to simulate optical field ionisation [201], allowing for inclusion of ionisation induced effects; these are utilised extensively in Chapters 5 and 6.

PIC calculations in three dimensions can be extremely computationally expensive, and hence in the past two-dimensional Cartesian simulations were common-place, however this can result in profoundly different self-focusing behaviour [35]. In addition, it is found that in PIC codes EM pulses do not propagate at the group velocity of the medium, but instead at a spuriously-altered, resolution-dependent velocity (named spurious numerical dispersion) which can disrupt the physics

being simulated, and lead to substantial numerical artefacts.

Three important modifications can be employed to make the simulation of metre-scale LWFA stages drastically less computationally intensive. Firstly, since LWFA's exhibit a high degree of cylindrical symmetry, it is possible to treat them using PIC algorithms with azimuthal Fourier decomposition of the electromagnetic field components [202, 203]. Instead of a 3D Cartesian grid, a set of 2D radial grids are used, each one representing an azimuthal mode (labelled m). For $m = 0$, the grid is independent of azimuthal angle θ; for $m \geq 0$, the mth grid consists of the fields that vary proportionally to $\cos(m\theta)$, taking into account deviations from cylindrical symmetry. Secondly, PIC algorithms have been developed that solve Maxwell's equations in Fourier space, these are known as pseudo-spectral analytical time domain (PSATD) algorithms [204, 205]. This allows for Maxwell's equations to be integrated analytically in time, and makes the algorithms free of spurious numerical dispersion. A third modification is the boosted-frame technique [206, 207]. Instead of running the simulation in the reference frame of the laboratory, the simulation can be run in a different Lorentz frame moving in the same direction as the laser. In the boosted frame, the plasma is Lorentz contracted and moves relativistically towards the laser.

The simulations in this thesis all use the relatively new code FBPIC [203] — a quasi-3D cylindrical code with PSATD solvers and the capability of running in the boosted frame. FBPIC requires reduced computational time per simulation compared to previous simulation studies on propagation in plasma channels [69, 78]. Furthermore, it is compatible with OpenPMD, the open source set of tools provided to visualise PIC simulation results, and thus it is an excellent tool for experimentalists. The PIC simulations in this thesis were all carried out and analysed by the author using between 1 and 24 GPUs on ARC[†] (University of Oxford) or SCARF[‡] (Rutherford Appleton Laboratory). Oscar Jakobsson provided significant assistance in getting started with running multi-GPU and boosted frame simulations.

[†] `https://www.arc.ox.ac.uk/`
[‡] `https://www.scarf.rl.ac.uk/`

3.5 Diagnosing Low-Density Plasma Channels

3.5.1 Characterisation of Plasma Channels

Knowledge of the axial density n_{e0} is critical to LWFAs since this dictates the accelerating field strength, the plasma wavelength, the dephasing and pump depletion lengths, and the critical power for self-focusing. Further, knowledge of the shape of the plasma channel is vital to characterise the transverse mode size w_m, and the attenuation length L_{att}.

Optical probing of the plasma channel is ideal because the short pulse lengths available from Kerr-lens modelocked lasers are capable of capturing the fast dynamics of plasma channel formation and expansion. Indeed, a small portion of the main laser pulse used to form the plasma channel can be picked off from the main beam before the interaction to form the optical probe pulse.

There are several available techniques including shadowgraphy [208–210], interferometry [101, 117, 152], wavefront sensing [211], spectral interferometry [212, 213] and others [214–216]. For the experiments detailed in this thesis, interferometry was chosen as the diagnostic for characterising plasma channels due to its relative ease in setup, and since it has previously been shown to measure hydrodynamically formed plasma channels reliably [117, 170].

3.5.2 Interferometry

Interferometry is a general technique that can be used to measure the phase encoded onto a probe laser beam by interfering it with a second, undisturbed laser beam. A laser beam is split into two identical copies which travel along different paths, before being recombined at a small offset angle to generate interference fringes. The measurement is sensitive to the phase difference between the two paths that which causes the otherwise straight fringes to deviate (see figure 3.8).

The phase shift experienced by a plane wave $E_{probe}(z,t) = E_0 \exp[i(kz - \omega t)]$ travelling through a plasma with refractive index $\eta(x,y,z)$ and electron density profile $n_e(x,y,z)$ is given by

$$\begin{aligned} \Delta\phi(x,y) &= \frac{2\pi}{\lambda}\int_P [\eta(x,y,z) - 1]\ \mathrm{d}z \\ &\approx -r_e \lambda_{probe} \int_{-\infty}^{\infty} n_e(x,y,z)\ \mathrm{d}z, \end{aligned} \tag{3.29}$$

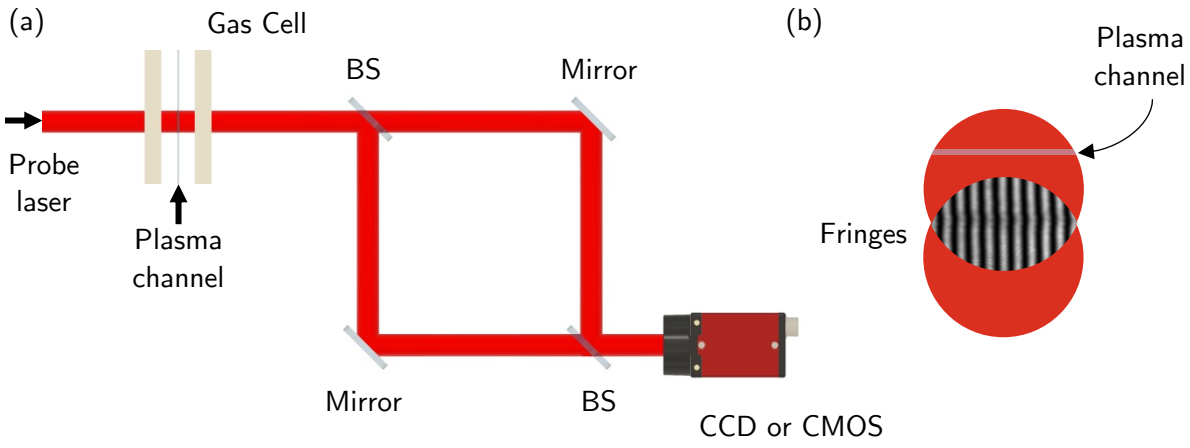

Figure 3.8: (a) Schematic of a folded wavefront Mach-Zehnder interferometer used to diagnose a laser produced plasma channel. The probe beam first passes through the gas cell containing the plasma channel, and is subsequently split and recombined by the Mach-Zehnder, generating fringes on the detector. (b) Cross-section of the two arms of the interferometer after recombination. The beams have been spatially offset in the vertical direction, and recombined with a horizontal angular offset in order to generate vertical fringes on the detector.

where $r_e \approx 2.818 \times 10^{-15}$ m is the classical electron radius.

Consider a second, reference plane wave travelling at some small angle θ with respect to the x-axis $E_{\text{ref}}(x,z,t) = E_0 \exp[i(kx\sin\theta + kz\cos\theta - \omega t + \psi)]$ where ψ is an arbitrary phase offset. Interference of E_{probe} and E_{ref} results in

$$\begin{aligned} I(x,y,z,t) &= \frac{c\epsilon_0}{2}\left|E_{\text{probe}} + E_{\text{ref}}\right|^2 \\ &= \frac{c\epsilon_0}{2}\left|E_0\exp[i(kx - \omega t + \Delta\phi(x,y))] + E_0\exp[i(kx\sin\theta + kz\cos\theta - \omega t + \psi)]\right|^2 . \end{aligned} \tag{3.30}$$

If the detector is defined to be at $z = 0$, then the intensity distribution observed in the plane of the detector, the interferogram, is

$$I(x,y,z,t) = \frac{c\epsilon_0}{2}E_0^2\left[1 + \cos\left(kx\sin\theta - \Delta\phi(x,y) - \psi\right)\right], \tag{3.31}$$

showing that, in the absence of plasma the interference pattern consists of a set of fringes evenly spaced by $\lambda_{\text{fringes}} = \lambda_{\text{probe}}/\sin\theta$. When plasma is present in a region of the $x-y$ plane, the fringes

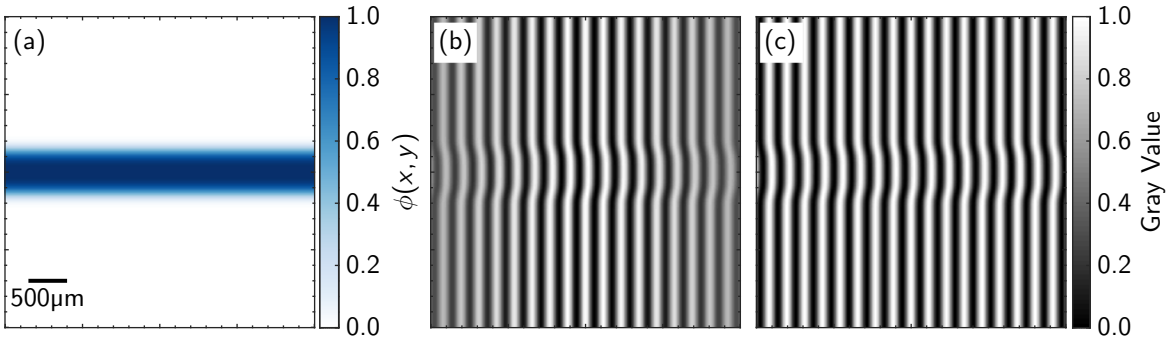

Figure 3.9: (a) Example phase shift produced by a $500\,\mu$m plasma column on a $4\,\text{mm} \times 4\,\text{mm}$ grid. (b) Simulated interferogram produced for the phase map shown in (a) with a $\tau_\text{L} = 40\,$fs laser pulse, $\lambda_\text{probe} = 800\,$nm, and a crossing angle of $0.2\,$deg. It is clear that the fringe visibility at the edges of the image is reduced compared to the centre. (c) The same simulated interferogram but with the pulse length stretched by a factor of 4, achieved experimentally by a band-pass interference filter.

will be shifted from their original positions.

3.5.3 Experimental Realisation

Interferometry with Short Pulse Durations

Omitted from equation 3.31 is a treatment on how the probe laser pulse duration affects interference. The two copies of the probe pulse will maximally interfere with each other when they are perfectly overlapped in time, that is, the path difference between the two copies $d_\text{MZ} = 0$. When this occurs, the fringe visibility, defined in terms of the maxima and minima of the measured fringe pattern $V = (I_\text{max} - I_\text{min})/(I_\text{max} + I_\text{min})$ is equal to 1. Since the beams pass across each other at an angle θ, the path difference $d = d(x)$ must be a function of the distance along the axis at which they cross, and hence $V = V(x)$ also. It can be shown that [217]

$$V(x) = \exp\left[-\frac{\ln(2)\sin^2\theta}{c^2\tau_\text{L}^2}\left(x - \frac{d}{\sin\theta}\right)^2\right]. \tag{3.32}$$

Equation 3.31 can be modified to include the contribution of the fringe visibility for a pulse of duration τ_L

$$I(x, y, z, t) = \frac{c\epsilon_0}{2} E_0^2 \left[1 + V(x) \cos\left(kx \sin\theta - \Delta\phi(x, y) - \psi\right)\right]. \tag{3.33}$$

Hence, the maximum distance over which the fringe visibility $V > 0.5$ is

$$x_{\text{vis}} = \frac{2c\tau_L}{\sin\theta}, \tag{3.34}$$

which for probe pulses used in experiments ($\tau_L \sim 40\,\text{fs}$) can result in the fringe visibility only extending across a small portion of the detector; a simulation demonstrating this is shown in figure 3.9. To account for this, a bandpass notch filter is placed directly in front of the detector to lengthen the pulse after it has traversed the plasma and extend the region of high visibility.

Folded Wavefront Mach-Zehnder Interferometer

Several different interferometry configurations exist. In this thesis, the folded wavefront Mach-Zehnder interferometer is employed, a schematic of which is shown in figure 3.8. The Mach-Zehnder interferometer requires more space than the commonly employed Michelson interferometer, but is capable of offering increased control over the fringe spacing and orientation, and object position on the detector. This increases the signal-to-noise ratio of the diagnostic, and allows small fringe shifts to be detected. The folded wavefront interferometer differs from other configurations by splitting and recombining the probe laser *after* it has passed through the plasma. Each copy of the beam contains phase shifts incurred from the plasma, however provided that the probe laser is larger in diameter than the plasma, and the two copies of the laser beam generated are recombined at a spatial offset, then the portion of one copy which passed through the plasma are interfered with a portion of the other copy that did not pass through the plasma. This scenario is shown in figure 3.8(b). The noise that remains emanates from local variations in the wavefront of the probe beam that cause a fringe shift when spatial offset is introduced; these fluctuations are in principle much smaller than those introduced by sending one copy of the beam down a completely separate path in the vacuum chamber.

Imaging

After the plasma, the probe pulse will diffract as it propagates to the detector, destroying the phase information by spreading it into the rest of the beam profile. This occurs faster for larger gradients in $\Delta\phi(x, y)$. Hence, it is necessary to image the plane containing the plasma onto the plane of the detector. It is possible to show that the optimal image plane is the plane at which the phase shift $|\Delta\phi(x, y)|$ is maximised [103].

Transverse and Longitudinal Interferometry

Plasma channels formed by hydrodynamic expansion have the advantage that optical diagnostic access is available from almost every direction since they have no external structure surrounding them, however it is not guaranteed that the plasma expansion will be the same for all points along z. Hence, it is favourable to probe the plasma channels along a direction transverse to the waveguide axis, which results in averaging over one transverse dimension, rather than with a co-propagating pulse that averages over longitudinal variations in the plasma (see figure 3.10).

Further, it is found that the phase shift incurred by passing longitudinally through a plasma column more than $\sim 1\,\text{cm}$ long is greater than 2π. For example, a $1\,\text{cm}$ long plasma column of density $n_e = 1 \times 10^{18}\,\text{cm}^{-3}$ suffers a phase shift 3.6π, almost 2 fringes on an interferogram. This causes the measured fringes to disconnect, and the phase cannot be recovered.

3.5.4 Recovering the Phase from a Fringe Pattern

The plasma phase shift can be recovered from a measured fringe pattern using a Fourier transform based method as described by Takeda *et al.* [218] or by using a continuous wavelet transform method [219]. Here, the former is employed. It begins from a more general form of equation 3.33

$$I(x, y) = a(x, y) + b(x, y)\cos\left[kx\sin\theta - \Delta\phi(x, y) - \psi\right], \tag{3.35}$$

where $a(x, y)$ represents background noise, primarily from imperfect optics and fringe contrast, and $b(x, y)$ represents is the fringe intensity which includes the fringe visibility.

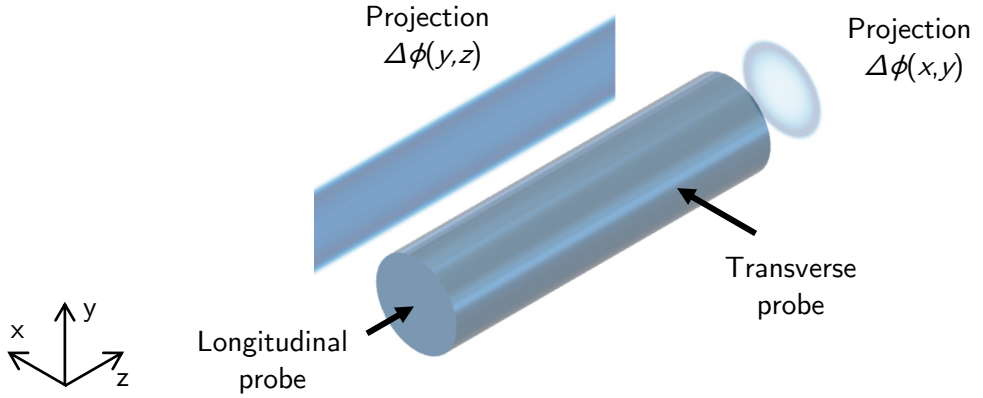

Figure 3.10: Illustration of two possible probing geometries for a hydrodynamically formed plasma channel, and the resulting projection. The longitudinal pulse propagates parallel to the optical axis, generating a projection linearly proportional to the average transverse electron density, whereas the transverse probe pulse provides information about the longitudinal evolution of the plasma channel.

By making the substitution

$$c(x,y) = b(x,y)\exp\left[-i(\Delta\phi(x,y)+\psi)\right], \tag{3.36}$$

this can be rewritten as

$$I(x,y) = a(x,y) + \frac{1}{2}\left[\exp(ikx\sin\theta)\,c(x,y) + \exp(-ikx\sin\theta)\,c^*(x,y)\right]. \tag{3.37}$$

The Fourier transform of equation 3.37 is given by

$$\mathcal{F}\left[I(x,y)\right] = A(k_x,k_y) + \frac{1}{2}\left[C(k_x - k\sin\theta, k_y) + C^*(k_x + k\sin\theta, k_y)\right], \tag{3.38}$$

where $A(k_x,k_y)$ and $C(k_x,k_y)$ are the Fourier transforms of $a(x,y)$ and $c(x,y)$ respectively. Equation 3.38 indicates there are three peaks in the frequency domain all at $k_y = 0$ and at $k_x = 0$, $k\sin\theta$ and $-k\sin\theta$ corresponding to each term respectively (see figure 3.11). The information relating to $\Delta\phi(x,y)$ is contained in the sidebands at $\pm k\sin\theta$, and hence it is necessary to isolate one of these sidebands by defining a box of dimensions K_x, K_y in frequency space centred on

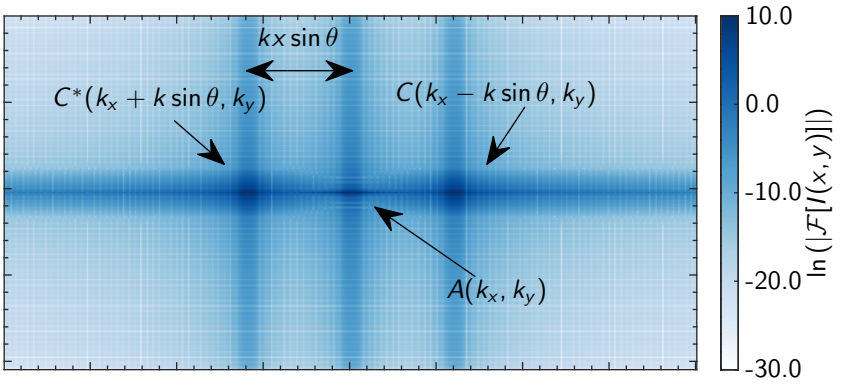

Figure 3.11: Fourier transform of the interferogram shown in figure 3.9(c) showing clearly the three peaks predicted by equation 3.38. The $\Delta\phi(x, y)$ information is contained in the side peaks, separated by $kx\sin\theta$.

$k_x = k\sin\theta$, and setting the value of $\mathcal{F}[I(x, y)] = 0$ outside of this region. This is given by

$$\mathcal{F}[I(x,y)]_{\text{isolated}} = \frac{1}{2}C(k_x - k\sin\theta, k_y). \tag{3.39}$$

Following this, the inverse Fourier transform is taken to give

$$\mathcal{F}^{-1}\left[\mathcal{F}[I(x,y)]_{\text{isolated}}\right] = \frac{1}{2}c(x,y), \tag{3.40}$$

which contains the desired information (see equation 3.36). Since $b(x, y)$ is real, the argument of $c(x, y)$ will provide the phase shift incurred by the plasma

$$\arg\left(\mathcal{F}^{-1}\left[\mathcal{F}[I(x,y)]_{\text{isolated}}\right]\right) = kx\sin\theta - \Delta\phi(x,y) - \psi. \tag{3.41}$$

The task is now to extract $\Delta\phi(x, y)$. A constant ψ term would be straightforward to remove, however in reality, $\psi = \psi(x, y)$ and contains phase variations due to the two beams propagating through slightly different paths before interfering, and that the initial probe wavefront is not perfectly flat. The $kx\sin\theta$ term, or carrier term, term adds a linear slope to one direction of the image and can be removed either by shifting the isolated sideband back to $k_x = 0$ before the inverse Fourier transformed. However by applying the same analysis routine to a reference image

taken close in time to the image containing the plasma, but without the plasma present, and subtracting it removes both the carrier term and the $\psi(x, y)$ variations:

$$\Delta\phi(x, y) = -\arg\left(\mathcal{F}^{-1}\left[\mathcal{F}\left[I_{\text{data}}(x, y)\right]_{\text{isolated}}\right]\right) + \arg\left(\mathcal{F}^{-1}\left[\mathcal{F}\left[I_{\text{ref}}(x, y)\right]_{\text{isolated}}\right]\right). \tag{3.42}$$

The code for the procedure outlined in this section was written in MATLAB by the author, with significant input from Dr. Robert Shalloo.

Phase Unwrapping

All phase retrieval methods require the arg function, which only returns values in the range $[-\pi, \pi)$. Where the overall phase shift $\Delta\phi(x, y)$ exceeds 2π, and thus the phase will become wrapped, introducing discontinuities (see figure 3.12). It is necessary to unwrap the phase to remove the discontinuities. This is simple to do by eye and in one dimension, but the problem becomes complicated in two dimensions since the discontinuities do not always span both dimensions, and give rise to singularities or residues. These become difficult because the possible ways to unwrap the phase become path dependent. However there is only one "correct" solution, and several algorithms exist to find it [220–222]. In this thesis, the Herraez method [221] is implemented using a code written in MATLAB [223].

Background Subtraction

For interferograms with low total phase shift, like the transverse interferometry data included in this thesis, variations in the wavefront of the probe beam can add a significant background to a phase map. These variations can be mitigated in experiment with care of probe optic cleanliness and by employing a spatial filter in the probe line. It is often found that recovered phase maps have a background phase that can be described as a second order polynomial, which can be removed by a polynomial subtraction. To do this, the region containing plasma is masked out of the image, and a two-dimensional, second-order polynomial is applied to the rest of the image. The fitted polynomial is removed from the image to leave only the plasma, and higher frequency noise.

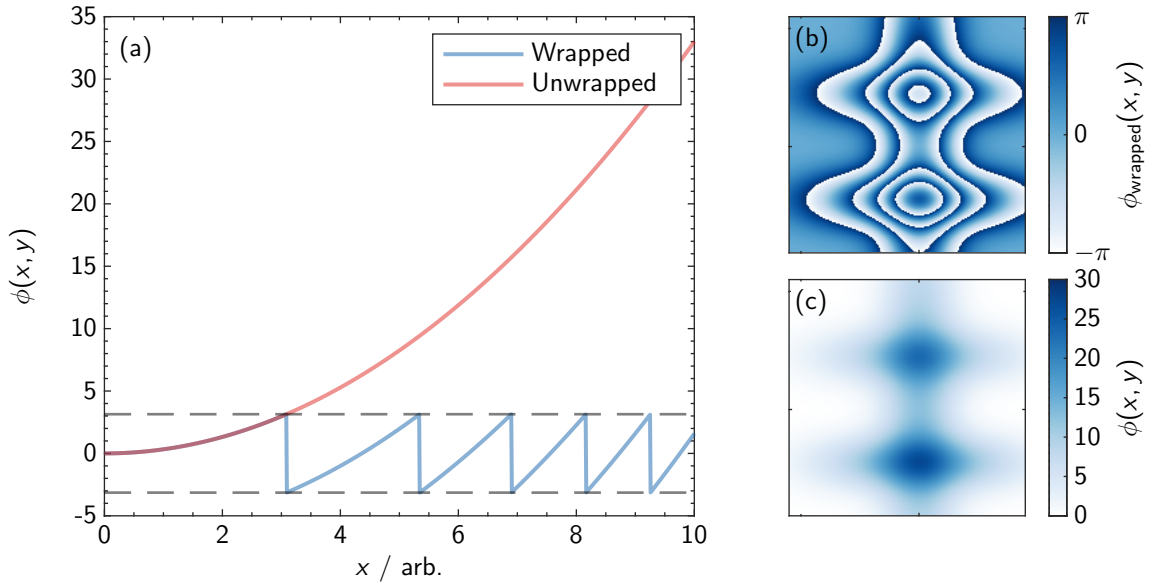

Figure 3.12: Examples of one-dimensional (a) and two-dimensional phase unwrapping (b-c). In the cas of (a), unwrapping is straightforward. x is scanned from $x = 0$ towards positive x. If a discontinuity occurs at x', then 2π is either added or subtracted to $\Delta\phi(x > x')$ depending on which direction the discontinuity jumped. (b) Example of a wrapped phase with several peaks, leading to resiudes that are complex to unwrap. (c) The unwrapped phase from (b) using the Herraez method [221].

Chapter 4

Optical Guiding in 100-mm-long HOFI Plasma Channels

4.1 Introduction

In this chapter, the first experiment employing HOFI plasma channels at petawatt (PW) scale laser facilities, and the formation of channels up to 100 mm long is reported. The experiment was undertaken at the Astra-Gemini TA3 laser at the Rutherford Appleton Laboratory (RAL) commencing June 2019 and lasting for six weeks; it followed directly on from a proof of principle experiment on the 20 TW Astra-Gemini TA2 laser in 2018. In that experiment, we demonstrated generation of a 16 mm, $n_{e0} \approx 1.5 \times 10^{17}\,\mathrm{cm}^{-3}$ HOFI plasma channel using an axicon lens; guide a pulse of intensity $4 \times 10^{17}\,\mathrm{W\,cm}^{-2}$ through those channels; and diagnose low-density plasma channels using sensitive transverse interferometry techniques [102]. This chapter builds directly on the work undertaken there, and details the experimental design and results of the follow-up experiment on the PW scale laser. Design challenges of long HOFI plasma channels and of PW-scale facility experiments are discussed. Optical guiding of laser pulses with a peak input intensity of $6 \times 10^{17}\,\mathrm{W\,cm}^{-2}$ through 100 mm long plasma channels is demonstrated with on-axis densities measured to be as low as $n_{e0} = (1.0 \pm 0.3) \times 10^{17}\,\mathrm{cm}^{-3}$. The transmission efficiency of the guided pulses through HOFI plasma channels is investigated in detail.

4.1.1 Experimental Objectives

In this experiment, the main objectives were to

- generate $\gtrsim 100$ mm long HOFI plasma channels with axial densities $\sim 1 \times 10^{17}$ cm^{-3};
- guide a high-intensity laser pulse with $w_m \approx 40$ μm through the plasma channel;
- develop understanding of HOFI plasma channel experiments on PW-scale lasers.

The experimental design was led by the author, who played the lead role in planning all aspects of the experiment with specific contributions to the gas cell design from Dr. Aarón Alejo, and the probe beam design by Jakob Jonnerby and Barnaby Matthews. The experimental campaign was also led by the author, who was assigned one of the "Target Area Operators" (along with Dr. Aarón Alejo) for the duration of the campaign. The analysis of all experimental results presented here were written and performed by the author, with input from Dr. Aarón Alejo.

4.2 Experimental Design and Setup

4.2.1 Gemini TA3 Laser

The Gemini TA3 laser at the Rutherford Appleton Laboratory, UK is a Ti:Sapphire laser system providing two, linearly-polarized ~ 300 TW pulses, denoted "North" and "South", with a central wavelength 800 nm. Each beam provides up to 15 J, and a full-width at half-maximum duration of 40 fs. Since experiments are strictly limited to six weeks in duration, they require careful design and planning to ensure that the objectives can be achieved in the allotted time. With this in mind, it was important to keep the design simple enough to be setup quickly, and to make daily alignment straightforward, whilst allowing flexibility to cope with any issues that arose. It was decided that the design should be similar to the successful proof-of-principle experiment with emphasis on improving the design, as opposed to making significant changes.

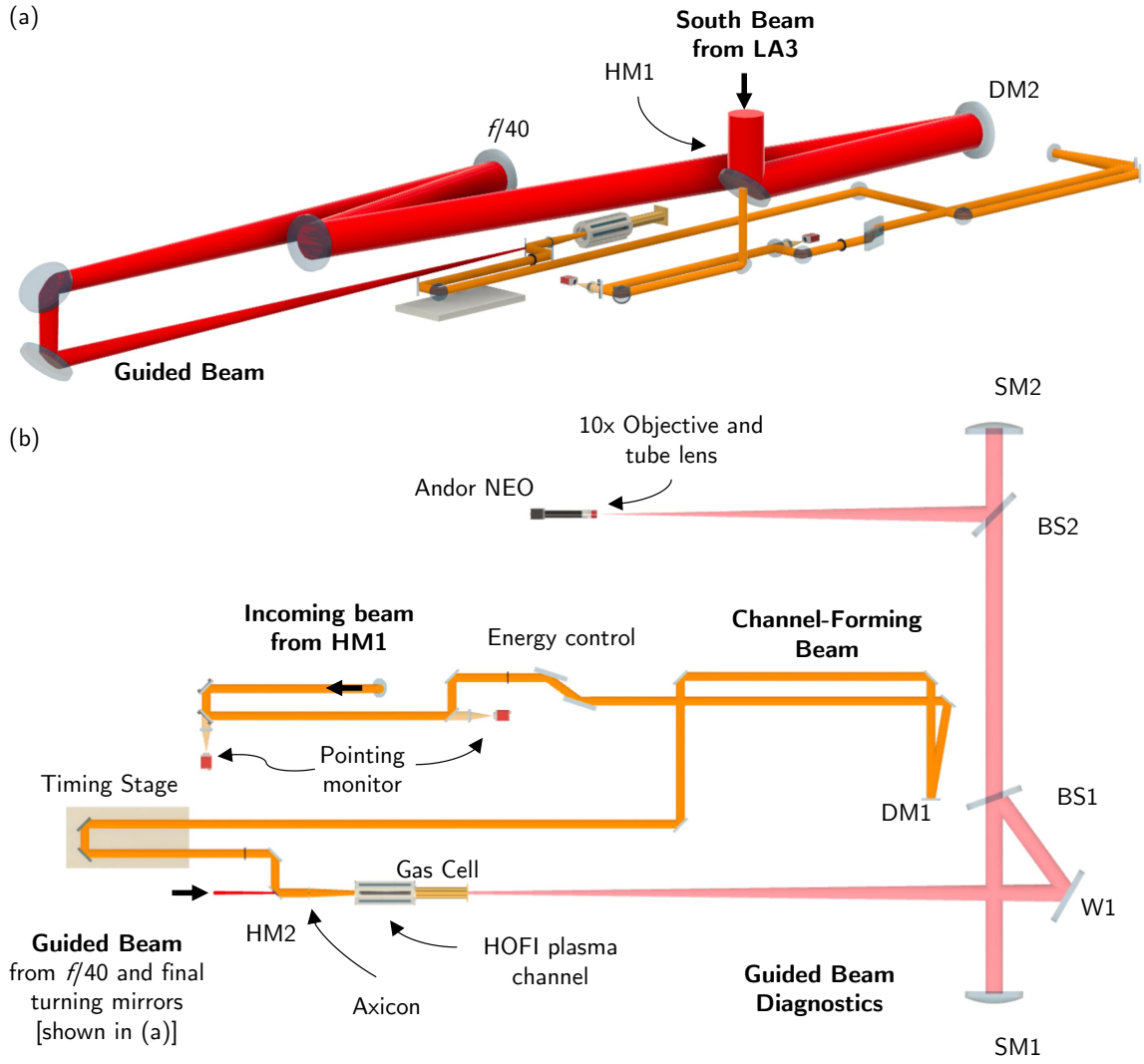

Figure 4.1: (a) Schematic of the Gemini TA3 vacuum chamber (guided beam diagnostics not shown). The collimated South beam from LA3 is split into the channel-forming beam (gold) and the guided beam (red) by an annular mirror (HM1). A periscope placed after the OAP was used to direct the guided beam into the gas cell. (b) Top-View of the Gemini vacuum chamber (guided beam not shown) and guided beam diagnostics (light red). The channel-forming beam passes through the energy control system, and reflects from deformable mirror. It then passes through the timing stage and is coupled into the gas cell.

4.2.2 Laser Beams and Diagnostics

Chamber Layout and Guided Pulse

Figure 4.1 shows the layout of the experiment. The beam used to generate the HOFI channels (hereafter denoted the "channel-forming beam"), and that to be guided (the "guided beam"), were

both derived from the South beam. The guided beam was formed from this beam by reflection from a high-reflectivity dielectric mirror (HM1) in which a hole of diameter $D_{\text{hole}} = 50\,\text{mm}$ had been drilled. The beam transmitted by the hole, which constituted the channel-forming beam, contained pulses up to 160 mJ in a diameter $D_{\text{ax}} = D_{\text{hole}} = 50\,\text{mm}$.

The guided pulse was setup mimicking successful LWFA experiments at the Gemini facility. The beam entering the chamber was fully compressed to 40 fs. After reflection from HM1, it was reflected from a deformable mirror (DM1) to flatten the wavefront, and subsequently focused by an off-axis paraboloid with a focal length of $f = 6\,\text{m}$ used at $f/40$. By replacing the final turning mirror with an uncoated glass wedge, it was possible to reduce the energy on target to approximately $\mathcal{E}_{\text{guided}} \approx 1.1\,\text{J}$ and run guiding experiments without the possibility of driving a significant wakefield.

Channel-Forming Beam

Drift in the pointing of the channel-forming beam was monitored by two CCD cameras placed behind dielectric beamline mirrors. The beam was passed through a pulse energy control system, comprising a half wave-plate and a pair of thin-film reflective polarizers. The beam was reflected from a deformable mirror (DM2), oriented at a small angle of incidence, and its polarization converted to circular by passing it through a zero-order quarter wave-plate oriented at 45° to the incident polarization. It was then sent to a retro-reflecting timing stage, reflected by a second holed mirror (HM2, $D_{\text{hole}} = 18\,\text{mm}$), and focused into the target gas cell by a fused silica axicon lens with base angle $\vartheta = 5.6°$, and 10 mm diameter hole in the centre. To flatten the wavefront, the beam at the surface of DM2 was imaged onto a Shack-Hartmann wavefront sensor (*Imagine Optic HASO4*), which was operated in a closed feedback loop. This was sufficient to optimise the axicon focus.

Simulations using the measured laser spectrum showed that material dispersion due to the axicon substrate stretched the pulse by approximately 40 fs [193] and thus reduced the intensity of the channel forming beam by a factor of ~ 2. This decrease was not expected to change the properties of the axicon focus or plasma formation substantially. The non-linear phase acquired by passing through the substrate of the axicon was approximately $\phi_{\text{NL}} \approx 3\,\text{rad}$ which may have led

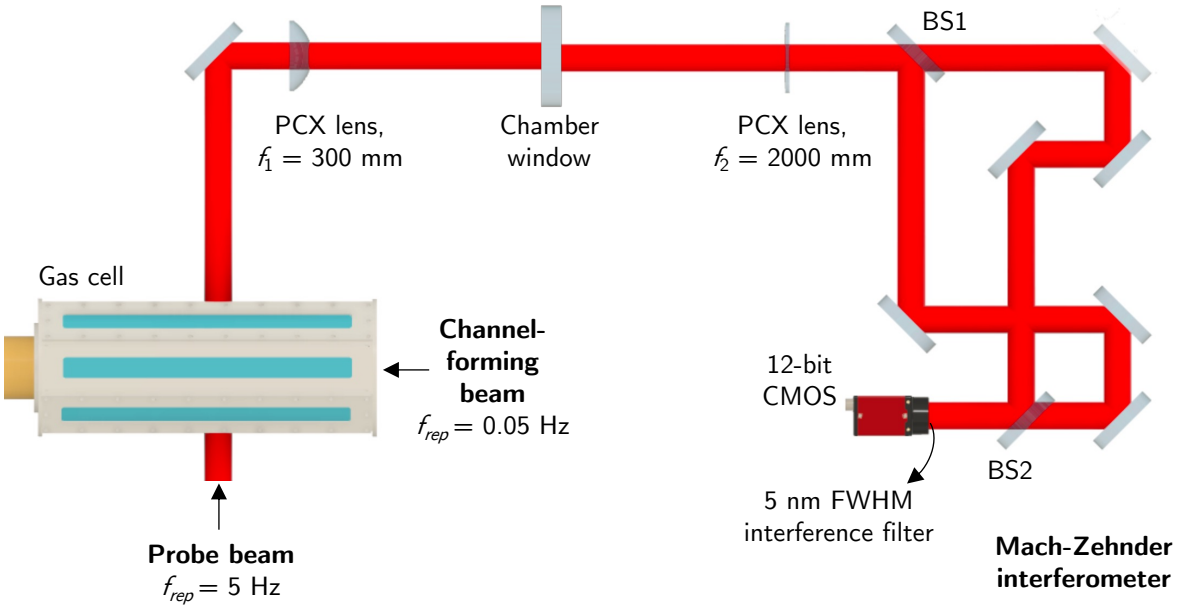

Figure 4.2: Schematic of probe layout. The 800 nm pulse, $f_{\text{rep}} = 5\,\text{Hz}$ derived from the North beam passes through a timing stage (not shown) and through the gas cell transversely. A planoconvex lens ($f_1 = 250\,\text{mm}$) was placed at a distance f_1 from the plasma channel. The light then passed out of the vacuum chamber through an optically flat UVFS window, and was focused by a second planoconvex lens ($f_2 = 2000\,\text{mm}$) to form an image of magnification 8 on the surface of a 12-bit CMOS detector. After the second lens, a folded wavefront Mach-Zehnder interferometer as shown in the figure was placed to generate fringes on the detector.

to further self phase modulation. It was not possible to directly measure the effect of self-phase modulation from the axicon lens, however it was not expected that such effects affected the temporal profile significantly.

Transverse Probe Beam

A transverse probe, derived from the North beam, was used to gather information about the electron density profile of the channel via folded wavefront interferometry (see figure 4.2). Since it was known that the signal-to-noise ratio of the retrieved phase maps would be low, it was important to minimise the experimental noise as much as possible. The primary noise sources in the interferograms were spatial and shot-to-shot variations in the wavefront of the probe laser pulse, and dust spots or other debris which led to diffraction patterns imprinted on the laser pulse. To improve background subtraction, the Gemini laser chain was adjusted to allow for 5 Hz operation

of the North beam whilst the full power South beam operated in single shot; reference shots were taken immediately before and after each data shot.

A four-pass retro-reflecting delay stage was installed inside the chamber to enable the probe beam to arrive at delays τ in the range $-0.1 < \tau < 4.3$ ns with respect to arrival the channel-forming beam. After this stage, a pointing stabilisation system was used to maintain the alignment of the beam over long periods of data taking and to correct small misalignments from the delay stage. This system consisted of two motorised mirrors and two leakage cameras placed behind dielectric mirrors, and beam pointing was maintained using a *Python* script written by Dr. Aarón Alejo. The probe beam was then passed through the cell perpendicular to the plasma channel, and the rays scattered by the plasma were collected and recollimated by a 2-inch plano-convex lens with focal length $f_1 = 300\,\text{mm}$. A planconvex lens with focal length $f_2 = 2000\,\text{mm}$ was used to reimage the plasma channel onto a 12-bit CMOS detector. The measured spatial resolution was $(9 \pm 1)\,\mu\text{m}$. A Mach-Zehnder interferometer (design as shown in figure 4.2) was placed between the imaging lens and the CMOS. This particular Mach-Zehnder allowed for independent control of the fringe spacing in each direction, and the spatial offset of the images with respect to one another. By doing this, it was possible to generate wide spatial fringes perpendicular to the channel z-axis, maximising the fringe deviation for any given shot, thus increasing the signal-to-noise ratio. A full characterisation of the retrieved phase maps from this diagnostic is provided in section 4.3.3.

Guided Pulse Diagnostics

Figure 4.1(b) shows the guided pulse far-field diagnostics. The light leaving the exit pinhole of the gas cell was reflected by an uncoated optical wedge (W1) and directed by a beamsplitter (BS1) to a spherical mirror (SM1) of focal length $f_1 = 3.175\,\text{m}$, used at $f/12.5$. The collimated light from the object plane, located a distance f_1 from SM1, was returned through BS1, and propagated out of the vacuum chamber through an optically flat window. Light was directed to a second combination of beamsplitter (BS2) and on-axis paraboloid (SM2, $f_2 = 2.0\,\text{m}$), to produce an image of the object plane. This was then reimaged onto a 16-bit CMOS camera (*Andor NEO 5.5*) with a 10x microscope objective and tube lens (*Mitutoyo M-Plan Apo* and *Mitutoyo MT-L* respectively). The first spherical mirror, SM1, was mounted on a translation stage, which allowed the longitudinal

position of the object plane to be adjusted over a range of $120\,\text{mm}$ permitting imaging of the focal plane, and the exit pinhole. An aperture located between the gas cell and W1 was used to prevent light from the channel-forming beam reaching the CCD. The resolution of the imaging system was limited by W1 and SM1, which in turn were fixed in position by the distance required for the guided beam to diffract and reduce in fluence enough to avoid burning W1. Calibration via a USAF target showed that the magnification was 6.5 and the resolution was $(9 \pm 1)\,\mu\text{m}$.

Prior to the focus, stability of the guided beam far-field was characterised by two separate diagnostics: (i) the low-power beam transmitted through a mirror inside the South Compressor was focused using an on-axis paraboloid ($f_{\text{leak}} = 1.2\,\text{m}$) and imaged by an 8-bit CCD camera; and (ii) a focus camera placed inside the vacuum chamber. It was not possible to measure the pointing stability of the $f/40$ beam inside the TA3 chamber on-shot. Hence, the available on-shot pointing measurements were only sensitive to movement prior to the target chamber.

4.2.3 Gas Cell

One of the most challenging aspects of HOFI experiments is the design of the system containing the target gas. HOFI experiments require a cell capable of holding a uniform body of gas up to pressures of $\sim 100\,\text{mbar}$, whilst allowing both the channel-forming beam and drive beams to be coupled in without blocking or distorting their wavefronts. In LWFA experiments with no external guiding mechanism, the gas cell is simply a box of uniform gas density with pinholes of radius r_{ph} at either end to couple the drive laser in and out. Since the drive beam focuses to a spot size $w_0 \approx 0.9\lambda f_{\#}$, it is relatively simple to couple this into the cell via a small pinhole. The degree of uniformity of the gas in the cell, and the longitudinal extent of the gas plumes extending out of the cell is set by the pinhole diameter, D_{ph}, which should be large enough to allow the drive laser spot to be coupled in, but small enough to prevent large gas plumes emanating from the pinhole. Such gas plumes create a long density up-ramp for the drive laser as the gas flows rapidly (at approximately sonic speeds) into the surrounding vacuum. To a first approximation, the scale length of the density up-ramp is equal to D_{ph} [103].

In contrast, for HOFI experiments, channel-forming beam comprises a disk of radius $r \gtrsim L_{\text{ch}} \tan\alpha$ at the cell entrance. For $\alpha = 2.5\,\text{deg}$, a 100 mm channel requires $D_{\text{ph}} \approx 9\,\text{mm}$, generating

a density up-ramp around 10 % of the channel length, which for this experiment was $\gtrsim 2z_R$. Previously, a modification of the simple gas cell had been proposed by Dr. Robert Shalloo [103] where the front window was replaced by a thin fused-silica window through which the channel-forming beam was coupled in. This windowed gas cell [see figure 4.3(a)] relies on the fact that the converging Bessel Beam is not intense enough to damage the glass or acquire excessive non-linear phase. These constraints can be estimated using simple geometric arguments, assuming that the converging annulus remains spatially uniform, and that the intense Bessel focus has not begun to form. With these assumptions, the non-linear phase acquired by a pulse passing through the material is approximately

$$\phi_{NL} \approx \frac{2\pi}{\lambda}\frac{F_{col}}{\tau} n_2 t_w, \tag{4.1}$$

where $n_2 \approx 2 \times 10^{-16}\,\mathrm{cm^2\,W^{-1}}$ is the non-linear refractive index of the window substrate, and t_w is the window thickness. For $t_w = 1\,\mathrm{mm}$, $\phi_{NL} \approx 1.4$, which is significant but less than that already accumulated by passing through the axicon substrate. However in the proof-of-principle experiment, plasma channel formation was not observed in the windowed gas cell [103]. Appreciable damage was observed on the thin window at the front of the cell that was attributed to deposits of debris from ablation of the rubber o-ring.

For this experiment, the cell was engineered to allow versatility and accommodate several different options* (see figure 4.2.3). In the first configuration, a $t_w = 1\,\mathrm{mm}$, UVFS window (*Eksma Optics*) was secured on the entrance of the cell. The channel forming focused through the window and formed a channel beginning $\sim 5\,\mathrm{mm}$ downstream of the window surface. The more intense drive beam travelled through a small pinhole $D_{ph} = 1\,\mathrm{mm}$ reaching focus at the front of the channel. The pinhole was machined into the glass by James Cowley using the Oxford TW Ti:Sapphire laser. To avoid debris from the o-ring, the window diameter ($D = 60\,\mathrm{mm}$) was much larger than the beam diameter at the window entrance.

The second configuration reverted to a simple gas cell by replacing the glass window for an aluminium one with an aperture large enough to couple in both the guided and channel-forming

*A supersonic gas jet was also considered for this experiment, and developed by L. Feder, B. Miao, J. Shrock and H. M. Milchberg at UMD [198], however at the time of the experiment this setup had yet to be tested, and the designed slit nozzle significantly blocked the incident channel-forming pulse.

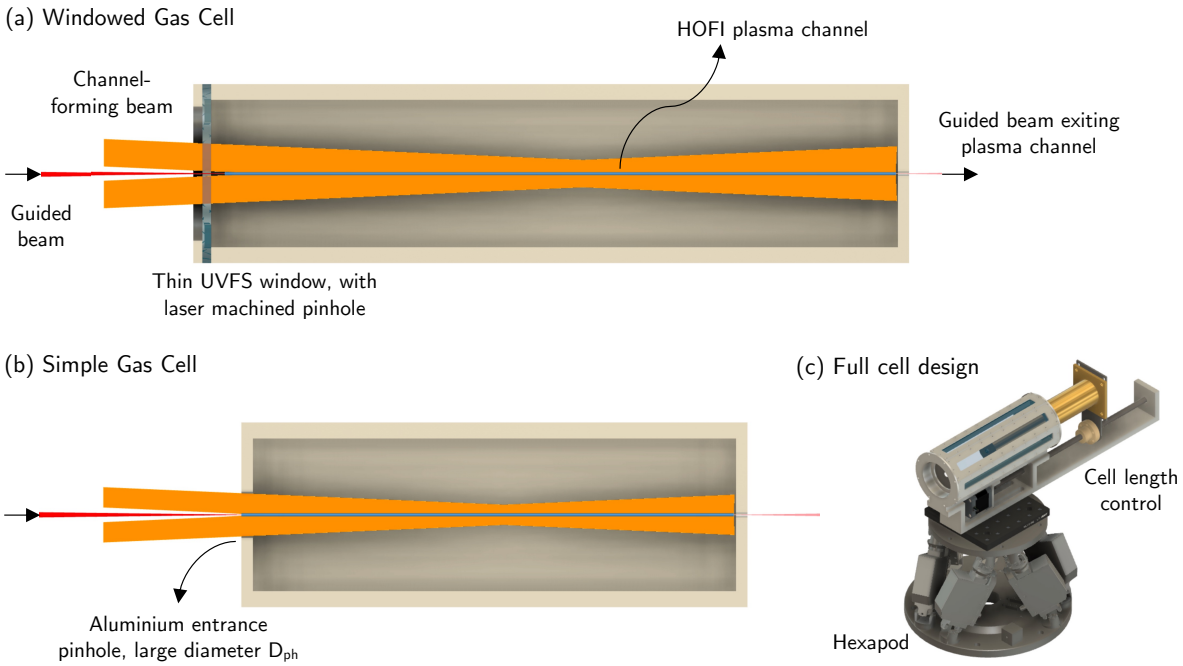

Figure 4.3: (a) Windowed gas cell concept design. The channel forming beam (gold) enters through the laser window, thickness t_w, whilst the high-intensity guided pulse enters through the laser machined pinhole (red). The HOFI plasma channel begins a short distance into the cell. (b) Simple gas cell. Both beams enter though a larger, aluminium pinhole. The HFO channel extends through the front pinhole. (c) Full cell design including plunger and stepper motor for precise length control, and hexapod for precise alignment.

beams [see figure 4.3(b)]. The largest possible aperture size that would still maintain suitable pressure in the cell was $D_{ph} = 9\,\text{mm}$, allowing for $L_{ch} = 100\,\text{mm}$. However it was acknowledged that for channels longer than $\sim 20\,\text{mm}$, gas uniformity close to the aperture was diminished due to formation of far-reaching gas plumes.

The main body of the cell was constructed from aluminium and was of octagonal cross-section, the distance between opposite faces being 92 mm [see figure 4.3(c)]. A set of 2 mm thick, optically flat UVFS windows of dimensions $225 \times 25\,\text{mm}$ were sealed to the sides of the cell to provide optical access all the way along the waveguide from a variety of transverse angles. In practice, only one angle and longitudinal position was used. A single, 5 mm inner diameter gas inlet was located 23 mm from the front of the gas cell. The fill pressure, which could be varied in the range 10 mbar to 100 mbar, was measured to a precision of 1 mbar by a pressure transducer connected directly to the gas cell. The exit pinhole was mounted on a tube, side-sealed to the body of the cell by an o-ring, which allowed its longitudinal position to be adjusted by driving the tube with a stepper motor. The gas cell was mounted on a Hexapod (*Physik Instrumente*) for precise alignment, and the z position was adjusted to achieve the best coupling of the guided beam, which was typically found to be within one z_R of the entrance.

4.3 Initial Results

4.3.1 Laser Setup

The transverse fluence profile of the collimated Gemini beam is shown in figure 4.4(a). The solid line shows the approximate portion transmitted through HM1. The straight edge observed at the bottom comes from a beam clip in the diagnostic measuring the near field, and was not present in the beam itself. The dashed line indicates the outer edge of a 140 mm ideal top-hat fluence profile, whilst the solid line represents how HM1 split the beam. The lower part of the beam had a significantly lower intensity than the upper section. The pulse length measured by a FROG diagnostic before the data runs was $\tau = (40 \pm 3)\,\text{fs}$.

The measured focal spot of the pulse to be guided is shown in figure 4.4(b) and is compared to

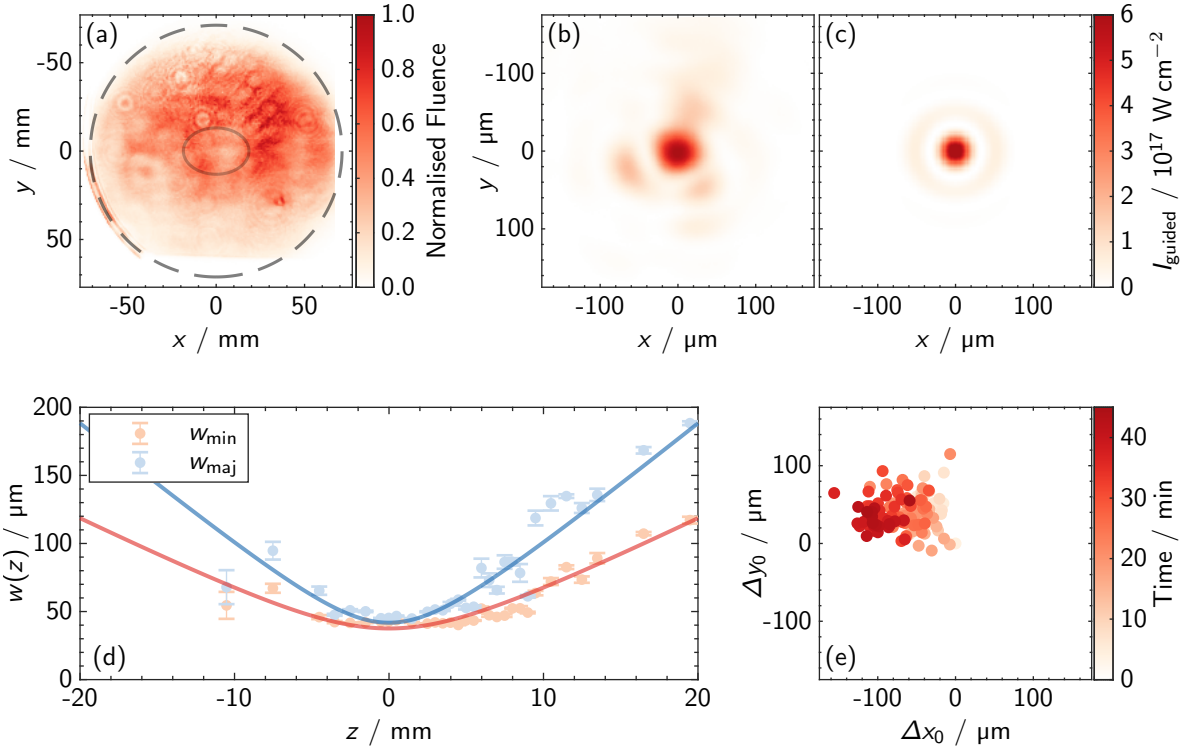

Figure 4.4: (a) Transverse fluence profile of the collimated Gemini TA3 South beam, measured via a leakage diagnostic placed behind the last turning mirror in the South beam compressor. The dashed line indicates the outer edge of a 140 mm ideal top-hat fluence profile, whilst the solid line shows how HM1 split the beam. (b) Measured focal spot of the guided beam focused by the $f/40$ after optimisation. The spot size was measured to be $w_0 = 38\,\mu$m (c) Calculated focal spot for an incident tenth order super-Gaussian with a size matching that of (a) and with a hole in the centre. (d) Measured minor (red) and major (blue) spot size as a function of distance from the laser focus. The Rayleigh range was estimated to be $z_R = 4.5$ mm. (e) The measured shot-to-shot variation of the guided beam centroid over a 45 minute period at $f_{rep} = 0.05$ Hz.

the simulated spot shown in figure 4.4(c), which simulated free space propagation of an ideal super Gaussian profile with a hole in the near field as produced by HM1. Without HM1, the focal profile was expected to be close to those shown in section 3.1.2, however the simulated profile exhibited a relatively more intense second ring and azimuthal asymmetry than the ideal case due to the hole. Despite the use of a deformable mirror, the measured focus exhibited more transverse structure than the simulated spot, which was attributed to non-uniformities in the collimated beam observed in figure 4.4(a). The peak focused intensity was measured to be $I_{peak} = 6.1 \times 10^{17}\,\mathrm{W\,cm^{-2}}$. Figure 4.4(d) shows how the measured spot size varies with longitudinal position in vacuum. The guided

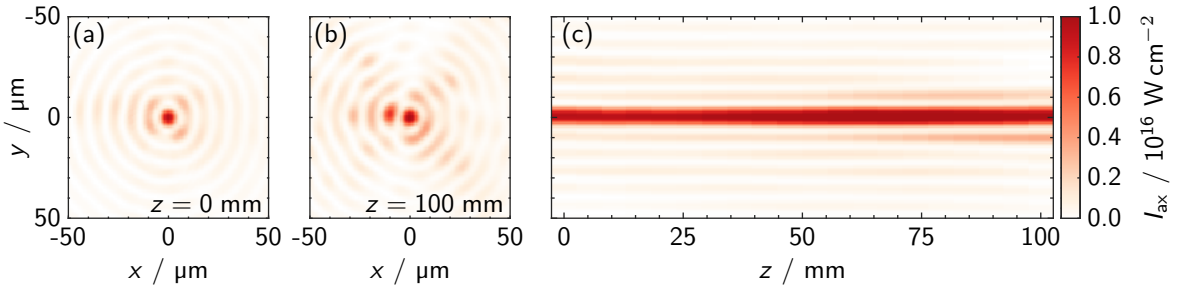

Figure 4.5: The measured transverse intensity profile of the channel-forming pulse focused by the axicon ($\vartheta = 5.6$ deg) at (a) the front and (b) back pinholes (c) Measured longitudinal intensity profile, obtained by taking lineouts of the transverse intensity profile at 5 mm intervals. Since the channel-forming beam was stable from shot-to-shot, transverse profiles in (a) and (b) and each profile in (c) were averaged over 10 consecutive shots.

beam waist was measured to be $w_0 \approx 38\,\mu$m, corresponding to a spot that was approximately 1.3 times diffraction limited and a Rayleigh range of $z_R = (4.5 \pm 0.8)$ mm. The position of the guided beam focal spot was monitored over a 45-minute period at a shot repetition rate of 0.05 Hz. The change in position of the beam centroid with respect to the first shot taken is plotted in figure 4.4(e); darker colours correspond to later in time. The beam displayed significant shot-to-shot jitter, the measured standard deviation of the beam pointing was $\Delta\theta_{\text{focus}} = (6 \pm 1)\,\mu$rad.

The measured transverse and longitudinal intensity profiles of the channel-forming pulse are shown in figure 4.5. It can be seen that the transverse intensity profile $I_{ax}(r)$ of the channel-forming beam was essentially independent of z over a distance of 100 mm. The profile matched closely to that expected for an axicon illuminated by a top-hat beam (see section 3.1.2). The first intensity minimum occurred at a radius $r = 7.1\,\mu$m, in close agreement with the expected value, and the peak intensity of the focused channel-forming beam increased with longitudinal position, from 7×10^{15} W cm^{-2}, between $z = 0$ and $z = 100$ mm. The transverse position of the axicon focus was found to be highly stable from shot-to-shot. At $z = 0$, the measured standard deviation of the shot pointing was found to be just $0.6\,\mu$m, almost insignificant compared to that of the beam to be guided.

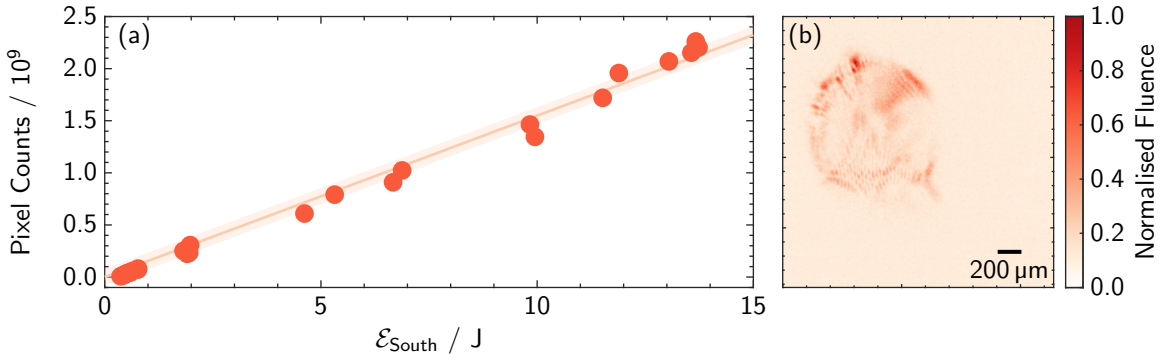

Figure 4.6: (a) Integrated optical flux on the guided diagnostic far-field CMOS plotted as a function of South beam laser energy. The red line shows a linear fit to the data. (b) Example background image as measured by the far field camera. For this shot, the guided pulse was blocked. There is a dim constant background observed due to dark current signal, and a brighter ring of light produced by scattering of the axicon beam from the back pinhole.

Calibrating the Guided Pulse Diagnostics

Before calculating the parameters of the guided beam, it was necessary to remove the background from the measured far-field camera signal. There were two main sources of background present: the scatter of the axicon beam from the rear pinhole, and a dark current background across the image. Both can be seen in figure 4.6(b), which shows an example of the far-field signal when imaging the rear pinhole, but with the guided beam not present. The scattered light from the axicon was not stable from shot-to-shot, and thus could not be directly subtracted.

The following procedure was employed to remove these two contributions to the background signal when analyzing the guided beams. An annulus, centred on the guided beam, and with inner and outer radii of $1.5w_{\text{guided}}$ and $3w_{\text{guided}}$ was defined. A 2-dimensional, quadratic polynomial was fitted to the signal within this annulus, and this fitted signal was removed from the raw CCD signal. Tests of this method using simulated guided spots added to the background signal shown in figure 4.6(b) showed that this approach allowed the energy of the guided beam to be recovered to within $10\,\%$ of the true value, and the spot size to be recovered via the D4σ method to within $5\,\%$.

The optical flux was first calibrated to the input beam energy. The gas cell was removed, the channel forming beam was blocked and SM1 was moved to image the focal plane of the $f/40$ beam. The energy of the guided beam was varied and the integrated optical flux was

measured and compared to a pre-calibrated energy meter placed behind a turning mirror before the compressor (see figure 4.6). By fitting a linear slope, it was found that the CCD measured $c_{\mathcal{E}} = (1.54 \pm 0.10) \times 10^8$ counts per joule of laser energy. The energy transmission of each shot was calculated by dividing the integrated CCD signal of the guided beam by the calibration $c_{\mathcal{E}}$ and the beam input energy (as measured by an energy meter placed inside the compressor). This calibration was valid as long as any changes in the spectrum of the guided beam resulting from its interaction with the plasma (see section 1.2.3) was not sufficient to change the transmission through the optics after the interaction and the quantum efficiency of the detector. For parameters considered in this experiment, the shift in wavelength remained small enough for the assumption to be valid.

4.3.2 Gas Cell Tests

Initial tests were carried out using the windowed gas cell configuration. A time-integrated image of the channel taken by an SLR camera placed above the chamber and imaging the plasma showed that several non-uniformities were observed in the plasma column, particularly near the front window (see figure 4.7). Almost no plasma was observed ~ 35 mm downstream of the laser window. This feature remained in the same place when the gas cell was scanned in z, and thus lack of plasma was attributed to damage on the front window preventing transmission of the channel forming light, and that this damage occurred close to the pinhole. Microscope images of several of these windows recorded before and after data runs showed that damage had been inflicted by both laser machining the pinhole, and the outer Bessel rings of the channel-forming beam, as shown in figure 4.7(b) and (c) respectively.

Here we re-evaluate the windowed gas cell proposed and tested in the proof-of-principle experiment and this experiment. When considering whether or not the cell window would be damaged, it was assumed that the transverse intensity profile of the incident channel-forming beam was constant over the surface of a disk, the dimensions of which decreased as the beam focused. However, this simplification is not realistic, and instead it is clear from figure 4.7 that Bessel rings were present on the window and the peaks of the rings ablated and darkened the window. Simulations undertaking by Aimee Ross following the angular spectrum method after

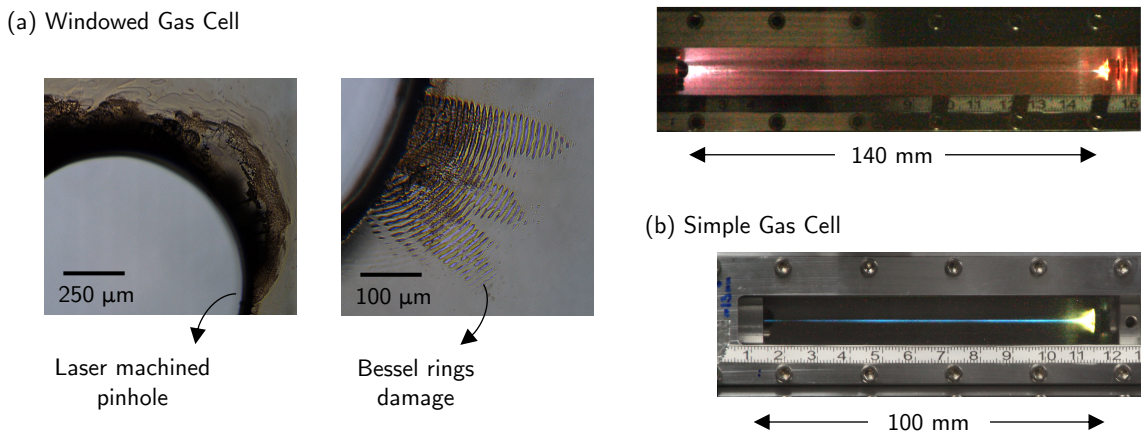

Figure 4.7: (a) Windowed gas cell. Left: damage observed on the thin window before data-taking, inflicted by laser machining of the pinhole. Middle: ablation and browning observed on the front surface of the thin window after data taking. The damage clearly resembles the transverse intensity profile of the channel-forming beam. Right: Time-integrated image of the visible plasma emission produced by the channel-forming beam focused into the gas cell at a fill pressure $P = 50$ mbar. It is clear that the plasma emission varied significantly with longitudinal position (b) Simple gas cell. Time-integrated image at a fill pressure $P = 26$ mbar. The scale visible at the bottom of the image is in cm. Note that the apparent decrease in plasma brightness near a scale reading of 2.5 cm arises from blackening of the cell window in that region, not from non-uniformity of the plasma.

the experiment showed that the beam forms Bessel rings a few cm prior to the focus leading to a $\sim 50\times$ increase in intensity compared to a uniform disc. This intensity was enough to significantly damage the window and prevent plasma formation close to the front of the cell.

Conversely, figure 4.7(c) shows a time-integrated SLR image of the visible plasma emission in the simple gas cell configuration. It can be seen clearly that the brightness and diameter of the plasma column were nearly uniform over the 100 mm length of the cell; the uniformity of the initial plasma is a consequence of the strong dependence on intensity of optical field ionisation, and the fact that the transverse intensity profile and the axial intensity of the channel-forming beam depend only weakly on z. For these reasons the simple gas cell was used for guiding experiments in the remainder of the experiment.

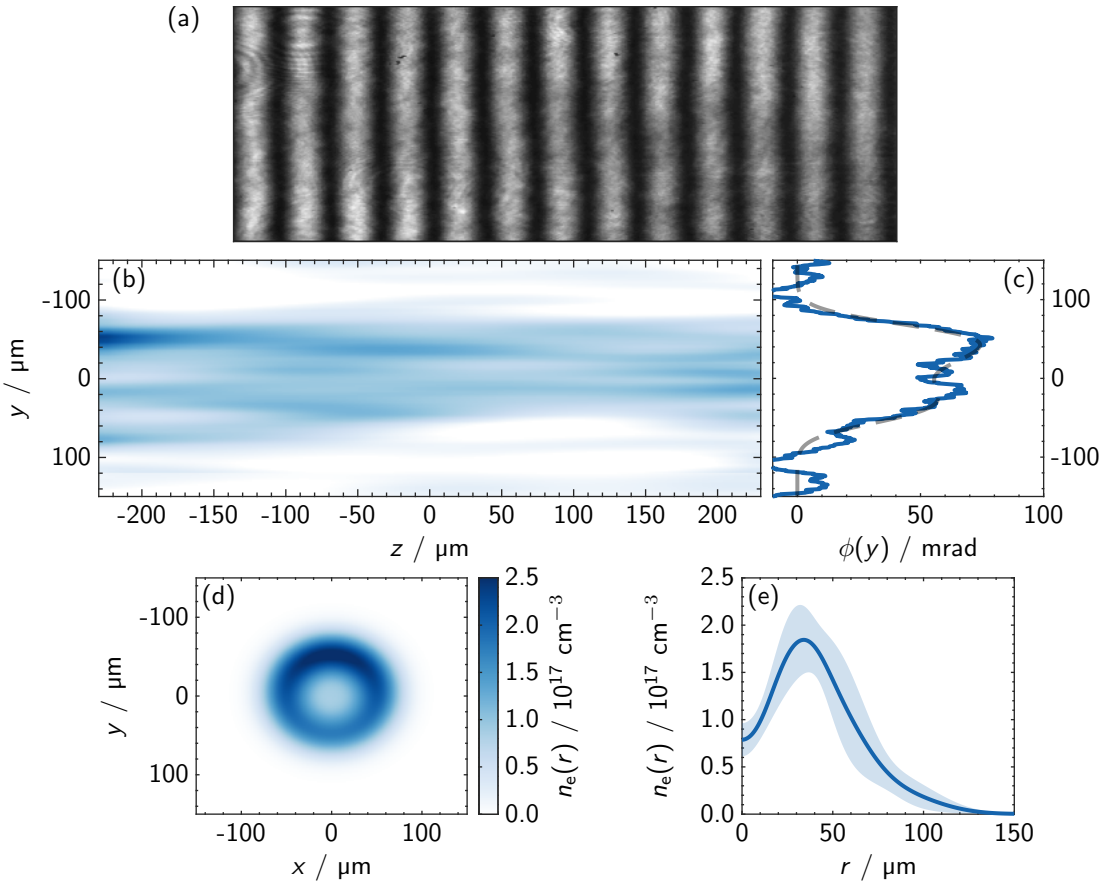

Figure 4.8: (a) Example fringe map measured by the transverse interferometry camera. For this shot, the fill pressure was $P = 27\,\text{mbar}$ and delay $\tau = 2.7\,\text{ns}$. (b) Recovered phase map $\phi(y, z)$ for the fringe map measured in (a). (c) Longitudinally averaged phase map (blue) together with fitted phase achieved by the density retrieval (dashed) for the same shot. (d) Retrieved electron density profile for the transverse probe shot shown in (a-c). A small asymmetry was observed upon recovery, though it is unlikely this would have affected the guiding significantly. (e) The rotationally averaged electron density profile, averaged over 5 shots taken under the same conditions as (a-d). The light band is one standard deviation wide.

4.3.3 Transverse Interferometry

The transverse electron density profiles of the HOFI plasma channels were deduced from transverse interferometry using the method described in section 3.5.4. Figure 4.8 shows an example measured fringe map at a delay of $\tau = 2.7\,\text{ns}$ after the channel forming pulse and fill pressure $P = 27\,\text{mbar}$, the extracted and fitted phase, and the subsequent retrieved n_e. Indeed, the total phase shift is small ($\phi_{\text{meas}} < 100\,\text{mrad}$) and the fringe shift almost not visible, however it was possible to infer

the electron density profile using the forward fitting method. For this particular shot, the the measured axial density was $n_{e0} \approx 9 \times 10^{16}\,\mathrm{cm}^{-3}$.

The temporal evolution of the transverse electron density profile of the plasma channel was found to be consistent with our earlier work [101, 102]. At $\tau \approx 0$ a cylindrical column of plasma, with a diameter of approximately 15 µm was formed; this expanded rapidly, driving a cylindrical shock wave into the surrounding gas, and forming a plasma channel within the region encircled by shock front. Figure 4.9 shows the measured transverse electron density profiles at $\tau = 3.0\,\mathrm{ns}$ for several initial fill pressures, averaged over a longitudinal distance $\Delta z = 1.2\,\mathrm{mm}$ centred at $z \approx 25\,\mathrm{mm}$. It can be seen that n_{e0} increases approximately linearly with P, as observed previously [102], and that the position of the shock front is approximately independent of P, as expected from Sedov-Taylor blast-wave theory [197]. The phase shifts measured for plasma channels with axial densities $n_{e0} \lesssim 1 \times 10^{17}\,\mathrm{cm}^{-3}$ were too small to be retrieved reliably, however it was possible to generate plasma channels with axial densities below this value. For these fill pressures, the axial density was inferred from 1D magnetohydrodynamics (MHD) simulations using the code HELIOS [166]; these results are shown in figure 4.9(b).

Several important properties of the channel were extracted, as shown in figures 4.9(b-d). The matched spot size w_m was calculated using the method described in 3.3.1 with a code written by Dr. Aarón Alejo. For $P = 67\,\mathrm{mbar}$, $w_m = (29\,^{+\,4}_{-\,3})$ µm, and the channel depth was measured to be $\Delta n_e = n_e(r_{shock}) - n_{e0} = (1.2 \pm 0.2) \times 10^{17}\,\mathrm{cm}^{-3}$ where r_{shock} is the measured radial position of the shock front. The channel depth was reduced to $\Delta n_e = (0.7 \pm 0.1) \times 10^{17}\,\mathrm{cm}^{-3}$ for an initial fill pressure of $P = 31\,\mathrm{mbar}$, whilst $w_m = (37 \pm 2)\,\mu\mathrm{m}$ was closer to w_0. Only modes satisfying $(2p + m + 1)^2 < \pi r_e r_m^2 \Delta n_e$ were expected to guide with low loss [115]. It was therefore expected that only low-order modes would propagate without significant loss, and that the plasma channels measured were essentially single-mode waveguides.

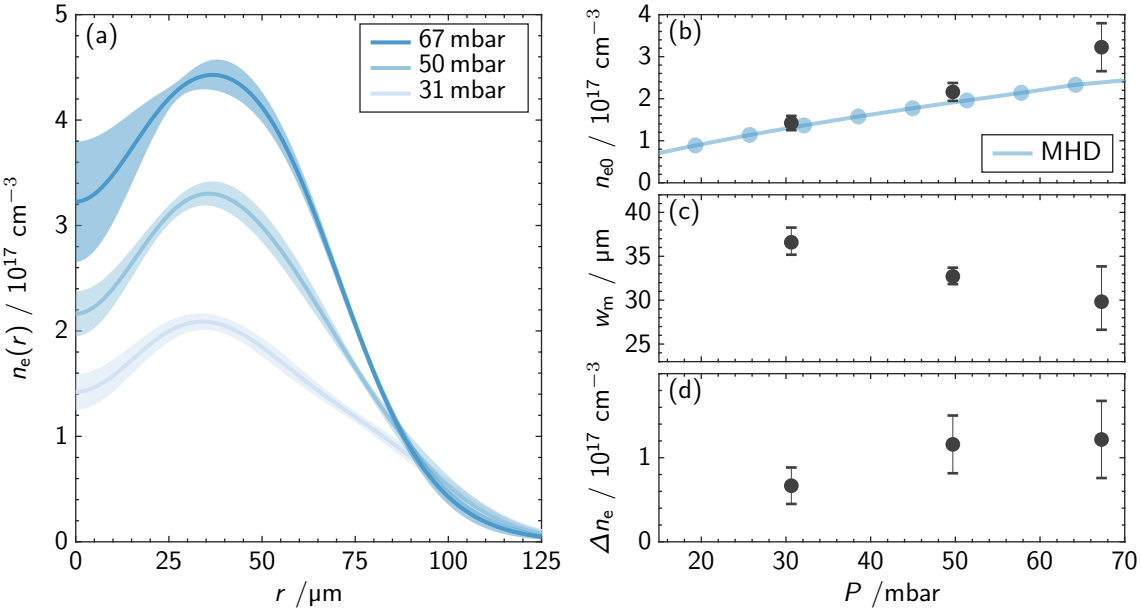

Figure 4.9: (a) Deduced electron density profiles of HOFI channels for $\tau = 3.0$ ns and several initial fill pressures. For each plot the light bands show the standard deviation obtained from averaging approximately 10 shots. (b) Comparison of the on-axis electron density measured by interferometry and that calculated by MHD simulations (blue) for $\tau = 3.0$ ns. (c) Variation of the measured matched spot size W_M with fill pressure. (d) Variation of the measured channel depth with P; for $\Delta n_e \lesssim 2 \times 10^{17}$ cm^{-3} the plasma channels were single-mode waveguides.

4.4 Optical Guiding Results and Discussion

4.4.1 Demonstrating Optical Guiding at Low Axial Densities

Figure 4.10 demonstrates guiding of high-intensity laser pulses in HOFI channels up to 100 mm long. Figure 4.10(a) shows the transverse fluence profile of the guided beam at focus, recorded by the forward diagnostic camera at full power. Figure 4.10(b) shows the profile of the beam at $z = 50$ mm in the absence of a HOFI channel, showing clearly the effect of diffraction over a distance of more than $10z_R$. Figure 4.10(c) shows the fluence profile in the same plane, but at a delay $\tau = 3.0$ ns after focusing the channel-forming beam into the cell filled to $P = 68$ mbar. The increase in the peak transmitted fluence is striking, and demonstrates clearly that the pulse was guided through the plasma channel generated by the channel-forming beam. For this pressure and timing, the on-axis density was measured to be $n_{e0} = (3.8 \pm 0.5) \times 10^{17}$ cm^{-3}.

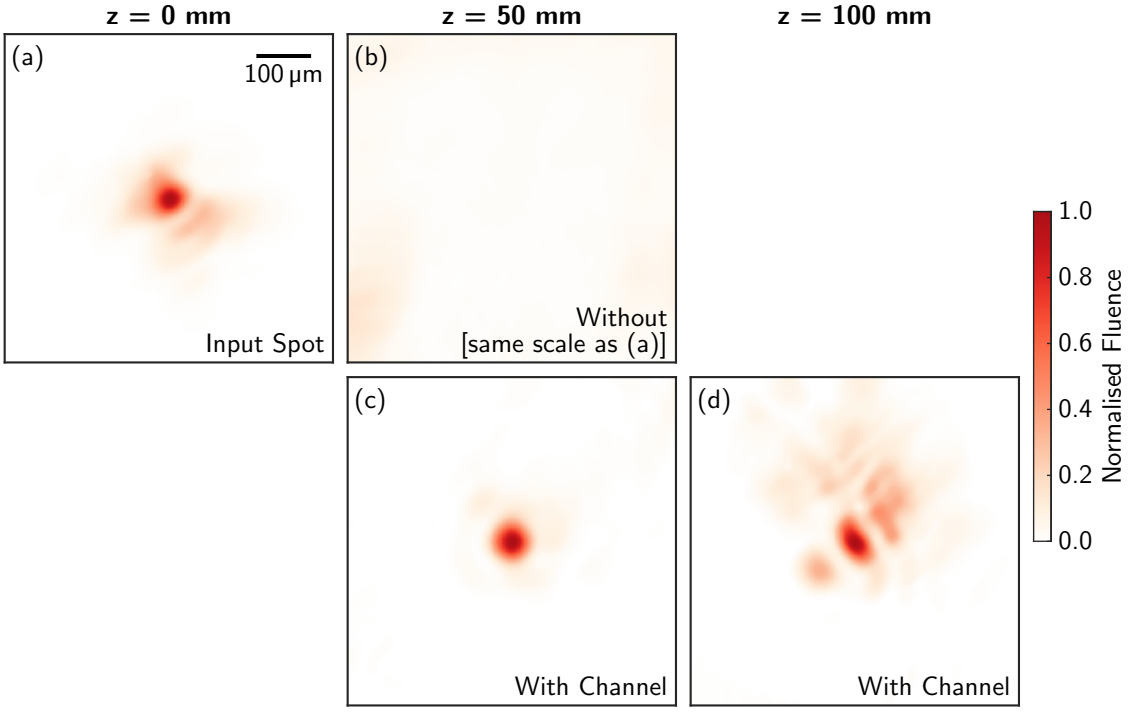

Figure 4.10: Measured transverse fluence profiles of the guided beam at: (a) focus in vacuum, with the cell removed; (b) $z = 50$ mm in vacuum, with the cell removed; (c) $z = 50$ mm, for $P = 68$ mbar and $\tau = 3.0$ ns; (d) $z = 100$ mm, for $P = 26$ mbar and $\tau = 2.7$ ns. The transverse scale is the same for all plots, as indicated by the scale bar shown in (a). In (b), the vacuum diffracted spot greatly overfilled the camera size. For plots (a), (c), and (d) the fluence is normalized to the peak value in that plot; the fluence scale for (b) is the same as in (a). Compared to (a), the fluence scales of (c) and (d) were increased by factors of approximately 4 and 7 respectively.

Although light from the channel-forming beam was removed from the CCD images, as described in section 3.1.3, regions in which the signal is below 5-10 % of the peak signal are likely to be contaminated by contributions from the channel-forming beam. Figure 4.10(d) shows the transverse fluence profile of the guided beam at the exit of a 100 mm long HOFI channel formed at a similar delay ($\tau = 2.7$ ns), but at a lower cell pressure of 26 mbar. For this shot, the measured on-axis electron density was $n_{e0} = (1.0 \pm 0.3) \times 10^{17}\,\mathrm{cm}^{-3}$. It is clear that guiding was also achieved in this case, the radius of the guided pulse was measured to be $w_{out} = (48 \pm 14)$ µm, close to that of the focal spot. The low intensity light in the transverse wings can be attributed to the axicon light that reached the CCD, which is relatively more intense than in figure 4.10(c), or scattering from partially ionized gas at the exit of the waveguide. In a significant proportion of shots, the

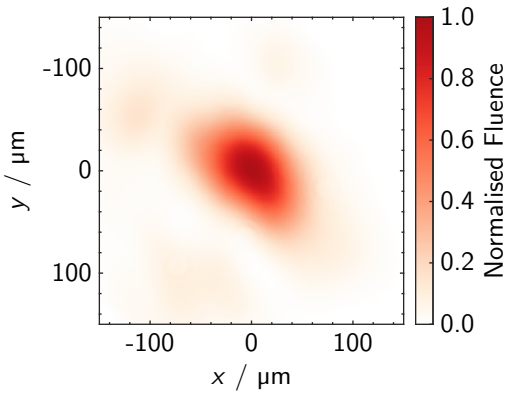

Figure 4.11: Example measured transverse fluence profile of the guided pulse at $z = 50$ mm for a fill pressure $P = 17$ mbar. The inferred axial density for this shot was $n_{e0} \approx 7 \times 10^{16}$ cm^{-3}, the lowest at which guiding was achieved in this experiment.

spatial offset and angular misalignment of the drive beam introduced by the shot-to-shot pointing jitter of Gemini affected the properties of pulse guiding. The guided spot size increased and energy transmission reduced with increasing offset, consistent with previous findings [171].

Optical guiding was also observed in 50 mm long channels for cell pressures as low as 17 mbar with a measured energy transmission of 29 % and $w_{out} \approx 55$ μm (see figure 4.11). It was not possible to measure the electron density profile interferometrically, however the inferred axial density from MHD simulations was $n_{e0} \approx 7 \times 10^{16}$ cm^{-3}.

4.4.2 Spatial Jitter of the Guided Pulse

Due to the spatial constraints of the chamber and time constraints of the experiment, it was not possible to measure the spatial offset of the guided pulse at the entrance of the plasma channel during data taking. As shown in figure 4.4(e), a separate measurement of the shot-to-shot jitter using the focal camera showed that $\Delta\theta_{focus} = (5 \pm 1)$ μrad. Using a leakage diagnostic placed in the compressor (the final mirror before HM1) it was possible to measure the spatial jitter acquired prior to the compressor during data taking. Figure 4.12(a) shows the change in pointing of the beam centroid of the South beam with respect to the first shot measured by the leakage diagnostic in the compressor measured at a different time on the same day as figure 4.4(e). The focus camera data is shown in blue for comparison. It was found that $\Delta\theta_{comp} = (5 \pm 2)$ μrad closely matching

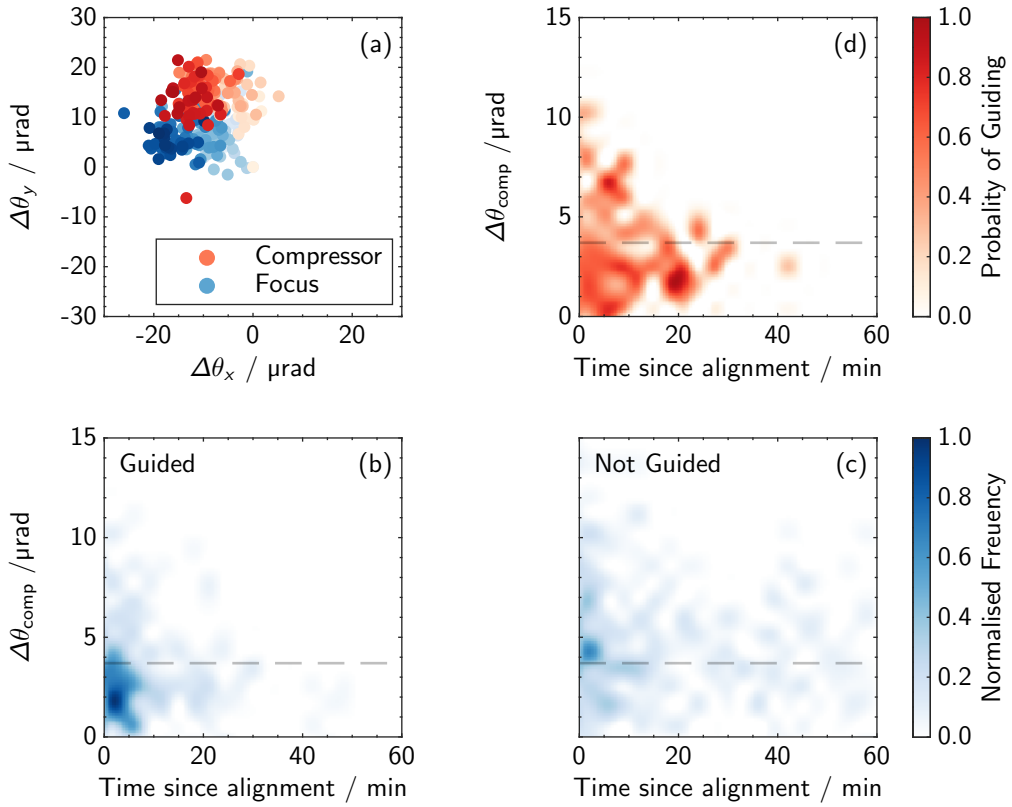

Figure 4.12: (a) The measured shot-to-shot variation of the South beam centroid as measured inside the compressor over a 45 minute period at $f_{rep} = 0.05$ Hz. Data from the focus camera is shown in blue for direct comparison. Darker colours correspond to later in time. (b-c) Frequency distribution of guided (b) and not guided or partially guided (c) shots as a function of the drive beam pointing, measured inside the South beam compressor, and the time since the most recent alignment. (d) The estimated probability of a high-intensity shot being guided for a given time and angular offset.

that separately measured in the chamber. This indicated that pointing jitter was dominated by contributions in the Gemini laser chain, rather than in the experimental chamber. It is also apparent that the beam drifted significantly on on timescales as short as 20 minutes, resulting in a high proportion of shots that were spatially offset from the channel entrance, and had an angular misalignment with respect to the channel axis.

Correlations between spatial offsets of the guided pulse and the output laser mode were investigated for approximately 2700 Gemini shots taken over 4 consecutive days for various values of P and τ. For this analysis, only conditions suitable for guiding were included. Figure 4.12 shows the frequency distributions of guided (b) and unguided (c) shots as a function of $\Delta\theta_{comp}$

and the delay since the most recent alignment. The grey line indicates one standard deviation of the shot-to-shot pointing variation measured in the compressor for those shots which had guided, $\Delta\theta_{\text{comp}} = 3.7\,\mu\text{rad}$. It is clear that the shots which were guided occurred when the measured jitter in the laser area was small, and the time since realignment was $\lesssim 20\,\text{min}$, whereas unguided shots were more evenly distributed. Figure 4.12(d) shows the probability of a shot being guided for a given $\Delta\theta_{\text{comp}}$ and time after alignment. Shots for which the misalignment was small had a significantly greater chance of being guided. Those shots where the measured deviation in the compressor was small, but which were not guided could still have been poorly aligned with the channel axis owing to further pointing jitter in the target chamber. It is expected that the correlations between quality of guiding and drive beam pointing at the entrance to the cell would be substantially stronger.

One can estimate the acceptance angle of the channel, that is the maximum pointing offset of an $f/40$ pulse that is still guided, $\gamma_{\text{acc}} \approx \Delta\theta_{\text{comp}} = 3.7\,\mu\text{rad}$. This corresponds to a movement of $\approx 22\,\mu\text{m}$ ($0.6w_0$). Even when the pulse was guided, the shot-to-shot variation of the output mode and energy transmission was noticeable; only a select few shots exhibited exemplary guiding characteristics. It should be noted that the shot-to-shot pointing jitter of state-of-the-art, petawatt class Ti:Sapphire systems are typically $< 3\,\mu\text{rad}$, [224, 225] and will only improve as the laser repetition rates increase and active feedback becomes common place.

4.4.3 Attenuation in HOFI Channels

Solving the paraxial Helmholtz equation numerically for the measured electron density profiles allows the expected coupling efficiency and attenuation to be calculated, as discussed in section 3.3.1. Figure 4.13 shows the results of these simulations for an electron density profile measured for $P = 26\,\text{mbar}$ and $\tau = 2.7\,\text{ns}$. For a Gaussian input beam, with spot size matched to that of the lowest-order mode of the channel [see figure 4.13(a)] the transverse fluence profile remained approximately the same shape, but the peak fluence reduced as light leaks out of the plasma channel. The calculated transverse fluence profile of the guided spot at $z = 100\,\text{mm}$ is shown in figure 4.13(d). As expected, the attenuation closely followed an exponential curve; the coupling efficiency and attenuation length are found to be $T(0) \approx 100\%$ and $L_{\text{att}} = (84 \pm 2)\,\text{mm}$. Figure 4.13(b) shows the simulated propagation of a beam with an input transverse profile equal to that

used in the experiment [see figure 4.10(a)], assuming a constant and flat transverse spatial phase at the plasma channel entrance. For $z \lesssim 50\,\mathrm{mm}$, it is clear that the transverse fluence profile evolved significantly, owing to the excitation of higher order modes which have higher propagation losses. For larger values of z the rate of decrease of $T(z)$ closely followed that of the lowest-order mode, although the overall transmission was reduced by a factor of ~ 2 in comparison. The uncertainties displayed here account for the uncertainties in the measured $n_e(r)$ shown in figure 4.8(e). The transverse fluence profile at $z = 100\,\mathrm{mm}$ for this simulation is shown in 4.13(e). The spot size of the guided mode is similar to that of the matched simulation, but there exists a halo of light which has leaked from the channel and propagated away from the axis [116].

It was possible to compare these calculations with the energy transmission directly measured by the far-field diagnostic. The channel length was controlled by driving the stepper motor of the gas cell to move the back pinhole further towards or away from the front. Figure 4.13(c) shows the energy transmission (blue), $T(z)$, measured for several channel lengths and $P = 26\,\mathrm{mbar}$ and $\tau = 2.7\,\mathrm{ns}$. Approximately 15 shots were recorded for each cell length, and those with an input pointing outside the measured acceptance angle of the channel were discarded. It can be seen that the experimental data show an approximately exponential decrease in $T(z)$ with z; a fit of the expression $T(z) = T(0)\exp(-z/L_{\mathrm{att}})$ to the data returned a coupling efficiency of $T(0) = \left(45\,^{+14}_{-11}\right)\,\%$ and $L_{\mathrm{att}} = (102 \pm 38)\,\mathrm{mm}$. Also plotted are the calculated energy transmissions from the simulations shown in figure 4.13(a) (unfilled red) and (b) (filled red).

The measured data agrees well with the calculated energy transmission for the real input beam. The attenuation length and coupling efficiency for the experimentally-measured input beam was deduced by fitting an exponential decay to the calculated transmission in the region $z \geq 50\,\mathrm{mm}$, where the guided beam is dominated by the lowest order mode. The attenuation length is found to be $L_{\mathrm{att}} = (84 \pm 2)\,\mathrm{mm}$, which agrees with the measured value to within errors, and is equal to that calculated for a matched input beam. The calculated coupling efficiency for the experimentally-measured input beam is $T(0) = (48 \pm 4)\,\%$. It should also be noted that this coupling efficiency agrees well with an analysis of the input spot shown in figure 4.10(a) as an overlap integral with the lowest order mode of the channel (assuming Laguerre-Gauss modes) — this showed that fractional power contained in the lowest-order Laguerre-Gauss mode was $(49 \pm 8)\,\%$.

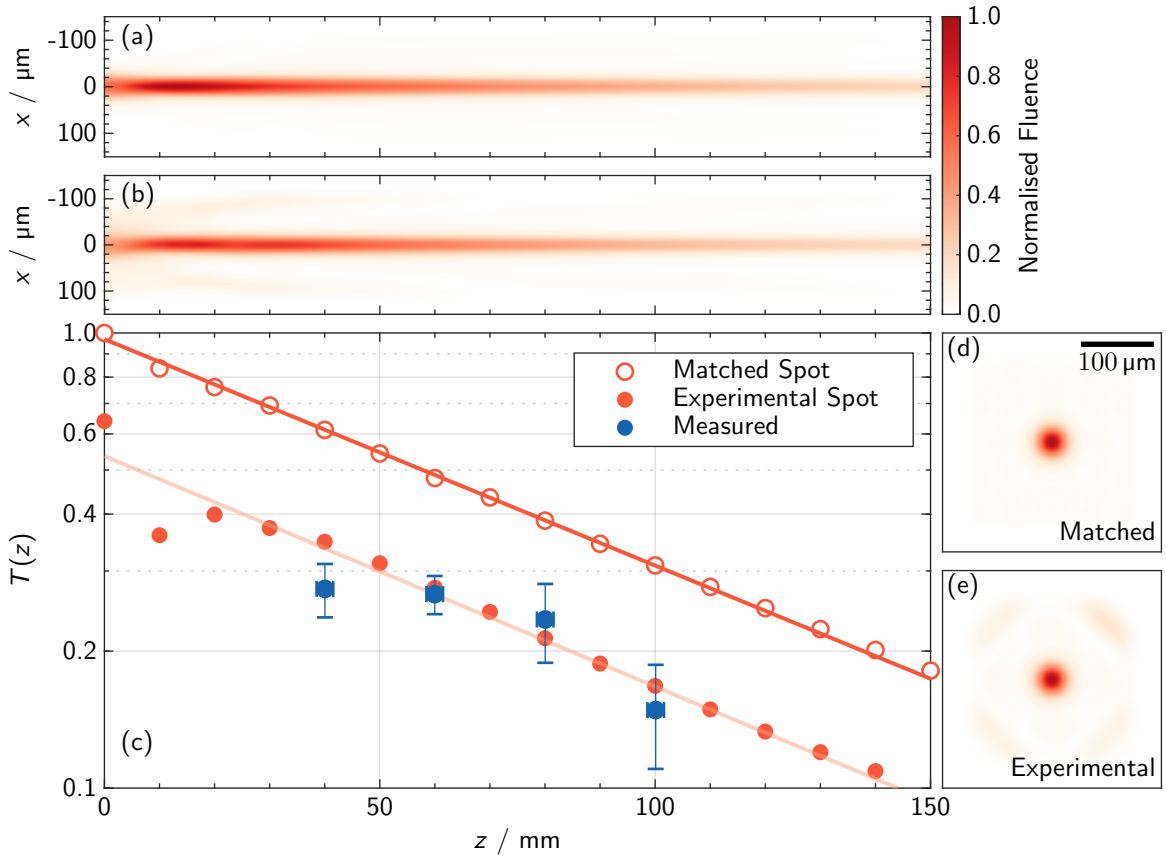

Figure 4.13: (a-b) Numerical simulations of optical guiding in the plasma channel formed at a cell pressure $P = 27$ mbar at delay $\tau = 2.7$ ns as shown in figure 4.8(e). Longitudinal variation of the transverse fluence profile of the guided beam for an input beam with (a) Gaussian transverse fluence profile matched to the plasma channel, (b) transverse fluence profile equal to that of the beam used in the experiments, as shown in figure 4.10(a). (c) Comparison of the measured and simulated energy transmission for plasma channels formed at $P = 26$ mbar and $\tau = 2.7$ ns. The blue line shows a fit of the function $T(z) = T(0)\exp(-z/L_{\text{att}})$ to the experimental data. The open red circles show the calculated transmission for a Gaussian input beam as shown in (a). The solid red circles show the calculated energy transmission for an input beam with a transverse intensity profile equal to the experimentally-measured profile as shown in (b). The red dashed line shows a fit of the function $T(z)$ to the calculated transmission for the realistic input spot in the region $z > 50$ mm. The simulated transverse fluence profile of the guided beam at $z = 100$ mm are shown for the matched simulation in (d) and the experimentally-measured profile in (e).

Other Factors Affecting the Coupling Efficiency

Since the simple gas cell was employed, a large entrance pinhole was required (see section 4.2.3).

The plumes created by gas flow through the pinholes would have had a longitudinal scale length

comparable to the pinhole diameter, which in turn $\approx 2z_R$. As such the plume regions might have played a role in coupling the guided beam into the main channel [226, 227]. The plasma channel would have extended into the entrance plume since the axicon focus extended into this region. Whilst it was not possible to measure the channel formation in the coupling region, it is possible to infer some of the general shape. It is evident from figure 4.9(a) that the shock position at a given τ is independent of P, and that the channel depth and axial density both fall as P reduces. These properties will cause the matched spot to increase with distance from the cell. For *collisionally-heated* hydrodynamic channels the density-dependent heating rate causes the channel to narrow near its entrance [227], which decreases the coupling efficiency. Narrowing of this type is unlikely to happen for HOFI channels and hence may lead to improved coupling compared to collisionally-heated hydrodynamic channels. Studies of these end effects are interesting possibilities for future work.

4.4.4 High-Intensity Guided Pulse Effects

The results presented above assume that neither the guiding nor energy transmission were affected significantly by wakefield excitation or relativistic self-guiding. Despite the use of a wedge to reduce the energy contained in the guided pulse to 1.1 J, the guided pulse ($a_0 \approx 0.55$) will have driven a sinusoidal plasma wave with a relative electron density of up to $\delta n_e/n_e \sim 5\%$, leading to a laser energy loss of approximately 1 mJ per mm of plasma. This is further discussed in chapter 4. Hence less than 9% of the energy of the guided pulse will have been transferred to the plasma wave over a 100 mm long channel. It should also be noted that relativistic self-focusing would not have been significant for the conditions of these experiments since, for the range of axial channel densities investigated, $0.1 \lesssim P_0/P_{crit} \lesssim 0.3$ where P_0 is the peak laser power and the critical power $P_{crit} = 17.4(\omega_0/\omega_p)^2$.

It is possible that the guiding observed in this work may have been assisted by ionization of the neutral or partially-ionized gas surrounding the plasma channel, since ionization of this type would have increased the channel depth. For example, in the simulations of matched guiding shown in figure 4.13, the ratios of the peak laser intensity at $2r_{shock}$ to that on axis is calculated to be 0.5 %. Hence, for the guided intensities achieved in this work, the laser fields leaking beyond the shock

front would be sufficient to ionize any neutral gas in this region. This effect was not simulated here nor included in the analysis, but is examined in detail in Chapter 5.

4.5 Conclusions and Future Outlook

Generation of 100 mm long plasma channels and optical guiding of laser pulses with a peak intensity of $6 \times 10^{17}\,\mathrm{W\,cm^{-2}}$ through such channels was demonstrated. Plasma channels were measured interferometrically to have axial densities as low as $n_{e0} = (1.0 \pm 0.3) \times 10^{17}\,\mathrm{cm^{-3}}$. The power attenuation length of this channel was measured to be $L_{att} = (102 \pm 38)\,\mathrm{mm}$. At the time this experiment was undertaken the plasma channels described in this work were the longest, and the lowest axial density, of any free-standing plasma channel demonstrated to guide laser pulses with intensities above $> 10^{17}\,\mathrm{W\,cm^{-2}}$.

Measurements of the energy transmission in the channels are in good agreement with numerical simulations of beam propagation through plasma channels with transverse electron density profiles equal to those measured interferometrically. The energy transmission observed in the present work was dominated by the relatively poor coupling of the non-ideal input beam which contained significant transverse structure, and by the channel attenuation length of around 100 mm. It is expected that substantially higher coupling will be possible for beams which are better matched to the lowest-order mode of the channels. This presents two clear paths to develop HOFI plasma channels — improving the attenuation length and the coupling efficiency. The former could be approached by employing methods to increase the channel depth and radial extent of the plasma, and is the subject of the next chapter. For the latter, an input beam matched to the lowest-order mode of the channel would increase the transmission substantially, whilst increasing the channel depth would permit the coupling of more modes.

The ability to create long, low-density and free-standing HOFI plasma channels suggests that they are well suited to high-repetition-rate, multi-GeV plasma accelerator stages. These channels were generated with only 0.7 mJ of channel-forming laser energy per millimeter of channel, consistent with the group's previous experiment [102].

This experiment provided several insights into development that would be required to demon-

strate a 10 GeV LWFA stage in a HOFI plasma channel. Firstly, it is necessary to improve the gas source design to reduce the large gas plumes at the front entrance pinhole. It is unlikely the the simple cell design used in this experiment could be extended to lengths greater than 100 mm. Secondly, achieving $L_{\text{att}} > 1$ m would lead to negligible propagation losses and permit efficient plasma wave generation. Third, it is clear that the guiding transmission was dominated by the quality of the input spot, and by the shot-to-shot jitter of the Gemini South beam. Thus, one would expect any accelerated electron beams to be highly sensitive to changes in the laser pointing at the channel entrance. Active stabilisation of both the shot-to-shot and long term pointing changes would make such a stage more consistent and reliable.

Chapter 5

Metre Scale, Conditioned Hydrodynamic Optical Field Ionised Plasma Channels

5.1 Introduction

In the previous chapter, high-intensity laser guiding in 100 mm long HOFI plasma channels was demonstrated at densities as low as $n_{e0} = (1.0 \pm 0.3) \times 10^{17}\,\mathrm{cm}^{-3}$. However independent examination of the transverse electron density profile and the energy transmission along the waveguide indicated that the power attenuation lengths of these channels were limited to $L_{att} \lesssim 100\,\mathrm{mm}$ — a consequence of the relatively small channel depth and radial extent. Since the desired stage length of a multi-GeV plasma channel in the quasilinear regime is on the metre scale, it is necessary to extend L_{att}. In this chapter, a phenomenon observed in the proof-of-principle experiment is investigated in detail through experiment and simulations. Through transverse interferometry measurements taken as the guided pulse arrives, it is shown that a neutral collar of gas which surrounds the initial HOFI channel is ionised by the guided pulse, increasing the channel depth and radial extent of the plasma. This leads to increased energy transmission of a high-intensity guided pulse relative to a low-intensity guided pulse. Using hydrodynamic simulations,

it is shown that the neutral collar of gas is formed by a "snowplough" effect: as the plasma electrons and ions expand out into the neutral gas, the displaced neutrals accumulate close to the shock front. Through particle-in-cell simulations, it is found that the leading edge of the guided pulse deepens the channel, and that the main body of the pulse is guided in the conditioned channel [228].

The experimental data presented here was undertaken using the TA2 Astra-Gemini laser at the Rutherford Appleton Laboratory. The experimental design and setup was led by Dr. Robert Shalloo and Dr. Christopher Arran who acted as target area operators for the experiment. The experiment setup and data taking was carried out by the Oxford LPA group, including this author. All of the experimental analyses shown here were written and carried out by the author. The hydrodynamic simulations presented in this work were all undertaken by Dr. Aarón Alejo and are shown here for completion. The particle-in-cell simulations undertaken were all carried out by the author, with input from Dr. Aarón Alejo and Oscar Jakobsson.

5.2 Experimental Setup

The Astra-Gemini TA2 laser is derived from the same front end as that used in the previous chapter, half of the pulses are diverted into a separate target area before the final amplifier and compressed to provide a peak power of $12.5\,\mathrm{TW}$ at at a repetition rate of up to $5\,\mathrm{Hz}$. For this experiment, the measured mean energy was $419\,\mathrm{mJ}$, and the duration measured by a SPIDER was $\tau_{\mathrm{FWHM}} = (45 \pm 3)\,\mathrm{fs}$.

The experimental layout is shown in figure 5.1. Upon entering the target chamber, the beam was split into the channel-forming beam (gold) and the guided or "conditioning" beam (red) by an annular dielectric mirror (HM1), $D_{\mathrm{hole}} = 30\,\mathrm{mm}$ (*Rainbow Research Optics*), as shown in figure 5.1. The channel-forming beam reflected from this mirror was transformed to circular polarisation by a quarter waveplate (QWP), focused by a fused silica axicon lens of base angle $\vartheta = 5.6\,\mathrm{deg}$ (*Doric Lenses*), and directed into a gas cell by a second annular turning mirror (HM2). The line focus generated extended throughout the 16-mm-long gas cell, with a peak axial intensity of $I_{\mathrm{ax}} \approx 5 \times 10^{15}\,\mathrm{W\,cm^{-2}}$.

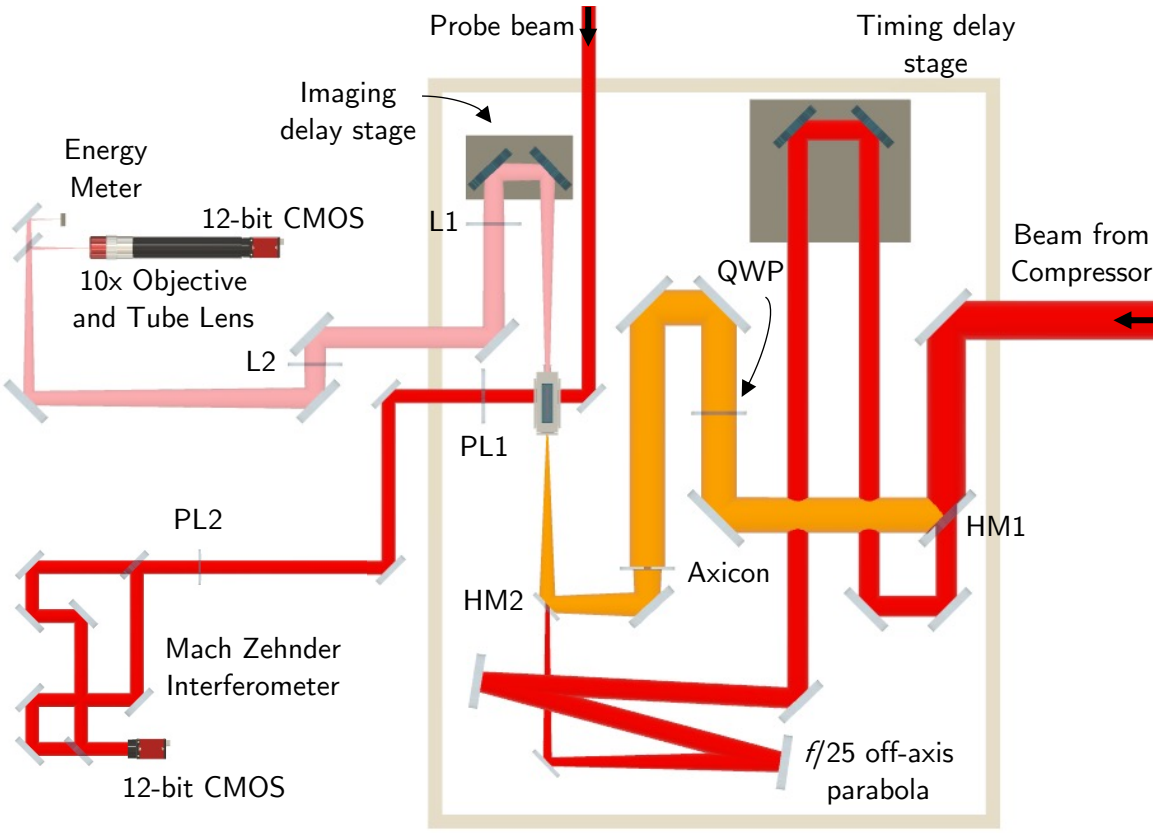

Figure 5.1: Schematic of the experimental chamber and diagnostics. The beam entered from the compressor on the right and was reflected from an annular mirror (HM1) with $D_{\text{hole}} = 30\,\text{mm}$, splitting the beam into the channel-forming beam (gold) and the conditioning beam to be guided (red). The channel-forming beam was focused by the axicon and coupled into the gas cell by reflection from HM2, whilst the guided beam was focused by an off-axis paraboloid, $f = 750\,\text{mm}$, and passed through the hole of HM2. The guided conditioning pulse was collected by an achromatic lens (L1, $f = 500\,\text{mm}$) and reimaged onto a 12-bit CMOS detector and a pyroelectric energy meter by a second achromatic lens (L2, $f = 750\,\text{mm}$). The probe beam (red) was passed through the plasma transversely, and then through a Mach-Zehnder interferometer similar to that used in the previous chapter. Light scattered from the plasma was collected and collimated by a $50.2\,\text{mm}$ diameter planoconvex lens (PL1) of focal length $f_1 = 250\,\text{mm}$, and subsequently imaged onto a 12-bit CMOS detector by a second, planoconvex lens (PL2) of diameter 50.2 mm and $f_2 = 1500\,\text{mm}$.

The conditioning pulse transmitted through the annular mirror was sent to a retro-reflecting delay stage and focused through the hole in the turning mirror by an off-axis paraboloid (OAP) mirror of focal length $f = 750\,\text{mm}$ used at $f/25$ to the entrance pinhole of the gas cell. The measured beam waist and Rayleigh range of the conditioning beam were $w_0 = (22 \pm 3)\,\mu\text{m}$ and $z_R = (1.1 \pm 0.4)\,\text{mm}$ respectively. By replacing the final turning mirror for an uncoated, optically

flat wedge, the conditioning pulse could be operated at two intensities. The high-intensity pulse had peak intensity $I_{\text{peak}}^{\text{high}} = 4.1 \times 10^{17}\,\text{W cm}^{-2}$ at the entrance pinhole corresponding to $a_0 \approx 0.43$, whilst the lower intensity mode had a peak intensity $I_{\text{peak}}^{\text{low}} \approx 1.6 \times 10^{16}\,\text{W cm}^{-2}$. For all results shown in this chapter, the timing between the channel-forming and guided beam was fixed at $\tau = 1.5\,\text{ns}$.

The channel-forming and conditioning pulses entered and left the hydrogen-filled gas cell via entrance and exit pinholes of diameter 1.5 mm and 0.8 mm respectively. The exit pinhole was mounted on a side-sealed cylinder which could slide along the cell axis in order to adjust the spacing of the pinholes. For all data shown here, the cell length was set to $16\,\text{mm}$. Fused silica windows mounted on the top and sides of the cell provided optical access. Hydrogen gas entered the cell approximately 5 mm from the front pinhole via a 4 mm inner diameter pipe; the fill pressure could be varied in the range 5 mbar to 120 mbar.

Short channels ($2\,\text{mm}$ and $4\,\text{mm}$) were probed using longitudinal interferometry by co-propagating a $400\,\text{nm}$ probe at a given delay behind the channel-forming pulse. These results have been reported previously [103]. To probe channels of length $L_{\text{ch}} = 16\,\text{mm}$, a separately compressed, $1\,\text{mJ}$ probe pulse with the same central wavelength as the main pulse was passed through the plasma transversely at $z \approx 3.5\,\text{mm}$. The delay τ between the arrival of the channel-forming beam and the arrival of the probe pulse could be varied in the range 0 ns to 6 ns by adjusting a retroreflecting delay stage. Light from the interaction region was collected and collimated by a 50.2 mm diameter planoconvex lens of focal length $f_1 = 250\,\text{mm}$, and subsequently imaged onto a 12-bit CMOS detector (*Allied Vision Mako*) by a second, planoconvex lens of diameter 50.2 mm and $f_2 = 1500\,\text{mm}$. Before reaching the detector, this light was passed through a Mach-Zehnder interferometer located inside the telescope to form equally spaced, straight fringes on the detector. The measured magnification and spatial resolution was 6.1 and $(8.7 \pm 0.9)\,\mu\text{m}$ respectively.

After leaving the gas cell, the conditioning pulse was collected and collimated by a 76.2 mm diameter, $f = 500\,\text{mm}$ focal length achromatic lens (L1). A retro-reflecting stage placed before this lens allowed the object plane to be varied from the entrance to the exit pinhole of the gas cell. The collimated light was subsequently reimaged onto a 12-bit CMOS detector (*Allied Vision Mako*) and a pyroelectric energy meter (*Gentec*) by $f = 750\,\text{mm}$, achromatic lens. Light from the

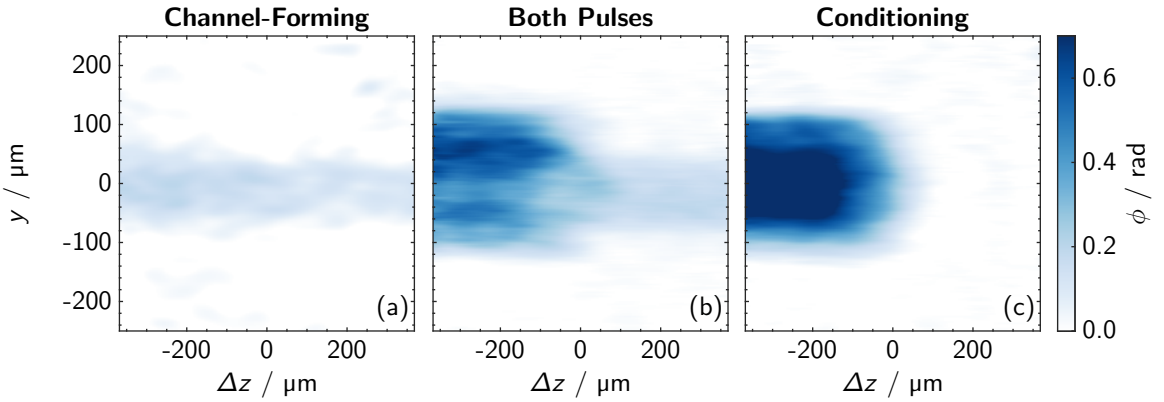

Figure 5.2: Example phase shifts measured by the transverse probe beam at $z \approx 3.5\,\text{mm}$ for: (a) the channel-forming pulse alone, (b) the channel-forming pulse and the conditioning pulse at a delay $\tau = 1.5\,\text{ns}$; and (c) the conditioning pulse alone.

channel-forming beam was blocked from reaching these diagnostics by an aperture. The energy transmission of this pulse could be measured by the pyroelectric energy meter or by integrating the CMOS signal as described in section 3.1.3.

5.3 Experimental Results

5.3.1 Transverse Interferometry of CHOFI Plasma Channels

The phase was retrieved using the methods described in section 3.5.4 from the fringe maps recorded by the CMOS [218]. Before the arrival of the conditioning pulse, where the phase shift was small ($\lesssim 100\,\text{mrad}$), the forward fitting method [102] was used to retrieve $n_e(r)$. After the conditioning pulse arrived, increased radial extent of the object and improved the signal-to-noise ratio of phase maps permitted using the inverse Abel transform.

Example measured phase maps at the moment when the conditioning pulse arrives at $\tau = 1.5\,\text{ns}$ are displayed in figure 5.2. The ionisation by the conditioning pulse occurs at $\Delta z \approx 0$. Most importantly, it is clear in figure 5.2(b) that the conditioning pulse increases the radial extent of the plasma by a factor of approximately 5 from that produced by the channel-forming pulse alone.

Further, the radial extent of the plasma generated by both pulses is essentially the same as that of the plasma produced by the conditioning pulse alone, as shown in figure 5.2(c). Evidently, the transverse wings of the guided conditioning pulse ionise neutral gas surrounding the HOFI plasma channel.

Figure 5.3(a) compares the transverse electron density profile before and immediately after the arrival of the conditioning pulse at $\tau = 1.5\,\text{ns}$. Little effect on the electron density is observed for radii within the radius of the shock front, $r_{\text{shock}} \approx 25\,\mu\text{m}$, generated by the channel-forming pulse. However, for $r > r_{\text{shock}}$, n_e increases substantially to form a deep, thick-walled conditioned HOFI (CHOFI) plasma channel: the depth of the channel was increased by a factor of 10 to $\Delta n_e = (1.3 \pm 0.1) \times 10^{18}\,\text{cm}^{-3}$; whereas, within the experimental uncertainty, the axial density remained at $n_{e0} = (2.4 \pm 1.0) \times 10^{17}\,\text{cm}^{-3}$. The radial extent of the plasma was increased by the conditioning pulse from $r_{\text{shock}} \approx 30\,\mu\text{m}$ to $r_{\text{max}} \approx 120\,\mu\text{m}$. The horizontal, grey line shows the density corresponding to full ionisation of the ambient gas when the cell was filled; note that in the region $r > r_{\text{shock}}$, n_e is comparable to that expected for full ionisation of the ambient gas, consistent with field ionisation of the neutral gas by the transverse wings of the conditioning pulse. Strikingly, close to the peak of the electron density in the measured HOFI plasma channel ($r \approx 50\,\mu\text{m}$) the measured electron density was greater than that which would be generated by ionisation of the neutral gas at its ambient density. This is consistent with a build up of neutral gas at the shock front as the expanding electrons and ions push out and displaced the cold, unionised gas.

5.3.2 Evolution of CHOFI Plasma Channels

The evolution of the plasma at various delays $\Delta\tau$ after the arrival of the conditioning pulse at $\tau = 1.5\,\text{ns}$ is shown in figure 5.3(a)-(f). For each plot, the mean of approximately 20 shots recorded at a repetition-rate of 5 Hz is shown, where the data has been averaged longitudinally over $\Delta z \approx 0.75\,\text{mm}$. The shaded regions are one standard deviation wide. For $\Delta\tau = 0.2\,\text{ns}$, the measured axial density remained approximately the same, and the channel wall thickened slightly. After this, electrons in the high density ring simultaneously move radially outwards and inwards, consistent with relaxation to a uniform pressure. This caused the position of the peak density to increase to $r = 100\,\mu\text{m}$ by $\Delta\tau \approx 1\,\text{ns}$ and the axial density to increase by a factor of ~ 2.5. Even

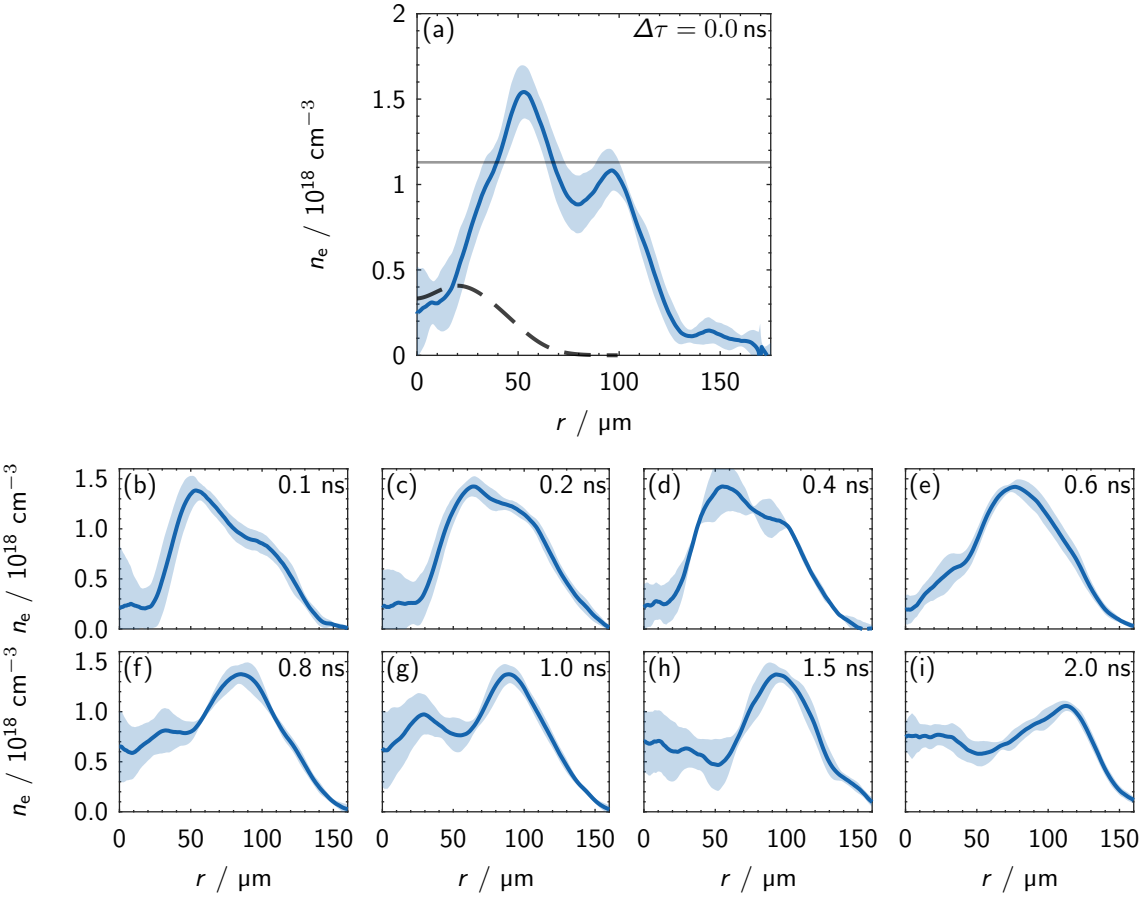

Figure 5.3: Formation and temporal evolution of the transverse electron density profiles $n_e(r)$ in the CHOFI waveguide. (a) Measured electron density profile immediately before (dashed) and after (solid) the arrival of the conditioning pulse at $\tau = 1.5$ ns ($\Delta\tau = 0$ ns). The horizontal, grey line shows the density corresponding to full ionisation of the ambient gas. (b)-(i) Electron density profiles measured at different additional delays $\Delta\tau$ (indicated) after the arrival of the channel-forming pulse, for a conditioning pulse arriving at $\tau = 1.5$ ns. All plots show the mean of approximately 20 shots recorded at a repetition-rate of 5 Hz, with the probe pulse crossing at $z \approx 3.5$ mm with respect to the front pinhole. The data is averaged longitudinally over approximately 0.75 mm. The shaded region is one standard deviation wide.

at $\Delta\tau \approx 2$ ns, where the channel structure has begun to decay to a more uniform plasma profile, the measured channel depth was greater than before the arrival of the conditioning pulse.

It is possible that the electron density profiles at these long delays could be desirable for guiding, and that the delay $\Delta\tau$ could provide some control over the shape of the plasma channel, as well as informing the observed phenomena. The evolution of the properties of the CHOFI plasma channel is shown in figure 5.4. The total number of electrons per unit length of waveguide

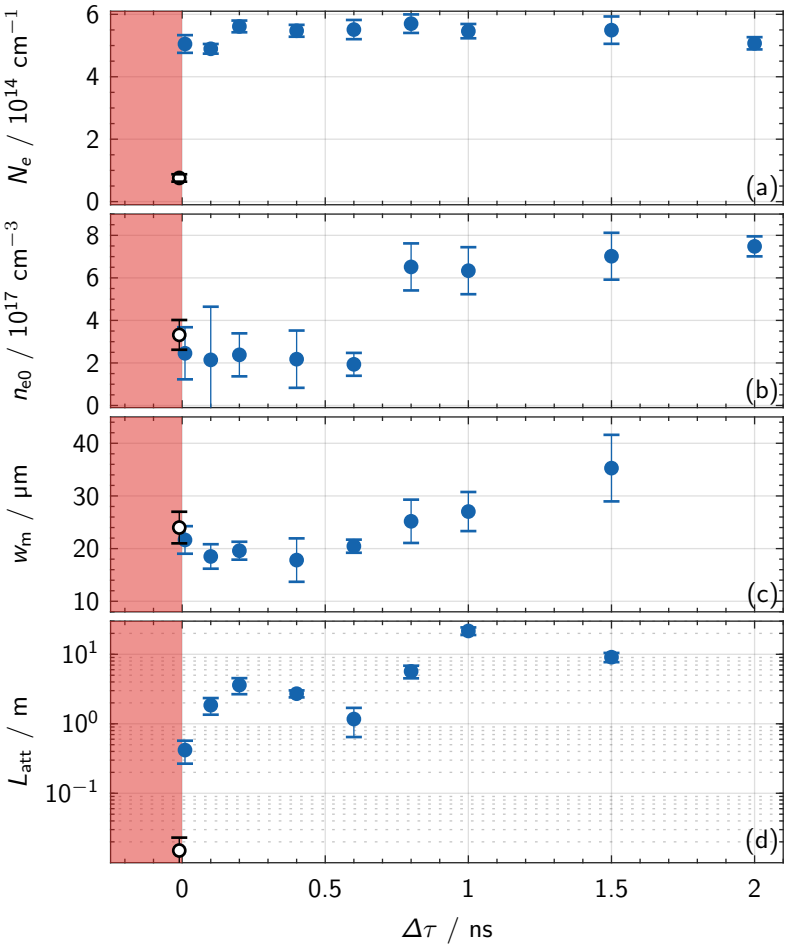

Figure 5.4: Temporal evolution of the properties of the CHOFI plasma channels as a function of delay $\Delta\tau$ after the arrival of the conditioning pulse: (a) Measured total number of electrons per unit length of waveguide, N_e; (b) the measured axial density n_e; (c) the calculated matched spot size w_m of the lowest order mode; and (d) the calculated attenuation length of the lowest order channel mode. The white circles show the same parameters of the HOFI channel immediately before the conditioning pulse arrives, indicated by the red region. In all cases, the error bars reflect the uncertainties in $n_e(r)$ depicted in Fig. 5.3.

$N_e = 2\pi \int_0^{r_{max}} n_e(r) r \, dr$, is shown in figure 5.4(a). Upon arrival of the conditioning pulse, N_e increased from $N_e = 7.6 \times 10^{13}\,\mathrm{cm}^{-1}$ to $N_e = 5.1 \times 10^{14}\,\mathrm{cm}^{-1}$ instantaneously due to ionisation of the neutral gas collar. Following this, the number of electrons per unit length increased for the first 0.2 ns after the conditioning pulse, indicating that the observed increase in the wall thickness observed arose from further ionisation close to the shock front. It should be noted that an interval of 0.2 ns is consistent with the timescale for hot electrons to collide with neutral gas under the plasma parameters calculated in hydrodynamic simulations (see section 5.4) [229].

Figure 5.4(b) shows the evolution of the axial density, showing that this remains close to that of the HOFI channel until $\Delta\tau \approx 0.6$ ns, whereupon it increases rapidly as electrons from the channel wall move towards the axis. Initially, the calculated matched spot size w_m remains close to that of the HOFI channel, $w_{m,HOFI} = (24 \pm 3)$ μm, since the shape of the plasma channel for $r \lesssim w_m$ is relatively unaffected by the ionisation. After $\Delta\tau \approx 0.5$ ns, w_m increased to $w_m = (35 \pm 6)$ μm as the channel depth decreased and the axial density increased.

The effect of the conditioning pulse on the propagation losses is most noteworthy. The calculated attenuation length increases immediately from $L_{att} = (15 \pm 8)$ mm to $L_{att} = (0.42 \pm 0.01)$ m. In the following 200 ps, the increase in N_e increases the thickness of the channel wall without significantly changing w_m, which results in a further increase of L_{att}. The largest L_{att} was achieved at $\Delta\tau = 1.0$ ns, where $L_{att} = (21 \pm 3)$ m, almost four orders of magnitude larger than achieved by the channel-forming pulse alone. It is evident that the calculated attenuation lengths make CHOFI plasma channels an ideal candidate for metre-scale plasma channels with very low propagation losses.

5.3.3 Guiding of the Conditioning Pulse

Optical guiding of the low- and high-intensity conditioning pulses was demonstrated over the length of the 16 mm long gas cell, corresponding to approximately $14.5 z_R$. A more complete set of guiding results for several different time delays and fill pressures are detailed in Dr. Robert Shalloo's thesis [103]. Figure 5.5 shows the transverse fluence profile of the low- and high-intensity conditioning pulses at the entrance and exit of the for $P = 40$ mbar and $\tau = 1.5$ ns. The measured axial density for these conditions was $n_{e0} = (2.4 \pm 0.1) \times 10^{17}$ cm^3 For each plot, the peak fluence is normalised in order to clearly illustrate the detail. For the low-intensity case, the measured energy transmission and output spot radius was $T = (21 \pm 4)\,\%$ and $w_{out} = (23 \pm 4)$ μm respectively. For the high-intensity configuration, $T = (60 \pm 3)\,\%$ and $w_{out} = (25 \pm 4)$ μm. Evidently, the mode profiles of the transmitted pulses were essentially the same for the two cases. These results are consistent with the interferometry results shown in figure 5.3. Importantly, the energy transmission was substantially higher for the high-intensity pulse.

Figure 5.5(d) shows the measured variation of energy transmission T as the peak input intensity

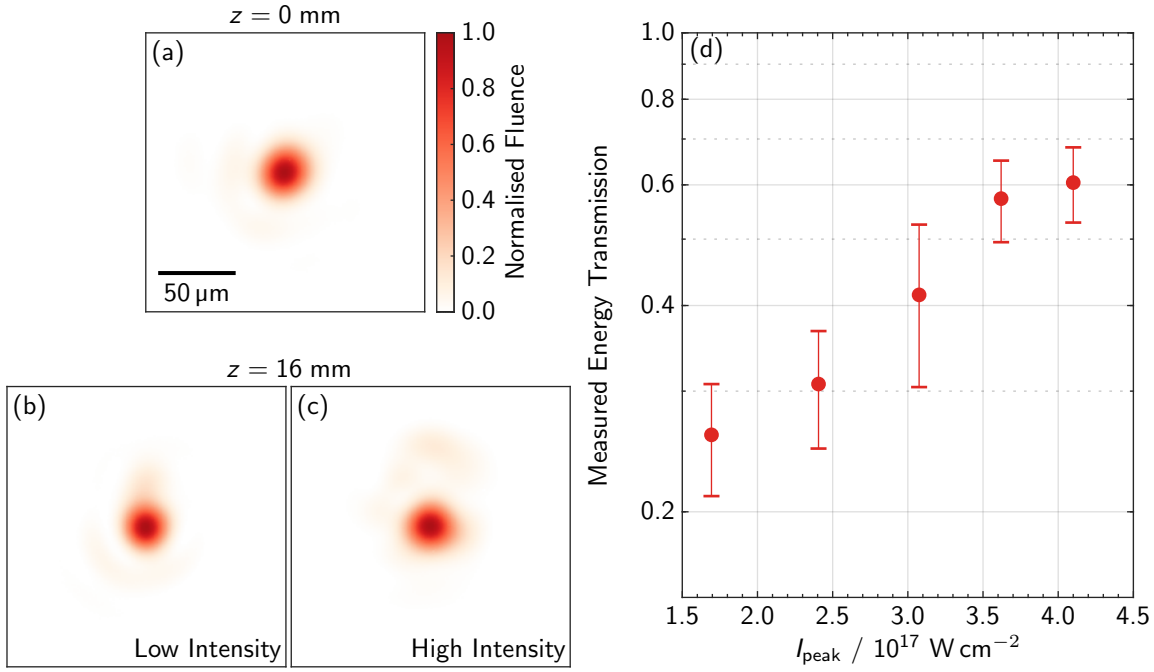

Figure 5.5: Measured properties of the guided conditioning pulse. The transverse fluence profile of the conditioning pulse at the input plane of the gas cell (a), and at the exit of the cell for the low- (b) and high-intensity (c) configurations. It is evident that the guided mode is similar in both the low- and high-intensity configurations. (d) Pulse energy transmission of the conditioning pulse as a function of input I_{peak}. The error bars shown correspond to one standard deviation after averaging 10 consecutive shots.

of the pulse was increased. It should be noted that since the channel-forming beam and conditioning beam energies could not be varied independently, the intensity of the channel-forming pulse also varied with the intensity of the conditioning pulse. However, for the intensity range considered here, the channel-forming pulse remained intense enough to fully ionise the hydrogen gas, and interferometric measurements indicated that properties of the HOFI channel were not significantly affected. The energy transmission increases substantially as the intensity of the pulse is increased, strongly indicating that the leading edge of the conditioning pulse improved the channel properties via ionisation, allowing the main body of the pulse to propagate with low losses. The coupling efficiency of the conditioning pulse, deduced from the overlap integral of the input spot with the calculated HOFI channel modes is estimated to be $T(0) \approx 65\,\%$, and hence at the highest input intensities the propagation losses of the conditioning pulse were low.

5.4 Hydrodynamic Simulations

Hydrodynamic simulations were employed to study the interaction between the expanding electrons and ions, and the surrounding neutral gas prior to the interaction with the conditioning pulse [228]. Simulations presented in this section were performed using the Eulerian code FLASH 4.6.2[165] by Dr. Aarón Alejo; they are included here for completion. A 3-temperature model was employed in the calculations, which allowed for independent evolution of the electron, ion, and radiation species [230]. Heat exchange was enabled to allow for energy exchange between electrons and ions. The energy diffusion and thermal conductivity modules were also activated, to improve the modelling of the species propagation. It was not possible to account for the diatomic nature of the hydrogen gas in these simulations.

The plasma column generated by the axicon was initialised by configuring a region, equal in radius to the highest intensity region generated by the axicon, with an electron temperature equal to that expected from OFI, $T_{e,0} = 10\,\text{eV}$. The temperature profile was described as $T_e = T_{e,0} \exp\left[-(r/r_0)^{22}\right]$ where $r_0 = 4\,\mu\text{m}$. Tabulated values were used for the equation of state (EoS) and ionisation fraction of atomic H, with tables obtained from the commercially available PROPACEOS package [166]. Radiation transport was modelled using multi-group diffusion, with a total of 6 energy groups distributed between 0.01 eV and 12 eV. Tabulated values were used for the Rosseland and Planck opacities, also obtained from the PROPACEOS package.

The electron and neutral density, n_e and n_H for a delay of $\tau = 1.5\,\text{ns}$, matching the arrival time of the experiment, is shown in figure 5.6(a) and (b) respectively. The formation of a high-density shock front is clearly observed, as expected for a Sedov-Taylor-like expansion. Also evident is significant cooling of the plasma as it expands, consistent with blast theory [197]. For this delay the plasma cools on-axis from 10 eV to 0.44 eV, which results in the fractional ionisation decreasing from $\bar{Z} \simeq 100\,\%$ to $\bar{Z} \simeq 44\,\%$, as shown in figure 5.6(c). The cooling is even more pronounced at the shock front, where $T_{e,\text{shock}} \simeq 0.1 - 0.2\,\text{eV}$ and hence $\bar{Z} \simeq 15\,\%$. Figure 5.6(d) shows the temporal evolution of the electron and neutral gas transverse density profiles. Although the initial temperature is sufficiently high to fully ionise the plasma column, a neutral gas collar appears in the early stages of the expansion.

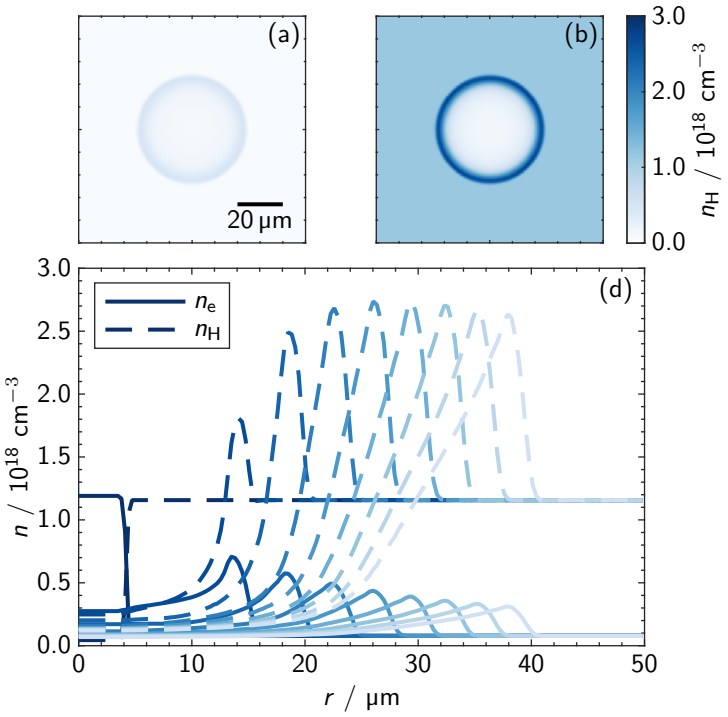

Figure 5.6: Hydrodynamic simulation of a HOFI plasma channel. (a-c) Properties of the plasma channel at $\tau = 1.5$ ns. (a) The electron density n_e and (b) the neutral density n_H distributions. (c) Temporal evolution of n_e (straight) and n_H (dashed) transverse density profiles at various delays τ given by the color scale on the right.

5.5 Propagation Simulations

5.5.1 Simulation Parameters

To provide insight into the formation of CHOFI channels, the ionisation dynamics, and to examine the prospect of generating metre-scale plasma channels, particle-in-cell simulations were undertaken with FBPIC [203]. Simulations were initialised with an electron and neutral density profile equal to that simulated for $\tau = 1.5$ ns [as shown in figure 5.6(a) and (b) respectively]. The ionisation energy for the neutral species was set to be 13.6 eV, equal to that for a hydrogen atom. The ionisation rates were calculated using the ADK model in the tunnelling regime [203]. The laser pulses were assumed to have a Gaussian temporal profile with $\tau_L = 40$ fs, and a Gaussian spatial profile with $w_0 = 21$ µm, closely matching to the experimental laser parameters.

Importantly, since PIC codes include ponderomotive effects and allow for temporal evolution of the laser, the laser effect on the plasma channel, and the effect of the plasma electrons on the laser pulse are included in these simulations. The simulation window was 400×2100 cells on the (r, z) cylindrical grid, and co-propagated with the conditioning laser pulse. The grid resolution was 0.046 µm and 1 µm in the longitudinal and transverse directions respectively. Each cell was initialised with 2 particles per cell along r and z, and 8 particles per cell along θ. At the transverse boundaries, perfectly matched layers with a large number of damping cells were used to absorb outward travelling radiation from leaky modes. Simulations were convergence tested with 2 and 3 azimuthal modes, and for boosted frames with $\gamma_{\text{boost}} = 1, 2, 10$, and 16. Those shown here employ 2 modes and $\gamma_{\text{boost}} = 1$. A linear density ramp of length 100 µm was included at the start of the simulation to prevent unwanted reflections from a density discontinuity. The laser pulse was focused at the top of the ramp, though since the ramp length was much shorter than the Rayleigh length of the laser pulse, the position of the laser focus relative to the start of the channel did not affect the laser coupling.

5.5.2 Neutral Collar Ionisation

The left column in figure 5.7 shows the transverse electron density and laser intensity profiles at four points in the channel for a conditioning pulse with a peak input intensity $I_{\text{peak}} = 6 \times 10^{17}\,\text{W cm}^{-2}$. Early in the propagation, the far leading edge of the pulse ionises the neutral gas surrounding the HOFI channel, creating a deep CHOFI channel in which the main body of the pulse is guided. As expected, the position at which ionisation first occurs corresponds to the position at which $I(r, z)$ first exceeds I_{th}, where I_{th} is the threshold laser intensity for ionisation [101]. Since the transverse intensity profile of the conditioning pulse is not perfectly matched to that of the lowest order mode of either the HOFI or CHOFI waveguides in the hydrodynamic simulations, the spot-size of the conditioning pulse oscillates during the first few centimetres of propagation [see figure 5.8(a)]. However, this variation primarily affects the wall thickness of the CHOFI channel, not its depth or the matched spot size of the CHOFI plasma channel. Higher-order modes are excited by this mismatch and leak out of the channel over the first few centimetres and ionise the surrounding neutral gas, significantly increasing the radial extent of the CHOFI plasma channel. These modes

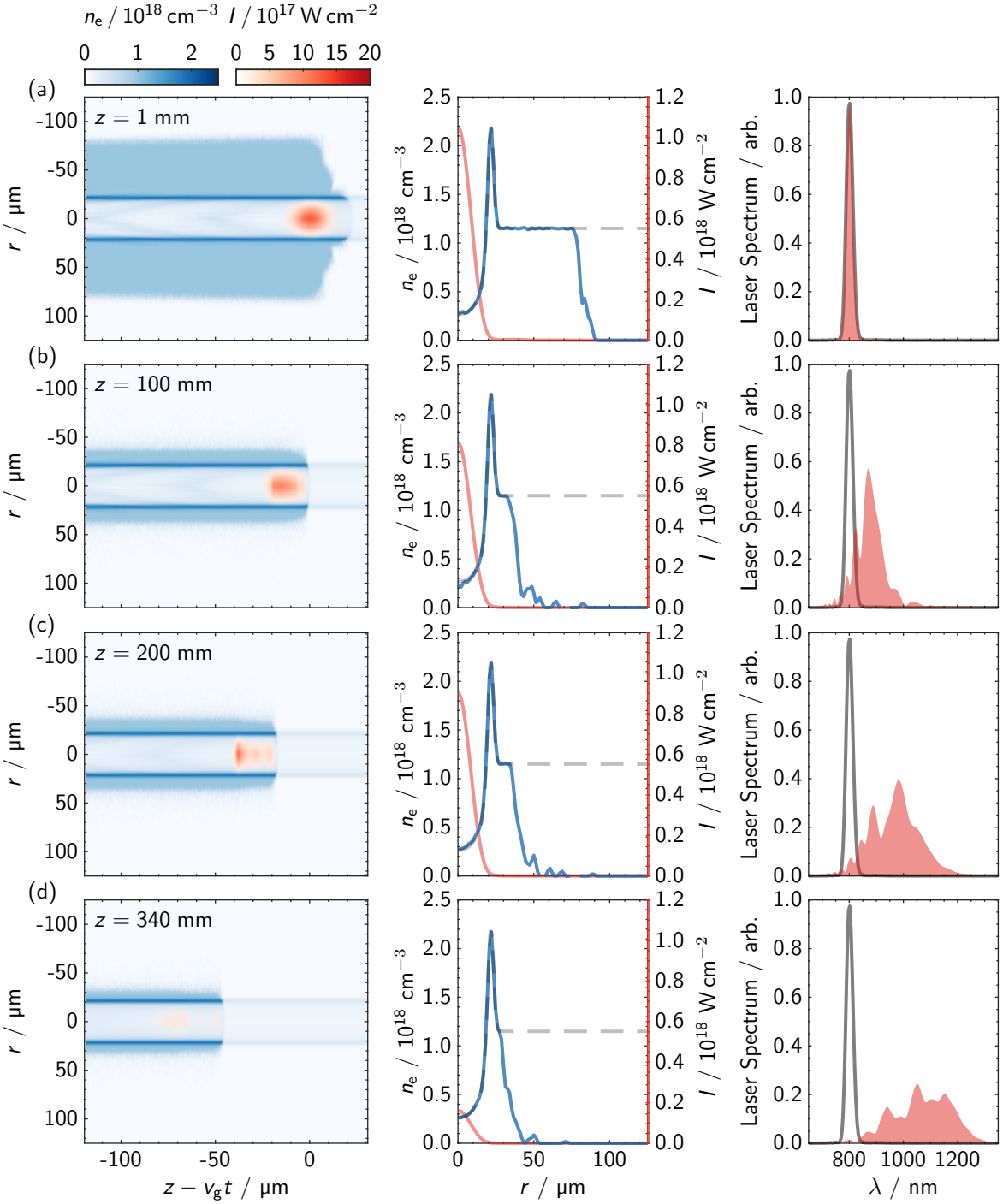

Figure 5.7: FBPIC simulation of a conditioning pulse ($I_{peak} = 6.0 \times 10^{17}$ W cm^{-2}) forming a CHOFI plasma channel after propagation distances of (a) $z = 1$ mm, (b) $z = 100$ mm, (c) $z = 200$ mm, and (d) $z = 340$ mm. Left: transverse profiles of the electron density (blue) and the laser intensity (red). The peak of the conditioning pulse is indicated by the dashed line. Middle: lineouts of the transverse electron density and laser intensity at the peak of the laser pulse. The grey dashed line indicates n_H retrieved from the hydrodynamic simulations. Right: calculated laser spectrum (red) compared to the initial spectrum (grey).

are expected to leak out of the plasma channel at a larger angle than the lowest order mode [116], consistent with the observed attenuation here.

After a few centimetres, the conditioning pulse adopts a stable configuration. This situation is shown in figure 5.7(b-c), which shows that the radial extent of the additional ionisation is reduced with propagation distance z. However, the high walls of the CHOFI channel clearly remain, and are sufficiently thick to ensure low-loss propagation of the bulk of the conditioning pulse. The conditioning pulse continues to propagate with low loss, and to generate a low-loss channel, until it can no longer ionise the neutral gas close to the shock front. Once this occurs, the conditioning pulse attenuates more rapidly as it would in the unconditioned HOFI plasma channel.

As shown by the middle column, the peak of the laser pulse (red) propagates in the deep, conditioned channel throughout the simulation, even as the radial extent of the CHOFI plasma channel is reduced further along the channel. Despite these longitudinal variations, the mode of the plasma channel is almost constant $w_{\mathrm{m,CHOFI}} = 15.8\,\mu\mathrm{m}$ throughout the simulation; the RMS change in the spot size after the initial oscillations is just $0.1\,\mu\mathrm{m}$ [see figure 5.8(a)] This is expected given the arguments in section 3.3.1 because the shape of the plasma channel in the region where modes are allowed to propagate remains unchanged through the simulation. This is an important result: the longitudinal variation in the radial extent of the walls of the channel does not affect the guided mode, and hence will not affect the properties of the wakefield and accelerated electrons. Further, this simulation shows that ionisation of the neutral collar is relatively stable to a degree of mis-matching of the conditioning pulse to the HOFI channel.

A linear plasma wakefield with a relative amplitude of $\delta n_{\mathrm{e}}/n_{\mathrm{e}} \approx 10\,\%$ is driven by the conditioning pulse. As the pulse propagates in the stable region, the laser pulse is gradually red-shifted caused by the plasma wakefield. The peak of the spectrum shifts from $800\,\mathrm{nm}$ to $1056\,\mathrm{nm}$ after $340\,\mathrm{mm}$ of propagation, as shown in figure 5.8(b). Figure 5.8(c) shows how the spectral broadening that occurs due to the wakefield also compresses the pulse, but this does not impede the conditioning. Since the mode structure of a plasma waveguide is wavelength independent [116], this spectral shift does not change the transverse profile of the guided conditioning pulse. Thus, the wakefield has no observable effect on the properties of the CHOFI channel. The wakefield is also expected to decay on a timescale of approximately 10 ps [231] which is much shorter than the timescale

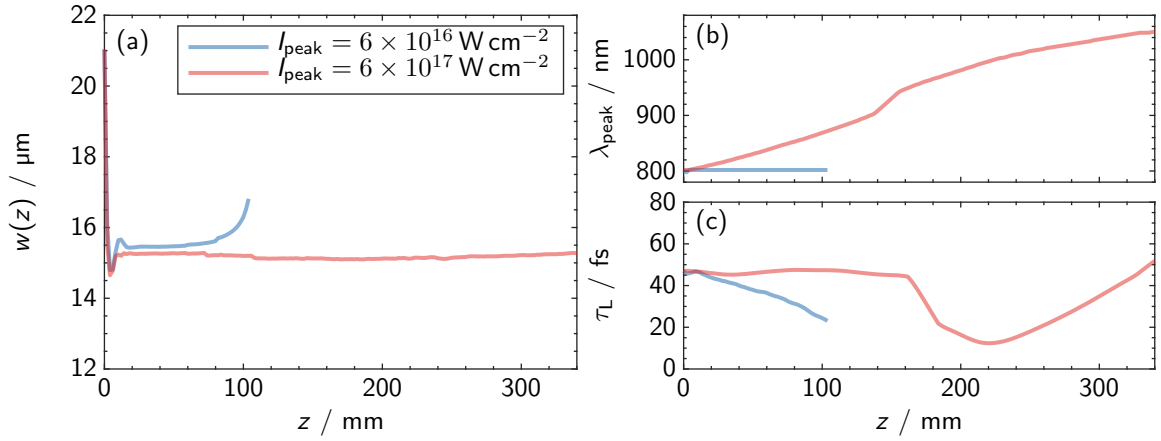

Figure 5.8: Evolution of (a) the spot-size, (b) the peak of the laser spectrum, and (c) the pulse duration of the conditioning laser pulse for simulations with input intensity $I_{peak} = 6 \times 10^{16}\,W\,cm^{-2}$ (blue) and $I_{peak} = 6 \times 10^{17}\,W\,cm^{-2}$ (red).

observed in figure 5.3 for significant evolution of the transverse electron density profile. Therefore any pulses guided subsequently will not be affected by wakefield generation.

Figure 5.8 also shows the properties of a conditoning pulse with an input intensity of $I_{peak} = 6 \times 10^{16}\,W\,cm^{-2}$ (blue), corresponding to $a_0 = 0.175$. As with the higher intensity simulation, the beam waist initially oscillates, but settles at a similar matched spot size $w_{m,CHOFI} = 15.4\,\mu m$. Futhermore, the wakefield is almost completely suppressed; the spectrum is not altered during propagation.

5.5.3 Energy Losses of the Conditioning Pulse

It is also interesting to consider the effect of the plasma on the conditioning pulse. Figure 5.9 shows the pulse energy transmission $T(z)$ of the *conditioning* pulse as a function of propagation distance z, for input intensities . The laser transmission was calculated by isolating the electric field of the laser from that of the wakefield and integrating at each timestep

$$T(z) = \frac{1}{\mathcal{E}_{init}} \pi \epsilon_0 \int_0^{R_1} \int_{Z_-}^{Z_+} |E(r,z)|^2 \; r \; dr dz, \tag{5.1}$$

where $(0, R_1)$ and (Z_-, Z_+) are the edges of the simulation box in r and z respectively, and $\mathcal{E}_{\text{init}}$ is the initial laser energy given by

$$\mathcal{E}_{\text{init}} = \left(\frac{\pi}{2}\right)^{3/2} \tau w_0^2 I_{\text{peak}}. \tag{5.2}$$

For intensities lower than $\sim 5 \times 10^{15}\,\text{W cm}^{-2}$, the conditioning pulse is not intense enough to ionise the neutral collar of gas, and hence it propagates in the HOFI channel and experiences high losses. For $I_{\text{peak}} = 6 \times 10^{16}\,\text{W cm}^{-2}$, only the peak of the pulse is intense enough to ionise the neutral collar and generate a deep, thick channel. The leading edge etches away rapidly, and the length of the CHOFI channel is limited to $\approx 100\,\text{mm}$. In contrast, the highest intensity conditioning pulse shown in figure 5.7 propagates with low losses over the length of the simulation. The calculated energy loss of the conditioning pulse in this case is $\sim 7\,\text{mJ}$ per centimetre of waveguide.

Three mechanisms by which the conditioning pulse depletes its energy are (i) ionisation of hydrogen, (ii) etching of the leading edge of the pulse due to leakage, and (iii) to driving a wakefield. It is important to understand which of these dominates the propagation losses of the conditioning pulse at different intensities. Firstly, it is possible to estimate the energy losses due to ionisation by summing the number of hydrogen atoms per unit length ionised by the conditioning pulse. The transverse profile of the conditioning pulse evolves over time, and the radius out to which the neutral gas is ionised, r_{ion}, also changes, the energy loss can be calculated as

$$\frac{d\mathcal{E}}{dz} = 2\pi \mathcal{E}_{\text{ion}} Z \int_0^{r_{\text{ion}}} n_{\text{H}} r \, \text{d}r, \tag{5.3}$$

where $Z = 1$ and $\mathcal{E}_{\text{ion}} = 13.7\,\text{eV}$ for atomic hydrogen. For a $1\,\text{m}$ CHOFI channel with $I_{\text{peak}} = 6 \times 10^{17}\,\text{W cm}^{-2}$, the total energy loss due to ionisation is expected to be $5 - 20\,\text{mJ}$, making its contribution to the losses small.

Calculating the photon number $N_\gamma(z)$ permits comparison of the effect energy transfer from the laser to the plasma with leakage from the channel. Channel leakage will cause $N_\gamma(z)$ to decrease as light leaks away from the axis and is absorbed by the boundaries of the simulation. Conversely, Bulanov *et al.* [232] showed that the photon number is conserved during wakefield excitation, only altering the spectrum of the laser. As such, the pulse energy lost to wakefield excitation is

manifested as a red shift of the pulse spectrum.

The energy of N_γ photons of frequency ω is $\mathcal{E} = N_\gamma \omega$. The total energy of the laser spectrum in one dimension (see equation 3.5) can also be expressed as

$$\mathcal{E} = \frac{\epsilon_0}{2} \int_{-\infty}^{\infty} |E(\omega)|^2 \, \mathrm{d}\omega. \tag{5.4}$$

Hence, the total photon number is

$$N_\gamma = \frac{\epsilon_0}{2} \int_{-\infty}^{\infty} \frac{|E(\omega)|^2}{\omega} \, \mathrm{d}\omega. \tag{5.5}$$

Extending to three-dimensions, and assuming a cylindrical geometry, provided the longitudinal momentum of the photons is much greater than their transverse momentum, total photon number can be written as

$$N_\gamma = \pi \epsilon_0 \int_{\omega=-\infty}^{\infty} \int_{r=0}^{\infty} \frac{|E(\omega)|^2}{\omega} r \, \mathrm{d}r\mathrm{d}\omega. \tag{5.6}$$

Thus for these simulations, the photon number at a given point in the simulation can be calculated in Fourier space as

$$N_\gamma(z) = \sum_r \sum_\omega |E_\mathrm{L}(\omega, r, z)|^2 \, \frac{r}{\omega}, \tag{5.7}$$

and making the assumption that channel leakage is independent of wavelength over the spectral bandwidth of the laser pulse, the relative loss in photon number due to leakage is equal to the relative energy loss due to leakage. If the leakage rate is not spectrally uniform, for example if red-shifted components are preferentially scattered out of the simulation by the wake, then the relative loss in photon number will underestimate the energy loss due to leakage. The same argument also applies if blue-shifted components are preferentially scattered.

Omitting the losses due to ionisation, the energy transmission can be written as $T(z) = T_\mathrm{wake}(z) + T_\mathrm{leak}(z)$, where $T_\mathrm{leak}(z) \approx N_\gamma(z)/N_\gamma(0)$. The relative photon number $N_\gamma(z)/N_\gamma(0)$ is plotted in figure 5.9. The grey line shows the results of a simulation with the same laser parameters but with an infinite parabolic plasma channel matched to the laser mode. It is clear that the photon number is conserved in this case since no light leaks out of the plasma channel.

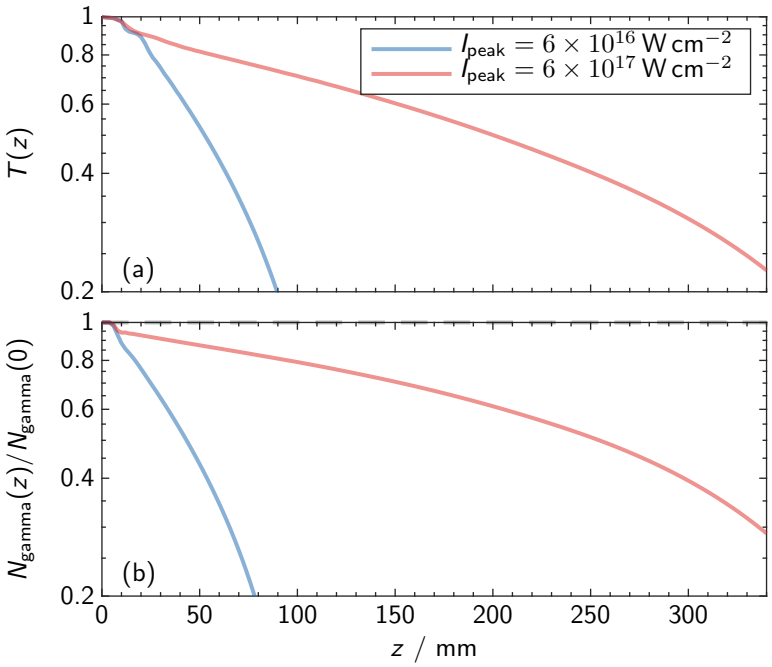

Figure 5.9: (a) Calculated pulse energy transmission $T(z)$ of the *conditioning* laser pulse as a function of propagation distance z, for peak input intensities of $6 \times 10^{16}\,W\,cm^{-2}$ (blue) and $6 \times 10^{17}\,W\,cm^{-2}$ (red). (b) The relative photon number $N_\gamma(z)/N_\gamma(0)$ for the same simulations. The grey, dashed line shows the results of a simulation with the same laser parameters but with an infinite parabolic plasma channel matched to the laser mode.

For both $I_{peak} = 6 \times 10^{16}\,W\,cm^{-2}$ and $I_{peak} = 6 \times 10^{17}\,W\,cm^{-2}$, after $1\,cm$ of propagation $T = T_{leak} = 0.85$, indicating that all of the initial losses come from excitation and leakage of higher order modes due to the small spot-size mismatch. In the stable propagation region, comparison of $T_{leak}(z)$ and $T(z)$ suggests that mode leakage dominates the losses in both cases, but that leakage occurs more rapidly for lower intensities since more of the leading edge is attenuated away. For $I_{peak} = 6 \times 10^{17}\,W\,cm^{-2}$, $\lesssim 10\,\%$ of the energy is transmitted to the plasma. However for $I_{peak} = 6 \times 10^{16}\,W\,cm^{-2}$, not only are the photon losses are significantly more rapid, as more of the leading edge is attenuated in the shallow HOFI channel, but the transmission losses are all due to the photon losses, not transfer to the plasma wakefield. One should expect that laser to plasma energy transfer dominates at higher intensities ($a_0 \sim 1$) since the efficiency of energy transfer to the plasma wave increases, and the leading edge of the pulse will begin ionising the plasma much earlier, reducing the photon losses.

5.6 Metre-Scale LWFA Stages using CHOFI Plasma Channels

5.6.1 Generating Suitable Plasma Parameters

Both the experimental and simulation results presented here demonstrate that the leading edge of a conditioning pulse can ionise neutral gas surrounding HOFI plasma channels to form a much deeper conditioned HOFI channel capable of guiding the main body of the conditioning pulse, and any subsequent pulse injected into the waveguide with low propagation losses. The simulations presented in section 5.5 demonstrate generation of CHOFI plasma channels up to $325\,\mathrm{mm}$ long, increasing the potential length of LWFA stages driven by these types of channels by over an order of magnitude, and to the lengths required for $\sim 10\,\mathrm{GeV}$ stages.

Control over the axial density and matched spot size of CHOFI channels is in principle possible by adjusting the delay τ between the channel-forming and conditioning pulses, and the initial gas density. Consider the hydrodynamic simulation results presented in section 5.4; increasing τ from $1.5\,\mathrm{ns}$ to $4\,\mathrm{ns}$ reduces the axial density from $n_\mathrm{e} = 2.4 \times 10^{17}\,\mathrm{cm}^{-3}$ to $n_\mathrm{e} \approx 7 \times 10^{16}\,\mathrm{cm}^{-3}$ and increases w_m to $31\,\mu\mathrm{m}$ whilst maintaining a suitably large attenuation length. Since heating of the initial HOFI channel is independent of density, it is in principle possible to create CHOFI channels at even lower densities, which would provide greater single-stage electron energy gain.

Further, some control over the *shape* of the CHOFI waveguide is possible by adjusting the delay $\Delta\tau$ between the conditioning pulse and the pulse to be guided as shown in figure 5.3. For small values of $\Delta\tau$ the CHOFI channel has a core of approximately uniform electron density, surrounded by high and thick walls; this profile is a good approximation to a near-hollow plasma channel, which can provide independent control of the focusing and accelerating fields for electron and positron acceleration [233]. For larger values of $\Delta\tau$ the core of the channel develops an approximately parabolic profile.

Several methods could be employed to extend this length even further. For example, one might employ two or more conditioning pulses, or further increase the intensity of the conditioning pulse. An optimum pulse shape may exist that minimises the laser energy depleted to form the CHOFI plasma channel. Whilst lengthening the conditioning pulse would reduce the amplitude of the

wakefield generated, it would also lengthen the portion of the leading edge of the pulse which is not intense enough to ionise the neutral gas collar. It might be possible to consider altering the spectral phase of the conditioning pulse such that the leading edge rises more sharply. This would be an interesting avenue to investigate in future experiments capable of multi-dimensional parameter space optimisation [59, 87, 234].

5.6.2 Energy Requirements of CHOFI Plasma Channels

The energy required to form HOFI plasma channels was discussed previously in section 3.2.1 and it was shown experimentally that approximately 1 mJ to 5 mJ per centimetre of HOFI channel was required for the channel-forming pulse. Evidently, the conditioning pulse itself adds to those energy requirements, thus it is important to consider the total laser energy required. Simulations in section 5.5 showed that efficient self-guiding of the conditioning pulse is achieved provided it ionises the neutral gas out to approximately $2w_{\mathrm{m,CHOFI}}$, which requires $I_{\mathrm{peak}} \gtrsim 3.5 \times 10^{17}\,\mathrm{W\,cm^{-2}}$ for the $21\,\mu\mathrm{m}$ spot size used here. The calculations showed that when this is satisfied, the propagation losses are approximately $7\,\mathrm{mJ\,cm^{-1}}$, due to erosion of the leading edge of the pulse, and pump depletion. This results in a total laser energy requirement of $1.2\,\mathrm{J}$ for a metre-long LWFA stage, which is small compared to the energy required for the driving laser.

5.6.3 LWFA Experiments Using CHOFI Plasma Channels

An important feature of the work presented here is that the conditioning pulse is self-guided by ionisation of the neutral gas at the edge of the initial HOFI channel. This self-guiding has three important consequences. First, as discussed, the energy of the conditioning pulse is used efficiently, which reduces the total laser energy required to create the CHOFI channel. Second, the generated CHOFI channel is robust to variations of the parameters or pointing of the conditioning pulse. Thirdly, a wide range of channel parameters and shapes are accessible with a simple experimental setup. We note that the conditioning pulse does not require transverse shaping, and should have the same spot size and central wavelength as the wakefield drive pulse. Hence the conditioning pulse could be generated very simply by introducing a small pre-pulse to the drive pulse, or, if the

drive pulse is intense enough, the conditioning pulse could be the leading edge of the drive pulse itself. This is discussed in detail in the following chapter.

5.6.4 Other Methods for Increasing the Transmission of HOFI Plasma Channels

It should be noted that recently, collaborators at the University of Maryland have demonstrated a different scheme to increased the attenuation length of HOFI plasma channels where the neutral collar of gas surrounding the plasma channel is ionised by a higher order Bessel beam [198]. The high order Bessel beam was generated by passing an auxiliary laser pulse through a spiral phase plate, and focusing it with the same axicon as the initial channel-forming pulse at a delay of between 2.5 ns and 4 ns. Further, the same group has undertaken work on enhanced guiding via ionisation of the neutral gas collar by a low-order Gaussian pulse similar to that shown in this chapter [235]. In that work, the presence of a neutral gas collar as inferred in section 5.3 and predicted by FLASH simulations was directly measured by two-colour interferometry.

5.7 Conclusions and Outlook

This chapter demonstrates low-density, low-loss, metre-scale plasma channels can be generated by ionization of the neutral gas collar surrounding a hydrodynamic optical-field-ionized plasma channel. CHOFI plasma channels with axial electron densities of $n_{e0} \approx 2 \times 10^{17}\,\mathrm{cm}^{-3}$ and matched spot sizes of $w_m \approx 25\,\mu\mathrm{m}$ were generated experimentally. The channel depth was increased by a factor of ten compared to the unconditioned HOFI plasma channel and power attenuation lengths of up to $L_{att} = (26 \pm 2)$ m were calculated from interferometric data. This mechanism is likely to have played a role in the experimental demonstration of guiding of high-intensity laser pulses in 100 mm long channels [236], shown in Chapter 4.

Hydrodynamic simulations of the dynamics of the plasma formed by the channel-forming pulse show that a low-density HOFI plasma channel is created by the channel-forming pulse, and that this is surrounded by a collar of neutral gas. PIC simulations show clearly that the leading edge of a conditioning pulse injected into this structure ionises the neutral gas in its transverse wings,

to form a deep CHOFI plasma channel which guides the bulk of the conditioning pulse — and any trailing laser pulses — with very low propagation losses. The properties of CHOFI channels, including their shape, can be controlled by adjusting the initial gas density, and the delays between the channel-forming, conditioning, and guided pulse.

Most importantly, the results in this chapter demonstrate that it is possible to significantly reduce the propagation losses of a HOFI plasma channel, thus enabling CHOFI plasma channels to fulfill a key requirement of multi-GeV LWFA stages. The total laser energy requirement of $\sim 1.2\,\mathrm{J}$ per meter of plasma channel is still $\lesssim 10\,\%$ of the laser energy required per stage for a $10\,\mathrm{GeV}$-scale LWFA. It might be possible to use some of the techniques discussed in section 5.6.1 to improve the energy efficiency of CHOFI plasma channel creation, and such experimental studies would be interesting areas for future investigation.

Further, whilst ponderomotive effects were included in the simulations presented here, such effects could have a much more significant impact on PW-scale pulse propagation in CHOFI plasma channels. Demonstrations of PW-scale pulse propagation and electron energy gain in CHOFI plasma channels is an important next step for this research.

Chapter 6

Electron Acceleration in CHOFI Plasma Channels

6.1 Introduction and Objectives

In the previous chapters, initial experiments demonstrating guiding over long distances (up to 100 mm), and with high energy transmission (CHOFI plasma channels) were detailed. This chapter focuses on combining this work and extending it to demonstrate PW-scale laser pulse guiding and multi-GeV electron acceleration in CHOFI plasma channels. The objectives of this chapter are to:

- develop an experimental design for CHOFI plasma channel experiments using PW-class laser facilities suitable for multi-GeV electron acceleration;
- simulate high-intensity ($a_0 > 1$) laser propagation in CHOFI plasma channels;
- simulate electron injection and acceleration in CHOFI plasma channels.

This chapter details the experimental design of an experiment at the TA3 Gemini laser at the Rutherford Appleton Laboratory (RAL) commencing October 2021 and lasting for six weeks. The scheduled start date was originally October 2020, however this was delayed by one year due to COVID-19. The experiment was planned to follow on from the six-week experiment at the same facility detailed in Chapter 4, with increased peak laser power and conditions adjusted to promote

electron acceleration in CHOFI plasma channels. A novel plasma source design is discussed that meets the constraints of HOFI and CHOFI experiments and PW-scale laser facilities. It is shown that using two axicons aligned co-linearly, plasma channels can be extended to $300\,\mathrm{mm}$ in length whilst also reducing the size of the front pinhole compared to previous experiments.

Further, this chapter details simulations of high-intensity pulse propagation and electron acceleration for this experiment, and a parallel experiment being undertaken at the ALEPH facility at Colorado State University (CSU), led by the group at the University of Maryland. That experiment was similar in design to the TA3 Gemini run discussed in this chapter. The predicted laser parameters for each experiment are shown in table 6.1. In that experiment, the plasma source was a $200\,\mathrm{mm}$ long gas jet designed by the group at the University of Maryland [198, 235].

In this chapter, a novel concept for density transition injection into a low-density plasma channel is proposed and simulated. It is shown that by truncating the plasma channel close to the position of the vacuum laser focus, down-ramp injection of electrons from the higher density neutral gas region can be achieved into the lower density plasma channel. This method has the potential to generate percent level energy spread, high peak energy beams without any significant changes to the experimental setup.

The experimental design for the TA3 Gemini laser experiment was led by the author, who played the lead role in planning for all aspects of the experiment, with specific contributions from Aimee Ross and Oscar Jakobsson on the laser diagnostics, and James Cowley and Warren Wang on the electron diagnostics. The concept design of the novel large volume gas target is the work of the author, with significant input from Barnaby Matthews (RAL), who designed systems for adjusting the cell length and altering the transverse position of the cell-mounted axicon.

The simulation campaign for both the TA3 Gemini laser experiment and the CSU experiment were led by the author with input from input from Oscar Jakobsson, Dr. James Chappell, and Emily Archer on the TA3 Gemini simulations, and Linus Feder on the CSU simulations. The work on the truncated plasma channel injection scheme is that of the author*.

*The TA3 Gemini laser was originally scheduled for October 2020, before the CSU experimental campaigns. However due to COVID-19, the experiment date was delayed by 12 months. Hence, it is not possible to present any experimental results of the Gemini experiment. The objective of this chapter is therefore to describe the design of the experiment, particularly its novel features.

	TA3 Gemini	ALEPH, CSU
Laser energy	≈ 8 J	Up to 9 J
Focusing optic	$f/40$	$f/25$
Pulse duration τ_{FWHM}	≈ 40 fs	≈ 40 fs
Spot-size w_0	35 µm $- 45$ µm	≈ 35 µm
Spot profile	Airy-like	Airy-like
a_0	$1.2 - 1.5$	$1.3 - 1.7$
f_{rep}	0.05 Hz	Up to 3.3 Hz

Table 6.1: Predicted laser parameters for the wakefield drive beam in the Gemini experiment, and for the CSU experimental campaigns.

6.2 Experimental Design

In the previous experiment using the Gemini laser (see Chapter 4), the facility was reconfigured to allow one beam to operate at 5 Hz at lower power for probing of the low density plasma channel. However this meant that the channel-forming and guided laser pulses had to be derived from the same beam which reduced the guided pulse energy For an electron acceleration experiment it is vital to maximise the energy in the drive laser pulse, and to produce a high quality laser spot. Therefore, in this experiment the channel-forming beam was derived from the second of the two Gemini beams, and a new 5 Hz probe beam was generated (see section 6.2.2).

6.2.1 Gas Cell

Design Constraints

As discussed in section 4.2.3, the primary experimental difficulty in HOFI and CHOFI setups is coupling both the large aperture channel-forming beam and the ultrahigh intensity drive laser pulse into the gas cell.

Due to the ultra-high focal spot intensity of PW lasers, the pinholes must be larger than for $10 - 100$ TW lasers in order that it is not burned and opened up in a few shots. For example, the ATLAS 3000 ~ 1 PW laser has measured $I > 10^{15}$ W cm^{-2} at $r \approx 500$ µm [237], larger than the threshold intensity to ionise hydrogen. Realistically for long term operation, it is necessary that $I(r \geq r_{\text{ph}}) \lesssim 10^{12}$ W cm^{-2}. This sets a minimum diameter on r_{ph} which will depend on the laser power, focusing optic and transverse focus quality of the drive pulse.

For PW lasers, not only must the gas be confined to the interaction region, but the gradient of the plasma at the onset must be *shorter* than the Rayleigh length of the drive (guided) laser z_R [237]. Gradients that were longer than this were found to cause filamentation and self-modulation of the focusing pulse, leading to distortions at the focus [237]. Since it is expected that the characteristic scale length of the gas plumes is $\sim 2r_{ph}$, the cell design should ensure that $r_{ph} \lesssim 2z_R$. This criterion is consistent with PIC simulations of CDWs which show a decrease in the maximum achievable drive laser coupling efficiency for gas plumes $L_{gas} \gtrsim z_R$ [226].

The rate at which gas escapes from the cell also determines the gas load into the target vacuum chamber. If the gas flow is too high for the chamber pumps, then the gas load will limit the repetition rate of an experiment. In practice, it might be possible to increase the number of vacuum pumps to accommodate for large gas flows, but this is not always possible, and so it is important to estimate and minimise the gas load for any design.

The above arguments impose several constraints on the gas cell:

- must be capable of generating plasma channels > 100 mm long;
- must be capable of holding uniform gas pressure up to ~ 100 mbar;
- gas plumes at either end of the must be on the scale of $\sim z_R$, where z_R is the Rayleigh length of the PW guided beam;
- must allow for coupling of a PW drive (guided) beam and any channel-forming beams without distortion;
- must have as minimal gas load as possible;
- must be capable of surviving extended periods of operation under vacuum without damage.

Previous Cell Designs

A simple gas cell was used successfully for channels 16 mm [102] and 100 mm long and guided pulses of peak intensity $I_{peak} \sim 10^{17}$ W cm^{-2} (see section 4.4.1). To form $L_{ch} = 100$ mm with $\alpha = 2.5$ deg, $D_{ph} \approx 9$ mm, much larger than typical experimental setups. For the gas system and cell used, the pressure in the cell was limited to $P \lesssim 27$ mbar, corresponding to $n_{init} \approx 1 \times 10^{18}$ cm^{-3} despite

being backed with $P > 1.5$ bar. This large drop in pressure suggests that the gas density close to the entrance pinhole was non-uniform. It is clear that this cell design *does not* satisfy the design constraints for a PW, metre-scale experiment.

The initial tests of the windowed gas cell (discussed in section 4.3.2) revealed that when the longitudinal position of the beginning of axicon focus was close to the entrance pinhole, the cell window was always damaged within a few shots. One could consider moving the window further away from the start of the axicon focus to reduce the laser intensity at the window. However, this arrangement leaves long sections of neutral gas along the axis between the start of the pinhole and the start of the channel. For a finite sized window and pinhole, the length of neutral gas though which the guided laser must travel to reach the start of the channel z_{neut} is non-zero. The minimum distance is given by

$$z_{\text{neut}} = \frac{r_{\text{ph}}}{\tan\alpha} + t_{\text{w}}. \tag{6.1}$$

If one also accounts for the gas plumes, $z_{\text{neut}}^{\text{eff}} \approx z_{\text{neut}} + D_{\text{ph}}$. One could imagine that some of the light could travel through the window and some through the pinhole to reduce z_{neut}, however the non-zero thickness of the pinhole will always cause there to be a region $z \approx t_{\text{w}}$ where a channel is not formed.

It is important to note that the gas in the region of z_{neut} is at a density $n_{\text{gas}} \sim 10^{18}$ cm$^{-3} \gg n_{\text{e0}}$. Assuming that the guided drive laser has $I_{\text{peak}} = 5 \times 10^{18}$ W cm^{-2} ($a_0 \approx 1.6$), then at z_{R} from focus, $a_0(z = -z_{\text{R}}) \approx 1.1$, and $a_0(z = -2z_{\text{R}}) \approx 0.8$, indicating that even before it is focused, the laser is capable of driving a significant wakefield. Even for pinholes of moderate radius and thickness, $r_{\text{ph}} = 2$ mm and $t_{\text{w}} = 1$ mm, $z_{\text{neut}} = 46.8$ mm which is almost $10z_{\text{R}}$ for an $f/40$ drive pulse. At these intensities, and for $n_{\text{gas}} \gtrsim 1 \times 10^{18}$ cm^{-3} significant laser evolution is predicted (see section 6.4.3). If a 40 fs laser pulse was focused to the pinhole, then $L_{\text{pd}} \approx z_{\text{neut}}$, resulting in almost complete energy depletion even before the pulse reaches the plasma channel. For the case where the laser pulse is focused to the front of the plasma channel, and is still converging in the region of z_{neut}, less of the energy would be depleted, however one could still expect significant evolution of the drive laser pulse including self-focusing, etching and steepening, aided by the high density of the ambient gas. Further, a 300 TW pulse exceeds the self-injection threshold for the

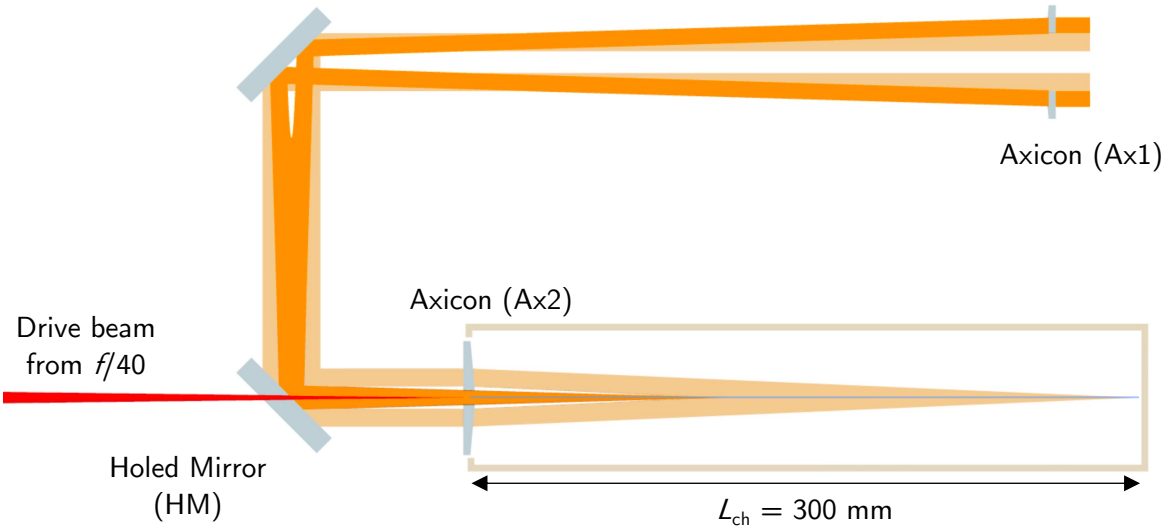

Figure 6.1: Schematic of the channel-forming beam design consisting of two axicons to form a 300 mm long plasma channel. The beam that passes through the hole in Ax1 is the same as that which is focused by it, two colours are only used to differentiate each part of the channel-forming beam.

neutral gas region, and thus one would expect significant, and continual self-injection in the neutral gas region. Electrons injected here will load the wakefield and degrade the bunch quality, making it difficult to achieve any form of controlled injection.

Equation 6.1 indicates that z_{neut} can be rapidly reduced by increasing α. However, α is constrained by the arguments presented in section 3.2.2. To attain $z_{neut} < z_R$ for the pinhole parameters above, $\alpha > 18$ deg is required, which is much larger than the upper limit discussed in that section.

Twin Axicon Gas Cell

Figure 6.1 shows the design of a channel-forming beam focused by two axicons — one placed outside of the cell to focus the channel-forming beam through the entrance pinhole as usual (Ax1), and one attached to the cell (Ax2) that forms a channel up to 300 mm long. Note that the first axicon is able to form the channel in the region of z_{neut} *and* the gas plumes extending from the entrance pinhole. Not only does this setup eliminate propagation through neutral gas, it also offers control over electron injection (see section 6.4.3).

It is possible to completely eliminate z_{neut} by slightly adjusting the approach angle of rays emanating from the first axicon (Ax1) α' such that

$$\tan\alpha' = \frac{r_{\text{ph}}}{r_{\text{ph}}/\tan\alpha + t_{\text{ph}}}. \tag{6.2}$$

It should be noted that this implies that $\alpha' < \alpha$. For $\alpha = 2.5\,\text{deg}$ $r_{\text{ph}} = 2\,\text{mm}$, and $t_{\text{ph}} = 3\,\text{mm}$, $\alpha' = 2.39\,\text{deg}$, indicating that the difference in angle is small enough not to change the plasma channel formation significantly ($\alpha'/\alpha \approx 0.96$). The required change in approach angle comes entirely from the non-zero t_{ph}.

Figure 6.2 shows a schematic of the designed gas cell. The second axicon is mounted to the cell via a movable plate which can be controlled by piezomotors (*Newport*). An o-ring is placed between the plate and the front surface of the cell to maintain the required seal. Similarly, the back pinhole is attached to a $100\,\text{mm}$ long plunger which moves along a rail driven by a stepper motor to change the length of the cell. This is also connected to the cell via a second o-ring to maintain a good seal. The cell is formed of two parts, a $100\,\text{mm}$ long first section, and a removable section which is $200\,\text{mm}$ long. The cell can be varied in length between 0 and 100 mm, and 200 and 300 mm by utilising the removable part and the plunger. Optically flat windows are mounted to the side of each section of the cell to provide access for diagnostics over most of the channel length.

A problem that was encountered in the previous experiment was that the cell filled slowly due to its large volume and the fact that only a single inlet was employed. Hydrogen gas flowed rapidly out of the entrance and exit pinholes, and limited the maximum pressure that could be achieved in the cell. For the new experiment, a novel cell-jet hybrid concept was invoked [238]. Each section is backed by a small slit or area $A \lesssim 1\,\text{mm}$ to increase the speed at which gas enters the cell. The bottom of the cell is conical to increase the uniformity of the gas as it exits the nozzle.

A uniform array of 14 outlets was placed directly above the laser axis to provide access for pressure transducers. Relative pressure transducers (*RS Components*) with response times of $< 1\,\text{ms}$ can be placed in any of the outlets to measure the gas density and fill time.

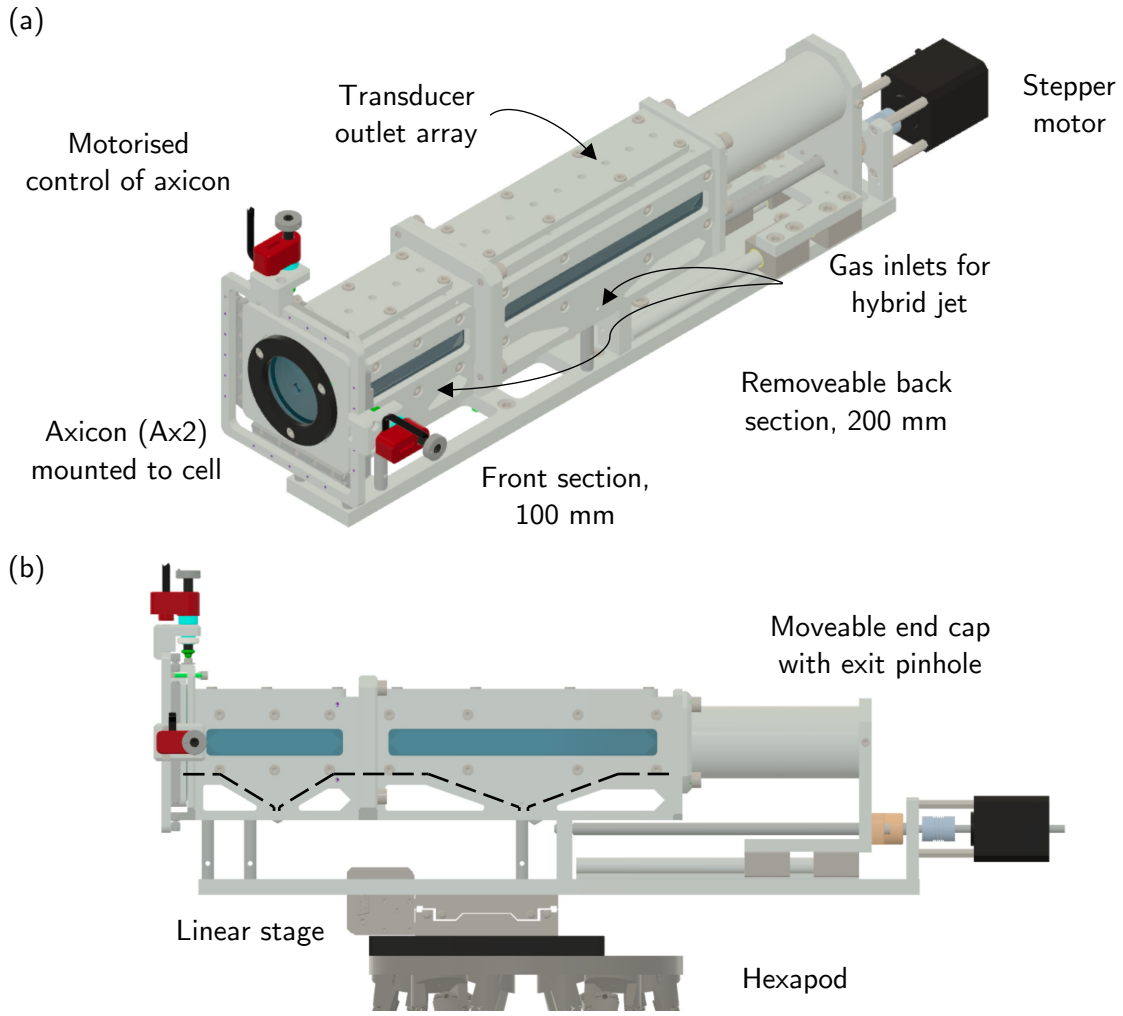

Figure 6.2: Schematic of the novel gas cell design. (a) The 300 mm long gas cell with the removable section attached. Ax2 is mounted to the front to the cell and can be moved independently of the cell. The top of the cell contains outlet ports for transducer measurements. (b) Side view of the cell upon its mount (hexapod and linear stage). The dashed line depicts a cross-section of the hybrid jet inlets taken along the laser axis.

6.2.2 Diagnostics

Two-Colour Interferometry

The probe beam is to be operated at 5 Hz in order to provide reference shots before and after each laser shot. In order to provide information about both the electron density profile and the neutral density profile, the plasma will be probed with simultaneously with two colours. The probe pulse passes through frequency-doubling crystal, transforming it into two co-propagating

pulses with frequencies ω and 2ω respectively. Both pulses are passed onto the same folded wavefront Mach-Zehder interferometer used in Chapter 4, constructed by the author. Beamsplitters that reflected $50\,\%$ of incident intensity at both $\lambda_1 = 800\,\text{nm}$ and $\lambda_2 = 400\,\text{nm}$ are used. The beam is then passed through the cell perpendicular to the plasma channel, and the rays scattered by the plasma were collected and recollimated by a 3-inch achromatic lens with focal length $f_1 = 200\,\text{mm}$. A second achromatic lens with focal length $f_2 = 1500\,\text{mm}$ will be used to re-image the plasma channel at a magnification of approximately 7.5. The predicted resolution at λ_1 and λ_2 is approximately $2\,\mu\text{m}$ and $1\,\mu\text{m}$ respectively. Simulations provided by the lens manufacturer indicate that the focal length change of the first lens over the range λ_1 to λ_2 varies by less than $0.5\,\%$. After the folded-wavefront interferometer, a dichroic mirror will be used to separate the two frequencies onto two 12-bit CMOS detectors, and interference filters were used to increase the fringe contrast (see section 3.5.3).

Guided Laser Pulse Diagnostics

In the previous experiment, the guided laser pulse diagnostics were setup specifically to diagnose the transverse mode and energy transmission of the guided pulse. In this experiment, it was intended to use diagnostics capable of characterising the wakefield in addition to mode-imaging diagnostics. As outlined in section 1.2.3, a laser pulse with $c\tau_\text{L} < \lambda_\text{p}$ will be red-shifted by the refractive index of the plasma as it drives a wakefield. For example, it was shown in figure 5.8 that the spectral peak of a conditioning pulse with $a_0 = 0.54$ was shifted by $\sim 300\,\text{nm}$ after 340 mm of propagation. Simulation of the spectral shift for the parameters of this experiment are discussed in section 6.3.1.

Since it is expected that $\lambda_\text{peak} \gg 1\,\mu\text{m}$, the far-field of the guided laser pulse will be measured by two separate cameras, a 16-bit CMOS (*Andor Neo*), and a 14-bit InGaAs sensor (*Xenics Xeva 640*) to cover a large spectral range. The quantum efficiency of both cameras is plotted in figure 6.3. Dielectric mirrors will be avoided in the beam path after the plasma channel and instead be replaced by uncoated wedges, and metallic mirrors capable of reflecting wavelengths up to 1700 nm efficiently. This will provide information about the mode structure of guided light of all wavelengths.

To diagnose the wakefield itself, the spectral shift will be measured via optical spectrometers.

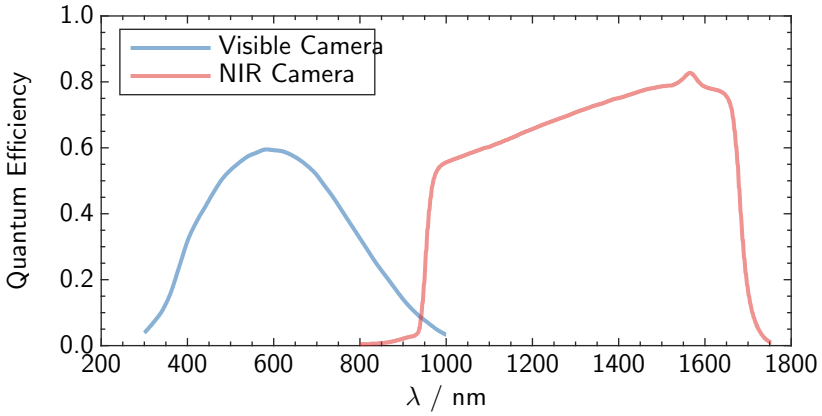

Figure 6.3: Quantum efficiency as a function of laser wavelength for the cameras to be used in the guided laser pulse diagnostics.

Like the far-field diagnostics, two spectrometers will be used to cover as large a range as possible. A Czerny-Turner imaging spectrometer (*Andor Shamrock*) will measure the optical spectrum in the wavelength range $700\,\text{nm} \lesssim \lambda \lesssim 900\,\text{nm}$, and a fibre-based spectrometer (*Ocean Optics NIRQuest*) will be used to cover $900\,\text{nm} \lesssim \lambda \lesssim 1700\,\text{nm}$.

Finally, a pyroelectric energy meter (*Gentec*) will be used to measure the total transmitted energy of the guided laser pulse. Combining this transmission measurement with the spectral measurements and the far-field measurements will provide a good estimate of the guided pulse laser transmission. The spectral measurements provide a good estimate of the driven wakefield provided the initial density n_{e0} is known from the transverse interferometry, making it possible to directly measure the energy losses in the waveguide to leakage out of the plasma channel, and via pump depletion to the plasma wave.

Electron Diagnostics

The most important parameters to determine of any generated electron bunch are the final electron energy, energy spread and the accelerated charge. To measure the electron beam energy, it is typical to employ a particle spectrometer; the beam passes through a magnetic field which deflects electrons transversely according to the electron momentum. The deflected electrons pass through a set of scintillating screens (typically Lanex) which emit light that can be detected via a CCD or CMOS.

The magnet has a peak magnetic field of $B_{\text{peak}} = 1\,\text{T}$, with a distance between the two magnets of $25\,\text{mm}$, that will be placed approximately $350\,\text{mm}$ from the end of the plasma channel. A complication arises due to the fluctuation in the pointing of the electron beam, which change the position at which they pass through the Lanex screen, leading to an apparent shift in electron energy. Since the pointing of the electron beam on a given shot is not known, this can lead to large uncertainty in the electron energy [35]. This problem gets worse for higher energies since the deflection is small.

Several solutions to this problem have been proposed for LWFA experiments. Typically, two Lanex screens are used so that a the trajectories of features in the measured spectrum can be used to deduce the trajectory of those electrons into the spectrometer [239]. In this experiment, the first screen will be replaced by a set of tungsten wire fiducials with known width and position [240]. The fiducials imprint a shadow on the electron beam which can be used to determine the input trajectory of the electron. The position of these shadows on the Lanex screen can be used to reconstruct the beam trajectory through the particle spectrometer, and accurately measure the electron energy spectrum.

Whilst it is possible to infer the electron beam charge density from the Lanex screen measurements, in practice large uncertainties are introduced by the imaging system that re-images the scintillating screen onto the detector. Hence, the electron beam charge will be measured by using a calibrated image plate [241]. The electron diagnostics for this experiment were designed and developed by James Cowley and Wei-Ting Wang.

Betatron Diagnostics

It is possible to measure the X-rays generated in the interaction by using a CCD camera capable of measuring wavelengths of just a few nm (*Andor iKon*). No turning optics are used for this diagnostic, the camera is placed along the line which X-rays would be generated at the back of the experimental area. The X-rays are transported out of the vacuum chamber via a Kapton window.

Optimising Diagnostics

In previous experiments that generated multi-GeV electron beams in plasma waveguides [15, 18, 19], the length of the experimental target area was sufficient to allow the electron beam to propagate up to 10 metres downstream (and sometimes be focused via quadrupoles) before being dispersed and measured via the electron spectrometer. Since the space in the Gemini target area is limited to just a few metres (around 3 m) this is not possible, and the electron spectrometer must be placed in the chamber, before the wedge that collects the light from the guided pulse. The aperture of the permanent magnet therefore limits the spatial resolution of the forward diagnostics. The theoretical best resolution for a 300 mm long cell with the magnet in place is $16\,\mu m$.

Further, the hole in the turning wedge after the interaction, which is required to allow the betatron radiation to pass through, further decreases the resolution, and the light collected by the forward diagnostics. This meant that it will not be possible to measure measure both the betatron radiation, and the guided laser pulse on the same shot.

6.3 Propagation Simulations

Simulations of multi-GeV acceleration in capillary discharge waveguides, and in the self-guided regime have been reported previously [157, 207, 242–244]. Experiments investigating multi-GeV acceleration in HOFI and CHOFI plasma channels have several differences. Firstly, the channels are leaky, hence only the lowest order can propagate the length of the stage, and does so with a shorter attenuation length than in CDWs. Simulations in the previous chapter showed this was a dominant loss process for lower intensity pulses (up to $I_{peak} = 6 \times 10^{17}\,W\,cm^{-2}$). Secondly, the leading edge of the pulse must ionise the neutral collar surrounding the HOFI plasma channel, and this process could affect the local refractive index of the plasma. Third, the measured and simulated channels presented so far have smaller w_m than CDWs at densities of around $n_{e0} \approx 1 \times 10^{17}\,cm^{-3}$. Finally, CDWs are somewhat limited by the D_{cap} required to avoid laser damage, and thus are limited by scaling laws that relate w_m and n_{e0} for a fixed D_{cap}, however CHOFI stages may offer more control over the plasma channel properties.

Detailed theoretical studies of intense ($a_0 > 1$) laser propagation in plasma channels have been

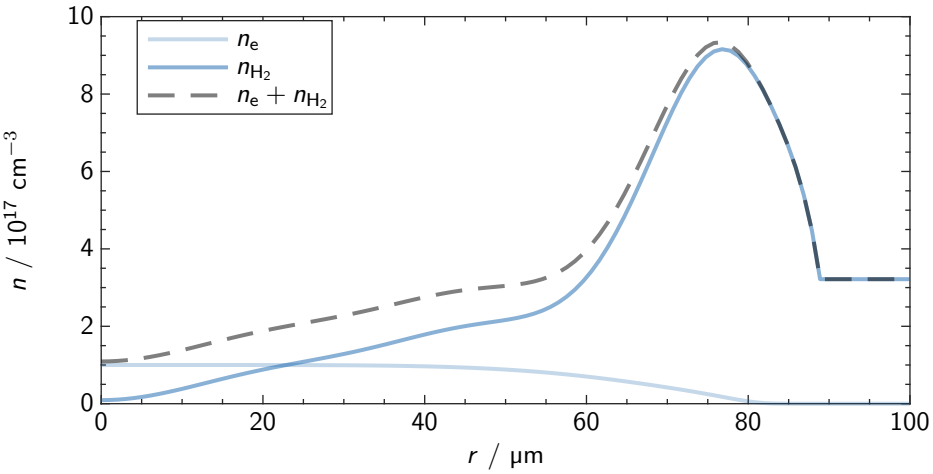

Figure 6.4: Electron (light blue) and neutral (blue) density profiles used in PIC simulations during this chapter. Data is from the measured profiles by Feder *et al.* [235] at a timing of $\tau = 2.5\,\text{ns}$. To change the axial density, the profile was linearly scaled; here $n_{e0} = 1 \times 10^{17}\,\text{cm}^{-3}$.

previously undertaken [245, 246]. It was found that the transverse laser intensity distribution along the laser pulse varied due to significant changes in the refractive index of the plasma behind its leading edge caused by ponderomotive effects. Quasi-matched propagation was observed when the laser pulse was focused to a spot-size slightly smaller than the low power matched spot-size (calculated using the methods detailed in section 3.3.1), and when that was the case, stable propagation was adopted with the back of the pulse being self-focused further.

6.3.1 High-Intensity Guiding in a CHOFI Plasma Channel

As part of the planning for the Gemini experiment, and parallel experiment at CSU, propagation of intense laser pulses through CHOFI plasma channels was investigated by the author. To match the expected experimental parameters, two changes were made to the simulations compared to those undertaken in Chapter 5. Firstly, the electron and neutral transverse density profiles were taken to be the profiles measured via two-colour interferometry by Feder *et al.* [235] (see figure 6.4). Secondly, the laser parameters were chosen to match those expected in the experiment (see table 6.1), and as a result the laser near-field profile was assumed to be a close to a top-hat[†].

[†]In FBPIC, this is represented by the flattened Gaussian laser formalism [247]

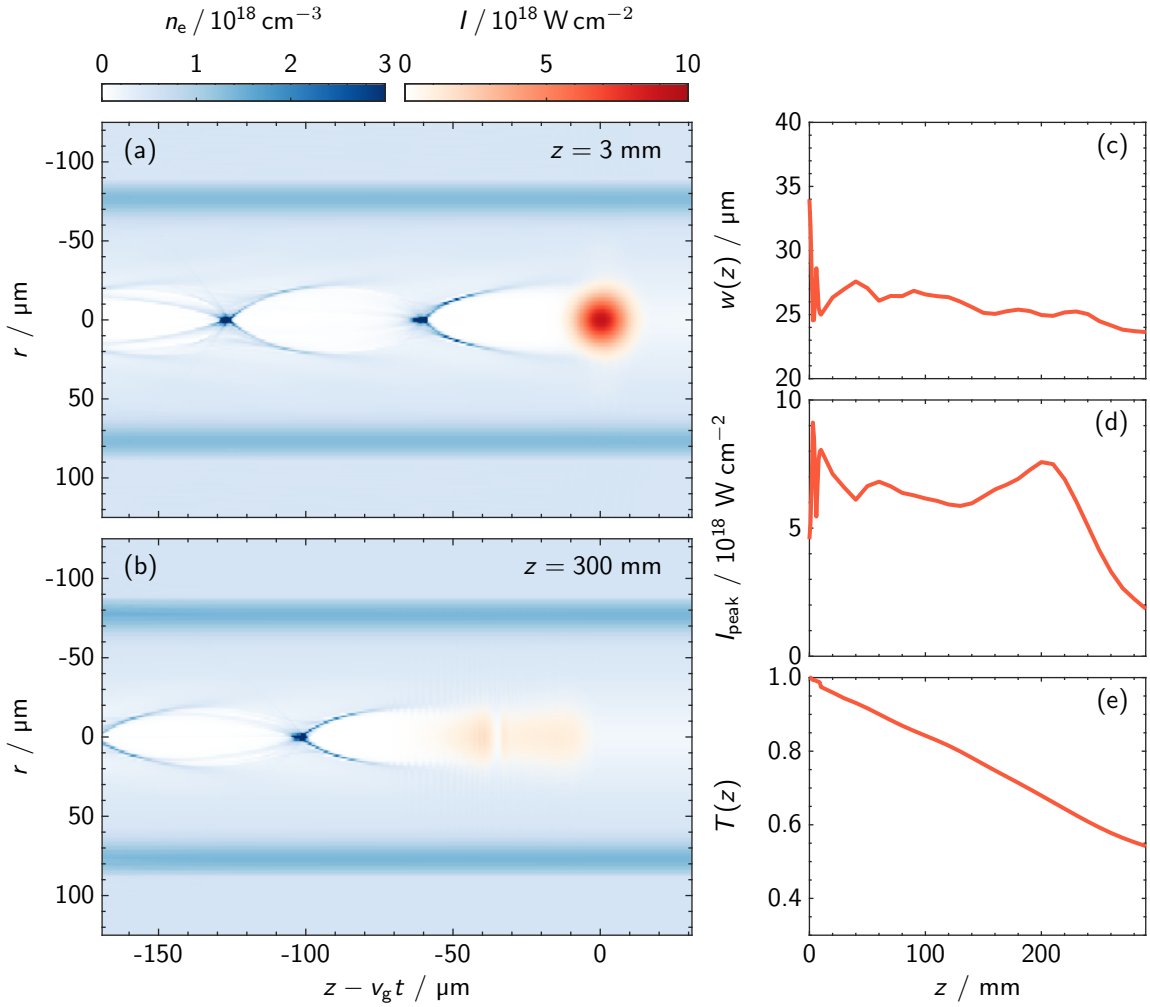

Figure 6.5: FBPIC simulation of a high-intensity pulse ($a_0 = 1.4$) driving a wakefield inside a CHOFI plasma channel. The electron density (blue) and laser intensity (red) transverse profiles are shown for (a) $z = 3$ mm and (b) $z = 300$ mm. Evolution of the laser spot-size, peak intensity, and the transmitted laser energy are shown in (c), (d) and (e) respectively.

For these simulations the window was 900 × 5000 cells on the (r, z) cylindrical grid, and co-propagated with the conditioning laser pulse. The grid resolution was 0.04 µm and 0.33 µm in the longitudinal and transverse directions respectively. Cells were initialised with 2 particles per cell along r and z, and 8 particles per cell along θ. To speed up the computation time, simulations were run in the boosted frame with $\gamma_{boost} = 8$ or 16 up to $L_{acc} = 300$ mm, matching the length of the novel gas cell. A range of laser intensities and axial densities were explored in these initial simulations.

Figure 6.5 shows a simulation of a laser pulse with $a_0 = 1.4$ focused to a spot-size $w_0 = 40$ µm at

the entrance of a CHOFI plasma channel with axial density $n_{e0} = 1.5 \times 10^{17}\,\mathrm{cm}^{-3}$. The calculated matched spot-size of the channel was $w_m = 29\,\mu\mathrm{m}$. Since the intensity of the leading edge was 6.7× greater than for the simulations described in the previous chapter, ionisation occurred on the very leading edge of the laser pulse, and out to a large radius ($r \gtrsim 200\,\mu\mathrm{m}$). As the pulse entered the channel, it was focused slightly by a combination of relativistic self-focusing, and the by the plasma channel, to match the mode size of the channel ($w_m \approx 29\,\mu\mathrm{m}$), increasing the peak intensity. Initially, mode beating was observed, and the peak intensity reached $I_{peak} \approx 1.2 \times 10^{19}\,\mathrm{W\,cm}^{-2}$ briefly [see figures 6.5(c) and (d)], before the mode oscillations were damped out and the pulse propagated with a stable spot size. Increased focusing at the back of the pulse due to the effect of the driven wakefield can be seen in figure 6.5(a), as predicted. As the pulse propagated, the spot-size remained stable, though the pulse significantly red-shifted, and underwent temporal modulations. After $300\,\mathrm{mm}$ of propagation, the peak of the laser spectrum had shifted beyond $\lambda_{peak} = 1100\,\mathrm{nm}$.

A strong wakefield was driven throughout the length of the plasma channel, as shown by the longitudinal electric field. The average accelerating field was calculated to be $\sim 20\,\mathrm{GV\,m}^{-1}$, indicating that an optimally injected test bunch could reach energies of $\sim 6\,\mathrm{GeV}$ in the $300\,\mathrm{mm}$ long stage. For these laser and plasma parameters, no electrons were trapped into the wakefield. This showed, as predicted, that self-injection was suppressed for the lower densities considered here.

6.3.2 Effect of Laser Intensity

The wakefield is to be diagnosed by the measured characteristics of the guided laser pulse. Hence it is important to consider the effects changes in input laser intensity, and axial density have on the guided laser pulse, and on the wakefield driven. Figure 6.6 shows the laser spectrum after $300\,\mathrm{mm}$ of propagation in a CHOFI channel, for various peak input intensities. For all simulations, $n_{e0} = 1.5 \times 10^{17}\,\mathrm{cm}^{-3}$.

Esarey *et al.* [26, 248] predict a frequency shift in the non-linear regime after a propagation

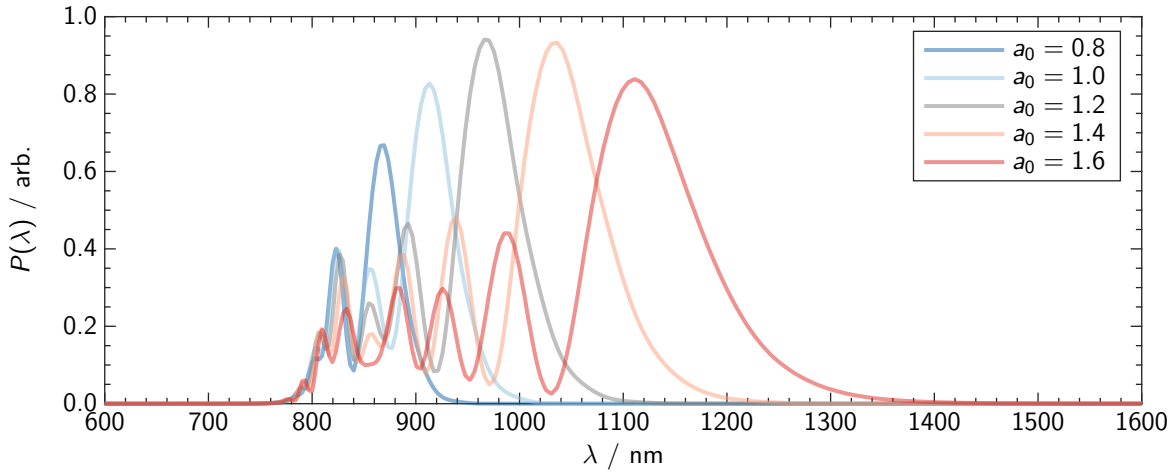

Figure 6.6: Calculated laser spectra after 300 mm of propagation. For all simulations, the CHOFI plasma channel used was the same as that shown in figure 6.4, with $n_{e0} = 1.5 \times 10^{17}\,\mathrm{cm}^{-3}$. As expected, the peak of the spectrum shifts is more red-shifted for higher intensities, as the laser drives a higher amplitude wakefield. New peaks appear due to self modulation of the laser pulse.

distance of $c\tau$ given by

$$\frac{\omega(\tau)}{\omega_0} \approx \left[1 - \frac{\omega_p^2}{\omega_0^2}\int_0^{c\tau} \frac{\partial}{\partial\xi}(1+\phi_{\mathrm{wake}})^{-1}\,\mathrm{d}(c\tau)\right]^{1/2}, \tag{6.3}$$

where $\omega_0 = \omega(\tau = 0)$, and ϕ_{wake} is the electrostatic potential of the plasma wave, which is dependent on the plasma wavelength, and the laser intensity. As expected, for a constant axial density, the frequency shift increases with increasing intensity.

6.4 Electron Injection and Acceleration Low Density Plasma Channels

Whilst many injection techniques have been previously described, there exist few to no demonstrations of electron injection into low-density plasma channels. For energy frontier experiments, self-injection of electrons into the plasma wave is typically employed, since this is the simplest way to generate a beam. However, self-injection requires $a_0 > 3$, relies on significant evolution of the laser pulse in the plasma bubble [41, 42] and is heavily suppressed at low densities [43]. For

stable, multi-GeV stages, it is desirable that laser pulse be matched to the plasma channel and laser evolution be minimised. Indeed, the propagation simulations detailed in the previous section confirm this; self-injection of electrons was only observed at the highest powers considered and with $n_{e0} > 3 \times 10^{17}\,\mathrm{cm}^{-3}$.

In order to avoid these problems, ionisation injection and density transition injection are considered here. Optical injection (described in section 1.2.4) was not considered for this experiment due to the complications of adding another beamline. It should be noted that whilst injection and trapping of low-emittance bunches is an active area of research in the field of LPAs, most experiments and numerical calculations are undertaken in short stages with densities $n_e \gtrsim 2 \times 10^{18}\,\mathrm{cm}^{-3}$. Electron injection at low densities has received less attention, and further, injection directly into a plasma channel has received little attention too. Until now, the only methods considered for the latter require another gas target before the plasma channel [72] or subsidiary laser pulses [55, 56], both of which are experimentally challenging and require fine tuning.

6.4.1 Unlocalised Ionisation Injection

A simple way to achieve ionisation injection is to dope the entire length of the channel with a higher-Z gas. The mechanism by which injection occurs was outlined in section 1.2.4. Chen *et al.* [53] showed that that trapping does not occur for resonant Gaussian laser pulses with $a_0 \lesssim 1.7$, and hence, for the laser parameters considered, some further focusing of the guided laser pulse is required, achieved through relativistic self-focusing, and by the plasma channel. It is also worth noting that ionisation injection is sensitive to the laser pulse length since electrons that are trapped are born close to the peak of the laser pulse. If $c\tau_L < \lambda_p$, then electrons will not be born into the accelerating and focusing phase of the wakefield. Here we are considering low densities where λ_p is longer than previous studies, and hence it is important to consider the lowest density, and thus largest λ_p, that still permits injection into the correct phase for pulses with $\tau_{FWHM} = 40\,\mathrm{fs}$.

Nitrogen (N_2) is the most commonly used gas for ionisation injection. However, since the 6th and 7th shells of N_2 require laser intensities $I_{peak} > 10^{19}\,\mathrm{W\,cm}^{-2}$ for BSI and the expected laser intensity is around $I_{peak} \approx 5 \times 10^{18}\,\mathrm{W\,cm}^{-2}$, it is unlikely that N_2 will permit injection for a laser spot size matched to the channel. Hence, argon (Ar) was also considered, which has many energy

levels with threshold ionisation intensities between $I_{th} = 1 \times 10^{18}\,\mathrm{W\,cm^{-2}}$ and $1 \times 10^{19}\,\mathrm{W\,cm^{-2}}$.

For ionisation injection the injected charge can be increased by increasing the dopant concentration. Hence, for a reduction in the axial density of the plasma by a factor of 10, the dopant concentration must be increased by a factor of 10 to produce a similar trapped charge, assuming the accelerating field is unchanged. However, the effect of higher-Z gases on the formation of the initial HOFI channel is unknown. The threshold intensities for ionisation of the outermost electron shells of Ar and N_2 are lower than for H_2, which acts to reduce the average electron temperature. Further, since Ar and N_2 are heavier than H_2, the ions move more slowly, and hence it is even possible that different ions will separate during the expansion of the channel. For large enough dopant concentrations, it is possible that the channel depth and shape will be significantly affected. As a result, the dopant concentration considered in simulations was restricted to $\leq 5\,\%$, limiting the total charge.

Argon Dopant

Figure 6.7 shows the results of a simulation run with the same parameters as section 6.3.1, but with a $5\,\%$ argon dopant throughout the plasma channel. The simulation was run with separate species for each of the argon shells in order to gain insight into the dynamics of ionisation injection. A number of interesting features were observed. Ionisation by the leading of the pulse of the first 12 shells of argon led to an increase in n_{e0} from $n_{e0} = 1.5 \times 10^{17}\,\mathrm{cm^{-3}}$ to $n_{e0} \approx 2.33 \times 10^{17}\,\mathrm{cm^{-3}}$. This increased self-focusing, and the peak intensity rose as high as $I_{peak} = 1.75 \times 10^{19}\,\mathrm{W\,cm^{-2}}$ (compared to $I_{peak} = 1.20 \times 10^{19}\,\mathrm{W\,cm^{-2}}$) without the dopant.

As the laser envelope evolved over the next $\approx 40\,\mathrm{mm}$, injection of electrons from the 14^{th} and 15^{th} shells of argon began. Figure 6.7(g) shows dQ/dz, i.e. the rate of increase of trapped charge with propagation distance z. Injection occurred primarily in the region $z \approx 35\,\mathrm{mm}$ to $z \approx 70\,\mathrm{mm}$. Before and after this, only a low charge was trapped as a_0 was too small, and ionisation of electrons close to the accelerating phase of the wake was halted. This can be likened to a long propagation version of self-truncated ionisation injection (STII) [62, 249] where the truncation is caused by transverse and temporal modulations of the laser envelope inside the plasma channel. After $z \approx 200\,\mathrm{mm}$, the laser energy had almost completely depleted due to the density

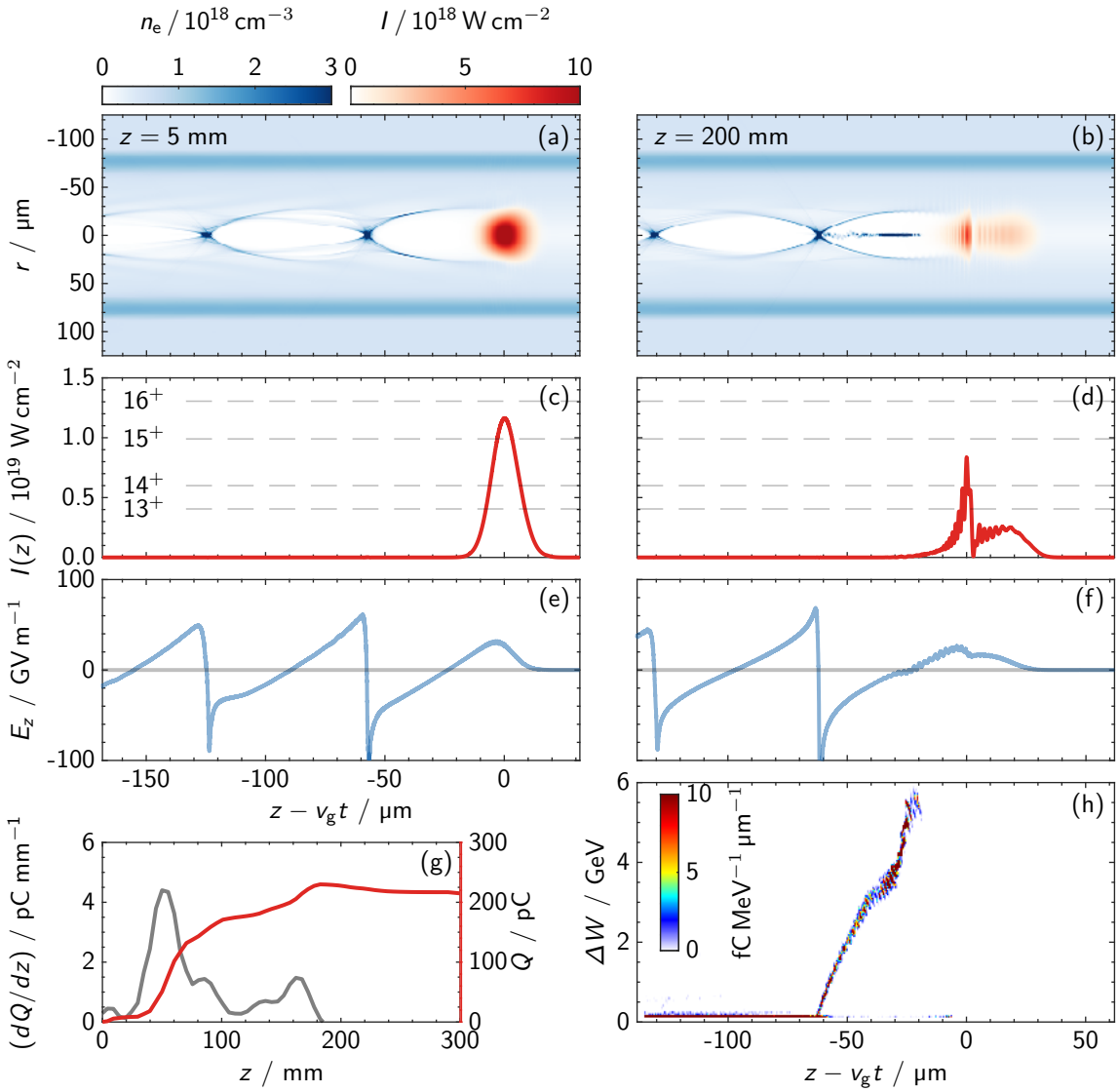

Figure 6.7: FBPIC simulation of a high-intensity pulse ($a_0 = 1.6$) driving a wakefield inside a CHOFI plasma channel with a $5\,\%$ argon dopant. Left: simulation after $z = 5$ mm, right: simulation after $z = 200$ mm.(a-b) transverse profiles of the electron density (blue) and the laser intensity (red). (c-d) Lineouts of the laser intensity profile along the optical axis. The grey dashed lines indicate the threshold intensities required to ionise each shell of argon calculated using BSI. (e-f) Calculated longitudinal electric field. (g) The rate of increase of trapped charge with propagation distance dQ/dz (grey), and the total trapped charge as a function of z (red). (h) Longitudinal phase space of the injected electrons.

increase arising from ionisation, and increased focusing. Hence, injection stopped completely, and acceleration terminated. By the end of the simulation ($z = 300$ mm) the laser had completely depleted and the significant injected charge became more dominant, driving its own wake [57].

The charge density of the trapped electrons at $z = 200$ mm is shown in figure 6.8. Three

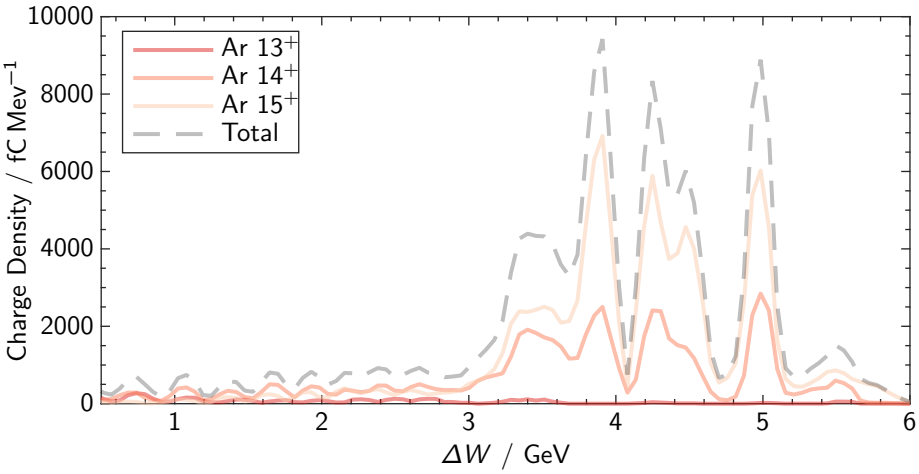

Figure 6.8: Charge density, $dQ/d(\Delta W)$, of the trapped electrons for the simulation shown in figure 6.7. Electrons with energies up to $\Delta W \approx 5.6\,\text{GeV}$ were observed, with most of the charge in three distinct peaks at $\Delta W = 3.9\,\text{GeV}$, $4.2\,\text{GeV}$ and $4.9\,\text{GeV}$.

distinct peaks are observed at $\Delta W = 3.9\,\text{GeV}$, $4.2\,\text{GeV}$ and $4.9\,\text{GeV}$. It was not the case that these peaks corresponded to different shells of argon, but instead corresponded to several regions along the channel at which ionisation injection occurred to a significant degree. Including all of the three peaks, the FWHM energy spread is $\sim 30\,\%$. Whilst this is still over an order of magnitude higher than desired, the results are promising for a scheme with such simplicity. Future simulations could look to optimise this further.

6.4.2 Localised Ionisation Injection

It is possible to consider ionsiation injection only in a small section of the plasma waveguide. Gonsalves *et al.* [157] and Maier *et al.* [58] have independently demonstrated localised ionisation injection of electrons in capillary targets (the former used a CDW, whilst the latter used the capillary as a gas cell [250]). In both cases, the dopant concentration and pressure of gas were varied between the front and back gas inlets to restrict the dopant species to the front section of the capillary. This generated a zone for injection, and then a zone for acceleration. This is not possible for the gas cells to be employed in these experiments. However it is possible in an elongated gas jet target such as that designed and constructed by the University of Maryland [198]. In that target, the elongated gas section is formed by placing several jets along the optical axis. A

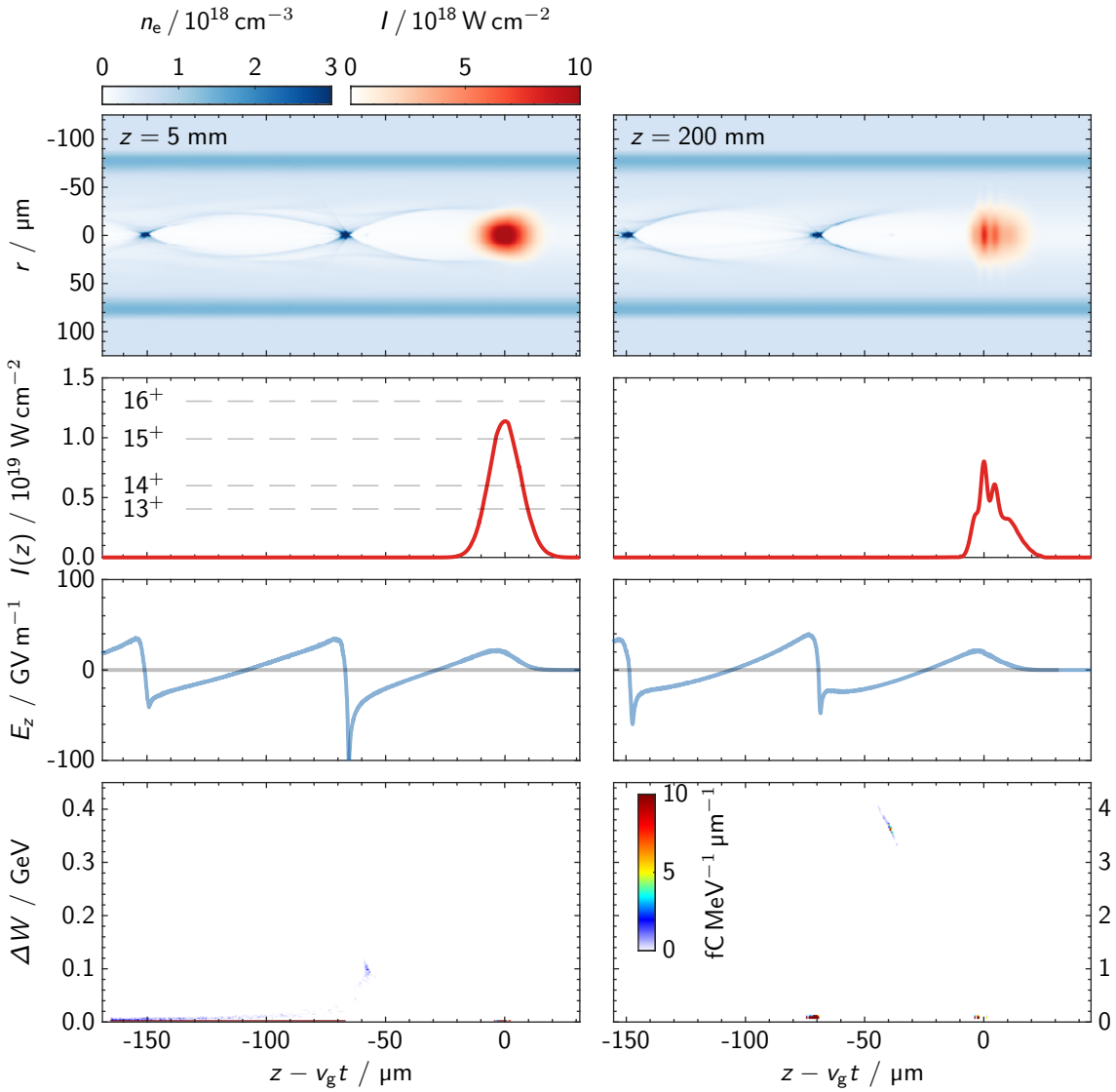

Figure 6.9: FBPIC simulation of a high-intensity pulse ($a_0 = 1.35$) driving a wakefield inside a CHOFI plasma channel with a $5\,\%$ argon dopant localised to the first 5 mm of the plasma. Left: simulation after $z = 5$ mm, right: simulation after $z = 200$ mm. Top: transverse profiles of the electron density (blue) and the laser intensity (red). Upper Middle: lineouts of the laser intensity profile along the optical axis. The grey dashed lines indicate the threshold intensities required to ionise each shell of argon calculated using BSI. Lower Middle: calculated longitudinal electric field. Bottom: longitudinal phase space of the injected electrons. The energy scale is 10× greater on the right plot.

dopant gas can be introduced to the first jet to localise the injection to a region of a few mm.

Figure 6.9 shows the results of a simulation that included a localised dopant of $5\,\%$ Ar in the first 5 mm of the jet. The axial density prior to ionisation was $n_{e0} = 1.0 \times 10^{17}$ cm^{-3}, matching that of the the undoped section. The laser was taken to have a near top-hat near field profile, and

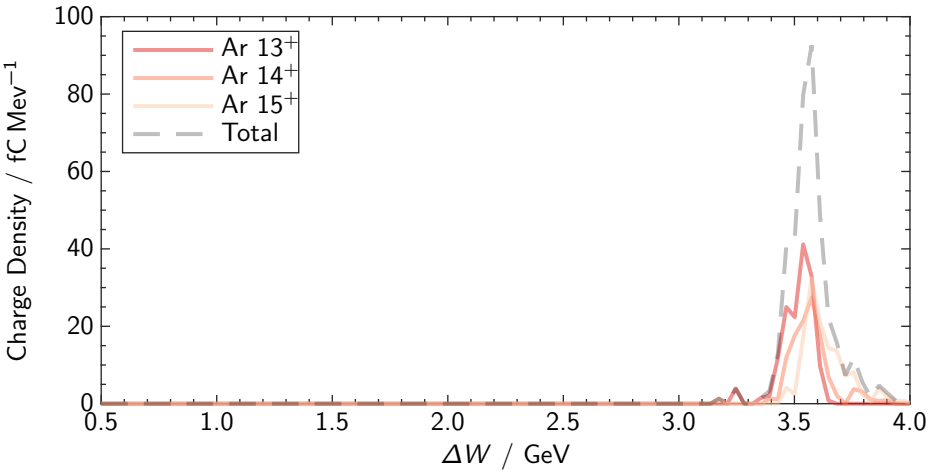

Figure 6.10: Charge density as function of beam energy for a simulation with $5\,\%$ localised argon dopant. Injection is triggered by the 13$^{\text{th}}$, 14$^{\text{th}}$ and 15$^{\text{th}}$ electrons. The peak energy was $\Delta W = 3.57\,\text{GeV}$ and FWHM energy spread was just $91\,\text{MeV}$.

hence an Airy-like focus, with $a_0 = 1.35$, and a spot-size of $w_0 = 35\,\mu\text{m}$. It was focused to the front of the jet section, where some focusing by the plasma channel occurred almost immediately since $w_\text{m} \approx 31\,\mu\text{m}$ was slightly lower than w_0. This triggered injection of the 13$^{\text{th}}$, 14$^{\text{th}}$ and 15$^{\text{th}}$ shells of argon. A small charge of $0.49\,\text{pC}$ was accelerated in the doped section up to around $120\,\text{MeV}$.

In the subsequent accelerating section, the laser propagated in the CHOFI channel with extremely low losses. The average accelerating field was approximately $25\,\text{GV m}^{-1}$, varying primarily due to temporal modulation of the laser pulse during propagation (see section 1.2.3). After $200\,\text{mm}$, the injected bunch had reached a peak energy of $\Delta W = 3.57\,\text{GeV}$ with FWHM energy spread of just $91\,\text{MeV}$, corresponding to a relative energy spread of just $2.5\,\%$ (see figure 6.10).

When the dopant concentration was increased, not only did the injected charge increase, but electrons from hydrogen were trapped in the first and second periods of the wake. This was attributed to the formation of a density down-ramp between the doped section – the density of which was increased to $n_{e0} = 2.1 \times 10^{17}\,\text{cm}^{-3}$ by ionisation of the dopant — and the main plasma channel.

6.4.3 Density Transition Injection

Density transition injection and post acceleration in the same plasma channel has received little attention until now, with most shock injection experiments being undertaken in mm long gas jets, at high densities. The group at LBNL have demonstrated controlled injection from the downramp of a Helium gas jet placed at the front of a CDW, and achieved acceleration up to $400\,\mathrm{MeV}$ with approximately $10\,\%$ energy spread [72].

In this section, a new method for generating the density transition is considered that is achieved by truncating the plasma channel near the laser focus to generate a down-ramp. It should be noted that Faure *et al.* [251] previously investigated injection by a density transition that was formed by a plasma channel crossing at an oblique angle with respect to the drive laser. Further, Scott *et al.* [252] investigated the injection of electrons via the down-ramp generated by an intense prepulse arriving $65\,\mathrm{ps}$ before the peak of the pulse.

Usually, the axicon line focus extends throughout the length of the gas cell, and hence, as discussed in Chapter 4, the HOFI channel extends into the gas density up-ramps outside the entrance pinhole. Figure 6.11 shows a model of a HOFI channel that has been truncated so that it starts 2 mm into the gas cell (a 2 mm density up-ramp has been assumed). The shock profile was generated by revolving the cylindrical shock measured in experiment (see figure 6.4) about a perpendicular axis located at the channel entrance. In reality, this is not quite correct since the Sedov-Taylor solution for cylindrical and hemi-spherical geometries differ and hence this approximation will over estimate the height of the shock, and r_{shock}.

An initial simulation of the case shown in figure 6.11 was undertaken using the Gemini laser parameters. The results are shown in figure 6.12. It is clear that significant charge was injected, the trapped charge was calculated to be $0.74\,\mathrm{nC}$ in the first period and $0.09\,\mathrm{nC}$ in the second. However, the results showed this case was far from ideal. Even before the laser pulse had reached focus, it had become intense enough to drive a significant wakefield. Relativistic self-focusing of the pulse was observed. The calculated self-focused spot-size (see equation 2.1) was $w_{\mathrm{sf}} \approx 18\,\mu\mathrm{m}$, significantly smaller than the input beam ($w_0 = 35\,\mu\mathrm{m}$) and the matched spot size of the plasma channel ($w_{\mathrm{m}} \approx 28\,\mu\mathrm{m}$). Further, since the plasma wavelength in the section of uniform gas was shorter than in the waveguide, this meant that $c\tau_{\mathrm{L}} > \lambda_{\mathrm{p}}/2$, and hence the pulse envelope exhibited

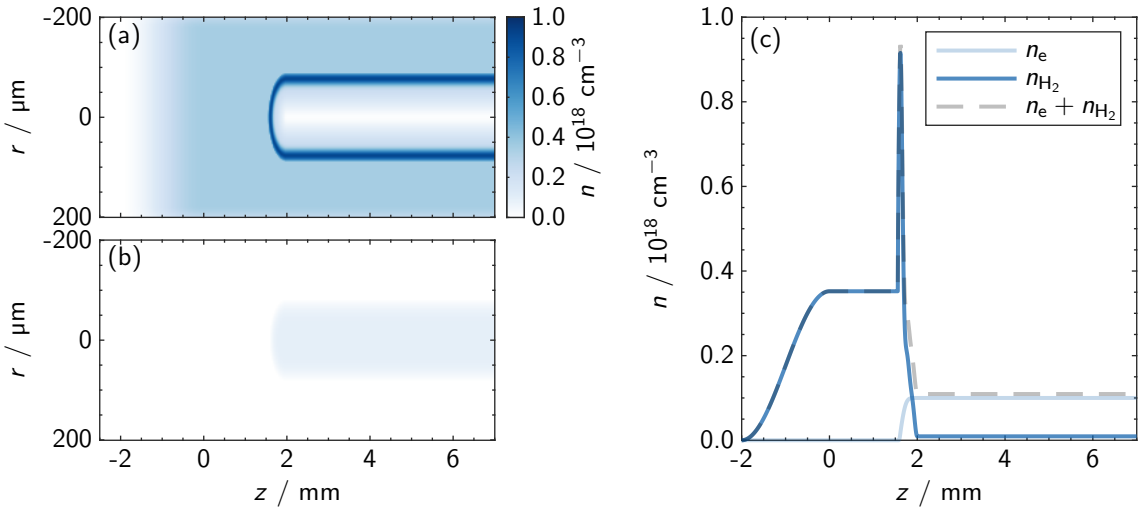

Figure 6.11: Approximated (a) neutral and (b) electron density profiles for the truncated CHOFI injection scheme. Here, the axicon focus is assumed to start 2 mm downstream of the front pinhole (located at $z = 0$), and a 2 mm long gas plume has been assumed extending from the front pinhole to $z = -2$ mm. Hence, the guided laser pulse travels through the gas plume, and 2 mm of uniform, neutral gas before entering the plasma channel. (c) Lineout of the electron and neutral density profiles along the optical axis. The axial density was set to be $n_{e0} = 1 \times 10^{17}\,\mathrm{cm}^{-3}$ inside the plasma channel.

significant modulations, which led to poor matching in the channel section. To attempt to account for the laser evolution, the position of the laser focus was shifted downstream with respect to z_{peak}, however this still led to poor matching into the plasma channel.

The relative height of the density transition, defined as

$$K = \frac{n_{e,max}}{n_{e0}}, \tag{6.4}$$

where $n_{e,max}$ is the maximum electron density along the optical axis was $K = 9.3$ for the example considered. Assuming a non-linear wakefield, the bubble radius increases by a factor of $\sqrt{K} \approx 3.1$. Thus, electrons trapped electrons were found between the back of the bubble and close to the centre of the bubble. For larger values of K, the volume of phase space covered by the trapped charge increases, and hence the energy spread increases significantly. For this reason, previous numerical studies of density transition injection have found that optimal trapping occurs for $K < 2$ [47, 253], where trapped electrons are restricted in a small volume close to the back of the period.

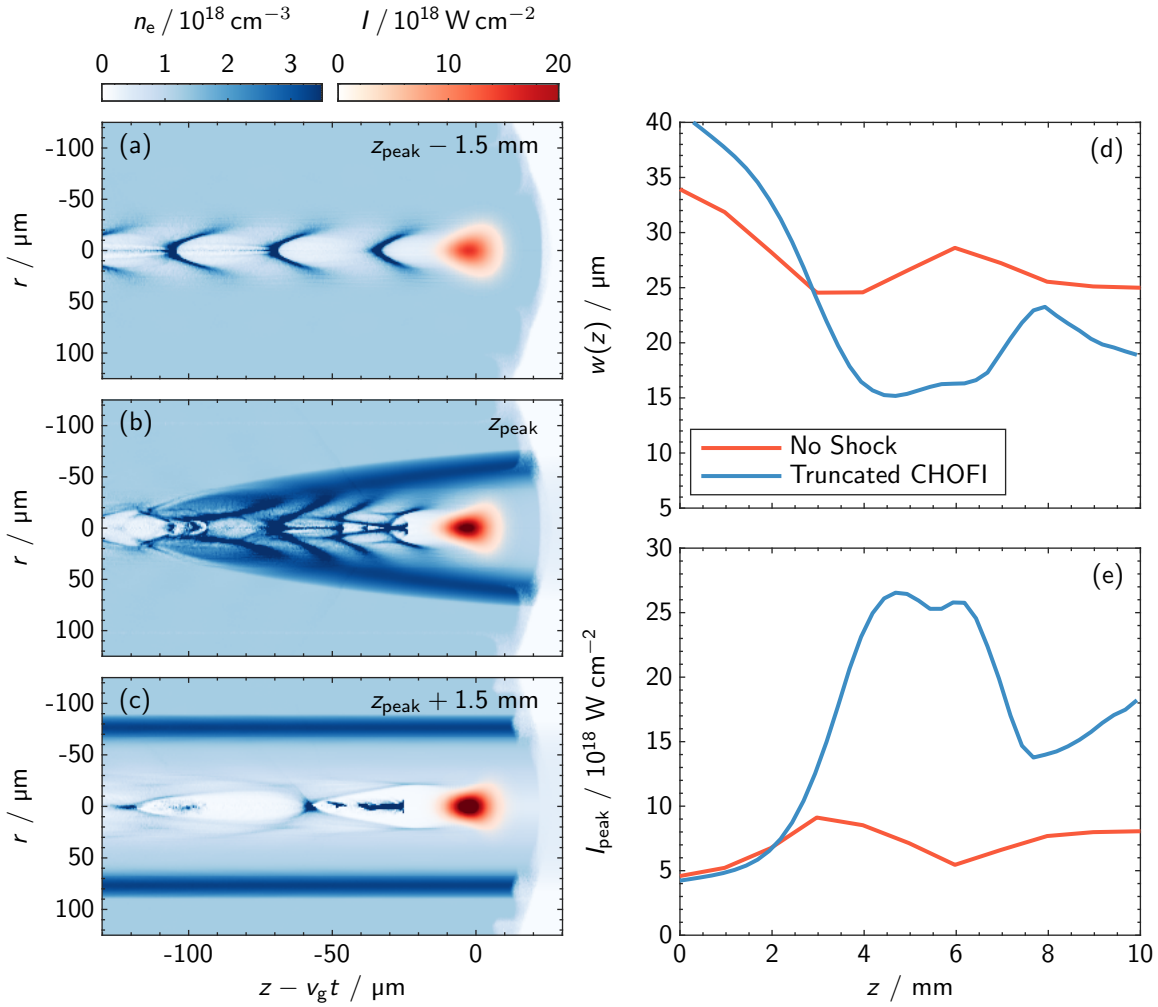

Figure 6.12: Transverse laser intensity (red) and electron density profiles (blue) at the start of the truncated CHOFI plasma channel at three points (a) $z = -1.5$ mm (b) 0 mm, and 1.5 mm with respect to the start of the plasma channel z_{peak}. The evolution of the spot-size (d) and peak laser intensity (e) is compared to the case where the channel is not truncated. Self-focusing in the neutral gas region causes significant laser evolution.

Reducing Laser Evolution and Electron Energy Spread

To reduce the self-focusing, and improve the laser coupling into the plasma channel, it was necessary to eliminate as much of the higher density, neutral gas region as possible. Further, to reduce the energy spread, it was necessary to reduce K. Therefore, it would be better to place the start of the plasma channel somewhere on the gas density plume where the shock height will be lower, and the neutral gas encountered by the drive pulse will be significantly reduced.

Simulating this scenario with a high degree of accuracy requires better knowledge of the gas

plumes emanating from the entrance pinhole *and* the shape of the hemispherical shock on the density gradient. This is a challenging hydrodynamic simulation problem (and experimentally challenging) in itself and beyond the scope of this work. Instead, a simpler scenario was simulated where the hemi-spherical shock approximated (see figure 6.11) was placed on the density ramp, and the height was scaled accordingly to achieve $K = 1 - 4$.

With a reduced strength of self-focusing, the amplitude of the wakefield was reduced, and the trapped electrons resembled more closely those found from previous simulations of down-ramp ($L_{tr} \gtrsim \lambda_p$) [44]. For a ramp $L_{tr} = 100\,\mu m$, it was required that $K > 3$ for charge to be injected into the first period of the plasma wake, however for $K \gtrsim 1.4$, trapping was observed in the second period, where a strong accelerating gradient still existed. By increasing the ramp length to $L_{tr} = 250\,\mu m$, which experimentally can be achieved by changing the rate at which the axicon line focus reaches I_{th}, the trapped charge increased in both the first and second wake periods. Trapping was also observed in the first period for a lower relative shock height ($K \gtrsim 2$). This finding is consistent with the theory presented in section 1.2.4.

6.5 Discussion

It should be noted that very recently, the group at LOA demonstrated mono-energetic electron acceleration to 1 GeV using HOFI plasma channels [254]. The plasma channels were generated using an axiparabola [255] and a $30\,mm$ long gas jet; controlled injection was achieved via a razor blade to produce a small scale density transition. They noted that energy stability of the accelerated beam was higher than previous GeV scale experiments, but limited by the pointing fluctuations of the guided laser pulse (which had shot-to-shot rms stability of $2\,\mu rad$).

In this chapter, design and simulations of petawatt laser guiding and multi-GeV electron acceleration is presented. To do so, a novel gas cell is presented the circumvents the problems encountered with all previous cell designs, and reduces the gas load required. Further, a study of electron injection into low density plasma channels is presented, and different mechanisms for electron trapping at these densities are compared. Initial simulations of electron trapping in a truncated CHOFI plasma channel are presented.

Using laser parameters closely matching those expected for the Gemini experiment, it is shown that a large energy spread electron beam can trapped and accelerated via unlocalised ionisation injection using an argon dopant. The final beam peak energy was $\Delta W \approx 4.5\,\mathrm{GeV}$, generated using a laser energy of just $\mathcal{E} \approx 9\,\mathrm{J}$, (where up to 1 J is used to create the CHOFI plasma channel). This marks a very promising step forwards in the field of LWFA, Leemans *et al.* [18] accelerated an electron bunch to $4.2\,\mathrm{GeV}$ using 16 J of laser energy. Of course, the simulations presented here are for plasma channels that are immune to laser damage, and have the potential to operate at kHz repetition rates.

It is clear that the novel cell design, combined with electron injection via the truncated CHOFI plasma channel presented here has the potential to generate a high energy electron gain $\Delta W > 5\,\mathrm{GeV}$, low energy spread $\lesssim 1\,\%$ electron beam in a single stage, with no other laser beams required for injection, and without the need for staging. This has the potential to provide the source of electrons required for a compact FEL [94].

Chapter 7

Conclusions and Future Work

The development of plasma waveguides with properties suitable for LPAs has been an active area of research for several decades. CDWs have been very successful to date, but this thesis aimed to develop, via experiments and simulations, HOFI plasma channels in order to form low density, metre scale plasma waveguides capable of operating at high repetition rates.

In Chapter 2, several techniques for generating plasma waveguides suitable for LWFAs were compared and contrasted. The first plasma channel ever generated was formed via a cylindrical hydrodynamic expansion of laser ionised gases. The plasma was heated through inverse bremsstrahlung (IB), however efficient heating required a minimum electron density $n_{\text{init}} \gtrsim 1 \times 10^{19}\,\text{cm}^{-3}$, limiting the axial plasma density to $n_{\text{e0}} \gtrsim 1 \times 10^{18}\,\text{cm}^{-3}$ [115]. A very significant advantage of optically-generated hydrodynamic plasma channels is that they are immune to laser damage making them ideal for high-repetition rate operation over extended periods. However, the fact that they are limited to relatively high on-axis plasma densities prevents their application to multi-GeV plasma acceleration stages.

In 2018, the HOFI plasma channel was proposed by the Oxford group as a potential solution for low density, high repetition rate operation. These waveguides are formed by hydrodynamic expansion of a plasma column that is formed and heated by optical field ionisation (OFI). Since OFI acts on the atomic level, the electron heating is independent of the initial density and hence it is possible to generate an initial plasma column with low density. The rate at which electrons were liberated by an ultrashort pulse and their subsequent kinetic energy was detailed.

Several required performance characteristics of plasma waveguides for a high-repetition rate ($f_{rep} \gtrsim 1\,$kHz), multi-GeV accelerator stage were discussed. It was shown that low densities ($n_{e0} \sim 10^{17}$ cm^{-3}), and long stages ($L_{acc} = 0.25 - 1$ m) were necessary, as well as some tunability of the matched spot-size and channel shape. Importantly, the transmission losses of the waveguide had to be minimised to maximise the efficiency of the LWFA stage. To function as an accelerator useful for applications, the limiting repetition rate must be $\geq 1\,$kHz with high shot-to-shot stability and reliability. Further, the energy cost of operating the waveguide was considered, and it was argued that it must be $\lesssim 10\,\%$ of the drive laser energy for each stage.

Prior to the onset of the work described in this thesis, the Oxford group had demonstrated the formation of, and guiding in, 16 mm long HOFI channels produced by an axicon lens, with an on-axis densities as low as $n_{e0} \approx 1.5 \times 10^{17}\,$cm^{-3} [102]. Design of experiments to guide multi-TW lasers in short plasma channels had been studied in depth [103], though gas cell designs for guiding PW scale laser pulses in longer plasma channels had yet to be developed.

In Chapter 4, an experiment using the TA3 Gemini laser at RAL extended HOFI plasma channels to lengths of 100 mm for the first time and demonstrated optical guiding of high-intensity laser pulses through such channels. HOFI plasma channels were measured via transverse interferometry to have axial densities as low as $n_{e0} = (1.0 \pm 0.3) \times 10^{17}\,$cm^{-3}. In that experiment, the guided pulse energy transmission observed was dominated by the coupling of the non-ideal input beam, and by the channel attenuation length. It was shown that the attenuation length L_{acc} was approximately $100\,$mm.

In Chapter 5, a new method for extending such plasma channels to the metre-scale, and reducing their propagation losses significantly was presented. By using a conditioning laser pulse to ionise the neutral gas collar that surrounds a HOFI plasma channel, the depth and radial extend of the plasma channel is increased significantly. Results from an earlier experiment conducted using the TA2 Astra-Gemini laser at RAL showed that the plasma channel depth instantaneously increased by a factor of 10 on the arrival of the conditioning pulse, and that the energy transmission of high-intensity pulses was significantly greater than for lower intensity pulses. This was attributed to conditioning of the plasma channel by the leading edge of the high-intensity laser pulse, generating a low-loss plasma structure in which the rest of the pulse was guided. Hydrodynamic simulations

indicated that the neutral collar surrounding the electron density peak was formed via a snowplough effect. As electrons and ions that are heated early in the channel formation move outwards, they displace cold, neutral atoms. PIC simulations demonstrated that the leading edge of a conditioning pulse injected into this structure ionises the neutral gas in its transverse wings, forming a deep CHOFI plasma channel which guides the bulk of the pulse — and any trailing laser pulses — with low propagation losses. It was found that leakage of the conditioning pulse out of the plasma channel was strongly related to its peak intensity. These CHOFI plasma channels offer significantly longer attenuation lengths, and increased tunability.

Building on the promising experimental and numerical results from Chapters 4 and 5, Chapter 6 aimed to develop the design of a metre-scale CHOFI plasma channel capable of accelerating electrons to the multi-GeV level. A novel cell design, able to generate CHOFI plasma channels up to 300 mm long, whilst minimising the gas load was proposed. It is hoped that such a design adhere to the constraints of a CHOFI plasma channel LWFA experiment. The diagnostics used in Chapter 4 were extended to provide further insight into the expansion of the CHOFI plasma channel, and the amplitude of the wakefield driven inside the plasma channel. PIC simulations were undertaken to investigate propagation and electron acceleration in CHOFI plasma channels for the first time. It was shown that low-loss propagation of high intensity laser pulses in experimentally measured plasma channels [235] could be achieved, and that a significant amplitude wakefield could be driven throughout a 300 mm long stage. Two different mechanisms capable of injecting electrons into the wakefield without significantly increasing experimental complexity were considered: ionisation injection, and density transition injection. A novel method for achieving density transition injection into a low density plasma channel via truncation of the CHOFI plasma channel was presented. It was shown via FBPIC simulations that ionisation injection via a localised and unlocalised dopant can trap electrons and lead to multi-GeV electron beams. The former provided energy gain of $\Delta W \approx 3.6$ GeV with an energy spread of just $2.5\,\%$.

By combining the results from these chapters, it is clear that long, low-density plasma channels can be formed by laser conditioning of HOFI structures, and that these plasma channels are capable of accelerating electrons to multi-GeV energies.

A limitation of the work considered here is the pulse energy required to form a metre-long

CHOFI plasma channel. As outlined in section 3.2.1, the laser technology already exists to form a metre-long HOFI structure. However, increased pulse energy (in ultrashort pulses) is required for CHOFI plasma channel formation, which might be harder to realize at high pulse repetition rates. An interesting direction of future research would be experimental designs and techniques to reduce the laser energy required to form CHOFI plasma channels.

The work considered here has been focused specifically on the first demonstrations of wake-field generation, PW-scale laser guiding, and electron acceleration in CHOFI plasma channels. Experiments of this type require high laser pulse energies, and hence experiments using current laser technology are limited to low repetition rates ($f_{\text{rep}} \lesssim 1\,\text{Hz}$) and constrained to just a few facilities worldwide. As discussed, any plasma channel that forms a multi-GeV accelerator to drive applications such as FELs must operate at high-repetition rates with high stability. Perhaps the most important direction for future study is the demonstration of kHz repetition rate (C)HOFI plasma channels, and optical guiding in such channels. This experiment would provide valuable insight into the stability of the channel formation process, and whether it can be improved using novel feedback and optimisation techniques [59, 87]. Development of novel laser technologies that provide high repetition rate, Joule-level, ultrashort pulses is an area of great interest. It is likely that these technologies will be ideally suited to providing a test-bed for metre-scale, CHOFI plasma channels and allow further study into the performance and stability of laser-based plasma channels.

A limitation of the experiments detailed in this thesis is the diagnosis of long, low density plasma channels. Since low densities incur small phase shifts on transverse probe laser pulses, the signal to noise ratio is low, and high uncertainties are unavoidable. Further, as the plasma channels get longer, with no change in the field of view of transverse diagnostics, it will only be possible to diagnose a small proportion of the plasma channel. Future studies should place importance on developing diagnostics that can provide reduced uncertainties, and measure a larger field of view.

In this thesis, formation of CHOFI plasma channels with Hydrogen gas was considered. Future experiments should aim to investigate the expansion and plasma channel formation with different gas species such as Helium and Nitrogen. Whilst these heavier elements require a higher intensity to ionise via OFI, the kinetic energy of liberated electrons is much greater. Since it is known that the effects of diatomic gases like Hydrogen are not well modelled by MHD codes, experiments using

a species such as Helium could provide a good benchmark for future simulations. Further, whilst the agreement between the calculated shock expansion and measured transverse electron density profiles is good qualitatively, better agreement between hydrodynamic simulation and experiment would aid understanding of laser based plasma waveguides.

Additionally, only channel formation using Ti:Sapphire laser pulses ($\lambda = 800\,\text{nm}$) was considered. Whilst the dependence of plasma channel formation on the laser wavelength was described phenomenologically in Chapter 3, it is likely that future, high-repetition-rate CHOFI plasma channels will be generated by lasers with a higher wall plug efficiency, and hence a different drive wavelength than Ti:Sapphire. Experiments and simulations to investigate how the formation of HOFI plasma channels depend on laser wavelength would therefore be interesting.

For experiments with high pulse energies, future experiments should aim towards demonstrating multi-GeV electron acceleration with low energy spread and low-emittance. This may be best achieved by employing an auxillary laser pulse to achieve controlled injection. Combining such injection techniques, with the low density plasma channels considered here would provide the basis for a stable, low energy spread bunch at high-repetition rates, and be immediately applicable to compact light sources and FELs.

Progress in this thesis has demonstrated that generating low density channels with lengths of order 1 m at kilohertz repetition rates is a realistic prospect. Whilst investigations of CHOFI plasma channels are still in their infancy, it is clear that these plasma channels are likely to be very well suited to multi-GeV LWFA stages.

References

[1] J. D. Cockcroft and E. T. S. Walton. *Proceedings of the royal society of London. Series A, containing papers of a mathematical and physical character* **136**, 830, pp. 619–630 (1932). (Cited on p. 1)

"Experiments with high velocity positive ions.—(I) Further developments in the method of obtaining high velocity positive ions".

[2] E. F. Haussecker and A. W. Chao. *Physics in Perspective* **13**, 2, p. 146 (2011). (Cited on p. 1)

"The Influence of Accelerator Science on Physics Research".

[3] A. P. Chernyaev and S. M. Varzar. *Physics of Atomic Nuclei* **77**, 10, pp. 1203–1215 (2014). (Cited on p. 1)

"Particle accelerators in modern world".

[4] T. Tajima and J. M. Dawson. *Physical Review Letters* **43**, 4, pp. 267–270 (1979). (Cited on pp. 2, 3)

"Laser Electron Accelerator".

[5] M. N. Rosenbluth and C. S. Liu. *Physical Review Letters* **29**, 11, pp. 701–705 (1972). (Cited on pp. 3, 4)

"Excitation of plasma waves by two laser beams".

[6] C. E. Clayton, C. Joshi, C. Darrow, and D. Umstadter. *Physical Review Letters* **54**, 21, pp. 2343–2346 (1985). (Cited on pp. 3, 4)

"Relativistic plasma-wave excitation by collinear optical mixing".

[7] Y. Kitagawa, T. Matsumoto, T. Minamihata, K. Sawai, K. Matsuo, K. Mima, K. Nishihara, H. Azechi, K. A. Tanaka, H. Takabe, and S. Nakai. *Physical Review Letters* **68**, 1, pp. 48–51 (1992). (Cited on p. 3)
"Beat-wave excitation of plasma wave and observation of accelerated electrons".

[8] J Krall, A Ting, E Esarey, and P Sprangle. *Physical Review E* **48**, 3, p. 2157 (1993). (Cited on p. 4)
"Enhanced acceleration in a self-modulated-laser wake-field accelerator".

[9] K. Nakajima, D. Fisher, T. Kawakubo, H. Nakanishi, A. Ogata, et al. *Physical Review Letters* **74**, 22, pp. 4428–4431 (1995). (Cited on p. 4)
"Observation of Ultrahigh Gradient Electron Acceleration by a Self-Modulated Intense Short Laser Pulse".

[10] C. Gahn, G. D. Tsakiris, A. Pukhov, J. Meyer-Ter-Vehn, G. Pretzler, P. Thirolf, D. Habs, and K. J. Witte. *Physical Review Letters* **83**, 23, pp. 4772–4775 (1999). (Cited on p. 4)
"Multi-MeV electron beam generation by direct laser acceleration in high-density plasma channels".

[11] W. P. Leemans, J. Van Tilborg, J. Faure, C. G. R. Geddes, Cs Tóth, C. B. Schroeder, E. Esarey, G. Fubiani, and G. Dugan. *Physics of Plasmas* **11**, 5, pp. 2899–2906 (2004). (Cited on p. 4)
"Terahertz radiation from laser accelerated electron bunches".

[12] S. P. D. Mangles, C. D. Murphy, Z. Najmudin, A. G. R. Thomas, J. L. Collier, et al. *Nature* **431**, 7008, pp. 535–538 (2004). (Cited on pp. 4, 5, 15, 18, 19)
"Monoenergetic beams of relativistic electrons from intense laser–plasma interactions".

[13] C. G. R. Geddes, Cs Toth, J. van Tilborg, E. Esarey, C. B. Schroeder, D. L. Bruhwiler, C Nieter, J. Cary, and W. P. Leemans. *Nature* **431**, 7008, pp. 538–541 (2004). (Cited on pp. 4, 5, 18, 19, 49)

"High-quality electron beams from a laser wakefield accelerator using plasma-channel guiding".

[14] J. Faure, Y. Gilnec, A. Pukhov, S. Kiselev, S. Gordienko, E. Lefebvre, J. P. Rousseau, F. Burgy, and V. Malka. *Nature* **431**, 7008, pp. 541–544 (2004). (Cited on pp. 4, 5, 18, 19)
"A laser–plasma accelerator producing monoenergetic electron beams".

[15] W. P. Leemans, B. Nagler, A. J. Gonsalves, Cs. Tóth, K. Nakamura, C. G. R. Geddes, E. Esarey, C. B. Schroeder, and S. M. Hooker. *Nature Physics* **2**, 10, pp. 696–699 (2006). (Cited on pp. 4, 5, 18, 19, 49, 140)
"GeV electron beams from a centimetre-scale accelerator".

[16] Xiaoming Wang, Rafal Zgadzaj, Neil Fazel, Zhengyan Li, S. A. Yi, et al. *Nature Communications* **4**, 1988 (2013). (Cited on pp. 4, 5, 18, 19, 30)
"Quasi-monoenergetic laser-plasma acceleration of electrons to 2 GeV".

[17] Hyung Taek Kim, Ki Hong Pae, Hyuk Jin Cha, I. Jong Kim, Tae Jun Yu, Jae Hee Sung, Seong Ku Lee, Tae Moon Jeong, and Jongmin Lee. *Physical Review Letters* **111**, 16, p. 165002 (2013). (Cited on pp. 4, 5, 18, 19)
"Enhancement of electron energy to the multi-gev regime by a dual-stage laser-wakefield accelerator pumped by petawatt laser pulses".

[18] W. P. Leemans, A. J. Gonsalves, H. S. Mao, K. Nakamura, C. Benedetti, C. B. Schroeder, Cs Toth, J. Daniels, D. E. Mittelberger, S. S. Bulanov, J. L. Vay, C. G R Geddes, and E. Esarey. *Physical Review Letters* **113**, 24, p. 245002 (2014). (Cited on pp. 4, 5, 18, 19, 40, 140, 155)
"Multi-Gev electron beams from capillary-discharge-guided subpetawatt laser pulses in the self-trapping regime".

[19] A. J. Gonsalves, K. Nakamura, J. Daniels, C. Benedetti, C. Pieronek, et al. *Physical Review Letters* **122**, 8, p. 84801 (2019). (Cited on pp. 4, 5, 18, 19, 41, 49, 140)

"Petawatt Laser Guiding and Electron Beam Acceleration to 8 GeV in a Laser-Heated Capillary Discharge Waveguide".

[20] S. Karsch, J. Osterhoff, A. Popp, T. P. Rowlands-Rees, Zs Major, et al. *New Journal of Physics* **9**, 11, pp. 415–415 (2007). (Cited on pp. 5, 18, 19)
"GeV-scale electron acceleration in a gas-filled capillary discharge waveguide".

[21] Nasr A.M. Hafz, Tae Moon Jeong, Il Woo Choi, Seong Ku Lee, Ki Hong Pae, Victor V. Kulagin, Jae Hee Sung, Tae Jun Yu, Kyung Han Hong, Tomonao Hosokai, John R. Cary, Do Kyeong Ko, and Jongmin Lee. *Nature Photonics* **2**, 9, pp. 571–577 (2008). (Cited on pp. 5, 18, 19)
"Stable generation of GeV-class electron beams from self-guided laser-plasma channels".

[22] S. Kneip, S. R. Nagel, S. F. Martins, S. P. D. Mangles, C. Bellei, et al. *Physical Review Letters* **103**, 3, p. 035002 (2009). (Cited on pp. 5, 18, 19)
"Near-GeV acceleration of electrons by a nonlinear plasma wave driven by a self-guided laser pulse".

[23] C. E. Clayton, J. E. Ralph, F. Albert, R. A. Fonseca, S. H. Glenzer, et al. *Physical Review Letters* **105**, 10, p. 105003 (2010). (Cited on pp. 5, 16, 18, 19)
"Self-guided laser wakefield acceleration beyond 1 GeV using ionization-induced injection".

[24] Haiyang Lu, Mingwei Liu, Wentao Wang, Cheng Wang, Jiansheng Liu, et al. *Applied Physics Letters* **99**, 9, p. 091502 (2011). (Cited on pp. 5, 18, 19)
"Laser wakefield acceleration of electron beams beyond 1 GeV from an ablative capillary discharge waveguide".

[25] J. S. Liu, C. Q. Xia, W. T. Wang, H. Y. Lu, Ch Wang, et al. *Physical Review Letters* **107**, 3, p. 035001 (2011). (Cited on pp. 5, 18, 19)
"All-optical cascaded laser wakefield accelerator using ionization-induced injection".

[26] E. Esarey, C. B. Schroeder, and W. P. Leemans. *Reviews of Modern Physics* **81**, 3, pp. 1229–1285 (2009). (Cited on pp. 5, 6, 8, 11, 12, 143)
"Physics of laser-driven plasma-based electron accelerators".

[27] Gerard A. Mourou, Toshiki Tajima, and Sergei V. Bulanov. *Reviews of Modern Physics* **78**, 2, pp. 309–371 (2006). (Cited on p. 5)
"Optics in the relativistic regime".

[28] M. C. Downer and R. Zgadzaj. *Reviews of Modern Physics* **90**, 3, p. 35002 (2018). (Cited on p. 5)
"Diagnostics for plasma-based electron accelerators".

[29] Paul Gibbon. Imperial College Press, (2005) (Cited on pp. 6, 8)
Short pulse laser interactions with matter: an introduction, 1st Edition
ISBN: 978-1860941351

[30] W. Lu, C. Huang, M. Zhou, W. B. Mori, and T. Katsouleas. *Physical Review Letters* **96**, 16, p. 165002 (2006). (Cited on pp. 8, 15, 30)
"Nonlinear theory for relativistic plasma wakefields in the blowout regime".

[31] Eric Esarey and Mark Pilloff. *Physics of Plasmas* **2**, 5, pp. 1432–1436 (1995). (Cited on p. 8)
"Trapping and acceleration in nonlinear plasma waves".

[32] W. Lu, M. Tzoufras, C. Joshi, F. S. Tsung, W. B. Mori, J. Vieira, R. A. Fonseca, and L. O. Silva. *Physical Review Special Topics - Accelerators and Beams* **10**, 6, p. 061301 (2007). (Cited on pp. 8, 30)
"Generating multi-GeV electron bunches using single stage laser wakefield acceleration in a 3D nonlinear regime".

[33] Eric Esarey, Phillip Sprangle, Jonathan Krall, and Antonio Ting. *IEEE Journal of Quantum Electronics* **33**, 11, pp. 1879–1914 (1997). (Cited on pp. 11, 14)
"Self-focusing and guiding of short laser pulses in ionizing gases and plasmas".

[34] W. B. Mori. *IEEE Journal of Quantum Electronics* **33**, 11, pp. 1942–1953 (1997). (Cited on pp. 11–13)

"The physics of the nonlinear optics of plasmas at relativistic intensities for short-pulse lasers".

[35] Kristjan Poder. PhD thesis. Imperial College London, 2016, pp. 82–98. (Cited on pp. 12, 68, 139)

"Characterisation of self-guided laser wakefield accelerators to multi-GeV energies"

URL: `https://spiral.imperial.ac.uk/handle/10044/1/56216`

[36] Guo-Zheng Sun, Edward Ott, YC Lee, and Parvez Guzdar. *The Physics of fluids* **30**, 2, pp. 526–532 (1987). (Cited on p. 12)

"Self-focusing of short intense pulses in plasmas".

[37] A. B. Borisov, A. V. Borovskiy, V. V. Korobkin, A. M. Prokhorov, O. B. Shiryaev, X. M. Shi, T. S. Luk, A. McPherson, J. C. Solem, K. Boyer, and C. K. Rhodes. *Physical Review Letters* **68**, 15, p. 2309 (1992). (Cited on pp. 12, 29)

"Observation of relativistic and charge-displacement self-channeling of intense subpicosecond ultraviolet (248 nm) radiation in plasmas".

[38] P. Monot, T. Auguste, P. Gibbon, F. Jakober, G. Mainfray, A. Dulieu, M. Louis-Jacquet, G. Malka, and J. L. Miquel. *Physical Review Letters* **74**, 15, pp. 2953–2956 (1995). (Cited on pp. 12, 29, 48)

"Experimental demonstration of relativistic self-channeling of a multiterawatt laser pulse in an underdense plasma".

[39] K. Krushelnick, A. Ting, C. I. Moore, H. R. Burris, E. Esarey, P. Sprangle, and M. Baine. *Physical Review Letters* **78**, 21, pp. 4047–4050 (1997). (Cited on pp. 12, 29, 35)

"Plasma channel formation and guiding during high intensity short pulse laser plasma experiments".

[40] J. Schreiber, C. Bellei, S. P. D. Mangles, C. Kamperidis, S. Kneip, S. R. Nagel, C. A. J. Palmer, P. P. Rajeev, M. J. V. Streeter, and Z. Najmudin. *Physical Review Letters* **105**, 23, p. 235003 (2010). (Cited on p. 14)
"Complete temporal characterization of asymmetric pulse compression in a laser wakefield".

[41] M. J. V. Streeter, S. Kneip, M. S. Bloom, R. A. Bendoyro, O. Chekhlov, et al. *Physical Review Letters* **120**, 25, p. 254801 (2018). (Cited on pp. 14, 144)
"Observation of Laser Power Amplification in a Self-Injecting Laser Wakefield Accelerator".

[42] M. S. Bloom, M. J. V. Streeter, S. Kneip, R. A. Bendoyro, O. Cheklov, et al. *Physical Review Accelerators and Beams* **23**, 6, p. 61301 (2020). (Cited on pp. 14, 144)
"Bright x-ray radiation from plasma bubbles in an evolving laser wakefield accelerator".

[43] S. P. D. Mangles, G. Genoud, M. S. Bloom, M. Burza, Z. Najmudin, A. Persson, K. Svensson, A. G. R. Thomas, and C. G. Wahlström. *Physical Review Special Topics - Accelerators and Beams* **15**, 1, p. 011302 (2012). (Cited on pp. 15, 144)
"Self-injection threshold in self-guided laser wakefield accelerators".

[44] S. Bulanov, N. Naumova, F. Pegoraro, and J. Sakai. *Physical Review E* **58**, 5, R5257–R5260 (1998). (Cited on pp. 16, 154)
"Particle injection into the wave acceleration phase due to nonlinear wake wave breaking".

[45] H. Suk, N. Barov, J. B. Rosenzweig, and E. Esarey. *Physical Review Letters* **86**, 6, pp. 1011–1014 (2001). (Cited on p. 16)
"Plasma electron trapping and acceleration in a plasma wake field using a density transition".

[46] A. V. Brantov, T. Zh Esirkepov, M. Kando, H. Kotaki, V. Yu Bychenkov, and S. V. Bulanov. *Physics of Plasmas* **15**, 7, pp. 916–926 (2008). (Cited on p. 16)
"Controlled electron injection into the wake wave using plasma density inhomogeneity".

[47] F. Massimo, A. F. Lifschitz, C. Thaury, and V. Malka. *Plasma Physics and Controlled Fusion* **59**, 8, p. 085004 (2017). (Cited on pp. 16, 152)
"Numerical studies of density transition injection in laser wakefield acceleration".

[48] K. Schmid, A. Buck, C. M. S. Sears, J. M. Mikhailova, R. Tautz, D. Herrmann, M. Geissler, F. Krausz, and L. Veisz. *Physical Review Special Topics - Accelerators and Beams* **13**, 9, p. 091301 (2010). (Cited on p. 16)
"Density-transition based electron injector for laser driven wakefield accelerators".

[49] A. Buck, J. Wenz, J. Xu, K. Khrennikov, K. Schmid, M. Heigoldt, J. M. Mikhailova, M. Geissler, B. Shen, F. Krausz, S. Karsch, and L. Veisz. *Physical Review Letters* **110**, 18, p. 185006 (2013). (Cited on pp. 16, 18)
"Shock-front injector for high-quality laser-plasma acceleration".

[50] K. K. Swanson, H. E. Tsai, S. K. Barber, R. Lehe, H. S. Mao, S. Steinke, J. Van Tilborg, K. Nakamura, C. G. R. Geddes, C. B. Schroeder, E. Esarey, and W. P. Leemans. *Physical Review Accelerators and Beams* **20**, 5, p. 051301 (2017). (Cited on p. 16)
"Control of tunable, monoenergetic laser-plasma-accelerated electron beams using a shock-induced density downramp injector".

[51] A. Pak, K. A. Marsh, S. F. Martins, W. Lu, W. B. Mori, and C. Joshi. *Physical Review Letters* **104**, 2, p. 025003 (2010). (Cited on pp. 16, 18, 19)
"Injection and trapping of tunnel-ionized electrons into laser-produced wakes".

[52] C. McGuffey, A. G. R. Thomas, W. Schumaker, T. Matsuoka, V. Chvykov, F. J. Dollar, G. Kalintchenko, V. Yanovsky, A. Maksimchuk, K. Krushelnick, V. Yu Bychenkov, I. V. Glazyrin, and A. V. Karpeev. *Physical Review Letters* **104**, 2, p. 025004 (2010). (Cited on pp. 16, 18, 19)
"Ionization induced trapping in a laser wakefield accelerator".

[53] M. Chen, E. Esarey, C. B. Schroeder, C. G. R. Geddes, and W. P. Leemans. *Physics of Plasmas* **19**, 3, p. 033101 (2012). (Cited on pp. 16, 145)
"Theory of ionization-induced trapping in laser-plasma accelerators".

[54] J. Faure, C. Rechatin, A. Norlin, A. Lifschitz, Y. Glinec, and V. Malka. *Nature* **444**, 7120, pp. 737–739 (2006). (Cited on pp. 16, 18, 19)
"Controlled injection and acceleration of electrons in plasma wakefields by colliding laser pulses".

[55] N. Bourgeois, J. Cowley, and S. M. Hooker. *Physical Review Letters* **111**, 15, p. 155004 (2013). (Cited on pp. 17, 18, 145)
"Two-pulse ionization injection into quasilinear laser wakefields".

[56] L. L. Yu, E. Esarey, C. B. Schroeder, J. L. Vay, C. Benedetti, C. G. R. Geddes, M. Chen, and W. P. Leemans. *Physical Review Letters* **112**, 12, p. 125001 (2014). (Cited on pp. 17, 18, 145)
"Two-color laser-ionization injection".

[57] J. Götzfried, A. Döpp, M. Gilljohann, M. Foerster, H. Ding, S. Schindler, G. Schilling, A. Buck, L. Veisz, and S. Karsch. *Physical Review X* **10**, 4, p. 41015 (2020). (Cited on pp. 18, 56, 147)
"Physics of High-Charge Electron Beams in Laser-Plasma Wakefields".

[58] Andreas R. Maier, Niels M. Delbos, Timo Eichner, Lars Hübner, Sören Jalas, Laurids Jeppe, Spencer W. Jolly, Manuel Kirchen, Vincent Leroux, Philipp Messner, Matthias Schnepp, Maximilian Trunk, Paul A. Walker, Christian Werle, and Paul Winkler. *Physical Review X* **10**, 3, p. 31039 (2020). (Cited on pp. 18, 20, 41, 148)
"Decoding Sources of Energy Variability in a Laser-Plasma Accelerator".

[59] R. J. Shalloo, S. J. D. Dann, J. N. Gruse, C. I.D. Underwood, A. F. Antoine, et al. *Nature Communications* **11**, 6355 (2020). (Cited on pp. 18, 20, 126, 159)
"Automation and control of laser wakefield accelerators using Bayesian optimization".

[60] L. Rovige, J. Huijts, I. Andriyash, A. Vernier, V. Tomkus, V. Girdauskas, G. Raciukaitis, J. Dudutis, V. Stankevic, P. Gecys, M. Ouille, Z. Cheng, R. Lopez-Martens, and J. Faure. *Physical Review Accelerators and Beams* **23**, 9, p. 93401 (2020). (Cited on p. 18)

"Demonstration of stable long-term operation of a kilohertz laser-plasma accelerator".

[61] F. Salehi, M. Le, L. Railing, M. Kolesik, and H. M. Milchberg. *Physical Review X* **11**, 2, p. 021055 (2021). (Cited on p. 18)

"Laser-Accelerated, Low-Divergence 1 MeV Quasimonoenergetic Electron Bunches at 1 kHz".

[62] J. P. Couperus, R. Pausch, A. Köhler, O. Zarini, J. M. Krämer, M. Garten, A. Huebl, R. Gebhardt, U. Helbig, S. Bock, K. Zeil, A. Debus, M. Bussmann, U. Schramm, and A. Irman. *Nature Communications* **8**, 487 (2017). (Cited on pp. 18, 146)

"Demonstration of a beam loaded nanocoulomb-class laser wakefield accelerator".

[63] M. F. Gilljohann, H. Ding, A. Döpp, J. Götzfried, S. Schindler, et al. *Physical Review X* **9**, 1, p. 11046 (2019). (Cited on p. 18)

"Direct Observation of Plasma Waves and Dynamics Induced by Laser-Accelerated Electron Beams".

[64] Matthias Fuchs, Raphael Weingartner, Antonia Popp, Zsuzsanna Major, Stefan Becker, et al. *Nature Physics* **5**, 11, pp. 826–829 (2009). (Cited on pp. 18, 22)

"Laser-driven soft-X-ray undulator source".

[65] S. Kneip, C. McGuffey, F. Dollar, M. S. Bloom, V. Chvykov, et al. *Applied Physics Letters* **99**, 9, p. 093701 (2011). (Cited on pp. 18, 22)

"X-ray phase contrast imaging of biological specimens with femtosecond pulses of betatron radiation from a compact laser plasma wakefield accelerator".

[66] J. M. Cole, J. C. Wood, N. C. Lopes, K. Poder, R. L. Abel, S. Alatabi, J. S.J. Bryant, A. Jin, S. Kneip, K. Mecseki, D. R. Symes, S. P. D. Mangles, and Z. Najmudin. *Scientific Reports* **5**, 13244 (2015). (Cited on pp. 18, 22)

"Laser-wakefield accelerators as hard x-ray sources for 3D medical imaging of human bone".

[67] K. Poder, M. Tamburini, G. Sarri, A. Di Piazza, S. Kuschel, et al. *Physical Review X* **8**, 3, p. 031004 (2018). (Cited on pp. 18, 19, 48)
"Experimental Signatures of the Quantum Nature of Radiation Reaction in the Field of an Ultraintense Laser".

[68] D. H. Froula, C. E. Clayton, T. Döppner, K. A. Marsh, C. P.J. Barty, et al. *Physical Review Letters* **103**, 21, p. 215006 (2009). (Cited on pp. 18, 19)
"Measurements of the critical power for self-injection of electrons in a laser wakefield accelerator".

[69] T. P A Ibbotson, N. Bourgeois, T. P. Rowlands-Rees, L. S. Caballero, S. I. Bajlekov, et al. *Physical Review Special Topics - Accelerators and Beams* **13**, 3, p. 031301 (2010). (Cited on pp. 18, 19, 69)
"Laser-wakefield acceleration of electron beams in a low density plasma channel".

[70] B. B. Pollock, C. E. Clayton, J. E. Ralph, F. Albert, A. Davidson, et al. *Physical Review Letters* **107**, 4, p. 045001 (2011). (Cited on pp. 18, 19)
"Demonstration of a narrow energy spread, 0.5 GeV electron beam from a two-stage laser wakefield accelerator".

[71] O. Lundh, J. Lim, C. Rechatin, L. Ammoura, A. Ben-Ismaïl, X. Davoine, G. Gallot, J. P. Goddet, E. Lefebvre, V. Malka, and J. Faure. *Nature Physics* **7**, 3, pp. 219–222 (2011). (Cited on pp. 18, 19)
"Few femtosecond, few kiloampere electron bunch produced by a laser-plasma accelerator".

[72] A. J. Gonsalves, K. Nakamura, C. Lin, D. Panasenko, S. Shiraishi, T. Sokollik, C. Benedetti, C. B. Schroeder, C. G. R. Geddes, J. van Tilborg, J. Osterhoff, E. Esarey, C. Toth, and W. P. Leemans. *Nature Physics* **7**, 11, pp. 862–866 (2011). (Cited on

pp. 18, 19, 145, 151)

"Tunable laser plasma accelerator based on longitudinal density tailoring".

[73] S. Fourmaux, K. Ta Phuoc, P. Lassonde, S. Corde, G. Lebrun, V. Malka, A. Rousse, and J. C. Kieffer. *Applied Physics Letters* **101**, 11, p. 111106 (2012). (Cited on pp. 18, 19)

"Quasi-monoenergetic electron beams production in a sharp density transition".

[74] S. Kneip, C. McGuffey, J. L. Martins, M. S. Bloom, V. Chvykov, et al. *Physical Review Special Topics - Accelerators and Beams* **15**, 2, p. 021302 (2012). (Cited on pp. 18, 19)

"Characterization of transverse beam emittance of electrons from a laser-plasma wakefield accelerator in the bubble regime using betatron x-ray radiation".

[75] R. Weingartner, S. Raith, A. Popp, S. Chou, J. Wenz, K. Khrennikov, M. Heigoldt, A. R. Maier, N. Kajumba, M. Fuchs, B. Zeitler, F. Krausz, S. Karsch, and F. Grüner. *Physical Review Special Topics - Accelerators and Beams* **15**, 11, p. 111302 (2012). (Cited on pp. 18, 19)

"Ultralow emittance electron beams from a laser-wakefield accelerator".

[76] S. Chen, N. D. Powers, I. Ghebregziabher, C. M. Maharjan, C. Liu, G. Golovin, S. Banerjee, J. Zhang, N. Cunningham, A. Moorti, S. Clarke, S. Pozzi, and D. P. Umstadter. *Physical Review Letters* **110**, 15, p. 155003 (2013). (Cited on pp. 18, 19)

"MeV-energy X rays from inverse compton scattering with laser-wakefield accelerated electrons".

[77] F. Albert, B. B. Pollock, J. L. Shaw, K. A. Marsh, J. E. Ralph, Y. H. Chen, D. Alessi, A. Pak, C. E. Clayton, S. H. Glenzer, and C. Joshi. *Physical Review Letters* **111**, 23, p. 235004 (2013). (Cited on pp. 18, 19)

"Angular dependence of betatron X-ray spectra from a laser-wakefield accelerator".

[78] P. A. Walker, N. Bourgeois, W. Rittershofer, J. Cowley, N. Kajumba, et al. *New Journal of Physics* **15**, 4, p. 045024 (2013). (Cited on pp. 18, 19, 69)
"Investigation of GeV-scale electron acceleration in a gas-filled capillary discharge waveguide".

[79] S. Corde, C. Thaury, A. Lifschitz, G. Lambert, K. Ta Phuoc, X. Davoine, R. Lehe, D. Douillet, A. Rousse, and V. Malka. *Nature Communications* **4**, 2528 (2013). (Cited on pp. 18, 19)
"Observation of longitudinal and transverse self-injections in laser-plasma accelerators".

[80] M. Z. Mo, A. Ali, S. Fourmaux, P. Lassonde, J. C. Kieffer, and R. Fedosejevs. *Applied Physics Letters* **102**, 13, p. 134102 (2013). (Cited on pp. 18, 19)
"Generation of 500 MeV-1 GeV energy electrons from laser wakefield acceleration via ionization induced injection using CO2 mixed in He".

[81] G. Sarri, D. J. Corvan, W. Schumaker, J. M. Cole, A. Di Piazza, et al. *Physical Review Letters* **113**, 22, p. 224801 (2014). (Cited on pp. 18, 19)
"Ultrahigh brilliance multi-MeV γ-ray beams from nonlinear relativistic thomson scattering".

[82] S. Steinke, J. Van Tilborg, C. Benedetti, C. G. R. Geddes, C. B. Schroeder, J. Daniels, K. K. Swanson, A. J. Gonsalves, K. Nakamura, N. H. Matlis, B. H. Shaw, E. Esarey, and W. P. Leemans. *Nature* **530**, 7589, pp. 190–193 (2016). (Cited on pp. 18, 19)
"Multistage coupling of independent laser-plasma accelerators".

[83] S. Kuschel, D. Hollatz, T. Heinemann, O. Karger, M. B. Schwab, et al. *Physical Review Accelerators and Beams* **19**, 7, p. 071301 (2016). (Cited on pp. 18, 19)
"Demonstration of passive plasma lensing of a laser wakefield accelerated electron bunch".

[84] P. A. Walker, P. D. Alesini, A. S. Alexandrova, M P Anania, N. E. Andreev, et al. *Journal of Physics: Conference Series* **874**, p. 012029 (2017). (Cited on p. 18)
"Horizon 2020 EuPRAXIA design study".

[85] R. W. Assmann, M. K. Weikum, T. Akhter, D. Alesini, A. S. Alexandrova, et al. *The European Physical Journal Special Topics* **229**, 24, pp. 3675–4284 (2020). (Cited on p. 18)
"EuPRAXIA Conceptual Design Report".

[86] G. Genoud, F. Wojda, M. Burza, A. Persson, and C. G. Wahlström. *Review of Scientific Instruments* **82**, 3, p. 033102 (2011). (Cited on p. 20)
"Active control of the pointing of a multi-terawatt laser".

[87] Soren Jalas, Manuel Kirchen, Philipp Messner, Paul Winkler, Lars Hübner, Julian Dirkwinkel, Matthias Schnepp, Remi Lehe, and Andreas R. Maier. *Physical Review Letters* **126**, 10, p. 104801 (2021). (Cited on pp. 20, 126, 159)
"Bayesian Optimization of a Laser-Plasma Accelerator".

[88] S. M. Hooker, R. Bartolini, S. P. D. Mangles, A. Tünnermann, L. Corner, J. Limpert, A. Seryi, and R. Walczak. *Journal of Physics B: Atomic, Molecular and Optical Physics* **47**, 23 (2014). (Cited on p. 21)
"Multi-pulse laser wakefield acceleration: A new route to efficient, high-repetition-rate plasma accelerators and high flux radiation sources".

[89] J. Cowley, C. Thornton, C. Arran, R. J. Shalloo, L. Corner, G. Cheung, C. D. Gregory, S. P. D. Mangles, N. H. Matlis, D. R. Symes, R. Walczak, and S. M. Hooker. *Physical Review Letters* **119**, 4, p. 044802 (2017). (Cited on p. 21)
"Excitation and Control of Plasma Wakefields by Multiple Laser Pulses".

[90] O. Jakobsson, S. M. Hooker, and R. Walczak. *Physical Review Letters* **127**, 18, p. 184801 (). (Cited on p. 21)
"Gev-Scale Accelerators Driven by Plasma-Modulated Pulses from Kilohertz Lasers".

[91] C. Benedetti, C. B. Schroeder, E. Esarey, and W. P. Leemans. *Physics of Plasmas* **21**, 5 (2014). (Cited on p. 21)
"Plasma wakefields driven by an incoherent combination of laser pulses: A path towards high-average power laser-plasma accelerators".

[92] H.-P. Schlenvoigt, K. Haupt, A. Debus, F. Budde, O. Jäckel, S. Pfotenhauer, H. Schwoerer, E. Rohwer, J. G. Gallacher, E. Brunetti, R. P. Shanks, S. M. Wiggins, and D. A. Jaroszynski. *Nature Physics* **4**, 2, pp. 130–133 (2008). (Cited on p. 22)
"A compact synchrotron radiation source driven by a laser-plasma wakefield accelerator".

[93] A. R. Maier, A. Meseck, S. Reiche, C. B. Schroeder, T. Seggebrock, and F. Grüner. *Physical Review X* **2**, 3, p. 031019 (2012). (Cited on p. 22)
"Demonstration scheme for a laser-plasma-driven free-electron laser".

[94] Wentao Wang, Ke Feng, Lintong Ke, Changhai Yu, Yi Xu, et al. *Nature* **595**, 7868, pp. 516–520 (2021). (Cited on pp. 22, 155)
"Free-electron lasing at 27 nanometres based on a laser wakefield accelerator".

[95] C. B. Schroeder, E. Esarey, C. G. R. Geddes, C. Benedetti, and W. P. Leemans. *Physical Review Special Topics - Accelerators and Beams* **13**, 10, p. 101301 (2010). (Cited on p. 22)
"Physics considerations for laser-plasma linear colliders".

[96] Anna Subiel, Vadim Moskvin, Gregor H. Welsh, Silvia Cipiccia, David Reboredo, Colleen DesRosiers, and Dino A. Jaroszynski. *Physica Medica* **42**, pp. 327–331 (2017). (Cited on p. 22)
"Challenges of dosimetry of ultra-short pulsed very high energy electron beams".

[97] K. Kokurewicz, E. Brunetti, G. H. Welsh, S. M. Wiggins, M. Boyd, A. Sorensen, A. J. Chalmers, G. Schettino, A. Subiel, C. DesRosiers, and D. A. Jaroszynski. *Scientific Reports* **9**, 1, p. 10837 (2019). (Cited on p. 22)
"Focused very high-energy electron beams as a novel radiotherapy modality for producing high-dose volumetric elements".

[98] Ian Blumenfeld, Christopher E. Clayton, Franz Josef Decker, Mark J. Hogan, Chengkun Huang, et al. *Nature* **445**, 7129, pp. 741–744 (2007). (Cited on p. 23)
"Energy doubling of 42 GeV electrons in a metre-scale plasma wakefield accelerator".

[99] Spencer Gessner, Erik Adli, James M. Allen, Weiming An, Christine I. Clarke, et al. *Nature Communications* **7**, p. 11785 (2016). (Cited on p. 23)
"Demonstration of a positron beam-driven hollow channel plasma wakefield accelerator".

[100] E. Adli, A. Ahuja, O. Apsimon, R. Apsimon, A. M. Bachmann, et al. *Nature* **561**, 7723, pp. 363–367 (2018). (Cited on p. 23)
"Acceleration of electrons in the plasma wakefield of a proton bunch".

[101] R. J. Shalloo, C. Arran, L. Corner, J. Holloway, J. Jonnerby, R. Walczak, H. M. Milchberg, and S. M. Hooker. *Physical Review E* **97**, 5, p. 053203 (2018). (Cited on pp. 24, 43, 46–48, 62, 70, 95, 118)
"Hydrodynamic optical-field-ionized plasma channels".

[102] R. J. Shalloo, C. Arran, A. Picksley, A. Von Boetticher, L. Corner, J. Holloway, G. Hine, J. Jonnerby, H. M. Milchberg, C. Thornton, R. Walczak, and S. M. Hooker. *Physical Review Accelerators and Beams* **22**, 4, p. 41302 (2019). (Cited on pp. 24, 48, 62, 79, 95, 104, 110, 132, 157)
"Low-density hydrodynamic optical-field-ionized plasma channels generated with an axicon lens".

[103] Robert Shalloo. PhD thesis. University of Oxford, 2018, pp. 71–131. (Cited on pp. 26, 74, 85, 86, 109, 114, 157)
"Hydrodynamic optical-field-ionized plasma waveguides for laser plasma accelerators"
URL: `https://ora.ox.ac.uk/objects/uuid:aa7a03d0-2d64-423f-be42-40e01479d312`

[104] M. Kristiansen and M. O. Hagler. *Nuclear Fusion* **16**, 6, pp. 999–1034 (1976). (Cited on p. 27)
"Laser heating of magnetized plasmas".

[105] K. A. Janulewicz, J. J. Rocca, F. Bortolotto, M. P. Kalachnikov, V. N. Shlyaptsev, W. Sandner, and P. V. Nickles. *Physical Review A* **63**, 3, p. 033803 (2001). (Cited

on p. 27)

"Demonstration of a hybrid collisional soft-x-ray laser".

[106] A. Butler, A. J. Gonsalves, C. M. McKenna, D. J. Spence, S. M. Hooker, S. Sebban, T. Mocek, I. Bettaibi, and B. Cros. *Physical Review Letters* **91**, 20, p. 205001 (2003). (Cited on p. 27)

"Demonstration of a collisionally excited optical-field-ionization xuv laser driven in a plasma waveguide".

[107] B. Dromey, M. Zepf, M. Landreman, and S. M. Hooker. *Optics Express* **15**, 13, p. 7894 (2007). (Cited on p. 28)

"Quasi-phasematching of harmonic generation via multimode beating in waveguides".

[108] Claire Ellen Max, Jonathan Arons, and A. Bruce Langdon. *Physical Review Letters* **33**, 4, pp. 209–212 (1974). (Cited on p. 29)

"Self-modulation and self-focusing of electromagnetic waves in plasmas".

[109] P. Sprangle, A. Ting, and C. M. Tang. *Physical Review A* **36**, 6, pp. 2773–2781 (1987). (Cited on pp. 29, 30)

"Analysis of radiation focusing and steering in the free-electron laser by use of a source-dependent expansion technique".

[110] C. D. Decker, W. B. Mori, K. C. Tzeng, and T. Katsouleas. *Physics of Plasmas* **3**, 5, pp. 2047–2056 (1996). (Cited on p. 29)

"The evolution of ultra-intense, short-pulse lasers in underdense plasmas".

[111] A. G. R. Thomas, Z. Najmudin, S. P. D. Mangles, C. D. Murphy, A. E. Dangor, C. Kamperidis, K. L. Lancaster, W. B. Mori, P. A. Norreys, W. Rozmus, and K. Krushelnick. *Physical Review Letters* **98**, 9, p. 095004 (2007). (Cited on pp. 29, 30, 48)

"Effect of laser-focusing conditions on propagation and monoenergetic electron production in laser-wakefield accelerators".

[112] J. E. Ralph, K. A. Marsh, A. E. Pak, W. Lu, C. E. Clayton, F. Fang, W. B. Mori, and C. Joshi. *Physical Review Letters* **102**, 17, p. 175003 (2009). (Cited on pp. 30, 48)
"Self-guiding of ultrashort, relativistically intense laser pulses through underdense plasmas in the blowout regime".

[113] K. Poder, J. M. Cole, J. C. Wood, N. C. Lopes, S. Alatabi, et al. *Plasma Physics and Controlled Fusion* **60**, 1, p. 014022 (2018). (Cited on p. 30)
"Measurements of self-guiding of ultrashort laser pulses over long distances".

[114] C. G. Durfee and H. M. Milchberg. *Physical Review Letters* **71**, 15, pp. 2409–2412 (1993). (Cited on pp. 31, 32, 48)
"Light pipe for high intensity laser pulses".

[115] C. G. Durfee, F. Lynch, and H. M. Milchberg. *Optics Letters* **20**, 8, p. 946 (1995). (Cited on pp. 31, 32, 95, 156)
"Mode properties of a plasma waveguide for intense laser pulses: erratum".

[116] T. R. Clark and H. M. Milchberg. *Physical Review E* **61**, pp. 1954–1965 (2 2000). (Cited on pp. 32, 64, 65, 101, 120)
"Optical mode structure of the plasma waveguide".

[117] T. R. Clark and H. M. Milchberg. *Physical Review Letters* **78**, 12, pp. 2373–2376 (1997). (Cited on pp. 32, 48, 60, 70)
"Time- and space-resolved density evolution of the plasma waveguide".

[118] C. G. Durfee, T. R. Clark, and H. M. Milchberg. *Journal of the Optical Society of America B* **13**, 1, p. 59 (1996). (Cited on pp. 32, 48)
"Mode control in a two-pulse-excited plasma waveguide".

[119] S. P. Nikitin, T. M. Antonsen, T. R. Clark, Yuelin Li, and H. M. Milchberg. *Optics Letters* **22**, 23, p. 1787 (1997). (Cited on pp. 33, 48)
"Guiding of intense femtosecond pulses in preformed plasma channels".

[120] J. Fan, T. R. Clark, and H. M. Milchberg. *Applied Physics Letters* **73**, 21, pp. 3064–3066 (1998). (Cited on pp. 33, 48)

"Generation of a plasma waveguide in an elongated, high repetition rate gas jet".

[121] S. P. Nikitin, I. Alexeev, J. Fan, and H. M. Milchberg. *Physical Review E* **59**, R3839–R3842 (4 1999). (Cited on p. 33)

"High efficiency coupling and guiding of intense femtosecond laser pulses in preformed plasma channels in an elongated gas jet".

[122] K. Y. Kim, I. Alekseev, J. Fan, E. Parra, and H. M. Milchberg. *AIP Conf. Proc.* **647**, p. 646 (2002). (Cited on p. 34)

"Plasma waveguides: Addition of end funnels and generation in clustered gases".

[123] P. Volfbeyn, E. Esarey, and W. P. Leemans. *Physics of Plasmas* **6**, 5 I, pp. 2269–2277 (1999). (Cited on p. 34)

"Guiding of laser pulses in plasma channels created by the ignitor-heater technique".

[124] E. W. Gaul, S. P. Le Blanc, A. R. Rundquist, R. Zgadzaj, H. Langhoff, and M. C. Downer. *Applied Physics Letters* **77**, 25, pp. 4112–4114 (2000). (Cited on p. 34)

"Production and characterization of a fully ionized He plasma channel".

[125] T. Ditmire, R. A. Smith, and M. H. R. Hutchinson. *Optics Letters* **23**, 5, p. 322 (1998). (Cited on pp. 35, 48)

"Plasma waveguide formation in predissociated clustering gases".

[126] V. Kumarappan, K. Y. Kim, and H. M. Milchberg. *Physical Review Letters* **94**, p. 205004 (20 2005). (Cited on pp. 35, 48)

"Guiding of Intense Laser Pulses in Plasma Waveguides Produced from Efficient, Femtosecond End-Pumped Heating of Clustered Gases".

[127] H. M. Milchberg, S. J. McNaught, and E. Parra. *Physical Review E* **64**, p. 056402 (5 2001). (Cited on p. 35)

"Plasma hydrodynamics of the intense laser-cluster interaction".

[128] I. Alexeev, T. M. Antonsen, K. Y. Kim, and H. M. Milchberg. *Physical Review Letters* **90**, 10, p. 4 (2003). (Cited on p. 35)
"Self-Focusing of Intense Laser Pulses in a Clustered Gas".

[129] H. Sheng, K. Y. Kim, V. Kumarappan, B. D. Layer, and H. M. Milchberg. *Physical Review E - Statistical, Nonlinear, and Soft Matter Physics* **72**, 3, p. 036411 (2005). (Cited on pp. 35, 48, 59)
"Plasma waveguides efficiently generated by Bessel beams in elongated cluster gas jets".

[130] A Ting, CI Moore, K Krushelnick, C Manka, E Esarey, P Sprangle, R Hubbard, HR Burris, R Fischer, and M Baine. *Physics of Plasmas* **4**, 5, pp. 1889–1899 (1997). (Cited on p. 35)
"Plasma wakefield generation and electron acceleration in a self-modulated laser wakefield accelerator experiment".

[131] K. Krushelnick, E. L. Clark, Z. Najmudin, M. Salvati, M. I. K. Santala, M. Tatarakis, A. E. Dangor, V. Malka, D. Neely, R. Allott, and C. Danson. *Phys. Rev. Lett.* **83**, pp. 737–740 (4 1999). (Cited on p. 36)
"Multi-MeV Ion Production from High-Intensity Laser Interactions with Underdense Plasmas".

[132] S. Fritzler, Z. Najmudin, V. Malka, K. Krushelnick, C. Marle, B. Walton, M. S. Wei, R. J. Clarke, and A. E. Dangor. *Phys. Rev. Lett.* **89**, p. 165004 (16 2002). (Cited on p. 36)
"Ion Heating and Thermonuclear Neutron Production from High-Intensity Subpicosecond Laser Pulses Interacting with Underdense Plasmas".

[133] M. S. Wei, S. P. D. Mangles, Z. Najmudin, B. Walton, A. Gopal, et al. *Phys. Rev. Lett.* **93**, p. 155003 (15 2004). (Cited on p. 36)
"Ion Acceleration by Collisionless Shocks in High-Intensity-Laser–Underdense-Plasma Interaction".

[134] S. Jackel and R. Burris and J. Grun and A. Ting and C. Manka and K. Evans and J. Kosakowskii. *Optics Letters* **20**, 10, pp. 1086–1088 (1995). (Cited on pp. 36, 37)
"Channeling of terawatt laser pulses by use of hollow waveguides".

[135] F. Dorchies, J. R. Marquès, B. Cros, G. Matthieussent, C. Courtois, T. Vélikoroussov, P. Audebert, J. P. Geindre, S. Rebibo, G. Hamoniaux, and F. Amiranoff. *Physical Review Letters* **82**, 23, pp. 4655–4658 (1999). (Cited on pp. 36, 38, 48)
"Monomode guiding of 1016W/cm2 laser pulses over 100 rayleigh lengths in hollow capillary dielectric tubes".

[136] C. Courtois, A. Couairon, B. Cros, J. R. Marquès, and G. Matthieussent. *Physics of Plasmas* **8**, 7, pp. 3445–3456 (2001). (Cited on p. 36)
"Propagation of intense ultrashort laser pulses in a plasma filled capillary tube: Simulations and experiments".

[137] B. Cros, C. Courtois, G. Matthieussent, A. Di Bernardo, D. Batani, N. Andreev, and S. Kuznetsov. *Physical Review E* **65**, 2, p. 026405 (2002). (Cited on pp. 37, 38)
"Eigenmodes for capillary tubes with dielectric walls and ultraintense laser pulse guiding".

[138] G. Genoud, K. Cassou, F. Wojda, H. E. Ferrari, C. Kamperidis, M. Burza, A. Persson, J. Uhlig, S. Kneip, S. P. D. Mangles, A. Lifschitz, B. Cros, and C. G. Wahlström. *Applied Physics B: Lasers and Optics* **105**, 2, pp. 309–316 (2011). (Cited on p. 38)
"Laser-plasma electron acceleration in dielectric capillary tubes".

[139] M. Hansson, L. Senje, A. Persson, O. Lundh, C. G. Wahlström, F. G. Desforges, J. Ju, T. L. Audet, B. Cros, S. Dobosz Dufrénoy, and P. Monot. *Physical Review Special Topics - Accelerators and Beams* **17**, 3, p. 031303 (2014). (Cited on p. 38)
"Enhanced stability of laser wakefield acceleration using dielectric capillary tubes".

[140] Tomonao Hosokai, Masaki Kando, Hideki Dewa, Hideyuki Kotaki, Syuji Kondo, Noboru Hasegawa, Kazuhisa Nakajima, and Kazuhiko Horioka. *Optics Letters* **25**, 1, pp. 10–12 (2000). (Cited on p. 39)

"Optical guidance of terrawatt laser pulses by the implosion phase of a fast Z-pinch discharge in a gas-filled capillary".

[141] Tomonao Hosokai, Masaki Kando, Hideki Dewa, Hideyuki Kotaki, Syuji Kondo, Noboru Hasegawa, Kazuhiko Horioka, and Kazuhisa Nakajima. *Nuclear Instruments and Methods in Physics Research, Section A: Accelerators, Spectrometers, Detectors and Associated Equipment* **455**, 1, pp. 155–160 (2000). (Cited on p. 39)
"Fast Z-pinch optical guiding for laser wakefield acceleration".

[142] Y. Ehrlich, C. Cohen, A. Zigler, J. Krall, P. Sprangle, and E. Esarey. *Physical Review Letters* **77**, 20, pp. 4186–4189 (1996). (Cited on p. 39)
"Guiding of high intensity laser pulses in straight and curved plasma channel experiments".

[143] A. Zigler, Y. Ehrlich, C. Cohen, J. Krall, and P. Sprangle. *Journal of the Optical Society of America B* **13**, 1, p. 68 (1996). (Cited on p. 39)
"Optical guiding of high-intensity laser pulses in a long plasma channel formed by a slow capillary discharge".

[144] Y. Ehrlich, C. Cohen, D. Kaganovich, A. Zigler, R. F. Hubbard, P. Sprangle, and E. Esarey. *Journal of the Optical Society of America B* **15**, 9, p. 2416 (1998). (Cited on p. 39)
"Guiding and damping of high-intensity laser pulses in long plasma channels".

[145] D. Kaganovich, A. Ting, C. I. Moore, A. Zigler, H. R. Burris, Y. Ehrlich, R. Hubbard, and P. Sprangle. *Physical Review E* **59**, 5, R4769–R4772 (1999). (Cited on p. 39)
"High efficiency guiding of terawatt subpicosecond laser pulses in a capillary discharge plasma channel".

[146] D. J. Spence, A. Butler, and S. M. Hooker. *Journal of Physics B: Atomic, Molecular and Optical Physics* **34**, 21, pp. 4103–4112 (2001). (Cited on p. 39)
"First demonstration of guiding of high-intensity laser pulses in a hydrogen-filled capillary discharge waveguide".

[147] D. J. Spence and S. M. Hooker. *Physical Review E - Statistical, Nonlinear, and Soft Matter Physics* **63**, 1 II, p. 015401 (2001). (Cited on p. 39)
"Investigation of a hydrogen plasma waveguide".

[148] D. J. Spence, A. Butler, and S. M. Hooker. *Journal of the Optical Society of America B* **20**, 1, pp. 138–151 (2003). (Cited on pp. 39, 48)
"Gas-filled capillary discharge waveguides".

[149] A. Butler, D. J. Spence, and S. M. Hooker. *Physical Review Letters* **89**, 18 (2002). (Cited on pp. 39, 40, 48)
"Guiding of High-Intensity Laser Pulses with a Hydrogen-Filled Capillary Discharge Waveguide".

[150] Kate Greene. *World Record for Compact Particle Accelerator* (Cited on p. 40). 2014 URL: https://newscenter.lbl.gov/2014/12/08/world-record-for-compact-particle-accelerator/.

[151] N. A. Bobrova, A. A. Esaulov, J. I. Sakai, P. V. Sasorov, D. J. Spence, A. Butler, S. M. Hooker, and S. V. Bulanov. *Physical Review E* **65**, 1, p. 016407 (2002). (Cited on p. 39)
"Simulations of a hydrogen-filled capillary discharge waveguide".

[152] A. J. Gonsalves, T. P. Rowlands-Rees, B. H P Broks, J. J A M Van Der Mullen, and S. M. Hooker. *Physical Review Letters* **98**, 2, p. 025002 (2007). (Cited on pp. 40, 41, 48, 70)
"Transverse interferometry of a hydrogen-filled capillary discharge waveguide".

[153] B. H. P. Broks, K. Garloff, and J. J.A.M. Van Der Mullen. *Physical Review E - Statistical, Nonlinear, and Soft Matter Physics* **71**, 1, p. 016401 (2005). (Cited on p. 40)
"Nonlocal-thermal-equilibrium model of a pulsed capillary discharge waveguide".

[154] M. Turner, A. J. Gonsalves, S. S. Bulanov, C. Benedetti, N. A. Bobrova, V. A. Gasilov, P. V. Sasorov, G. Korn, K. Nakamura, J. Van Tilborg, C. G. Geddes, C. B. Schroeder, and E. Esarey. *High Power Laser Science and Engineering* **9**, May, pp. 1–10 (2021). (Cited on p. 40)

"Radial density profile and stability of capillary discharge plasma waveguides of lengths up to 40 cm".

[155] A. J. Gonsalves, F. Liu, N. A. Bobrova, P. V. Sasorov, C. Pieronek, J. Daniels, S. Antipov, J. E. Butler, S. S. Bulanov, W. L. Waldron, D. E. Mittelberger, and W. P. Leemans. *Journal of Applied Physics* **119**, 3, p. 033302 (2016). (Cited on p. 41)

"Demonstration of a high repetition rate capillary discharge waveguide".

[156] N. A. Bobrova, P. V. Sasorov, C. Benedetti, S. S. Bulanov, C. G. R. Geddes, C. B. Schroeder, E. Esarey, and W. P. Leemans. *Physics of Plasmas* **20**, 2, p. 020703 (2013). (Cited on p. 41)

"Laser-heater assisted plasma channel formation in capillary discharge waveguides".

[157] A. J. Gonsalves, K. Nakamura, C. Benedetti, C. V. Pieronek, S. Steinke, et al. *Physics of Plasmas* **27**, 5, p. 053102 (2020). (Cited on pp. 42, 140, 148)

"Laser-heated capillary discharge plasma waveguides for electron acceleration to 8 GeV".

[158] G. A. Bagdasarov, N. A. Bobrova, O. G. Olkhovskaya, V. A. Gasilov, C. Benedetti, S. S. Bulanov, A. J. Gonsalves, C. V. Pieronek, J. Van Tilborg, C. G. R. Geddes, C. B. Schroeder, P. V. Sasorov, S. V. Bulanov, G. Korn, and E. Esarey. *Physics of Plasmas* **28**, 5 (2021). (Cited on p. 42)

"Creation of an axially uniform plasma channel in a laser-assisted capillary discharge".

[159] L. V. Keldysh. *Sov. Phys. JETP* **20**, 5, pp. 1307–1314 (1965). (Cited on p. 43)

"Ionization in the field of a strong electromagnetic wave".

[160] N. H. Burnett and P. B. Corkum. *Journal of the Optical Society of America B* **6**, 6, p. 1195 (1989). (Cited on p. 43)

"Cold-plasma production for recombination extreme-ultraviolet lasers by optical-field-induced ionization".

[161] P. B. Corkum, N. H. Burnett, and F. Brunel. *Physical Review Letters* **62**, 11, pp. 1259–1262 (1989). (Cited on pp. 43–45)
"Above-threshold ionization in the long-wavelength limit".

[162] R. R. Freeman and P. H. Bucksbaum. *Journal of Physics B: Atomic, Molecular and Optical Physics* **24**, 2, pp. 325–347 (1991). (Cited on p. 44)
"Investigations of above-threshold ionization using subpicosecond laser pulses".

[163] A. Perelomov, V. Popov, and M. Terent'ev. *Soviet Journal of Experimental and Theoretical Physics* **23**, 5, p. 924 (1966). (Cited on p. 45)
"Ionization of Atoms in an Alternating Electric Field".

[164] Maxim V Ammosov, Nikolai B Delone, and Vladimir P Krainov. *Sov. Phys. JETP* **64**, 3, pp. 1191–1194 (1986). (Cited on p. 45)
"Tunnel Ionization Of Complex Atoms And Atomic Ions In Electromagnetic Field".

[165] B. Fryxell, K. Olson, P. Ricker, F. X. Timmes, M. Zingale, D. Q. Lamb, P. MacNeice, R. Rosner, J. W. Truran, and H. Tufo. *The Astrophysical Journal Supplement Series* **131**, 1, pp. 273–334 (2000). (Cited on pp. 46, 116)
"FLASH: An Adaptive Mesh Hydrodynamics Code for Modeling Astrophysical Thermonuclear Flashes".

[166] J. J. MacFarlane, I. E. Golovkin, and P.R. Woodruff. *Journal of Quantitative Spectroscopy and Radiative Transfer* **99**, 1-3, pp. 381–397 (2006). (Cited on pp. 46, 95, 116)
"Helios-CR — a 1-D radiation- magnetohydrodynamics code with inline atomic kinetics modeling".

[167] Lyman Spitzer. Courier Corporation, (2006) (Cited on pp. 46, 47)
Physics of fully ionized gases, 2nd Edition
ISBN: 978-0486449821

[168] N. Lemos, T. Grismayer, L. Cardoso, J. Geada, G. Figueira, and J. M. Dias. *Physics of Plasmas* **20**, 10, p. 103109 (2013). (Cited on pp. 47, 48)
"Effects of laser polarization in the expansion of plasma waveguides".

[169] N. Lemos, T. Grismayer, L. Cardoso, G. Figueira, R. Issac, D. A. Jaroszynski, and J. M. Dias. *Physics of Plasmas* **20**, 6, p. 063102 (2013). (Cited on pp. 47, 48)
"Plasma expansion into a waveguide created by a linearly polarized femtosecond laser pulse".

[170] N. Lemos, L. Cardoso, J. Geada, G. Figueira, F. Albert, and J. M. Dias. *Scientific Reports* **8**, 1, p. 3165 (2018). (Cited on pp. 47, 70)
"Guiding of laser pulses in plasma waveguides created by linearly-polarized femtosecond laser pulses".

[171] J. Lynch C. Durfree and H. Milchberg. *Physical Review E* **51**, 3, pp. 2368–2387 (1995). (Cited on pp. 48, 98)
"Development of a plasma waveguide for high intensity laser pulses".

[172] C. E. Clayton, K. C. Tzeng, D. Gordon, P. Muggli, W. B. Mori, C. Joshi, V. Malka, Z. Najmudin, A. Modena, D. Neely, and A. E. Dangor. *Physical Review Letters* **81**, 1, pp. 100–103 (1998). (Cited on p. 48)
"Plasma wave generation in a self-focused channel of a relativistically intense laser pulse".

[173] W. P. Leemans, B. Nagler, A. J. Gonsalves, Cs Tóth, K. Nakamura, C. G R Geddes, E. Esarey, C. B. Schroeder, and S. M. Hooker. *Nature Physics* **2**, 10, pp. 696–699 (2006). (Cited on p. 48)
"GeV electron beams from a centimetre-scale accelerator".

[174] Sterling Backus, Charles G. Durfee, Margaret M. Murnane, and Henry C. Kapteyn. *Review of Scientific Instruments* **69**, 3, pp. 1207–1223 (1998). (Cited on p. 51)
"High power ultrafast lasers".

[175] Colin N. Danson, Constantin Haefner, Jake Bromage, Thomas Butcher, Jean Christophe F. Chanteloup, et al. *High Power Laser Science and Engineering* **7**, March (2019). (Cited on p. 51)
"Petawatt and exawatt class lasers worldwide".

[176] Donna Strickland and Gerard Mourou. *Optics Communications* **56**, 3, pp. 219–221 (1985). (Cited on p. 51)
"Compression of amplified chirped optical pulses".

[177] Gerard Mourou. *Reviews of Modern Physics* **91**, 3, p. 30501 (2019). (Cited on p. 51)
"Nobel Lecture: Extreme light physics and application".

[178] Donna Strickland. *Reviews of Modern Physics* **91**, 3, p. 30502 (2019). (Cited on p. 51)
"Nobel Lecture: Generating high-intensity ultrashort optical pulses".

[179] Simon Martin Hooker and Colin E Webb. Oxford University Press, (2010) (Cited on p. 51)
Laser Physics, 1st Edition
ISBN: 978-0198506928

[180] Joseph W Goodman. Roberts and Company Publishers, (2005) (Cited on p. 52)
Introduction to Fourier optics, 3rd Edition
ISBN: 978-0974707723

[181] B. Beaurepaire, A. Vernier, M. Bocoum, F. Böhle, A. Jullien, J. P. Rousseau, T. Lefrou, D. Douillet, G. Iaquaniello, R. Lopez-Martens, A. Lifschitz, and J. Faure. *Physical Review X* **5**, 3, p. 031012 (2015). (Cited on p. 53)
"Effect of the laser wave front in a laser-plasma accelerator".

[182] J. Vieira, S. F. Martins, F. Fiúza, C. K. Huang, W. B. Mori, S. P. D. Mangles, S. Kneip, S. Nagel, Z. Najmudin, and L. O. Silva. *Plasma Physics and Controlled Fusion* **54**, 5 (2012). (Cited on p. 53)
"Influence of realistic parameters on state-of-the-art laser wakefield accelerator experiments".

[183] *Lasers and laser-related equipment — Test methods for laser beam widths, divergence angles and beam propagation ratios — Part 3: Intrinsic and geometrical laser beam classification, propagation and details of test methods* (Cited on p. 54). 2004

[184] K. W. DeLong, R. Trebino, J. Hunter, and W .E. White. *Journal of the Optical Society of America B* **11**, 11, pp. 2206–2215 (1994). (Cited on p. 54)
"Frequency-resolved optical gating with the use of second-harmonic generation".

[185] C. Iaconis and I. A. Walmsley. *Optics Letters* **23**, 10, pp. 792–794 (1998). (Cited on pp. 54, 55)
"Spectral phase interferometry for direct electric-field reconstruction of ultrashort optical pulses".

[186] Rick Trebino. *Nature Photonics* **5**, 4, pp. 189–192 (2011). (Cited on p. 54)
"Measuring the seemingly immeasurable".

[187] Miguel Miranda, Cord L. Arnold, Thomas Fordell, Francisco Silva, Benjamín Alonso, Rosa Weigand, Anne L'Huillier, and Helder Crespo. *Optics Express* **20**, 17, p. 18732 (2012). (Cited on p. 54)
"Characterization of broadband few-cycle laser pulses with the d-scan technique".

[188] D. J. Kane and R. Trebino. *Ieee Journal of Quantum Electronics* **29**, 2, pp. 571–579 (1993). (Cited on p. 54)
"Characterization of Arbitrary Femtosecond Pulses Using Frequency-Resolved Optical Gating".

[189] A. Borot and F. Quéré. *Optics Express* **26**, 20, p. 26444 (2018). (Cited on p. 55)
"Spatio-spectral metrology at focus of ultrashort lasers: a phase-retrieval approach: erratum".

[190] G. Pariente, V. Gallet, A. Borot, O. Gobert, and F. Quéré. *Nature Photonics* **10**, 8, pp. 547–553 (2016). (Cited on p. 55)
"Space-time characterization of ultra-intense femtosecond laser beams".

[191] S. P. D. Mangles, G. Genoud, S. Kneip, M. Burza, K. Cassou, B. Cros, N. P. Dover, C. Kamperidis, Z. Najmudin, A. Persson, J. Schreiber, F. Wojda, and C. G. Wahlström. *Applied Physics Letters* **95**, 18, p. 181106 (2009). (Cited on p. 55)
"Controlling the spectrum of x-rays generated in a laser-plasma accelerator by tailoring the laser wavefront".

[192] G. Genoud, M. S. Bloom, J. Vieira, M. Burza, Z. Najmudin, A. Persson, L. O. Silva, K. Svensson, C. G. Wahlström, and S. P. D. Mangles. *Physics of Plasmas* **20**, 6, p. 064501 (2013). (Cited on p. 55)
"Increasing energy coupling into plasma waves by tailoring the laser radial focal spot distribution in a laser wakefield accelerator".

[193] A. J. Ross, A. Alejo, A. von Boetticher, J. Cowley, J. Holloway, J. Jonnerby, A. Picksley, R. Walczak, and S. M. Hooker. *Journal of Physics: Conference Series* **1596**, p. 012049 (2020). (Cited on pp. 58, 82)
"Numerical modelling of chromatic effects on axicon-focused beams used to generate HOFI plasma channels".

[194] František Batysta, Roman Antipenkov, Jonathan T. Green, Jack A. Naylon, Jakub Novák, Tomáš Mazanec, Petr Hříbek, Charalampos Zervos, Pavel Bakule, and Bedřich Rus. *Optics Express* **22**, 24, p. 30281 (2014). (Cited on p. 61)
"Pulse synchronization system for picosecond pulse-pumped OPCPA with femtosecond-level relative timing jitter".

[195] Leonid I Sedov. *Prikl. Mat. Mekh* **10**, 2, pp. 241–250 (1946). (Cited on p. 61)
"Propagation of strong blast waves".

[196] Sir Geoffrey Taylor. *Proceedings of the Royal Society of London. Series A. Mathematical and Physical Sciences* **201**, 1065, pp. 175–186 (1950). (Cited on p. 61)
"The formation of a blast wave by a very intense explosion. - II. The atomic explosion of 1945".

[197] Gregory J. Hutchens. *Journal of Applied Physics* **88**, 6, pp. 3654–3658 (2000). (Cited on pp. 62, 95, 116)
"Approximate near-field blast theory: A generalized approach".

[198] B. Miao, L. Feder, J. E. Shrock, A. Goffin, and H. M. Milchberg. *Physical Review Letters* **125**, 7, p. 74801 (2020). (Cited on pp. 62, 86, 127, 130, 148)
"Optical Guiding in Meter-Scale Plasma Waveguides".

[199] T. D. Arber, K. Bennett, C. S. Brady, A. Lawrence-Douglas, M. G. Ramsay, N. J. Sircombe, P. Gillies, R. G. Evans, H. Schmitz, A. R. Bell, and C. P. Ridgers. *Plasma Physics and Controlled Fusion* **57**, 11, p. 113001 (2015). (Cited on p. 68)
"Contemporary particle-in-cell approach to laser-plasma modelling".

[200] W. P. Huang, C. L. Xu, W. Lui, and K. Yokoyama. *IEEE Photonics Technology Letters* **8**, 5, pp. 649–651 (1996). (Cited on p. 68)
"The perfectly matched layer (PML) boundary condition for the beam propagation method".

[201] Alistair Lawrence-Douglas. PhD thesis. University of Warwick, 2013, pp. 53–81. (Cited on p. 68)
"Ionisation effects for laser-plasma interactions by particle-in-cell code"
URL: `http://wrap.warwick.ac.uk/57465/`

[202] A. F. Lifschitz, X. Davoine, E. Lefebvre, J. Faure, C. Rechatin, and V. Malka. *Journal of Computational Physics* **228**, 5, pp. 1803–1814 (2009). (Cited on p. 69)
"Particle-in-Cell modelling of laser-plasma interaction using Fourier decomposition".

[203] Rémi Lehe, Manuel Kirchen, Igor A. Andriyash, Brendan B. Godfrey, and Jean Luc Vay. *Computer Physics Communications* **203**, pp. 66–82 (2016). (Cited on pp. 69, 117)
"A spectral, quasi-cylindrical and dispersion-free Particle-In-Cell algorithm".

[204] A. T. Lin, J. M. Dawson, and H. Okuda. *Physics of Fluids* **17**, 11, pp. 1995–2001 (1974). (Cited on p. 69)
"Application of electromagnetic particle simulation to the generation of electromagnetic radiation".

[205] Q. H. Liu. *Microwave and Optical Technology Letters* **15**, 3, pp. 158–165 (1997). (Cited on p. 69)
"The PSTD algorithm: A time-domain method requiring only two cells per wavelength".

[206] J. L. Vay. *Physical Review Letters* **98**, 13, p. 130405 (2007). (Cited on p. 69)
"Noninvariance of space- and time-scale ranges under a Lorentz transformation and the implications for the study of relativistic interactions".

[207] J. L. Vay, C. G. R. Geddes, E. Esarey, C. B. Schroeder, W. P. Leemans, E. Cormier-Michel, and D. P. Grote. *Physics of Plasmas* **18**, 12, p. 123103 (2011). (Cited on pp. 69, 140)
"Modeling of 10 GeV-1 TeV laser-plasma accelerators using Lorentz boosted simulations".

[208] Pradipta Kumar Panigrahi and Krishnamurthy Muralidhar. Springer, (2012) (Cited on p. 70)
Schlieren and shadowgraph methods in heat and mass transfer, 2nd Edition
ISBN: 978-1461445340

[209] Alexander Buck, Maria Nicolai, Karl Schmid, Chris M. S. Sears, Alexander Sävert, Julia M. Mikhailova, Ferenc Krausz, Malte C. Kaluza, and Laszlo Veisz. *Nature Physics* **7**, 7, pp. 543–548 (2011). (Cited on p. 70)
"Real-time observation of laser-driven electron acceleration".

[210] M. B. Schwab, A. Sävert, O. Jäckel, J. Polz, M. Schnell, T. Rinck, L. Veisz, M. Möller, P. Hansinger, G. G. Paulus, and M. C. Kaluza. *Applied Physics Letters* **103**, 19, p. 191118 (2013). (Cited on p. 70)
"Few-cycle optical probe-pulse for investigation of relativistic laser-plasma interactions".

[211] G. R. Plateau, N. H. Matlis, C. G. R. Geddes, A. J. Gonsalves, S. Shiraishi, C. Lin, R. A. Van Mourik, and W. P. Leemans. *Review of Scientific Instruments* **81**, 3, p. 033108 (2010). (Cited on p. 70)
"Wavefront-sensor-based electron density measurements for laser-plasma accelerators".

[212] J. van Tilborg, A. J. Gonsalves, E. H. Esarey, C. B. Schroeder, and W. P. Leemans. *Optics Letters* **43**, 12, pp. 2776–2779 (2018). (Cited on p. 70)
"Density characterization of discharged gas-filled capillaries through common-path two-color spectral-domain interferometry".

[213] J. Van Tilborg, A. J. Gonsalves, E. Esarey, C. B. Schroeder, and W. P. Leemans. *Physics of Plasmas* **26**, 2, p. 023106 (2019). (Cited on p. 70)
"High-sensitivity plasma density retrieval in a common-path second-harmonic interferometer through simultaneous group and phase velocity measurement".

[214] J. Daniels, J. Van Tilborg, A. J. Gonsalves, C. B. Schroeder, C. Benedetti, E. Esarey, and W. P. Leemans. *Physics of Plasmas* **22**, 7, p. 073112 (2015). (Cited on p. 70)
"Plasma density diagnostic for capillary-discharge based plasma channels".

[215] Fernando Brandi and Leonida Antonio Gizzi. *High Power Laser Science and Engineering* **7**, pp. 6–8 (2019). (Cited on p. 70)

"Optical diagnostics for density measurement in high-quality laser-plasma electron accelerators".

[216] J. M. Garland, G. Tauscher, S. Bohlen, G. J. Boyle, R. D'Arcy, L. Goldberg, K. Põder, L. Schaper, B. Schmidt, and J. Osterhoff. *Review of Scientific Instruments* **92**, 1, p. 013505 (2021). (Cited on p. 70)
"Combining laser interferometry and plasma spectroscopy for spatially resolved high-sensitivity plasma density measurements in discharge capillaries".

[217] Jason Mark Cole. PhD thesis. Imperial College London, 2016. (Cited on p. 72)
"Diagnosis and application of laser wakefield accelerators"
URL: `https://spiral.imperial.ac.uk/handle/10044/1/42222`

[218] Mitsuo Takeda, Hideki Ina, and Seiji Kobayashi. *Journal of the Optical Society of America* **72**, 1, p. 156 (1982). (Cited on pp. 74, 110)
"Fourier-transform method of fringe-pattern analysis for computer-based topography and interferometry".

[219] Paolo Tomassini, Antonio Giulietti, Leonida A. Gizzi, Marco Galimberti, Danilo Giulietti, Marco Borghesi, and Oswald Willi. *Applied Optics* **40**, 35, p. 6561 (2001). (Cited on p. 74)
"Analyzing laser plasma interferograms with a continuous wavelet transform ridge extraction technique: the method".

[220] Richard M. Goldstein, Howard A. Zebker, and Charles L. Werner. *Radio Science* **23**, 4, pp. 713–720 (1988). (Cited on p. 77)
"Satellite radar interferometry: Two-dimensional phase unwrapping".

[221] Miguel Arevallilo Herráez, David R. Burton, Michael J. Lalor, and Munther A. Gdeisat. *Applied Optics* **41**, 35, p. 7437 (2002). (Cited on pp. 77, 78)
"Fast two-dimensional phase-unwrapping algorithm based on sorting by reliability following a noncontinuous path".

[222] Dennis C Ghiglia and Mark D Pritt. Vol. 4. Wiley New York, (1998) (Cited on p. 77)
Two-dimensional phase unwrapping: theory, algorithms, and software, 1st Edition
ISBN: 978-0471249351

[223] M. F. Kasim. *Fast 2D phase unwrapping implementation in MATLAB* (Cited on p. 77). `https://github.com/mfkasim91/unwrap_phase/`. 2017

[224] Kei Nakamura, Hann Shin Mao, Anthony J. Gonsalves, Henri Vincenti, Daniel E. Mittelberger, Joost Daniels, Arturo Magana, Csaba Toth, and Wim P. Leemans. *IEEE Journal of Quantum Electronics* **53**, 4, pp. 1–21 (2017). (Cited on p. 100)
"Diagnostics, Control and Performance Parameters for the BELLA High Repetition Rate Petawatt Class Laser".

[225] N. Delbos, C. Werle, I. Dornmair, T. Eichner, L. Hübner, S. Jalas, S. W. Jolly, M. Kirchen, V. Leroux, P. Messner, M. Schnepp, M. Trunk, P. A. Walker, P. Winkler, and A. R. Maier. *Nuclear Instruments and Methods in Physics Research, Section A: Accelerators, Spectrometers, Detectors and Associated Equipment* **909**, January, pp. 318–322 (2018). (Cited on p. 100)
"LUX – A laser–plasma driven undulator beamline".

[226] D. A. Dimitrov, R. E. Giacone, D. L. Bruhwiler, R. Busby, J. R. Cary, C. G. R. Geddes, E. Esarey, and W. P. Leemans. *Physics of Plasmas* **14**, 4, p. 043105 (2007). (Cited on pp. 103, 132)
"Coupling of laser energy into plasma channels".

[227] Jianzhou Wu, James H. Cooley, Thomas M. Antonsen, and Howard M. Milchberg. *Physics of Plasmas* **12**, p. 043105 (2005). (Cited on p. 103)
"Effective coupling of ultra-intense laser pulses to funnel-mouthed plasma waveguides".

[228] A. Picksley, A. Alejo, R. J. Shalloo, C. Arran, A. von Boetticher, L. Corner, J. A. Holloway, J. Jonnerby, O. Jakobsson, C. Thornton, R. Walczak, and S. M. Hooker.

Physical Review E **102**, 5, p. 53201 (2020). (Cited on pp. 107, 116)
"Meter-Scale, Conditioned Hydrodynamic Optical-Field-Ionized Plasma Channels".

[229] Wolfgang Lotz. *Zeitschrift für Physik* **216**, 3, pp. 241–247 (1968). (Cited on p. 113)
"Electron-impact ionization cross-sections and ionization rate coefficients for atoms and ions from hydrogen to calcium".

[230] *FLASH 4.6.2 User Guide - Section 13* (Cited on p. 116). `http://flash.uchicago.edu/site/flashcode/user_support/`. 2019

[231] J. Jonnerby, N. Bourgeois, L. Corner, J. Holloway, A. Picksley, A. J. Ross, R. Walczak, and S. M. Hooker. *Measurements of Ion Motion in Laser Wakefield Accelerators, In preparation* (Cited on p. 120)

[232] S. V. Bulanov, I. N. Inovenkov, V. I. Kirsanov, N. M. Naumova, and A. S. Sakharov. *Physics of Fluids B* **4**, 7, pp. 1935–1942 (1992). (Cited on p. 122)
"Nonlinear depletion of ultrashort and relativistically strong laser pulses in an underdense plasma".

[233] C. B. Schroeder, E. Esarey, C. Benedetti, and W. P. Leemans. *Physics of Plasmas* **20**, 8, p. 080701 (2013). (Cited on p. 125)
"Control of focusing forces and emittances in plasma-based accelerators using near-hollow plasma channels".

[234] S. J. D. Dann, C. D. Baird, N. Bourgeois, O. Chekhlov, S. Eardley, et al. *Physical review accelerators and beams* **22**, 4, p. 041303 (2019). (Cited on p. 126)
"Laser wakefield acceleration with active feedback at 5 Hz".

[235] L. Feder, B. Miao, J. E. Shrock, A. Goffin, and H. M. Milchberg. *Physical Review Research* **2**, 4, p. 43173 (2020). (Cited on pp. 127, 130, 141, 158)
"Self-waveguiding of relativistic laser pulses in neutral gas channel".

[236] A. Picksley, A. Alejo, J. Cowley, N. Bourgeois, L. Corner, L. Feder, J. Holloway, H. Jones, J. Jonnerby, H. M. Milchberg, L. R. Reid, A. J. Ross, R. Walczak, and S. M. Hooker. *Physical Review Accelerators and Beams* **23**, 8, p. 81303 (2020). (Cited on p. 127)

"Guiding of high-intensity laser pulses in 100mm-long hydrodynamic optical-field-ionized plasma channels".

[237] Stefan Karsch. *Private communication* (Cited on pp. 131, 132). Jan. 1, 2021

[238] C. Aniculaesei, Hyung Taek Kim, Byung Ju Yoo, Kyung Hwan Oh, and Chang Hee Nam. *Review of Scientific Instruments* **89**, 2, p. 025110 (2018). (Cited on p. 135)

"Novel gas target for laser wakefield accelerators".

[239] A. A. Soloviev, M. V. Starodubtsev, K. F. Burdonov, I. Yu Kostyukov, E. N. Nerush, A. A. Shaykin, and E. A. Khazanov. *Review of Scientific Instruments* **82**, 4, p. 043304 (2011). (Cited on p. 139)

"Two-screen single-shot electron spectrometer for laser wakefield accelerated electron beams".

[240] Xiantao Cheng, Rafal Zgadzaj, Aaron Bernstein, Max Laberge, Joseph M. Shaw, and Michael C. Downer. *2018 IEEE Advanced Accelerator Concepts Workshop, ACC 2018 - Proceedings*, pp. 1–5 (2019). (Cited on p. 139)

"Compact high-resolution multi-gev electron spectrometer for PW-laser-driven plasma accelerators and approximate trajectory method for spectrum analysis".

[241] B. Hidding, G. Pretzler, M. Clever, F. Brandl, F. Zamponi, et al. *Review of Scientific Instruments* **78**, 8 (2007). (Cited on p. 139)

"Novel method for characterizing relativistic electron beams in a harsh laser-plasma environment".

[242] W. P. Leemans, R. Duarte, E. Esarey, S. Fournier, C. G. R. Geddes, D. Lockhart, C. B. Schroeder, C. Toth, J. L. Vay, and S. Zimmermann. *AIP Conference Proceedings*

1299, pp. 3–11 (2010). (Cited on p. 140)

"The Berkeley Lab Laser Accelerator (BELLA): A 10 GeV laser plasma accelerator".

[243] Carlo Benedetti, Carl Schroeder, Timon Mehrling, Blagoje Djordjevic, Stepan Bulanov, Cameron Geddes, Eric Esarey, and Wim Leemans. *2018 IEEE Advanced Accelerator Concepts Workshop, ACC 2018 - Proceedings*, pp. 2–6 (2019). (Cited on p. 140)

"INFRNO modeling of 10 GeV-class electron beams from a laser-plasma accelerator driven by the BELLA laser".

[244] S. Y. Kalmykov, S. A. Yi, A. Beck, A. F. Lifschitz, X. Davoine, et al. *New Journal of Physics* **12**, p. 045019 (2010). (Cited on p. 140)

"Numerical modelling of a 10-cm-long multi-GeV laser wakefield accelerator driven by a self-guided petawatt pulse".

[245] C. Benedetti, C. B. Schroeder, E. Esarey, and W. P. Leemans. *Physics of Plasmas* **19**, 5, p. 053101 (2012). (Cited on p. 141)

"Quasi-matched propagation of ultra-short, intense laser pulses in plasma channels".

[246] C. Benedetti, F. Rossi, C. B. Schroeder, E. Esarey, and W. P. Leemans. *Physical Review E - Statistical, Nonlinear, and Soft Matter Physics* **92**, 2, p. 023109 (2015). (Cited on p. 141)

"Pulse evolution and plasma-wave phase velocity in channel-guided laser-plasma accelerators".

[247] M. Santarsiero, D. Aiello, R. Borghi, and S. Vicalvi. *Journal of Modern Optics* **44**, 3, pp. 633–650 (1997). (Cited on p. 141)

"Focusing of axially symmetric flattened Gaussian beams".

[248] E. Esarey, A. Ting, and P. Sprangle. *Physical Review A* **42**, 6, pp. 3526–3531 (1990). (Cited on p. 143)

"Frequency shifts induced in laser pulses by plasma waves".

[249] Ming Zeng, Min Chen, Zheng Ming Sheng, Warren B. Mori, and Jie Zhang. *Physics of Plasmas* **21**, 3, p. 030701 (2014). (Cited on p. 146)
"Self-truncated ionization injection and consequent monoenergetic electron bunches in laser wakefield acceleration".

[250] J. Osterhoff, A. Popp, Zs Major, B. Marx, T. P. Rowlands-Rees, et al. *Physical Review Letters* **101**, 8, p. 085002 (2008). (Cited on p. 148)
"Generation of stable, low-divergence electron beams by laser-wakefield acceleration in a steady-state-flow gas cell".

[251] J. Faure, C. Rechatin, O. Lundh, L. Ammoura, and V. Malka. *Physics of Plasmas* **17**, 8, p. 083107 (2010). (Cited on p. 151)
"Injection and acceleration of quasimonoenergetic relativistic electron beams using density gradients at the edges of a plasma channel".

[252] R. H. H. Scott, N. Bourgeois, C. Thornton, J. Cowley, Wolf Rittershofer, Tobias Klein, Jens Osterhoff, D. R. Symes, C. Hooker, and S. M. Hooker. *Physical Review Accelerators and Beams* **23**, 11, p. 111301 (2020). (Cited on p. 151)
"Electron trapping and re-injection in prepulse-shaped gas targets for laser-plasma accelerators".

[253] F. Massimo, A. F. Lifschitz, C. Thaury, and V. Malka. *Plasma Physics and Controlled Fusion* **60**, 3, p. 034005 (2018). (Cited on p. 152)
"Numerical study of laser energy effects on density transition injection in laser wakefield acceleration".

[254] Kosta Oubrerie, Adrien Leblanc, Olena Kononenko, Ronan Lahaye, Igor A. Andriyash, Julien Gautier, Jean-Philippe Goddet, Lorenzo Martelli, Amar Tafzi, Kim Ta Phuoc, Slava Smartsev, and Cedric Thaury. *Controlled acceleration of GeV electron beams in an all-optical plasma waveguide* (Cited on p. 154). 2021
eprint: `arXiv:2108.03000`.

[255] Slava Smartsev, Clément Caizergues, Kosta Oubrerie, Julien Gautier, Jean-Philippe Goddet, Amar Tafzi, Kim Ta Phuoc, Victor Malka, and Cédric Thaury. *Optics Letters* **44**, 14, p. 3414 (2019). (Cited on p. 154)

"Axiparabola: a long-focal-depth, high-resolution mirror for broadband high-intensity lasers".